The Plasma Nitriding of Tool and Bearing Steels

by

Robert Bennett

Doctor of Philosophy

The University of Aston in Birmingham

June 1987

The University of Aston in Birmingham

Plasma Nitriding of Tool and Bearing Steels

Robert Bennett

Ph.D. Thesis

1987

There is some evidence to suggest that nitriding of alloy steels, in particular high speed tool steels, under carefully controlled conditions might sharply increase rolling contact fatigue resistance. However, the subsurface shear stresses developed in aerospace bearing applications tend to occur at depths greater than the usual case depths currently produced by nitriding. Additionally, case development must be limited with certain materials due to case spalling and may not always be sufficient to achieve the current theoretical depths necessary to ensure that peak stresses occur within the case.

It was the aim of this work to establish suitable conditions to overcome this problem by plasma nitriding. To assist this development a study has been made of prior hardening treatment, case development, residual stress and case cracking tendency.

M2 in the underhardened, undertempered and fully hardened and tempered conditions all responded similarly to plasma nitriding - maximum surface hardening being achieved by plasma nitriding at 450°C. Case development varied linearly with increasing treatment temperature and also with the square root of the treatment time.

Maximum surface hardness of M50 and T1 steels was achieved by plasma nitriding in 15%nitrogen/85%hydrogen and varied logarithmically with atmosphere nitrogen content.

The case-cracking contact stress varied linearly with nitriding temperature for M2. T1 and M50 supported higher stresses after nitriding in low nitrogen plasma atmospheres.

Unidirectional bending fatigue of M2 has been improved up to three times the strength of the fully hardened and tempered condition by plasma nitriding for 16hrs at 400°C. Fatigue strengths of T1 and M50 have been improved by up to 30% by plasma nitriding for 16hrs at 450°C in a 75%hydrogen/25%nitrogen atmosphere.

Keywords

High Speed Steel
Plasma Nitriding
Residual Stress
Rolling Contact Fatigue
Bending Fatigue

Acknowledgements

The author would like to thank the following people:

Mr. H.C.Child, F.I.M. for his help and encouragement, and Dr. S.Murphy for his time and attention.

Dr. Malcolm Hampshire for his help and advice, and RHP Ltd. and Rolls-Royce Ltd. for supplying the BT1 and M50 steels used in this work.

Dr. David Kirk for his help and advice on the residual stress work.

Finally, thanks are due to Mrs. B.Johnson for her help in the production of this thesis.

List of Figures

List of Figures

List of Figures

List of Tables

1. Introduction

High speed steels are essentially high hardness, high alloy steels, which have high strength and a resistance to temper softening. In the fully hardened condition these steels are generally regarded as brittle, as might be expected in consideration of their high hardness.

The ideal hardened and tempered structure for high speed steels is one of a fine grained tempered martensite matrix with sub-microscopic precipitates of alloy secondary hardening carbides. Small, spheroidal and uniformly distributed primary M_6C and MC type carbides should also be present.

The main characteristics of the high speed steels are obtained by heat treatment and are essentially hot hardness and strength, wear resistance and, to a lesser extent, toughness. All of these properties may be found, to some greater or lesser degree, as pre-requisites for most tooling applications.

Many engineering components need not only a hard wear resistant surface but also some degree of fatigue resistance eg. gear wheels in machines and motor vehicle gearboxes. Parts used in more arduous situations eg. bearings in aerospace applications require the additional properties of some of the high speed steels. This is becoming even more apparent in view of future aerospace requirements for next generation aero-engine bearings to operate at up to $3*10^6$DN, where DN is the product of the bearing bore diameter in mm and the shaft speed in rpm.

The need for high wear resistance and good fatigue strength in these situations can be achieved by surface hardening techniques, where the fatigue strength is improved by a combination of the higher endurance limit of the hardened case and the compressive residual stresses generated within it, and the tougher core material.

Surface treatments may be classified as mechanical or thermal eg. shot peening and induction or flame hardening, or thermochemical as with nitriding, carbonitriding and carburising.

Nitriding by gaseous and liquid salt bath processes are two of the most popular and long established methods of conferring a hard wear resistant surface on ferrous materials. However, more recently, the heat treatment industry has shown increased interest in the more modern process of plasma nitriding for tool, bearing and stainless steel treatment.

There is some evidence to suggest that nitriding of alloy steels, in particular high speed tool steels, under carefully controlled conditions might sharply increase rolling contact fatigue resistance. However, the subsurface shear stresses developed in bearing applications tend to occur at depths greater than the usual case depths currently produced by nitriding. Additionally, case depth development must be limited with certain materials due to case spalling and may not always be sufficient to achieve the current theoretical depths necessary to ensure that peak stresses occur within the case.

It is the aim of this current work to establish suitable conditions for the heat treatment of three steels - M2, T1 and M50 - to overcome these problems by the use of the plasma nitriding process. To assist this development, a study of prior hardening treatment, case development parameters, case cracking tendency and the residual stresses inherent in surface hardened layers is necessary.

2. Literature Survey

2.1. Rolling Bearings

2.1.1. Introduction

The basic idea of rolling bearings has been known for centuries. From using a tree trunk as a roller came development of the wheel and axle. Inevitably bearings based on rolling motion were developed for use in complex machine mechanisms. Rolling bearings, employing balls or rollers, are used to permit rotary motion of a shaft and are an essential part of everyday constructions such as jet and internal combustion engines, miniature instruments and bridges.

Utilisation of rolling bearings was at first obstructed by the unsuitability of materials used in their construction. However, since the advent of superior bearing steels and better manufacturing techniques, over the past half century the position has improved dramatically.

Rolling bearings comprise several parts; hardened inner and outer raceways, roller or ball rolling elements and usually a 'cage' to retain the rolling elements in place. P S Houghton[1] listed the main factors influencing the choice of one bearing type over another. The most prominent advantages are;

(a). Reduced starting friction at low speeds.
(b). Self aligning bearings will accommodate slight assembly misalignment.
(c). Both axial and radial loads can often be accommodated by one unit.
(d). Replacement is easy.
(e). Maintenance and lubrication costs are low.

The drawbacks may be;

(a). Failure may occur without warning.

(b). Higher initial costs.

(c). Whilst rolling bearings have a shorter length than the equivalent plain type, the outer diameter is necessarily larger.

2.1.2. Bearing Types

R K Allen[2] asserts that all rolling bearings may be classified under the general heading "Angular Contact Bearings" and shows this in a 'family tree' diagram, Figure 2.1. This general grouping may be further split into two broad categories: ball bearings having point contact, and roller bearings which commonly display line contact.

(A). Radial Ball Bearings

1. Single Row Deep Groove, Conrad Assembly: This is the most popular rolling bearing, having inner and outer raceway grooves with curvature radii of about 52% that of the ball diameter for most applications - see Figure 2.2. These bearings are capable of carrying high loads and also some thrust loading.
2. Single Row, Deep Groove, Filling Slot Assemblies: Machining filling slots into the raceway groove sidewalls, permits additional elements to be fitted thus improving load carrying capacity but reducing thrust load capability.
3. Single Row, Angular Contact Ball Bearings: These are designed for radial/thrust loads or heavy thrust loads. Thrust may only be supported in one direction and capacity depends upon the contact angle (Figure 2.3). Radial bearings have contact angles $\alpha < 30°$ whereas thrust assemblies tend towards $\alpha > 30°$.

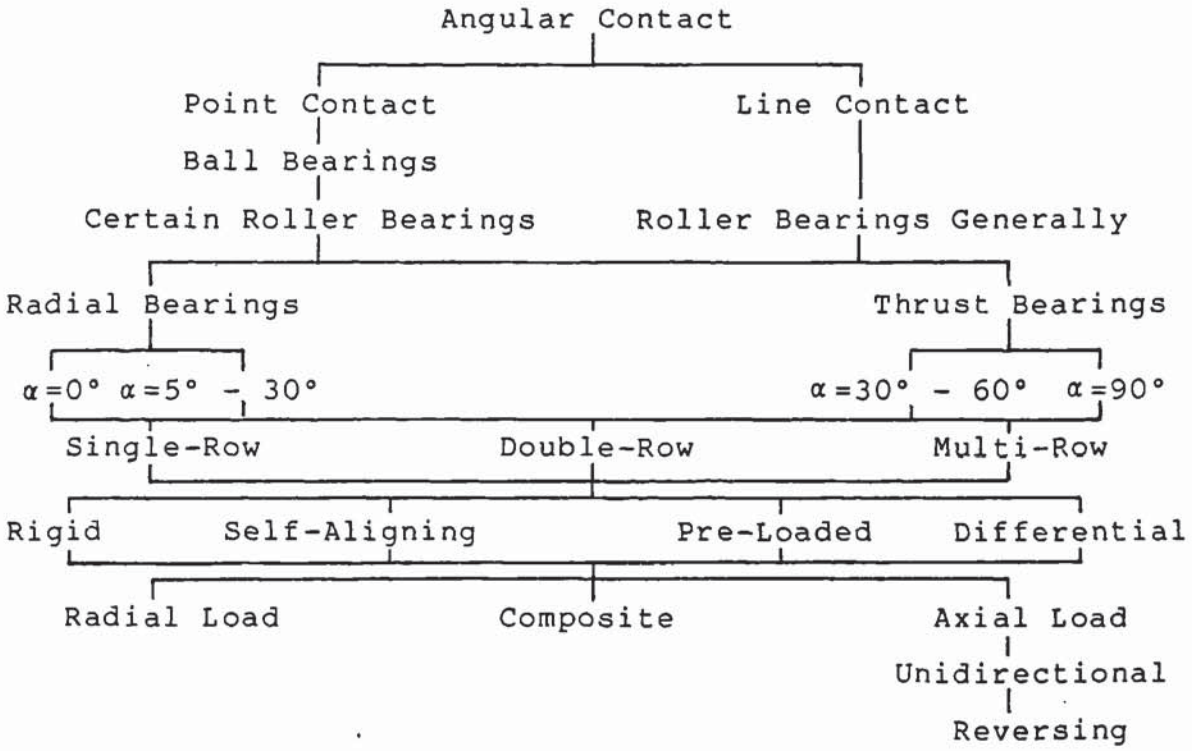

Fig.2.1. Angular Contact Bearings.[2]

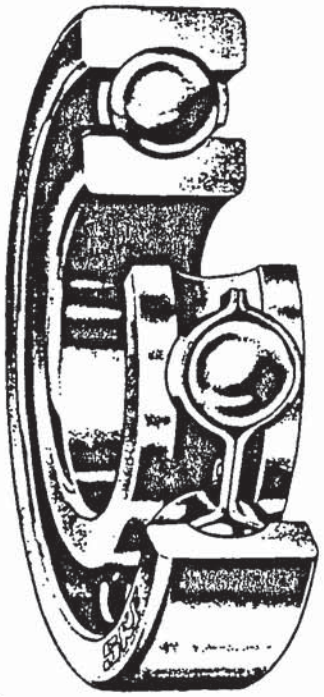

Fig.2.2. A Single Row, Deep Groove Conrad Assembly.

4. Ball Thrust Bearings: These carry high thrust loads but may also accommodate some radial load. At a contact angle of 90° no radial loading is possible.

Groups 1 to 3 may also be used in tandem or as double-row assemblies to take heavier loads or to accommodate thrust loading in either direction.

(B). Roller Bearings

Roller bearings are used for large load bearing applications ie. larger than can be carried by ball bearing assemblies.

1. Cylindrical Roller Bearings: These are used for high speed operation because they have low frictional torque characteristics. The ends of the rollers may be 'crowned' to reduce high stresses there. Figure 2.4.
2. Needle Roller Assemblies: So-called due to the high length to diameter ratio of the rollers, these bearings are used where radial space is restricted and the rollers may even bear directly onto a hardened shaft removing the need for an inner race.
3. Tapered Roller Bearings: Single row bearings can support heavy radial and thrust loading. These bearings are restricted to low speeds of operation due to frictional forces generated at the guide flange.
4. Spherical Roller Assemblies: The outer raceway of these bearings is partially spherical and they are therefore internally self-aligning. High frictional forces restrict the use of these bearings to low speed applications.

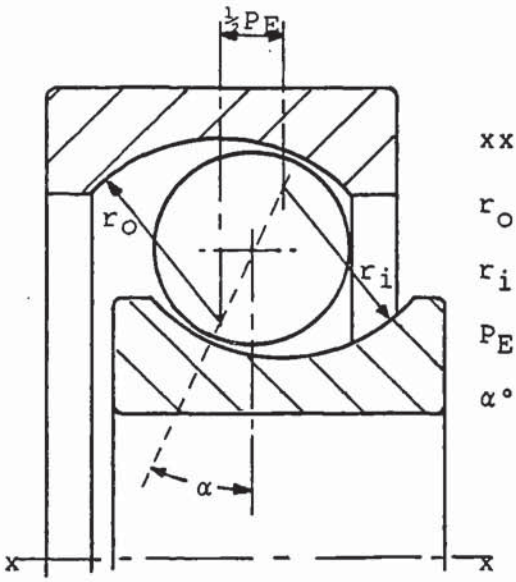

xx - bearing rotation axis

r_o - outer track radius

r_i - inner track radius

P_E - free end-play

α° - contact angle

Fig.2.3. The Free Contact Angle on a Radial Ball Bearing.[1]

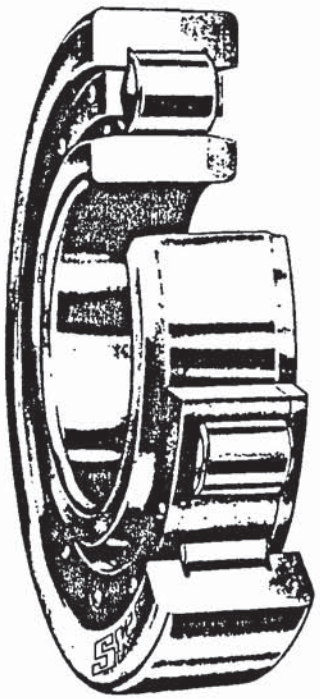

Fig.2.4. A Radial Cylindrical Roller Bearing.

2.1.3. Bearing Materials

Steels used in bearing assemblies need good surface finish, wear and fatigue resistance under high compressive loadings and must be heat treatable to at least 58Rc hardness.

Service life of bearings is limited by the fatigue life of the rolling surfaces, which is influenced by many factors. The main influences in the fatigue of rolling elements are the operating conditions of loading, environment and the nature of the lubricant, and the material properties[3].

The use of rolling bearings in high technology fields has highlighted the need for bearing materials capable of withstanding operation at elevated temperatures. Conventional materials such as bronze, cast iron and the ball bearing steel EN31 or SAE52100[4] are only serviceable up to about 180°C. (or the approximate tempering temperature) due to softening and loss of fatigue resistance above this temperature[5]. High temperature operation then, may be considered to prevail above this threshold level[6].

Problems of high temperature operation may be overcome by the use of copious quantities of coolant to maintain low temperatures for lubricants and conventional bearing materials, but this may cause problems at higher speeds of rotation due to excessive power loss through heat transfer to the lubricant[7]. In addition to this problem, limited space and cooling capacity in modern design concepts have placed onerous demands upon the materials used.

Steels used at elevated temperatures must have adequate hot hardness, oxidation resistance and dimensional stability. High speed tool steels containing tungsten and molybdenum

have high tempering temperatures and are thus well suited to elevated temperature applications. Other suitable materials are sintered carbides, refractory metals and ceramics, all of which may be used for particularly arduous rolling contact applications.

A safety factor has been proposed, for elevated temperature work, such that tempering of materials used should exceed the maximum service temperature by 45 to 50°C. This restricts the most commonly used high speed steels, AISI M50 and AISI T1, to operating temperatures of about 450 to 500°C. (Table 2.1 shows typical chemical analyses for these materials). AISI T15 ie. 1.55%C, 0.3%Mn, 0.3%S, 4.5%Cr, 5.0%V, 13%W, 5%Co with optional 0.5%Mo, has also been studied in the U.S.A.[8] but use of this material is unlikely to alter the temperature constraints unduly.

Various effects such as uneven stressing, temperature, lubricant type and environment may often cause one element of a bearing to fail prematurely. Replacement by a superior material has not proved successful in overcoming the problem since elastic/plastic properties of materials in contact have a significant effect upon rolling contact fatigue resistance[9].

	C	Mn	Si	Cr	V	W	Mo	Co
M2	0.85	0.30	0.30	4.00	2.00	6.00	5.00	-
T1	0.75	0.30	0.30	4.00	1.00	18.0	0.70	-
M50	0.80	0.25	0.25	4.00	1.10	-	4.25	-

Table 2.1. Typical Chemical Analyses

2.1.4. Bearing Lubricants

The ideal situation for lubricants is when the two surfaces in rolling contact are separated by a reasonably thick film of lubricant that will support the prevalent load. To date modern bearings, used in the extremes of temperature, pressure and vacuum prevalent in aerospace applications, have been reasonably well protected by such lubricants as molybdenum disulphide, but they still suffer fatigue when operating for long periods and under heavy loads.

Dry film lubricants which can be used to very high temperatures (eg. approximately 650°C.) are disadvantaged by elevated temperature service since they cannot readily act as a coolant as well as a lubricant. Therefore much work has been carried out on ester based fluids[7,10] - operational up to approximately 220°C - polyalkylene glycols, diesters and polyphenyl ethers[5] for use as lubricants.

It is apparent that future developments in bearing materials for high temperature applications must be accompanied by similar developments in the field of high temperature lubricants.

2.2. Contact Stress and Deformation

Rolling bearings in service depend primarily on surface endurance rather than tensile strength to give satisfactory performance. It is important therefore to have some understanding of the conditions and stresses near the element surfaces in rolling contact.

2.2.1. Surface Stresses

Under theoretical conditions of zero load, anelastic rolling elements may be divided into two broad categories; those having line contact and those with point contact. However these conditions are impossible to achieve under practical conditions. Boussinesq[11] developed a theory for the simple radial distribution of stress within a semi-infinite solid (Figure 2.5). He said that for a surface free of shear stress, the radial stress 'σ_r' would be (using Polar Co-ordinates) given by:

$$\sigma_r = \frac{2F\cos\theta}{\pi r} \qquad \ldots\ldots(2.1)$$

This equation shows that as r tends to 0, i.e. line contact, σ_r becomes infinitely large; a condition which is impossible without the onset of gross yielding or material failure at the surface. Therefore even the smallest force would produce infinite stress and thus a certain degree of elastic (or plastic) deformation must take place until a contact area sufficient to support the load is established. Even the hardest material will deform to some extent.

The contact area developed may be circular, elliptical or rectangular (Figure 2.6). The contact zone is finite and may be defined by the classical theory developed by Hertz[12] in 1881.

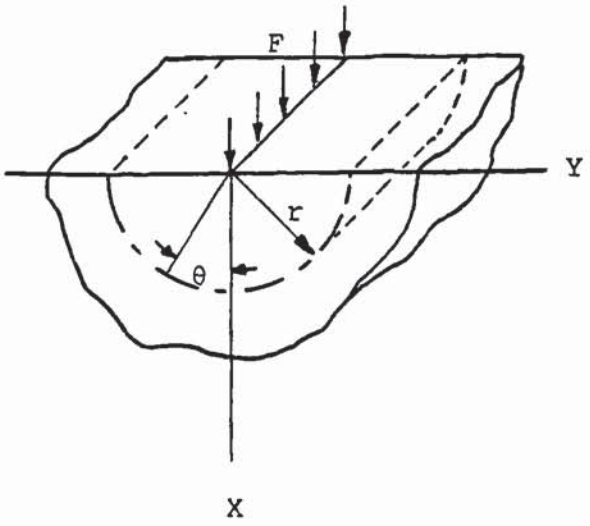

Fig.2.5. A Line Load Acting on a Semi-Infinite Body - Model for Boussinesq Analysis.

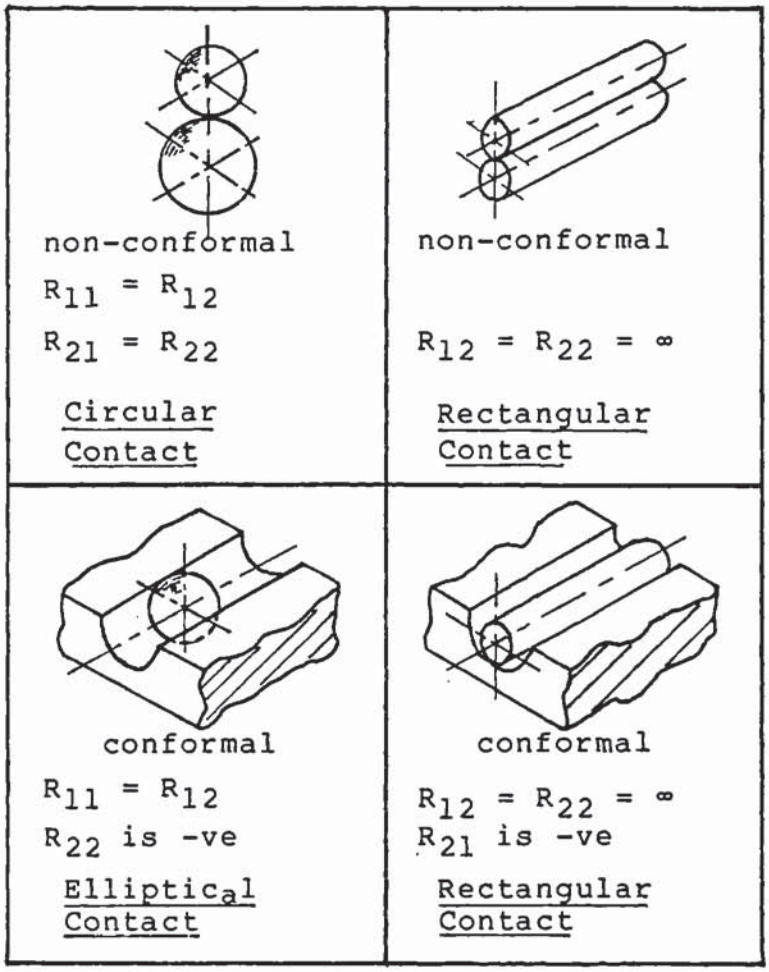

Fig.2.6. Contact Deformation Areas arising from Different - Contact Body Configurations.

In his studies Hertz made several assumptions:

1. All deformation occurs in the elastic region of the material studied.
2. No tangential forces are induced i.e. no shear stresses are considered.
3. Contact areas are flat and small compared to the radii of curvature of the bodies under load.
4. Radii of curvature of the contact areas are large compared to the dimensions of these areas.

Although his investigations were not specifically related to rolling bearings, subsequent work by such authors as Stribeck, Goodman and Allen[2] has shown his deductions to be acceptable as a basis for research and many of his expressions to be accurate enough for practical purposes.

The mathematical derivations of Hertz's equations are quite complex and are interrelated with elasticity theory as demonstrated by Timoshenko and Goodier[13] who studied the distribution of stress over the contact area and the shape and size of the pressure area when solid elastic bodies roll together.

The stress distribution in two contacting bodies is equivalent to the pressure distribution of the applied load. The bodies under an applied load 'F' form a contact 'ellipse' with semi-major and semi-minor axes 'a' and 'b'. It is possible to construct an 'ellipsoid of rotation' upon this contact area (Figure 2.7), vertical co-ordinates corresponding to stresses normal to the pressure area[14].

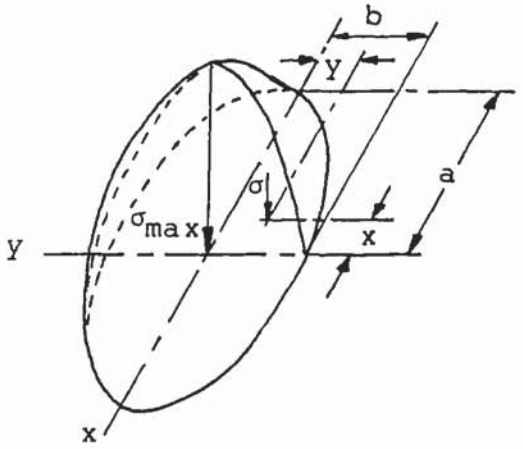

Fig.2.7. Ellipsoidal Surface Compressive Stress - Distribution for Point Contact.

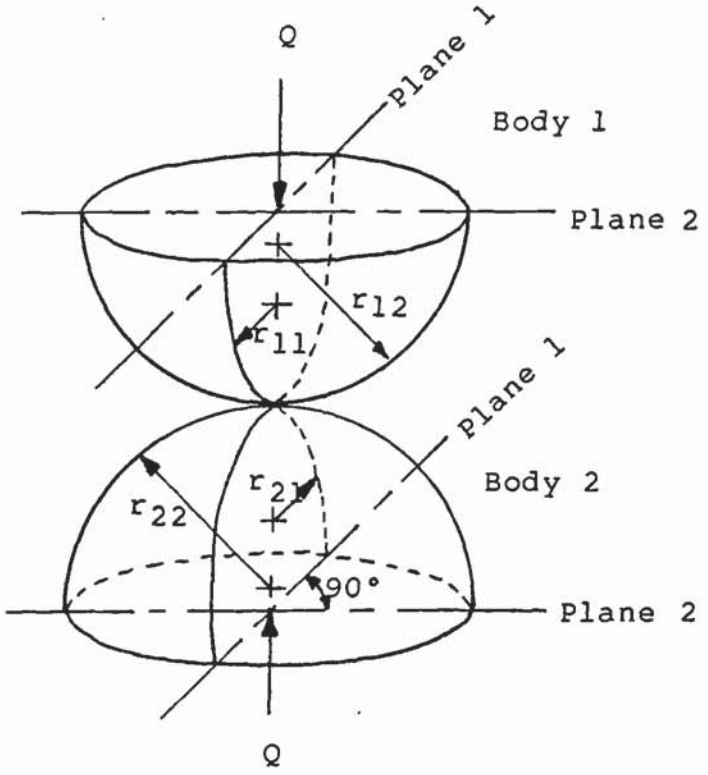

Fig.2.8. Radii of Curvature of Two Contacting Bodies.

This construction is therefore called the normal stress ellipsoid and is described (using Cartesian notation) by the Hertz equation:

$$z = \frac{3F}{2\pi ab}\left[1 - \frac{x^2}{a^2} - \frac{y^2}{b^2}\right]^{\frac{1}{2}} \qquad \ldots\ldots(2.2)$$

- where 'πab' is the area of the projected pressure ellipse and

$$a = a^*\left[\frac{3F}{2\Sigma_\rho}\left\{\frac{(1-\nu_1^2)}{E_1} + \frac{(1-\nu_2^2)}{E_2}\right\}\right]^{1/3} \qquad \ldots\ldots(2.3)$$

$$b = b^*\left[\frac{3F}{2\Sigma_\rho}\left\{\frac{(1-\nu_1^2)}{E_1} + \frac{(1-\nu_2^2)}{E_2}\right\}\right]^{1/3} \qquad \ldots\ldots(2.4)$$

a^* and b^* are the dimensionless semi-axes and are functions of the radii of curvature of the contacting bodies as described by Figure 2.8. The definition of these terms involves the curvature sum 'Σ_ρ', curvature difference 'F_ρ' and complete elliptic integrals and is therefore quite involved. However calculation of Σ_ρ and F_ρ is relatively easy and tables/graphs are available from which to derive the terms a^* and b^* (see Appendix 1).

At any point on the periphery of the contact area:

$$\left[1 - \frac{x^2}{a^2} - \frac{y^2}{b^2}\right]^{\frac{1}{2}} = 0 \qquad \ldots\ldots(2.5)$$

- and therefore 'z', the vertical stress component is zero at the boundary of the pressure area.

At the centre of the base where $x = 0$, $y = 0$:

$$\left[1 - \frac{x^2}{a^2} - \frac{y^2}{b^2}\right]^{\frac{1}{2}} = 1 \qquad \ldots\ldots(2.6)$$

- which is the maximum value attainable and thus this is the point of maximum stress.

$$z = \sigma_{max} = p_{max} = \frac{3F}{2\pi ab} \qquad \ldots\ldots(2.7)$$

The mean stress, $\sigma_{mean} = p_{mean}$ (mean pressure) = $F/\pi ab$, so that

$$\sigma_{max} = p_{max} = 1.5p_{mean} \qquad \ldots\ldots(2.8)$$

For the special case of the elliptical eccentricity factor $K = a/b = \infty$ ie. ideal line contact, then:

$$z = \frac{2F}{\pi ab}\left[1 - \frac{y^2}{b^2}\right]^{\frac{1}{2}} \qquad \ldots\ldots(2.9)$$

and

$$\sigma_{max} = p_{max} = \frac{2F}{\pi ab} \qquad \ldots\ldots(2.10)$$

(See Figure 2.9)

2.2.2. Sub-Surface Stresses

Hertz, in his studies, considered only surface conditions. The engineer might logically expect failure to occur first in the centre of the pressure area where maximum stressing occurs. However it has been demonstrated by Scott[3] and Davies and Day[14] that rolling contact fatigue may be originated below the surface as well as upon it. It is therefore important to understand the magnitude, location and 'character' of the sub-surface stresses.

Halling and Nuri[16] assert that under plane strain conditions (ie. as in the Boussinesq example) maximum shear stress (τ_{max}) always occurs in the 'xz' plane and :

$$\tau_{max} = \frac{\sigma_r}{2} = -\frac{F.\cos\theta}{\pi r} \qquad \ldots\ldots(2.11)$$

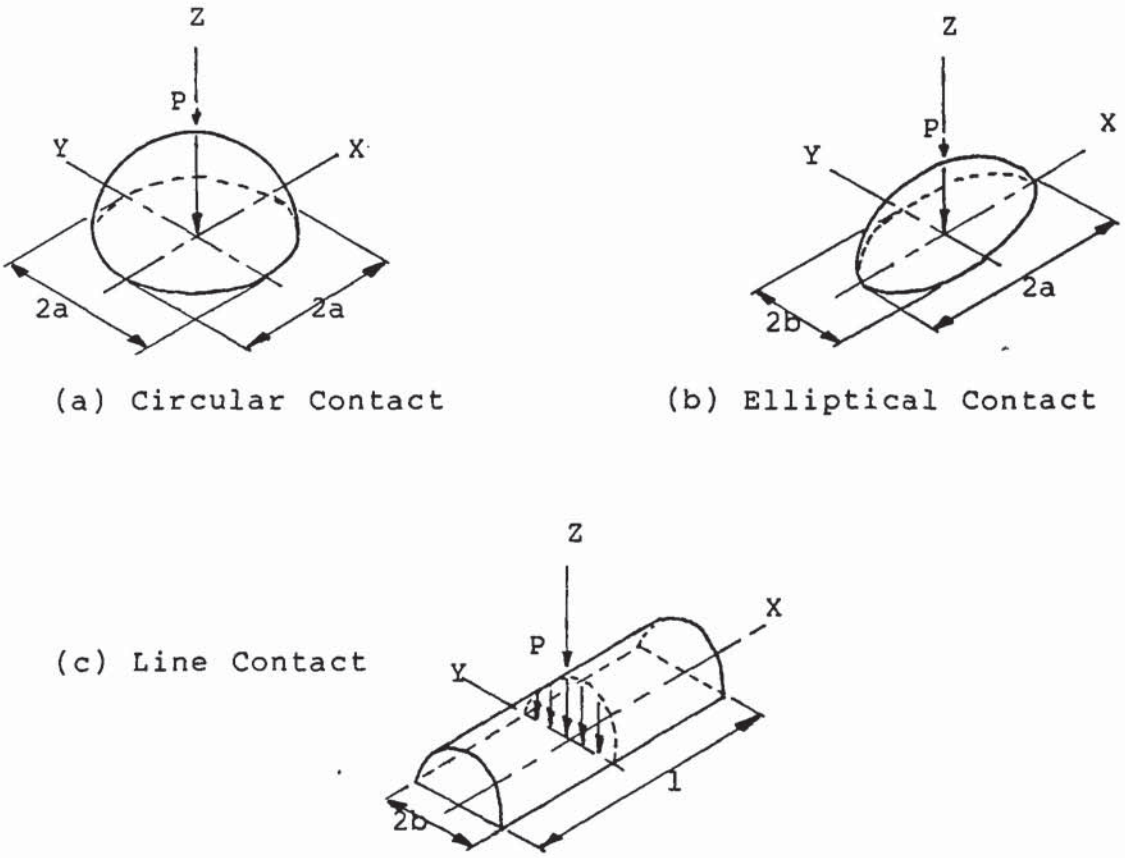

Fig.2.9. Surface Stress Distributions.

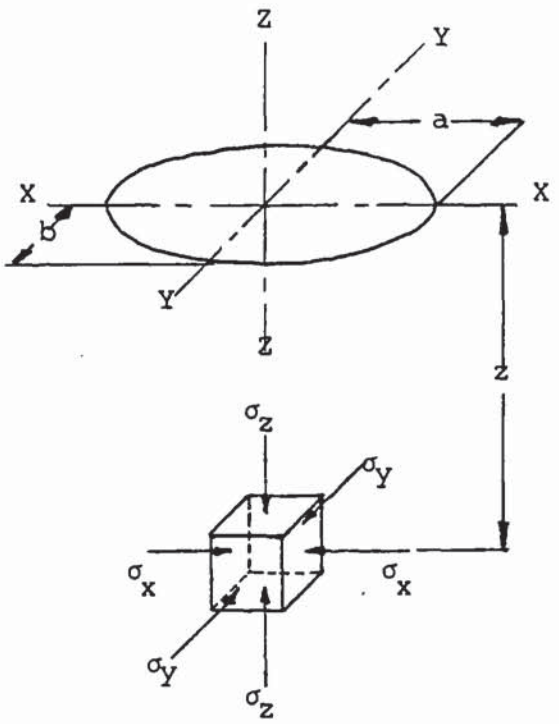

Fig.2.10. Principal Stresses Occurring on an Element - Along the z-axis Below the Contact Surface.

By plotting of isochromatic circles of τ_{max}, it can be shown that, as τ_{max} increases to 'j' (material yield shear stress) yielding occurs first at the surface. When shear stresses are also considered:

$$\tau_{max} = \left\{\left[\frac{\sigma_x - \sigma_z}{2}\right]^2 + \tau_{xz}^2\right\}^{\frac{1}{2}} \quad \ldots\ldots(2.12)$$

(as defined by Mohr's circle of stresses). Isochromatic circles now show τ_{max} to occur below the surface and that as the load increases, τ_{max} doesn't attain the yield shear stress until the maximum contact pressure (p_{max}) is more than twice the flow shear stress. It might be expected that surface yielding would occur at '2j' ie. equivalent to the tensile yield stress, but because of the compressive principal stresses at the centre of the contact area, p_{max} may exceed this value without any plastic flow. So the hydrostatic components of the stress system don't contribute to plastic flow and therefore contact pressures can exceed the critical values which ought to cause material yielding. Additionally, even after sub-surface yield initiation, there is little plastic flow because the plastic zone is constrained by 'elastic' material on all sides.

As the load increases further the plastic zone grows and spreads to the surface causing indentation. This occurs when the mean contact pressure reaches approximately three times the tensile yield stress.

Thomas and Hoersch[17] and Jones[18] derived equations to calculate the three principal stresses at any depth below the surface along the z-axis. Because the maximum Hertzian stress acts along the z-axis, the principal stresses must attain maximum values there also (Figure 2.10).

The principal stresses are compressive and diminish as depth increases, and may be calculated using the equations below[13]:

$$\sigma_x = -2\nu p_{max} - (1 - 2\nu)p_{max}\left[\frac{b}{a + b}\right] \quad \ldots\ldots(2.13)$$

$$\sigma_y = -2\nu p_{max} - (1 - 2\nu)p_{max}\left[\frac{a}{a + b}\right] \quad \ldots\ldots(2.14)$$

$$\sigma_z = -p_{max} \quad \ldots\ldots(2.15)$$

- where σ_z is the largest of the stresses. The main shear stress τ_{max}, resulting from stresses σ_y and σ_z, according to the equation:

$$\tau_{max} = \frac{1}{2}(\sigma_z - \sigma_y) \quad \ldots\ldots(2.16)$$

- reaches a maximum value at some depth below the surface on the z-axis and occurs at an angle of 45° to the surface. - (Figure 2.11).

This depth has been calculated as 0.467b and 0.786b for point and line contact respectively, where 'b' is the semi-minor axis of the contact ellipse. For theoretical point contact the shear stress at 0.467b is approximately $0.3p_{max}$.

As a rolling element passes over the surface of a bearing raceway, the maximum shear stress on the z-axis fluctuates from 0 to τ_{max}. For an element rolling in the y-direction, the shear stress in the 'yz-plane' ie. the orthogonal shear stress 'τ_{yz}', varies from negative to positive as y changes from less than to more than zero. Therefore the maximum variation of this shear stress for any point over which the element rolls, is $2\tau_{yz}$ at a given depth.

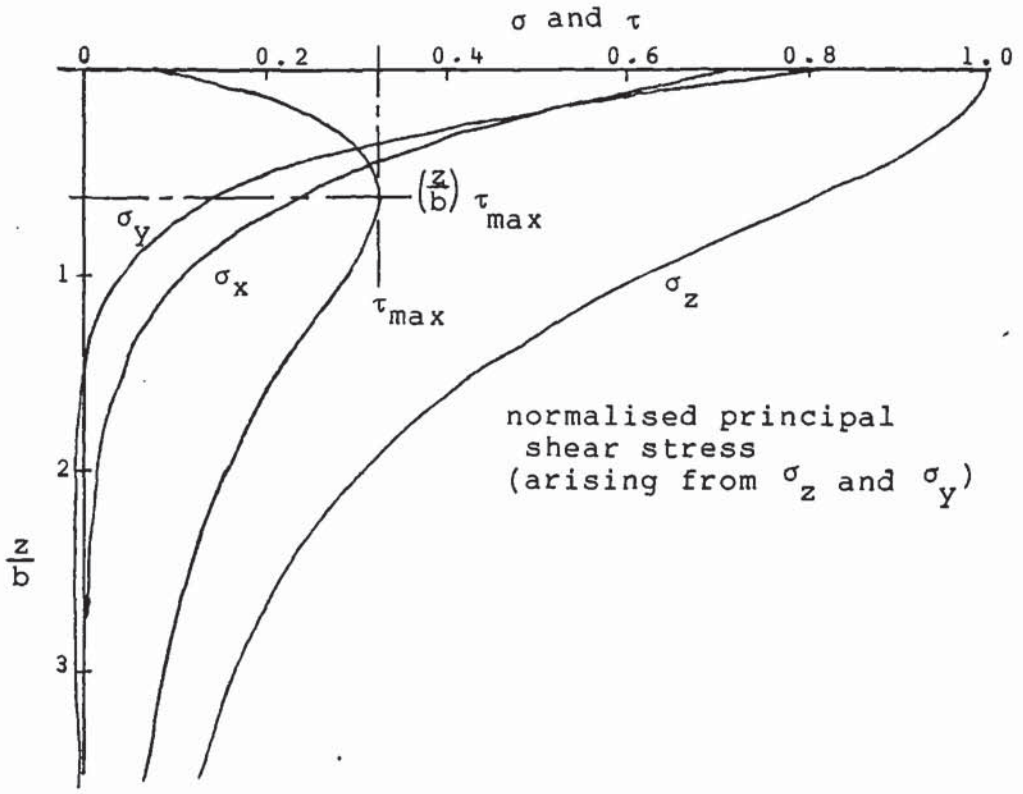

Fig.2.11. The Variation of Pricipal and Shear Stresses - with Depth from the Surface.

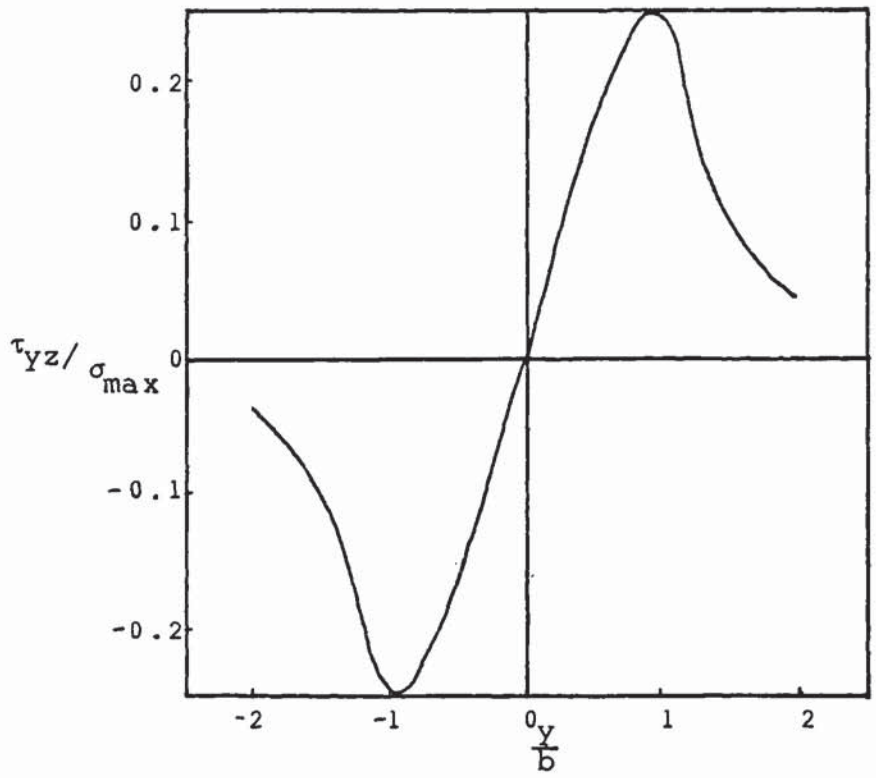

Fig.2.12. τ_{yz}/σ_{max} versus y/b for b/a = 0 and z = z_0

τ_{yz} occurs in an orthogonal plane, with respect to the external load, that is parallel to the surface and also to the y-axis. Figure 2.12 shows this alternating shear stress for a theoretical line contact. The largest orthogonal shear stress for line contact occurs at a depth of 0.5b and at 0.35b for a point contact, the double stress amplitudes being $0.5p_{max}$ and $0.43p_{max}$ respectively.

Since the maximum orthogonal shear stress amplitude (Figure 2.12) is greater than the maximum shear stress it might be inferred that this is the significant factor in fatigue failure under rolling load. However, it occurs closer to the surface and recent work has shown the maximum shear stress to be the dominant component.

There are other stresses acting on the rolling surface. Timoshenko and Goodier[13], in consideration of circular contact areas and using polar co-ordinate notation, state that the periphery of the contact 'ellipse' is in pure shear as a consequence of the stresses σ_r and σ_θ. σ_r is tensile in nature and is given by:

$$\sigma_r = \frac{1}{3}(1 - 2\nu)p_{max} \qquad \text{.....(2.17)}$$

- the other stress, σ_θ, acting circumferentially and being equal in size but opposite in sign to σ_r. This stress is approximately $0.13p_{max}$ ie. much smaller than the maximum shear stress but it is on the surface and might potentially aid surface spalling initiated by the maximum shear stress.

It is possible to use the depth to maximum shear stress, $z_{\tau max}$, as a criterion for case depth requirements in case hardened bearings.

It has been generally accepted within the bearing industry that case depth, on case hardened components, should approximate to three times the depth to maximum shear stress. This ensures that any crack initiation due to the shear stress will occur within a region of supposed high compressive stress thus opposing any propagation of the crack. This criterion does not really make any consideration of the much higher core hardnesses available in the high speed steels now being used in rolling bearings.

Recent studies imply that this safety factor may be over-conservative in its magnitude with respect to case hardened high speed steels. The influence of surface residual stresses and their importance to the development of a more reasonable criterion will be discussed later.

2.3. Tools

2.3.1. Introduction

Although the first use of steel was probably for tools, nowadays tool steels represent less than one percent of the total steel production. Current tool steels tend to be made of widely differing chemical compositions, to bestow favourable properties for specific applications. Tool steel uses may all be grouped under five basic metal forming processes (Table 2.2).

1. Forming	(a) Cold (b) Hot
2. Shearing	(a) Blanking (b) Shearing (c) Cutting (shear blades and slitters) (d) Trimming
3. Cutting (Mat'l Removal) Machining	(a) Metal Cutting (b) Non-metal Cutting (c) Chipping
4. Moulding	(a) Die Casting (b) Plastic Moulding (c) Ceramic Moulding (d) Powder Moulding
5. Miscellaneous	(a) Wear Parts (b) Percussion Tools (c) Gauges

Table 2.2 - The Five Basic Metal Forming Processes[19]

2.3.2. Applications

Die blocks and inserts or cold heading dies and punches, as used in hot and cold forming, are subject to sliding contact in service and must necessarily endure high cyclic stresses. Selection of a steel for this application then, would require consideration of wear resistance, toughness, machinability for forming the dies and, in the case of hot forming tools, hot hardness.

Cutting tools, as used in material removal (lathe tools and chisels) and shearing (punches and piercers etc.), are also subject to high stresses. These, like forming tools, require wear resistance and toughness. Hot hardness is also a necessity for machining tools. Low susceptibility to heat treatment distortion is also desirable.

Die casting and plastic, ceramic or powder forming are all moulding operations, and steels used for these tools often operate under the most severe conditions. The moulding steels require high strength, hardness and often corrosion resistance and machineability, in addition to the properties necessary for the tools already mentioned.

Wear parts e.g grinder plates, require wear resistance as do bearing races and balls. Gauges need high hardness, size stability and good surface finish. All may be classified as miscellaneous applications.

It is obvious therefore that one of the first criteria of material selection for a tooling application is to identify the necessary properties of the tool. There are three major facets of tool steels which control, more than any other, the selection of one type over another for a particular application. These are wear resistance, toughness and hot hardness[19].

Although the semi-high and high speed steels are not known for their toughness characteristics, they do have good wear resistance and hot hardness and are used in many applications. The most popular of the high speed steels is AISI M2, a tungsten-molybdenum type steel which may be used in many cold forming applications.

AISI T1 and the semi-high speed steel M50 are the tool steels favoured by the bearing industry in Europe and the United States for bearing raceways and rolling elements. Table 2.1 shows typical chemical analyses for these steels.

2.3.3. High Speed Tool Steels

2.3.3.1. Structure-Property Relationships in H.S.S.

High speed steels have many characteristics in common throughout the grouping despite widely varying chemical composition. These steels essentially have medium to high carbon with about 4% chromium, up to 5% vanadium and varying amounts of either tungsten or molybdenum or both. They may also contain up to 12% cobalt[19]. Carbon and cobalt are austenitising elements - tungsten, molybdenum, chromium and vanadium all being ferrite stabilisers. High percentages of ferritising elements coupled with a low carbon content may lead to the formation of intermetallic compounds and the retention of ferrite after hardening; an undesirable situation[20].

The major alloying elements of tool steels also form carbides, vanadium being the strongest and chromium the weakest of the carbide formers. Mukherjee[21] however, asserts that cobalt is not normally considered as a carbide former even though it can occur in M_6C type carbides with molybdenum and tungsten.

All high speed steels with sufficient carbon to provide excess alloy carbides after heat treatment will harden to a minimum of Rc63. However, the most important property common to all high speed steels is the retention of high hardness at elevated temperatures.

It is generally accepted that hot hardness is attributable to the precipitation of strong secondary hardening carbides of high stability while the high wear resistance of these steels is due to the large volume fractions of undissolved primary alloy carbides[21]. For toughness one desires tempered martensite formed from a fine grained austenitic structure and, to impart dimensional stability, complete transformation to martensite of a uniform structure with low carbide segregation.

In practice the steels are used in the hardened and tempered condition and all display tempered martensite, undissolved alloy carbides and, in most instances, a small amount of retained austenite.

2.3.3.2. The Importance of Alloy Elements

Roberts[19] and Mukherjee[21] are two of the many workers who have studied the effects of individual elements upon properties. In general, increasing the carbon content increases the likelihood of retained austenite and lowers the solidus and liquidus temperatures. Thus it is important to 'link' the carbon content to that of the alloying elements, in particular vanadium[20], to avoid hardening and stability problems. It is well known that carbon increases the hardness of martensite and that it is thus of paramount importance to the hardening process of most commercial steels. Since most of the carbon is 'tied up', in the form of alloy carbides, some of it must be redistributed to the matrix by partial carbide dissolution during austenitising and prior to quenching.

Tungsten and molybdenum, being from the same group of transition metals and of similar atomic size, behave similarly and therefore are interchangeable to some extent. Tungsten is about twice the atomic weight of molybdenum and may be replaced by about half as much molybdenum to produce a particular type of alloy carbide phase. These elements both form stable secondary hardening carbides to give improved hot hardness while chromium improves corrosion (scaling) resistance and inhibits softening during tempering. Vanadium forms very hard stable carbides and thus confers resistance to grain growth during hardening, wear resistance and secondary hardening. These alloying elements also generally improve the hardenability.

It is apparent that the alloying elements, as carbides, exert considerable influence upon the properties of high speed steels. They do so via the composition of the matrix, affecting directly the hot hardness and temper resistance and indirectly the wear resistance due to its dependence on carbide volume fraction and hardness.

Nitrogen in these steels can form nitrides with the alloying elements which may resemble the carbides. This is due to the similarity in atomic size of carbon and nitrogen atoms. Stevens et al[22] assert that nitrogen stabilises M_6C and MC type carbides and may be advantageous. Due to the replacement of carbon atoms by nitrogen in the lattice structure these phases may more correctly be described as carbonitrides and not nitrides or carbides.

2.4. Heat Treatment

Heat treatment is carried out to effect an improvement in the cast or worked structure, of a metal, to confer superior physical and mechanical properties upon it.

2.4.1. Hardening and Tempering

The hardening treatment involves austenitising, oil or air quenching followed by a series of tempering treatments to 'soften back' the hardened structure to the desired level of hardness.

The austenitising process dissolves 'free carbides' in the structure. As the hardening temperature is increased, so does the solution of the pro-eutectic/pro-eutectoid carbides, thereby effecting a redistribution of the 'tied-up' alloying elements from carbides into the austenite matrix. Matrix enrichment, particularly with carbon, gives a suppression of the M_f temperature to less than ambient - resulting in the presence of retained austenite in the hardened structure.

The MC and M_6C type eutectic carbides, being larger and more thermodynamically stable, are not taken into solution as readily as the smaller $M_{23}C_6$ pro-eutectoid carbides. $M_{23}C_6$ carbides are taken completely into solution at temperatures in excess of 1090°C.[23] and thus provide the bulk of the carbon available in the matrix for the hardening effect of the martensite transformation during quenching. Additionally, matrix enrichment progresses towards saturation to such an extent that further dissolution of the more stable eutectic carbides is inhibited - making complete austenitisation practically impossible without a substantial increase in the hardening temperature.

The remaining carbides help to restrict austenitic grain growth, which would otherwise be rapid at the temperatures used for hardening[19].

Just as hardening temperature is an important control parameter, so is the time at temperature for similar reasons, since dissolution of carbides takes a finite time to occur. As-quenched hardness increases to a maximum as the hardening temperature is elevated and then decreases with further temperature rise as retained austenite becomes an increasing proportion of the hardened structure (Figure 2.13)[21]. Lower hardening temperatures favour improved toughness but have lower hardnesses after tempering. High temperatures detract from both toughness and, if retained austenite is present in any quantity, hardness.

Quenching is carried out to transform austenite to martensite. Usually transformation is incomplete and the quenched structure contains a small amount of retained austenite. Primary carbides are unaffected and are embedded in the martensitic matrix. High speed steels, having high hardenability, are capable of fully hardening during air cooling. This reduces the possibility of cracking or distortion due to the high residual stresses imposed by rapid cooling.

The M_s temperature for M2 occurs at 150 to 180°C. after austenitising at approximately 1200°C. The transformation to martensite is not complete at room temperature and, the transformation rate falls with decreasing temperature[24] to such an extent that austenite is still present at temperatures approaching -80°C.

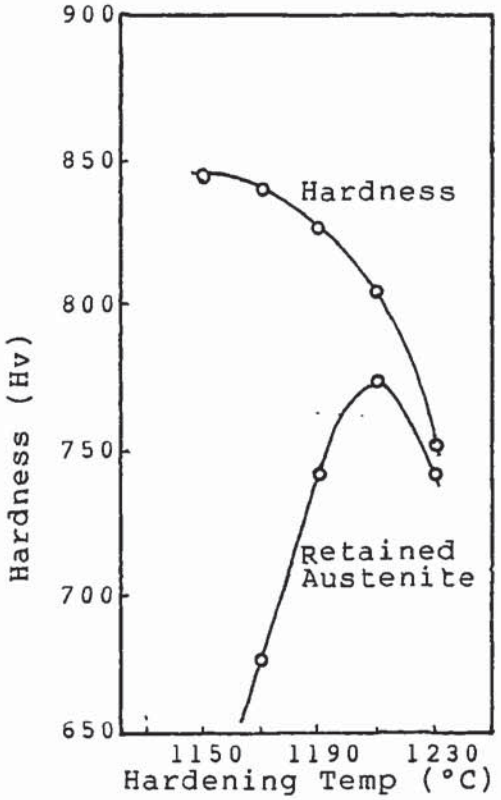

Fig.2.13. Relationship Between Hv, Retained Austenite - and Hardening Temperature in M2 H.S.S.

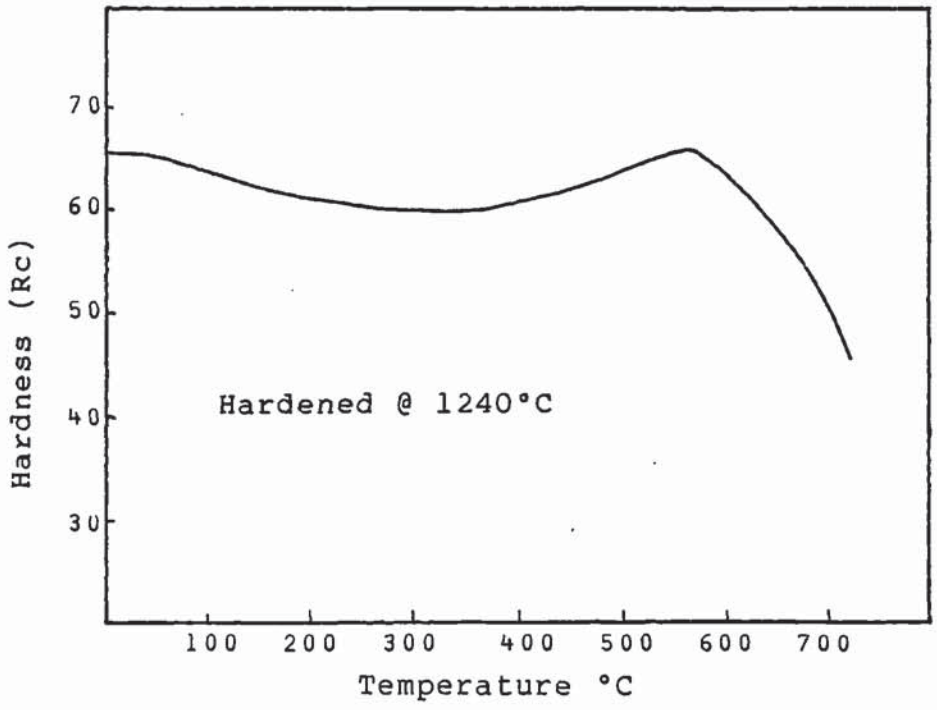

Fig.2.14. Tempering Curve for BM2-Type Steel.[27]

Cias[25] observed that at cooling rates slower than approximately $3°C.s^{-1}$, a high temperature reaction occurred, causing destabilisation of the austenite by depletion of matrix alloy elements to form carbide precipitates. This resulted in a reduction of the amount of retained austenite at room temperature. However, the martensite formed was also somewhat depleted in carbon and the hardness suffered.

Support for this is given by Horton[26] who surmised that due to the high interstitial carbon content of the steel and since solubility of the alloy elements in austenite must decrease with falling temperature, precipitation must occur provided that the cooling rate is slow enough ie. the thermodynamics for nucleation and growth are favourable.

Tempering consists of heating the hardened steel to below the critical temperature, and holding at that temperature long enough to achieve desired changes in stress and structure. Tempering is time dependent but logarithmic laws apply such that the first period of treatment is the most important. In most cases the hardened structure is one of martensite and carbide with a small amount of retained austenite.

During treatment the martensite is tempered, secondary hardening carbides precipitate and begin to grow, and on cooling some of the retained austenite decomposes to untempered secondary martensite. Cooling to sub-zero temperatures after tempering can transform still more of the retained austenite although probably not all of it. So in order to remove or stabilise any remaining austenite and to temper the secondary martensite, it is normal practice with these steels to carry out multiple tempering operations.

During tempering these steels exhibit secondary hardening due to the precipitation and growth of submicroscopic carbides (Figure 2.14)[27]. Payson[28] and Mukherjee[21] consider that the transformation of retained austenite plays no part in secondary hardening although, if there is a significant amount of austenite present, room temperature hardness can benefit by its transformation to martensite.

The tempering of steel can be divided into four overlapping parts. The first stage is associated with softening. On tempering up to about 270°C, the tetragonal martensite decomposes by carbon rejection, to a more cubic structure. The rejected carbon is precipitated as epsilon carbide, which is hexagonal in nature and approximates to $Fe_{2.4}C$. It is metastable and subsequently disappears with the appearance of Fe_3C at 300 to 400°C. ε-carbide precipitates as thin plates with an orientation of[29]:

$$\begin{matrix}\{001\}_\alpha & // & \{00\bar{0}1\}_\varepsilon \\ \{101\}_\alpha & // & \{10\bar{1}1\}_\varepsilon\end{matrix}$$

The initial precipitation of $Fe_{2.4}C$ may result in a slight hardening but the overall effect, as dissolution and precipitation of Fe_3C at higher temperatures proceeds, is softening with an associated reduction in specific volume and increased magnetism. The precipitated Fe_3C has a habit plane of {110} or {112} in the martensite ie. different to the $Fe_{2.4}C$, and is therefore thought to nucleate separately after the ε-carbide has gone back into solution[29].

The second stage, occurring at about 400 to 565°C, involves the partial re-solution of Fe_3C and a precipitation from the tempered martensite of M_2C alloy carbides and can be recognised by a pronounced hardening effect.

The third stage occurs on cooling and relates to the transformation of retained austenite. The $\gamma \rightarrow \alpha'$ reaction is probably preceded by the precipitation of alloy carbides from the austenite thus raising the M_s temperature and destabilising the austenite. A large increase in the specific volume is associated with this transformation, as is increased room temperature and hot hardness.

The fourth stage, usually associated with high temperatures (above about 650°C), is not often seen in commercial tempering, but involves re-solution of the M_2C and remaining Fe_3C type carbides and precipitation of M_6C and $M_{23}C_6$ carbides. Drastic softening occurs in this stage.

The alloying elements, other than the interstitial carbon, have no real effect in the early stages of low temperature tempering, but they may stabilise ε-carbide a little and inhibit the softening effect associated with Fe_3C formation. The restriction of growth of the Fe_3C particles by such elements as Cr and Si can therefore render more easy transformation of Fe_3C to alloy carbides, or alternatively re-solution of Fe_3C and precipitation of alloy carbides at new sites primarily associated with dislocations inherited from the α' transformation[30].

There is some controversy over the nature of the carbides taking part in secondary hardening. Kuo[31] asserts that W_2C is the dominant carbide in T1 tool steel while Mukherjee concludes that V_4C_3 is the dominant secondary hardening carbide in steels M50, M2 and T1.

The surface chemistry of the steel is very important in heat treatment. In tools most of the work is carried by the surface of the material and, since chemical composition tends to control the properties and behaviour of the steel, it is essential that there is no surface degradation during processing. Thus decarburisation can result in the surface not hardening fully and the residual stress system generated during cooling and structural transformation may result in surface cracking. In rolling bearing applications the core is also of great importance since too soft a core may result in case collapse during service.

By implication, if elements such as carbon, can be lost from the surface they may also be introduced by absorption from the treatment atmosphere. Pickup of elements may be either detrimental eg. scaling (oxygen), or beneficial where the treatment atmosphere and conditions are deliberately contrived to inject an element into the surface eg. carbon or nitrogen.

2.4.2. Surface Thermochemical Treatments

Thermochemical treatments are often used where an improvement of service performance and cost advantage is desired for tools and dies. There are many processes available and most have drawbacks as well as advantages. A few of the more popular processes will be considered in brief.

2.4.2.1. Carburising

The object of carburising is to increase the carbon content of the steel at its surface in order to develop optimum physical properties after quenching[32]. This may be achieved in several ways : gas, liquid, vacuum or plasma carburising.

Carburising, one of the oldest heat treatment processes known, was for many years carried out by pack carburising[33]. Although the component is surrounded by solid carbonaceous matter, the main carbon transfer method is by gaseous reactions at the metal surface.

Modern techniques use sealed quench furnaces with controlled atmospheres of nitrogen or endothermic gas (and more recently lean endothermic gas[34]) as a carrier, with a hydrocarbon feedstock to supply the carburising reactions. However for tool steels very close control of the gaseous atmosphere is desired since these gases contain oxidants as well as carburants which could lead to preferential oxidation of alloy elements. Also, alloy elements in the steel have a profound effect upon the effective carbon potential necessary for correct treatment at optimum carburising rates[32].

Liquid carburising uses a salt such as barium or sodium cyanide. The salt, together with other bath additions, reacts at the metal surface to deposit carbon into the austenitic matrix. The chemical reactions at the metal surface also generate gaseous carbon monoxide and nitrogen.

Gas and salt bath treatments, for various reasons of control and health and safety, are not necessarily the best processes to use. However, for high speed steel treatment, these are still more popular in industry than the more desireable vacuum carburising technique.

The advantages quoted for vacuum carburising of tool steels are : better control of case depth and surface carbon level, no preferential oxidation of alloying elements such as

chromium and vanadium by oxidants present in conventional gas carburising atmospheres, and hardening without the necessity for a separate treatment[35].

The steel is heated under vacuum, then a hydrocarbon gas e.g methane (CH_4) is admitted to the chamber to effect carbon transfer to the metal surface. This is followed by removal of the gas and heating the sample to a higher temperature to diffuse the carbon into the metal and achieve the desired case depth and carbon profile. The chamber may subsequently be filled with an inert gas, usually nitrogen, to quench the sample thus effectively carburising and hardening in one treatment.

There are essentially three reactions capable of carbon transfer from an atmosphere to the steel:

$$CO\uparrow + H_2\uparrow \rightarrow [C] + H_2O\uparrow \qquad \ldots\ldots(2.18)$$

$$2CO\uparrow \rightarrow [C] + CO_2\uparrow \qquad \ldots\ldots(2.19)$$

$$CH_4\uparrow = [C] + 2H_2\uparrow \qquad \ldots\ldots(2.20)$$

Gas processes rely upon the balance of all three reactions to effect carburising whereas vacuum carburising relies upon equation (2.20). The methane decomposition rate under vacuum conditions, where the partial pressures of H_2 and CH_4 are typically 40% and 20% respectively, is about $4.1*10^{-6}$ $mol.cm^{-2}.min^{-1}$ and favours high surface carbon levels and rapid diffusion[36].

Vacuum carburising may be carried out to enhance the wear resistance of a steel surface and also improve fatigue resistance[37] and hardness.

2.4.2.2. Nitriding

There are three basic processes commercially available for carrying out nitriding.

(1) Salt Bath Nitriding.
(2) Gaseous Nitriding.
(3) Plasma or Ion Nitriding.

(1). Salt Bath Nitriding

Liquid bath nitriding was based on low temperature, molten cyanide salt baths[38,39] and was developed primarily to improve wear and seizure resistance in steels. Modern requirements for 'safe' treatments has resulted in the development of non-toxic salt bath processing i.e using non-cyanide base salts[40]. Process times may be from 10 minutes up to 1.5 hours depending upon the properties required.

On plain carbon, low alloy steels, such as used in automotive components, salt bath nitriding often produces porous, poly-phased compound layers which may suffer reduced load carrying capacity and a tendency to spall in service. Since porosity increases with treatment time, the duration of treatments is commonly restricted to short periods. This is a contributing factor in the greater popularity of the gaseous nitriding technique for applications other than tooling.

The majority of tools and tool steels are predominantly treated in salt baths, although some companies, notably the Lucas Electrical Co. Ltd. do treat some parts eg. ejector pins for die-casting and punches for cold extrusion, by gas techniques.

(2). Gaseous Nitriding

This process is usually carried out in sealed quench and pit or bell type furnaces using variations of nitrogen, endothermic gas (for nitrocarburising) and ammonia mixtures to supply the nitrogen in a form suitable for diffusion and layer formation[41-44].

Treatment is carried out at approximately 490 - 580°C. i.e a ferritic treatment, and involves the catalytic decomposition of ammonia gas at the metal suface into nascent nitrogen and hydrogen, according to the reaction:

$$2NH_3 = 2[N] + 3H_2\uparrow \qquad \ldots\ldots(2.21)$$

The dissociated hydrogen and a large proportion of the nitrogen recombine to form molecular hydrogen and nitrogen. The remaining nascent nitrogen at the metal surface diffuses into the steel, preferentially along grain boundaries (at which the catalytic breakdown of NH_3 is favoured), to produce interstitial solid solution and precipitation hardening due to alloy nitrides. Carbonitrides may also be formed.

Alloy steels, containing strong nitride-forming elements e.g aluminium, chromium, vanadium, molybdenum, respond very well to nitriding treatments and develop good diffusion cases. Plain carbon steels 'on the other hand', have a tendency to form an intermetallic compound layer of iron nitride on the surface with a diffusion zone below it which may precipitate iron nitride needles on slow cooling.

The intermetallic compound layer formed by nitriding - (termed 'white layer' by Homerberg[45]) - is formed upon the surface of the metal and may be up to 25 - 50μm thick depending on treatment time and temperature as well as atmosphere flow rate and ammonia concentration.

Loh[46] states that conventional gas nitriding techniques produce "brittle and friable" compound layers that "spall easily during service". However, this layer can confer good hardness, wear and corrosion resistance while the diffusion layer imparts improved fatigue resistance[41], probably because of the induced compressive stresses.

Many automotive components produced by the Lucas Electrical Co. Ltd. using plain carbon and low alloy steels depend entirely upon the white layer for their good service performance with respect to low load-bearing applications and corrosion resistance.

It is widely believed that the formation of the white layer on the metal surface is difficult to avoid in gaseous nitriding although, contrary to Loh's[46] denial, careful control of the process parameters of undissociated ammonia percentage and flow rate can give some measure of control over layer formation.

(3) Plasma Nitriding

Plasma nitriding is the newest of the nitriding techniques, even though the principles were first propounded in the 1930's by Egan[47] and later by Malcolm[48]. Since then much research has been carried out to make the process into a commercially viable reality.

The process involves the application of plasma physics. The workpiece, in an evacuated chamber containing a low pressure gas (nitrogen or nitrogen and hydrogen for nitriding), is connected as the cathode, the chamber wall being the anode of an electrical circuit. Applying a d.c. potential of between 300 to 1500V[46,49,50] ionises the gas and establishes a 'glow discharge'.

In essence, the atoms and molecules of the gas are ionised, the positively charged ions being accelerated by the electrical field towards the cathode where they collide and transform some of their kinetic energy into heat. At the same time some of these colliding ions absorb electrons and change to neutral atoms - (Figure 2.15). A current flow is established by this phenomenon. Figure 2.16 shows the typical voltage-current characteristic curve of a gas discharge. Plasma nitriding is carried out in what is commonly called the abnormal glow region where the plasma completely covers the workpiece (Figure 2.17) and promotes uniform heating and case development[51].

Treatment times may be up to 30 hours depending on the material and the case depth desired. However, the speed advantage over conventional nitriding techniques is diminished for treatments longer than about 20 hours duration[49].

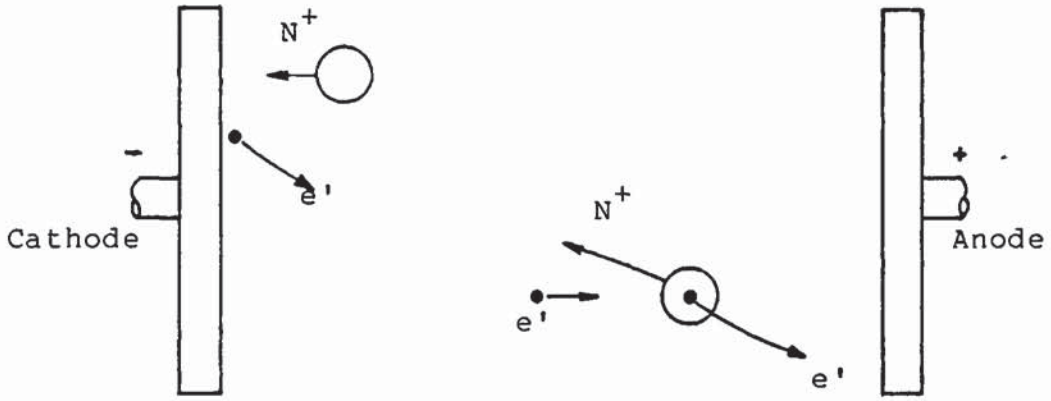

Fig.2.15. The Ion-Electron-Discharge Mechanism.

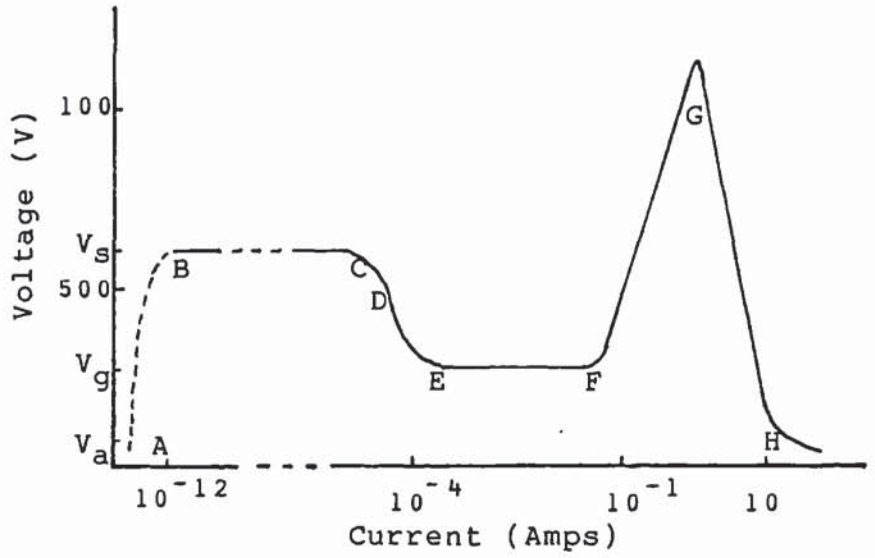

Fig.2.16. Voltage-Current Characteristic for a DC - Electric Discharge.

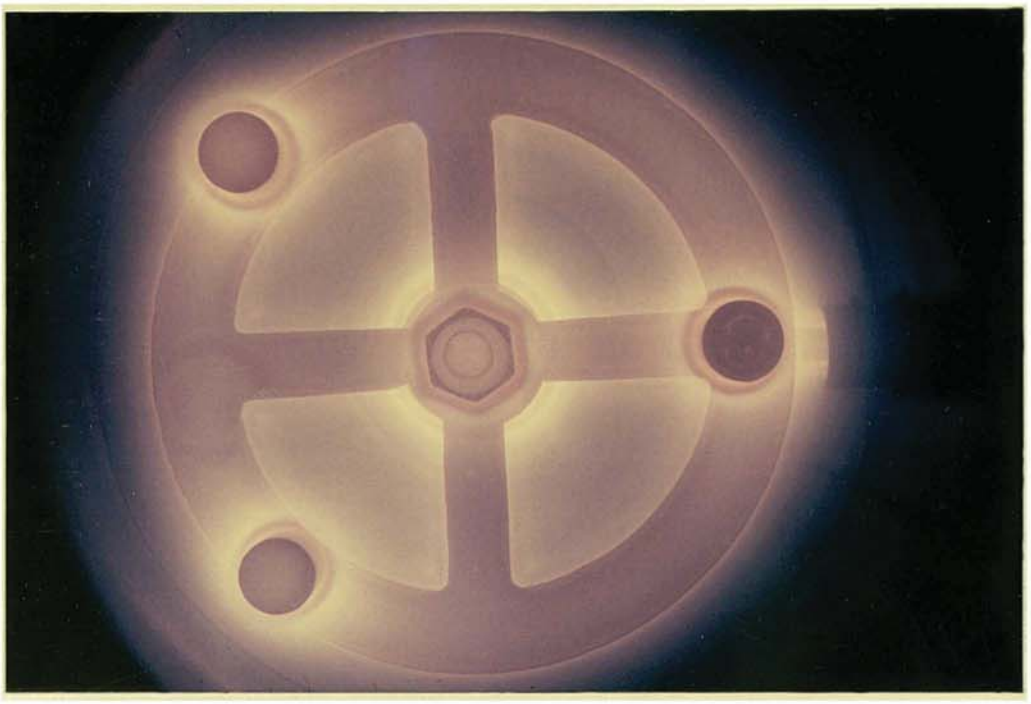

Fig.2.17. The Plasma Glow During Nitriding.

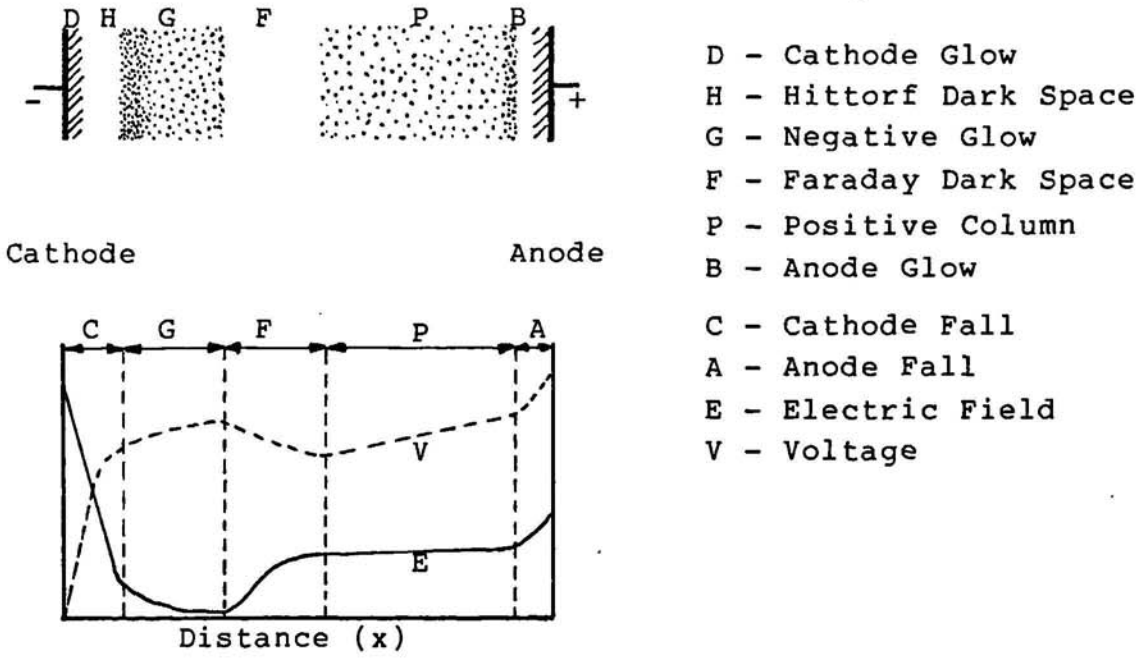

Fig.2.18. Regions Within the Glow Discharge.

2.5. Plasma Nitriding

Plasma nitriding is essentially a low temperature (350 - 580°C.), low pressure (0.1 - 10torr) process. The upper and lower temperature bounds are controlled by both metallurgical and economic factors.

(a). The upper limit for steels is set by the preference for a ferritic treatment. This is desirable since the problem of distortion, which can occur whenever an austenite - martensite structural transformation takes place on cooling, is virtually eliminated. Because the ferrite-austenite transition occurs at about 590°C in the iron-nitrogen system this sets the upper temperature limit.

(b). The lower limit is set by the need for speed - the diffusion rate of nitrogen, on which the process depends, falls drastically as the temperature decreases. The advantage of plasma nitriding over the more conventional processes in this respect is that nitriding is feasible down to 315°C, although for practical purposes one is unlikely to work below about 350°C. Other ferritic processes are only practical at higher temperatures in the range 490 to 580°C.

The process offers good control of the microstructure through precise atmosphere composition and pressure management. Blind holes can be treated satisfactorily if the product of cavity width and treatment pressure are maintained at more than 2cm-torr[52]. This avoids coalescence of adjacent negative glows and therefore surface hot spots and ensures full coverage of the surface with a thin 'glow seam'[46].

Plasma nitriding can treat the whole range of ferrous materials as well as non-ferrous metals such as titanium and its alloys[53,54].

The advantages of the process may be briefly summarised as follows:

(1) Metallurgical

Operating conditions ensure a uniform glow seam and therefore uniform treatment of all exposed surfaces - particularly important for complicated shapes such as gears etc. where uneven case depth can often result in premature failure.

Loh[46] states that single-phase compound layers may be formed, something not possible with conventional gas techniques.

Plasma nitriding is well established as a means of improving the physical properties of treated materials so that wear and fatigue resistance, and load carrying capacity are all enhanced. Corrosion resistance is also improved for most steels, but as with gas nitriding, high-alloy and stainless steels may be adversely affected. The breakdown of the stable spinel-type surface oxides and Cr depletion of the matrix due to the formation of chromium nitrides may inhibit corrosion resistance and surface passivity.

(2) Technical

The process can operate over a wide temperature range - approximately 350 - 1000°C and, as already mentioned, surface passivity is not a problem since cathodic sputtering breaks down stable surface oxides.

Sputtering also offers dimensional stability as observed by Jones et al[51] and Michel and Gantois[55].

Selective nitriding is possible by use of mechanical masks to prevent full coverage of the surface by the treatment plasma.

(3) Economic

Plasma nitriding is initially faster than salt bath or gas nitriding. Treatment times half as long for the same case depth have been quoted[46] 'though these times are questionable. Edenhofer[56] claims that this speed means a furnace throughput three times faster than an equivalent gas unit.

Power consumption depends on the surface area of the charge and there is no need to heat up the whole furnace chamber. Therefore energy savings of more than 50% are reputed to be possible.

Gas usage is low - about 5% of that for gas techniques - and post treatments may be eliminated in most cases due to the inherently high quality of surface finish obtained.

(4) Environmental

Pollution is nil and so there is no environmental hazard.

There are very few disadvantages to the process other than:

(a) Cleanliness is essential to prevent unstable arc discharges during the heating cycle.

(b) Similar sized components only may be treated in one batch due to power/surface area relationships.

(c) Plant cost is high.

So it can be seen that the advantages far outweigh the problems associated with plasma nitriding and this is becoming increasingly obvious to commercial heat treatment specialists both in Europe and America.

2.6. Plasma Physics

2.6.1. Gas Discharges

The gas discharge phenomenon is a fundamental part of everyday life and has been studied for many years.

Electrical discharges in gases at low pressures, are generated when a potential difference is established between two electrodes. Figure 2.16 shows the voltage - current characteristics for various gas discharges, the most important of which may be classified broadly as:

(1) Townsend discharges having currents up to 10^{-6}A.
(2) Glow discharges at 10^{-6}A to approximately 10^{-1}A and
(3) Arc discharges of high current - 10A upwards.

The low current flow regions of the curve (A-C) are of no great interest with respect to plasma nitriding technology, and the normal glow discharges (E-F), are used primarily for lighting applications - fluorescent tubes, glow lamps etc.. The plasma nitriding process is associated with the high current and power densities of the anomalous glow discharge (F-G).

2.6.1.1. Normal Glow Discharges

The relative mobility of cations and electrons through the plasma result in a positive space charge around the cathode - the heavier cations are slower than the highly mobile electrons[50]. Accordingly, there are several zones in the plasma as described in Figure 2.18.

Pressure increases cause collapse of the negative zones towards the cathode while the positive column expands. The current density 'i' increases directly with the square of

the pressure 'p'. Pressure increases in excess of 100 torr cause positive column collapse with consequent heating prior to arc formation.

Electrons, released by secondary electron emissions, accelerate towards the anode through the positive column. Collisions with atoms and molecules of the gas cause an 'avalanche' of cations towards the cathode, which causes further secondary electron emission etc.. Therefore, since the electric field and gas densities are enough to initiate discharge, a self sustaining state may be achieved.

Due to the space charge generated around the cathode the major part of the potential drop occurs directly in front of it (Figure 2.18) - the cathode fall region. The cathode glow results from de-excitation of positive ions and ion neutralisation[57] since the emitted electrons do not have sufficient energy to ionise or excite gas atoms/molecules.

An atom exists in one or another of a series of definite characteristic energies E_1, E_2,....E_n. Increasing an atom's internal energy from say E_1 to E_2 causes excitation of it's electrons. This excitation is the movement of an electron to a higher energy level than it currently occupies and requires a quantum of energy (a photon) to occur.

De-excitation is the fall-back of an excited electron and results in the release of a photon of energy. Energy liberation on electron transition back to a lower energy level produces photons in the visible spectrum. However if the transition is for an electron back to its ground state of lowest energy, the photon release is in the ultra-violet region.

The energy of the released photon can be found from:

$$E = \frac{hc}{\lambda} = h\nu \qquad \ldots\ldots(2.22)$$

- where h = Planck's constant
  c = velocity of light
  λ = wavelength
  ν = wave frequency

The Hittorf or cathode dark space is where the gas is ionised by electrons which have not lost any energy in de-excitation of ions in the cathode glow. A charge avalanche results but no light is emitted by excitation or de-excitation of the gas. For a given current, the width of the cathode dark space '$d_{c.n}$' increases as pressure decreases, so that:

$$d_{c.n} * p = C \qquad \ldots\ldots(2.23)$$

where C is a constant, characteristic of the gas used.

Electrons, having passed through the cathode fall region gain energy, because of the electrostatic field, sufficient to excite the gaseous atoms/molecules and produce the negative glow. The width of this zone depends on the energy level of these emerging electrons. The electric field decreases here and so does the energy of the electrons. Consequently light emitted is also reduced (Figure 2.18)[54].

The density of ions in the negative glow is large and many recombinations take place which is in contrast to the Faraday dark space where the electric field strength is low and no ionisation or excitation takes place. Any current in this region is due to the diffusion of charged particles as it is in the cathode fall zone.

The anode fall region extends from the anode wall to the boundary of the positive column and it's potential fall is approximately equal to the ionisation potential of the gas. There is a net negative charge near the anode and the positive ions which pass through the positive column are created here due to the increased probability of excitation via the accumulation of electrons. This gives rise to the anode glow.

2.6.1.2. The Anomalous Glow Discharge

In normal glow discharges the cathode is not fully covered by the discharge. In order to maintain a constant current density and voltage across the electrodes, as the current increases so does the area covered by the discharge. The current cannot exceed $I_F = i_n S$, where S is the surface area of the electrode. When $I = I_F$ full coverage is achieved and an anomalous glow has been established. As current increases now so does the current density and the cathode fall potential.

Aston[58] saw that (for plane cathodes in common gases) the cathode fall in potential for anomalous glows '$V_{c.an}$' was:

$$V_{c.an} = D_1 + \frac{D_2 * \sqrt{i}}{p} \qquad \ldots\ldots(2.24)$$

and the dark space thickness '$d_{c.an}$' was given by:

$$p * d_{c.an} = D_3 + \frac{p * D_4}{\sqrt{i}} \qquad \ldots\ldots(2.25)$$

where the constants D_{1-4} are dependent upon gas composition and cathode material. So for a given gas and cathode, $V_{c.an}$ and $p.d_{c.an}$ vary as functions of the anomalous current density 'i_{an}' and gas pressure 'p'.

By manipulation of equations (2.24) and (2.25)

$$p.d_{c.an} = D_3 + \frac{D_2 * D_4}{V_{c.an} - D_1} \quad \ldots\ldots(2.26)$$

It can be seen that as the cathode fall potential increases the dark space width decreases and thus charge density near the cathode rises. So, increasing voltage increases the electric field strength and the cathode and gas heat up as $V_{c.an}$ and i_{an} increase. Hudis[59] asserts that a current density of about 6mA cm^{-2} (1350V) could maintain ferrous material at 500°C.

2.6.2. The Plasma State

Plasma is regarded as the fourth state of matter, is more active/reactive than the others and is the normal state at temperatures in excess of 10^5K. However, the plasma state is easily achieved in gas discharges.

A plasma consists of atomic and molecular ions, neutral atoms and molecules and electrons. In general, electrons have higher kinetic energies than ions which in turn have higher energies than atoms and molecules.

According to Loh[46], plasmas may be classified as follows:

(1) CTE Plasma : ie. they are in complete thermodynamic equilibrium e.g thermonuclear plasmas.

(2) LTE Plasma : Local thermodynamic equilibrium as in arcs and electrode flames (also known as hot plasmas).

(3) non-LTE Plasma: Often known as the cold plasma.

The plasma of glow discharges is non-LTE.

In anomalous glows where the plasma is contracted towards the cathode, nearly all of the potential drop occurs only a few millimetres in front of the cathode[50]. Most of the collisions and ionisation takes place in the cathode fall zone and it is here that the plasma state of the gas is achieved. The gas outside the zone remains essentially un-ionised but somewhat enriched in 'charge carriers'.

The ionisation process may occur in several ways. Negative ions may be formed via electron capture by molecules when electron energy is low : 6 to 7eV or less.

ie. $$e' + MX \rightarrow (MX^-)^* \rightarrow MX^- + h\nu \quad \ldots\ldots(2.27)$$

where $(MX^-)^*$ is the activated state of the negative molecule which on de-excitation gives up photons of energy of frequency ν. The energy might alternatively be given up to another molecule so that:

$$(MX^-)^* + MX \rightarrow MX^- + (MX)^* \quad \ldots\ldots(2.28)$$

Higher energy electrons might split up molecules,

e.g $$e' + MY \rightarrow (MY^-)^* \rightarrow M^- + Y^* \quad \ldots\ldots(2.29)$$

or $$e' + MY \rightarrow M^+ + Y^- + e' \quad \ldots\ldots(2.30)$$

where space charges depend on the relative electro-negativities of the constituent atoms of the molecule.

For highly energetic electrons, (10 to 14eV), outer shell electrons might be displaced to leave positively charged molecules. Thus:

$$e' + XY \rightarrow (XY)^+ + 2e' \quad \ldots\ldots(2.31)$$

and these cations may then dissociate to atomic ions.

Ion species in plasma nitriding are complex. The constituent ion concentrations depend not only on gas composition and pressure but also the cathode temperature and the applied potential. Preferential formation of one species rather than another relies upon the 'appearance potential' of the constituent atoms/molecules which, in part, is a function of the ionisation potential and bond dissociation energy of the neutral molecule.

The first ionisation potential is the energy necessary to remove the highest energy electron of a neutral species to infinity. Each successive ionisation requires progressively more energy to liberate the more strongly held lower energy level electrons, so that the formation of N^{2+} ions needs about 3 times the energy for N^{+} formation from nascent nitrogen. Thus the majority of the cations in plasma nitriding are singly charged - only a small percentage of the whole having double space charges. Most of the ions however, are neutralised before reaching the workpiece so that it tends to be excited neutrals carried by their momentum which hit the cathode.

The average energy of bombarding ions in plasma nitriding is of the order of 30 to 50eV, much of this being lost in collisions with outcoming electrons and sputtered particles.

2.6.3. Ion Interactions with the Cathode

Ionic bombardment is an essential feature of the plasma nitriding process. Energy is lost by incident ions and gained by the atoms and electrons of the target material. Figure 2.19 shows diagrammatically some of the interactions possible during ion nitriding.

These interactions may be split into two broad categories:

(a) Elastic effects where colliding ions and electrons interact with lattice atoms resulting in sputtering of the target.

(b) Inelastic effects where cations react with lattice electrons to yield optical and X-radiation together with secondary electron emission.

2.6.3.1. Sputtering

This phenomenon may be described as the removal of atoms or molecules from the workpiece matrix by impacting ions, neutrals and electrons. Originally considered as a volatilisation of the surface by high energy incident ions[49], workers in the late fifties modified this idea to the concept of sputtering as 'cascades' of atomic collisions by the lattice recoil from incident ions.

Sigmund[60] proposed sputtering based on random collision processes. Collision cascades are initiated when the transmitted energy from the impacting ions is greater than the displacement energy of a lattice atom. Sputtering occurs if and when the cascade interacts the surface with atoms of energy greater than the surface binding energy.

Sputtering can only occur if the incident ion energy exceeds a threshold value which for iron and its alloy elements is 20 to 30eV. Above the threshold, sputtering rate increases to a maximum as the ionic energy increases, then decreases with higher ion energies due to ion penetration of the surface.

So, the sputtering rate increases with several parameters:

(1) The mass of the impinging ion - the low mass of the hydrogen ion has low sputtering yield in terms of atoms per impacting ion ie. less than 0.1

(2) The cathode fall, $V_{c.an}$

(3) The discharge current

(4) Decreasing pressure.

It is clear that most of these parameters may be readily controlled by the operator. Sputtering may be used as a tool to control dimensional growth of the workpiece and layer formation to such an extent that good dimensional stability is an inherent feature of the plasma nitriding process.

2.6.3.2. Secondary Electron Emission

Electron emissions from an ion bombarded surface are called secondary electron emissions. As with sputtering, electron emission yield is dependent upon impacting ion energies - increasing with higher energies up to the point where ion penetration prevails. Lighter ions produce larger numbers of high energy electrons.

Electron emission can only happen if sufficient energy is available, and generally no electron release will occur if the ionisation potential of the ion is less than twice the work function of the cathode material (4.77eV for iron). At low ion energy levels, <1KeV, there are two forms of electron emission - potential and kinetic emission. Kinetic emission prevails at higher ion energy levels. Since the ionisation potential for H_2^+ and N_2^+ from their gases are 15.43 and 15.55eV[61] respectively, potential emission is the dominant process and is the means by which secondary electron emission sustains the glow in plasma nitriding.

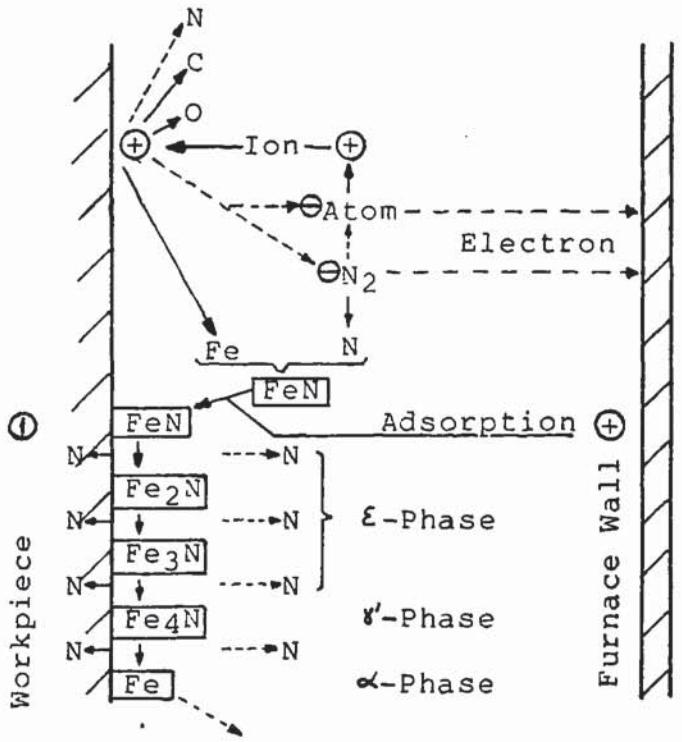

Fig.2.19. Surface Reactions During Plasma Nitriding.

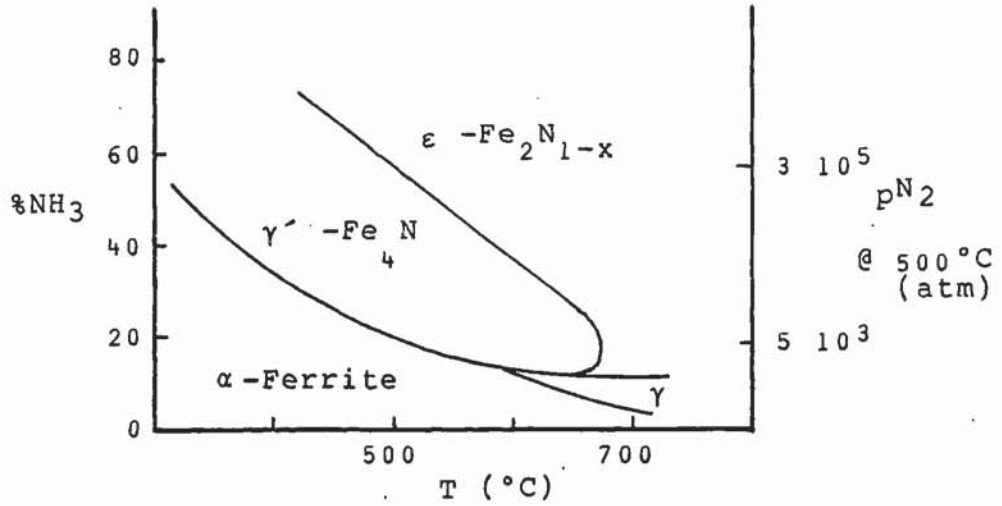

Fig.2.20. Equilibrium of Phases formed on Iron - in Ammonia/Hydrogen Gas Mixtures.

2.7. Nitriding Mechanisms

2.7.1. Nitrogen Transfer

Surface hardening of iron and steels by nitriding is brought about by the interaction of nitrogen, in interstitial solid solution, with substitutional solute alloying elements[62]. Nitriding usually results in an intermetallic compound layer formed on the surface supported by a diffusion layer below it[63].

In salt baths nitrogen may be transferred by several mechanisms. Using baths containing mostly sodium cyanide, sodium cyanate and sodium carbonate might, according to Astley[64], result in the reactions:

$$2NaCN + O_2\uparrow \rightarrow 2NaCNO \qquad \ldots\ldots(2.32)$$

which decomposes at the metal surface to:

$$4NaCNO \rightarrow Na_2CO_3 + 2NaCN + CO\uparrow + 2[N] \qquad \ldots\ldots(2.33)$$

The $CO\uparrow$ liberated is likely to cause a sooting problem, but chloride additions to the bath have been found to alleviate this problem by the promotion of fluidity of the bath salts.

Rozendaal et al[63] described possible reactions which might be occuring in salt bath nitrocarburising as follows:

$$4CNO^- \rightarrow 2[N] + CO\uparrow + CO_3^{2-} + 2CN^- \qquad \ldots\ldots(2.34)$$

Additionally, aeration of the bath by agitation would result in oxidation of the cyanates, so that -

$$2CNO^- + O_2\uparrow \rightarrow 2[N] + CO\uparrow + CO_3^{2-} \qquad \ldots\ldots(2.35)$$

In gaseous nitriding, nitrogen transfer is dependent upon the breakdown of ammonia gas at the metal surface according to the reaction:

$$NH_3\uparrow \rightarrow \frac{3H_2}{2}\uparrow + [N] \qquad \ldots\ldots(2.36)$$

At nitriding temperatures of 500 - 575°C[65], most of the ammonia dissociates thermally into molecular nitrogen and hydrogen and takes no real part in the nitriding process other than as a 'bulking agent'. Thermal dissociation accelerates with increasing temperature above about 600°C. The nitrogen potential at the metal surface may be determined by consideration of the equilibrium relationship[66]:

$$wt\%[N] = \frac{k \cdot p_{NH_3}}{p_{H_2}^{3/2}} \qquad \ldots\ldots(2.37)$$

where k is the equilibrium constant at a given temperature, and is given by[67]:

$$k = e^{(-\Delta G^{\ominus}/RT)} \qquad \ldots\ldots(2.38)$$

- and p_{H_2} and p_{NH_3} are the partial pressures of hydrogen and ammonia in the atmosphere. Since thermal dissociation of the ammonia occurs simultaneously with the catalytic breakdown, in order to determine the nitriding potential of the gas, equation (2.37) needs to be modified so that:

$$\frac{p_{NH_3}}{p_{H_2}^{3/2}} = \frac{(1-y)}{(3y/4)^{3/2}} \qquad \ldots\ldots(2.39)$$

where the atmosphere composition is expressed with respect to the exit gas and is (1-y) parts ammonia to (y) parts of fully dissociated ammonia[65]. A similar treatment may be carried out to determine the potential in salt baths.

Transfer in plasma nitriding is somewhat different and there is still much controversy over the controlling mechanism. Loh[46] points out that hydrogen and nitrogen-hydrogen ionic molecules are present in significant amounts in the plasma.

He also asserts that the majority of the ionic species are neutralised in transit to the cathode and that the main colliding components are excited neutral species.

Tibbets[68], in consideration of the work done by Hudis[69], says that ionic bombardment by nitrogen-hydrogen species plays only a secondary part in nitrogen transfer since it is possible to nitride using nitrogen-argon atmospheres. He proposes transfer by neutral species and N in particular - asserting that the dissociation rate constant for N_2 in the positive column is $4*10^{-14}cm^3s^{-1}$ and $6*10^{-11}cm^3s^{-1}$ for the cathode fall region and that this accounts for the increased flux of nitrogen to the work surface and therefore increased nitriding rate.

Jones et al[51] carried out work based on a study of cathode current density and measurement of ions bombarding the cathode using a combined rf+dc discharge. They propose partially dissociated ammonia ions as the controlling factor of ion nitriding - confirming previous work by Hudis[69] and contrary to work at that time not completed by Tibbets[68]. However they deny, the postulation put forward by Keller[70] and Edenhofer[49], that sputtering of iron from the surface (followed by formation of FeN in the cathode fall region, and subsequent condensation on the surface) is the controlling mechanism.

It is apparent that clarification of the available data is still necessary to finally determine just what is the controlling factor. It would appear that all of the mechanisms proposed so far play some part in the process but which is the dominant factor is unclear and is almost certain to change under different operating conditions.

2.7.2. Compound and Diffusion Layer Formation

When the nitriding potential of a treatment atmosphere is such that the concentration of nitrogen in ferrite exceeds that necessary for the formation of γ'-Fe_4N or ε-Fe_2N_{1-x} nitrides, then these phases may form at the surface. Gaseous nitriding in ammonia atmospheres usually leads to compound layer formation (commonly called 'white layer'). Figures 2.20[71] and 2.21 show the conditions for the formation of the various phases of the Fe-N system. Nitrogen concentration at any depth is dependent on the diffusion rate and can be calculated from the normal diffusion equations. The alloying elements present and their concentrations affect the nitriding rate since alloy/nitrogen interaction, ease of precipitate nucleation and growth and temperature, all play vital roles in the quantity of nitrogen available at the diffusion layer boundary.

Lightfoot and Jack[65] proposed a model for case development. Where substitutional alloy element diffusion is neglected, the diffusion front only proceeds after all of the alloying element at the interface is reacted, and nitrogen take-up from the atmosphere is rapid to maintain the equilibrium surface nitrogen concentration. Their analysis shows depth 'ξ' in time 't' is given by:

$$\xi^2 = \frac{2[N].D.t}{r[x]} \qquad \ldots\ldots(2.40)$$

where [N] = surface nitrogen concentration (at.%)

[x] = original alloy element concentration (at.%)

r = ratio of nitrogen to alloy element in the nitride phase, and

D = diffusivity of nitrogen.

This implies faster nitriding rates are possible by increasing the surface concentration of nitrogen or by decreasing the alloy element concentration.

When nitriding in an atmosphere capable of forming γ'-Fe_4N or ε-Fe_2N_{1-x} then formation will occur at the surface and a concentration gradient will be set up across the compound layer. A steep gradient in γ'-Fe_4N ensures rapid growth inwards. Higher concentrations of nitrogen at the surface (as with higher potential gaseous atmospheres) favours formation of ε-Fe_2N_{1-x} with γ'-Fe_4N in contact with the substrate. This accommodates the steep concentration gradient developed. However, since there is probably an incubation period for the nucleation of γ'-Fe_4N it may not form and ε-nitride growth inwards would be rapid to maintain some semblance of equilibrium. ε-nitride grows faster than γ'-Fe_4N anyway due to its higher solubility limits for carbon and nitrogen.

If ε-nitride is formed according to the diagram (Figure 2.20) from a lower potential atmosphere, growth would be more gradual and γ'-Fe_4N formation might be expected. This may also happen when ε-nitride attains a certain thickness.

So, it might be implied that formation and growth of γ'-Fe_4N is slower than it is for ε-Fe_2N_{1-x} and nitriding in the presence of surface nitrides depends on local equilibria between the surface and substrate.

Lightfoot and Jack[65] conclude that nitriding of steels is controlled by the equilibrium of saturated ferrite with γ'-Fe_4N after a short incubation period and that layer formation is not necessary for optimum rates.

However, in chromium steels, where there is no local equilibrium between the ferrite and surface Fe_4N, optimum nitriding rates will not be achieved without the presence of white layer.

Ion nitriding, according to Edenhofer[49], sets up a higher nitrogen concentration at the surface via the condensation of FeN. This forms very early in the treatment and gives very steep concentration gradients. This partly explains the faster case development so characteristic of plasma treatments but is not the sole reason. After 1 - 2 hours treatment in gas processes the concentration gradients are similar to those in plasma nitriding since the saturation level of nitrogen in ferrite is reached, due to the build up of coherent iron nitride phases.

It has been shown that the nitrogen diffusion rate in iron is 'altered' by plasma nitriding. In gas nitriding, diffusion of nitrogen is initially intergranular in accordance with the high-energy grain boundary sites being favourable to dissociation of the ammonia to liberate nascent nitrogen. But, nitrogen diffusion along grain boundaries is inhibited due to the presence of carbide (Fe_3C) and the occlusion of nitrogen by this carbide for the formation and growth of carbonitrides. This is an effective waste of the nitrogen and impedes further diffusion along the grain boundary. The reduced nitrogen availability also inhibits the transcrystalline diffusion which is characterised by the formation of a fine dispersion of nitrides in the ferrite.

In plasma nitriding, transgranular diffusion takes place from the outset of treatment due to the even surface concentration of nitrogen present. Therefore a planar diffusion front is initiated. In addition, sputtering of the surface results in removal from the near surface of iron and alloy elements including carbon. Effectively, local decarburisation of the grain boundaries results and formation of carbonitrides is suppressed while nitrogen diffusion along grain boundaries is not impeded. An added benefit of the process is that, with the suppression of carbonitride formation at the grain boundaries, brittleness - a real danger in gas and salt bath nitriding, is effectively reduced.

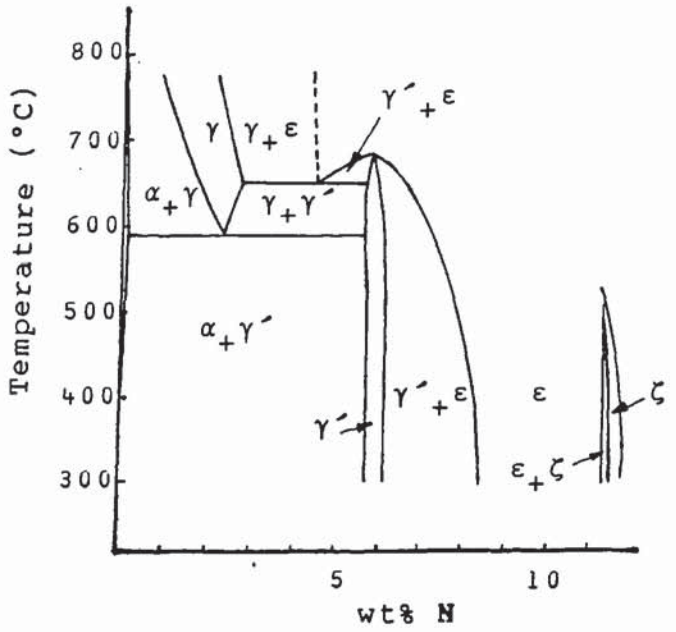

Fig.2.21. The Iron-Nitrogen Equilibrium Diagram.

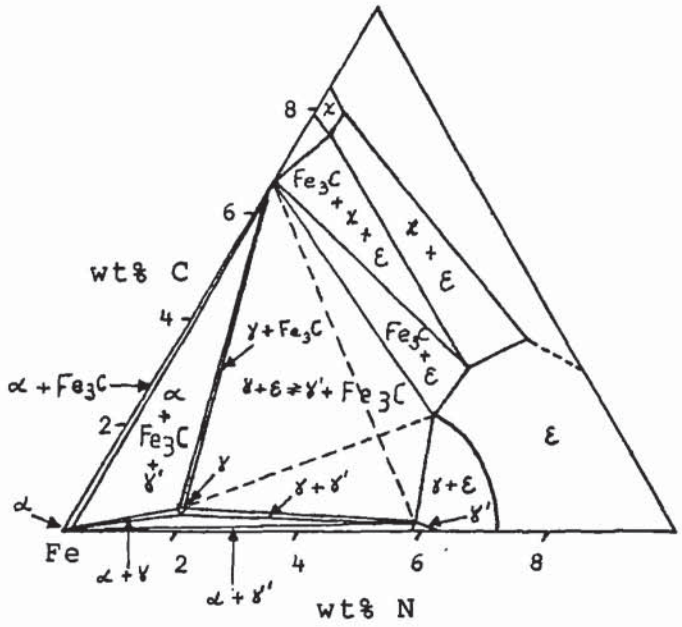

Fig.2.22. The Iron-Carbon-Nitrogen Ternary Phase Diagram - @ 575°C.

2.8. The Structure of Nitride Layers

The metallurgical structure of layers formed by any of the nitriding processes is essentially the same[72]. Generally, increased temperatures and treatment times lead to deeper diffusion zones and thicker compound layers. However, plasma nitriding should be able to produce either:

(a) A poly-phased compound layer supported by a diffusion zone,

or (b) A mono-phased layer on a diffusion zone,

or (c) A diffusion zone alone.

2.8.1. The Compound Layer

Zlatanović and Tomčik[73] state that the gas atmosphere strongly influences the compound layer formed, in that mono- or poly-phased layers or no compound layer at all may be formed if one alters the hydrogen, nitrogen and carbon content of the atmosphere to suit as shown by Figure 2.22. Staines and Bell[74] assert that nitrogen-hydrogen mixtures favour γ'-Fe_4N layer formation while mixtures containing a hydrocarbon such as methane increasingly favour ε-$Fe_{3-2}C_xN_y$ carbo-nitride. Rie and Lampe[75] also found that carbon-free atmospheres favour γ'-Fe_4N nitride stating that as the carbon content of the steel increases - so does the occurrence of ε-carbo-nitride.

Zlatanović[73] says that surface nitrogen saturation occurs very quickly - something which is not supported by the work of Rozendaal et al[76], who state that the surface concentration of nitrogen approaches equilibrium slowly.

A surface compound layer forms when the rate of nitrogen supply at the surface exceeds the rate of diffusion into the metal matrix. The quantity of nitrogen provided at the surface can be described by[76] :

$$J_N = k(C_{eq} - C_s) \qquad \text{.....(2.41)}$$

where k = reaction rate coefficient

C_{eq} = Nitrogen concentration in ferrite in equilibrium with the atmosphere.

C_s = Actual nitrogen concentration at the surface.

Nitrogen diffusion in ferrite is governed by Ficks second law. Accordingly :

$$\frac{\partial C}{\partial t} = D.\frac{\partial^2 C}{\partial x^2} \qquad \text{.....(2.42)}$$

where D = The diffusion coefficient which is assumed to be independent of nitrogen concentration[76]

C = The nitrogen concentration at a depth 'x' and a time 't'.

These conditions apply where no γ'-nitride is formed at the surface. Where the nitriding potential of the treatment gas is great enough to facilitate γ'-Fe_4N formation, the equations may be used to determine the time necessary for the surface nitrogen level to reach the critical concentration 'C_s^{CR}' to form the compound layer.

γ'-Fe_4N is relatively ductile and has a face centred cubic lattice structure with ordered interstitial N[54]. Edenhofer and Bewley[77] state that γ'-nitride layers tend not to exceed about 10 μm in thickness - probably due to the small solubility range of nitrogen in the compound layer yielding a shallow concentration gradient for thicknesses greater than approximately 8 μm[46].

ε-$Fe_{3-2}N$ is formed from higher potential gaseous atmospheres and tends to be stabilised by the presence of carbon - when the compound tends towards the carbo-nitride form. Staines and Bell[74] feel that the formation of a homogeneous ε-nitride layer is difficult due to the presence of carbon in the substrate metal of most steels. They also say that complete suppression of compound layer is possible by plasma nitriding in atmospheres containing less than about 10% nitrogen.

ε-nitride is thought to be slightly less ductile than γ'-nitride - probably due to its hexagonal close packed structure rather than the face centred structure of γ'-Fe_4N which has more glide planes for slip to occur. Multi-phased layers of $\varepsilon + \gamma'$-nitride tend to be rather brittle and Edenhofer[72] attributes this to the inherent residual stresses set-up by lattice misfit between the cph and fcc structures of the component phases. This might easily lead to micro-crack formation under the smallest loads. However, provided the compound layer is relatively thin this tendency of layers towards brittleness is somewhat reduced and the full advantages of the hard, wear and scuffing resistant white layer can be well utilised.

White layer formation is to some extent controlled by the amount of alloying elements present in the steel to be treated. In high speed steels where the alloy element content is high, white layer formation is inhibited and so only thin layers are able to form. On plain carbon steels white layer forms relatively easily and, in general, due to the lower hardness of the diffusion layer formed, an epsilon nitride compound layer is preferable for most applications[39] involving wear and scuffing.

The growth of the compound layer relies on the diffusion of nitrogen through the layer whereas the diffusion layer depends on diffusion through the matrix lattice[77]. Robino and Inal[78] say that nitrogen diffuses faster through the compound layer than it does through the developing diffusion zone - increasingly so as the alloy content increases.

2.8.2. The Diffusion Layer

The diffusion layer may be described as the depth to which nitrogen has diffused through the matrix, as a concentrated interstitial solid solution or after cooling, as a fine dispersion of alloy and iron nitride precipitates.

The diffusion case is controlled by the rate of bulk nitrogen diffusion from the surface to the reaction front of the developing case[78]. Case depth development follows a parabolic rate law and varies directly with the square root of the treatment time for a particular treatment temperature. Also, nitriding depth is inversely proportional to the alloy element content[54,78,79] while the hardenability is directly proportional to the alloy content[54,79].

The hardening effect associated with the diffusion zone is achieved by the formation of an interstitial nitrogen solid solution and the precipitation of a fine dispersion of alloy nitrides[77,80]. Lakhtin et al[80] state that the precipitation of nitrides depends on the thermodynamic activity and distribution of nitride forming alloying elements between carbides and the ferrite matrix and also upon the stability of carbides in the presence of nitrogen.

Nitride or carbo-nitride precipitation may result either from the partial dissolution of carbides already present[78,80] or, from direct nucleation and growth from solid solution at regions of alloy element segregation[80].

Lakhtin et al[80] showed that formation of nitrides by dissolution of iron, tungsten or molybdenum carbides is unlikely since the nitrogen concentration would have to be far in excess of the limit of solubility in solid solution. Formation of nitrides from solid solution according to the reaction :

$$n[N] + m[M] = M_mN_n \qquad \ldots\ldots(2.43)$$

might be more reasonable for these elements.

The nitrogen concentration necessary to form nitrides from the solid solution can be found from:

$$\log C_N^n + \log C_M^m = -\frac{1530}{T} - 1 + \frac{\Delta G^{\ominus}_{M_mN_n}}{4.57T} \qquad \ldots\ldots(2.44)$$

where C_M is the alloy element wt% in solid solution and not the total concentration in the steel.

Higher concentrations of alloying element favour formation of nitrides from solid solution rather than by carbide dissolution.

Alloy elements may be divided into three groups according to their mechanism of nitride precipitation[80] :

Group I elements are characterised by nitride formation from carbide - nitride transformation e.g Ti,Zr.

Group II elements such as W,Mo (and Cr up to 2%) form nitrides from solid solution.

Group III elements such as V and Cr (>2 to 6%) form nitrides by both mechanisms.

It has been shown[78,79] that nitrides often form near clusters of undissolved carbide. According to the theory of Lakhtin et al, these would be likely to be either vanadium or chromium nitrides, and Edenhofer and Bewley[77] testify that hardening is due to the dispersion of fine chromium nitrides precipitated in the matrix. However, nitrides of chromium formed from carbide rather than from solid solution would require more nitrogen to 'drive' the reaction cf. 0.1wt%N in solid solution for $Cr_{23}C_6 \rightarrow CrN$ with 0.001wt%N for $Cr \rightarrow CrN$. Similarly $VC \rightarrow VN$ requires 0.001wt%N in solid solution compared to 10^{-5}wt%N for $V \rightarrow VN$.

So, it would appear that the hardening process in the diffusion zone would primarily depend upon nitride precipitation - principally CrN from solid solution and VN - this probably from carbide dissolution since almost 90% of the available vanadium is likely to be 'tied-up' in the form of carbides.

Edenhofer[54] and Robino and Inal[78] both assert that maximum hardening in plasma nitriding occurs at about 450°C. due to the thermodynamics of precipitation of chromium nitrides. This was also pointed out by Edenhofer and Bewley[77]. Robino and Inal qualify this by saying that at lower temperatures nitrogen take-up and density of precipitation is low while at higher temperatures (or longer times) growth of the precipitates can lead to a fall-off in hardening effect.

Bell[39] pointed out that fatigue resistance of nitrocarburised steels depends on the solid solution retention of nitrogen - best results showing 120% improvement in fatigue strength over mild steel. Rozendaal et al[76] stated that fatigue properties are thought to be strongly influenced by the residual stresses, induced by nitriding in the surface layers - at the same time pointing out that since nitrogen concentration builds up gradually at the surface there should be an optimum treatment time to ensure maximum compressive stresses in the case. They also described equations to calculate this optimum time.

2.9. Residual Stress

Residual stress may be defined as the stress which remains after all applied forces have been removed from an object[81], and is the result of non-uniform plastic flow arising from a previously performed operation. In heat treatment of metals, residual stress may occur because of thermal and/or structural transformation processes[82].

Residual stresses are manifest in two forms[83]:

(1) Macrostresses - which vary progressively across a component.

(2) Microstresses - which vary over short inter-atomic distances.

Micro- and macrostresses in steels are directly affected by heat treatment, and macrostress is, in part, dependent upon microstress. These stresses have been described with reference to lattice strain[63,84]:

Macrostrain is a measure of the fractional change in the average lattice parameter (a_o), ie.

$$\varepsilon = \frac{(a_1 - a_o)}{a_o} \qquad \ldots\ldots(2.45)$$

Microstress is the lattice parameter variation with respect to the average value, so that:

$$e = \frac{\Delta a}{a_1} \qquad \ldots\ldots(2.46)$$

Residual stresses arising from thermal processes occur as a result of thermal gradients being set up across the section of the specimen. Thermal gradients are a natural consequence of accelerated cooling (as in quenching or welding processes) and the thermal conductivity of the material.

Relatively poor heat conductors such as steel are much more likely to develop large thermal gradients. On cooling, the metal surface loses heat more rapidly than its core, producing a stress due to different relative rates of contraction. The core, being hotter and still relatively plastic, 'collapses' to accommodate this stress. Further cooling reverses the situation since the core has more heat to lose than the surface. This leaves the surface in residual compression since, at lower temperatures, the surface and core are less likely to plastically deform to relieve the generated stress - the material is less plastic at lower temperatures. To complete the stress system the core is held in tension. Clearly thermal residual stresses are greatest in materials of high elastic modulus and coefficient of expansion[82].

Quench hardening in steels raises the prospect of phase transformation effects being superimposed on those of thermal gradients. This can lead to several different stress patterns depending upon the transformation characteristics, cooling rate and section size. For a steel quenched at a rate sufficient to ensure complete transformation to martensite, and where thermal stresses are secondary to transformation stresses, the surface may well be left in residual tension with the core in compression. On cooling, the martensite transformation, involving a volume expansion of about 4% (due to lattice distortion), begins first at the surface. As before , the core accommodates the generated stress - this time by expanding. Further cooling results in core transformation. Restraint by the cool surface results in generated stresses being partly relieved by elastic expansion of the surface and contraction of the core - leaving the surface in tension.

On cooling a high speed steel through the critical range 230°C to room temperature (230°C is the approximate M_s for these steels, M_f being about -100°C), one might expect approximately 85% completion of the austenite - martensite transformation. Unrestrained material would show around 3.5% net volume expansion due to the transformation. Cooling over the same temperature range would result in approximately 0.75% net volume contraction due to the thermal expansivity of the material. Combining the two effects yields an overall volume expansion of approximately 2.75%.

In lower hardenability steels where only partial transformation to martensite occurs, the core may be of ferrite and pearlite. The pearlite reaction results in a smaller volume expansion than for martensite but more importantly is a higher temperature reaction occuring where plasticity is still moderate. Here, the surface transforms to martensite as cooling proceeds - the core being hotter partially transforming to pearlite at about the same time. Since the core is still relatively plastic, any stresses arising will be relieved by deformation here. Further cooling causes thermal contraction only so that the surface is 'thrown' into compression as if thermal stresses alone had acted.

The effects of a component left with its surface in tension can be quite drastic e.g quench cracking or distortion can often result. Failing this, the service life of a component can be severely reduced, particularly in fatigue situations, if these stresses are not relieved by tempering. The benefits of a component with surface compressive stresses however, can be just as marked.

It is readily accepted that the major benefit of compressive surface residual stresses is in its contribution to improved fatigue life. Here, the residual stress acts to counteract the tensile stresses generated in bending fatigue and numerous workers have noted marked fatigue life and strength improvements for various heat treatments, which markedly alters the residual stress system existing after treatment to a situation of compressive surface residual stress.

2.9.1. Residual Stress Measurement Techniques

There are two broad groups of measuring techniques available to industry and these are either destructive or non-destructive. In all cases residual stress may only be determined indirectly - strains are actually measured and stress values are then derived from the available data.

Most techniques depend upon the destruction or deformation of the sample under examination and therefore can be prohibitive to makers of complex, expensive or 'one off' components. All of the destructive techniques have a common factor and that is measurement of the strain left after distortion or after the selective removal of the surface regions of the component. Gabe and West[85] reviewed several techniques (including X-ray stress analysis) which they considered to be of particular interest to the electroplating industry. The bent strip method seems to be most popular here. One side of a metal strip is plated and the resultant deflection is measured to establish the stress present in the plate. This may be done either after or during the plating process.

A derivative of this process is the spiral contractometer where plating is allowed on the outside surface of a helix which is fixed at one end - the other end being attached to a pinion and lever system. Measurement of stress comes from the angular deflection of the helix as it coils or uncoils during plating.

The Sachs boring technique depends on two strain gauges glued to the metal surface so that they are perpendicular to one another. Removal of core material by drilling alters the stress system prevalent at the surface and this is detected by the strain gauge transducers.

Stickels and Janotik[86] describe another technique in their work on 52100 bearing steels. They 'etched away' the surface layers from one side of a strip and measured the resultant deformation.

All of these techniques measure the residual macrostresses present and only indirectly take into account the microstresses present in the treated structure. Furthermore, they cannot be readily used on components since they depend on movement to detect the strain present and this by its very nature leads to partial relaxation of the stresses present. To account for this it is necessary to carry out quite involved mathematical treatments of the test data accumulated.

The X-ray diffraction residual stress technique is a non-destructive operation which once more depends upon the measurement of strain. This technique depends on the lattice distortion resulting from the presence of residual stress and is derived from the lattice strain.

X-ray diffraction measures the surface strain and if subsurface stress measurements are required - selective removal of the surface layers is necessary - the process becomes destructive in nature. The X-ray diffraction method is capable of measuring microstress by accounting for strain over short inter-atomic distances. These stresses result in diffraction peak broadening.

Another non-destructive method is the use of strain gauges cemented to the metal surface where changes in strain are measured by the electric resistivity of the gauges. Strain gauges may be used to calibrate the X-ray diffraction technique.

Since X-ray stress analysis is to be used in the present work this technique will be discussed in a little more detail.

2.9.2. X-Ray Diffraction Residual Stress Measurement

Analysis of lattice strains and the corresponding stresses, which forms the basis of the X-ray technique of residual stress analysis, follows from the classical theory of elasticity[81].

In his derivation of the basic principles involved, Cullity[87] first takes the case of a cylindrical rod in uniaxial tension (Figure 2.23) under a stress σ_y = force/cross sectional area . The stress (σ_y) produces a strain 'ε_y' in the direction of the stress and may be derived from the final and original bar lengths (l_f and l_o respectively) so that:

$$\varepsilon_y = \frac{l_f - l_o}{l_o} \qquad \text{.....(2.47)}$$

Further, strain is related to stress and the modulus of elasticity (E) by:

$$\sigma_y = \varepsilon_y E \qquad \ldots\ldots(2.48)$$

Poisson contractions in the transverse direction produce attendant strains. Accordingly, for isotropic materials:

$$\varepsilon_x = \varepsilon_z = -\nu\varepsilon_y \qquad \ldots\ldots(2.49)$$

The X-ray technique relies on diffraction from lattice planes to determine changes in the plane spacing under the influence of residual stress. The spacing of planes parallel to the direction of stress (and therefore the strain perpendicular to the stress direction) is measured to give:

$$\varepsilon_z = \frac{d_n - d_o}{d_o} \qquad \ldots\ldots(2.50)$$

- where 'd_n' and 'd_o' are the lattice plane spacings parallel to the bar axis in the presence of stress and the spacing of planes in the stress free state respectively. Tensile stress will cause dilation of the lattice spacing of planes perpendicular to the direction of stress and contraction in planes parallel to the stress direction.

Combining equations 2.48 to 2.50 yields:

$$\sigma_y = \frac{-E}{\nu} \cdot \frac{(d_n - d_o)}{d_o} \qquad \ldots\ldots(2.51)$$

where σ_y is the stress under study. It is clear that knowledge of d_o is necessary to determine the stress.

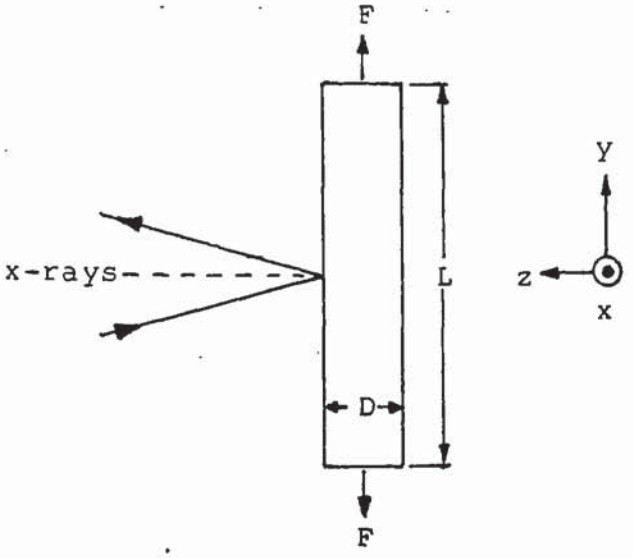

Fig.2.23. Bar in Pure Tension with x-rays Reflected from - Planes Parallel to the axis.

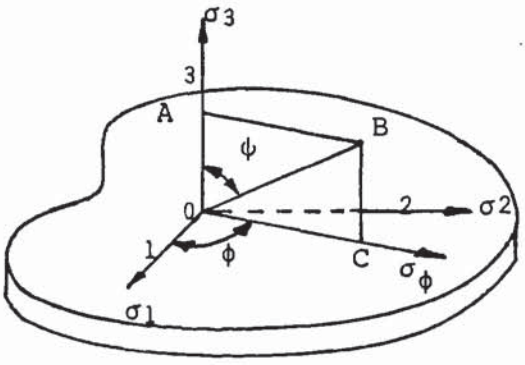

Fig.2.24. Stresses at the Surface of a Stressed Body. $\sigma_3=0$

In real situations a component is subject to multiple stresses - the principals acting in two or three directions and perpendicular to one another. However stress acting at right angles to a free surface is always zero, giving rise to a plane stress situation in the region where stress measurement is usually desired ie. at the surface. The strain perpendicular to the surface is not zero and is given by:

$$\varepsilon_3 = -\nu(\varepsilon_1 + \varepsilon_2) = -\frac{\nu}{E}(\sigma_1 + \sigma_2) \quad \ldots\ldots(2.52)$$

where σ_1 and σ_2 are the principal stresses acting in the plane of the surface, ε_1 and ε_2 being the corresponding strains. Combining equations (2.50) and (2.52) yields an expression:

$$\frac{d_n - d_o}{d_o} = -\frac{\nu}{E}(\sigma_1 + \sigma_2) \quad \ldots\ldots(2.53)$$

Again d_o must be known and it is only possible to derive the sum of the principal stresses.

To find a stress σ_ϕ acting in some direction on the surface (Figure 2.24), more than one lattice spacing measurement is necessary and by prudent use of an approximation the need to know d_o can be eliminated.

Here ε_3 (strain on planes parallel to the surface) is measured as is ε_ϕ (strain on planes with their normal inclined at some angle 'ψ' to the surface normal). A figure of 45° is often used for the angle ψ. The plane spacings of importance in this analysis are shown in Figure 2.25 where (b) and (c) describe the X-ray beam orientations necessary to measure the lattice parameters d_n and d_i.

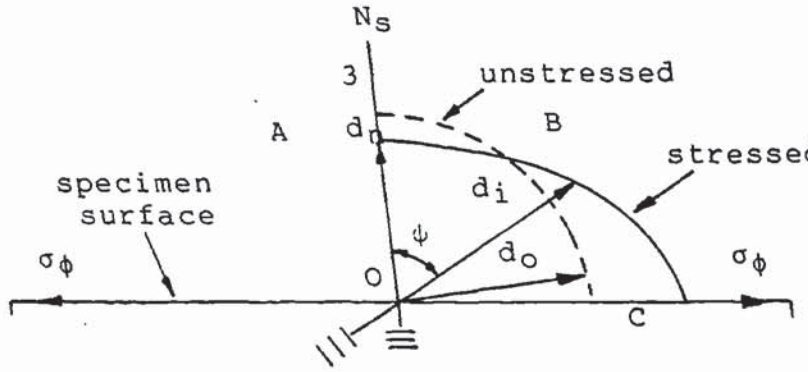

(a) Vector diagram of plane spacings d for a tensile stress

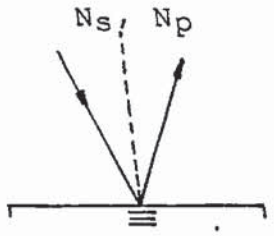

(b) Measurement of d_n

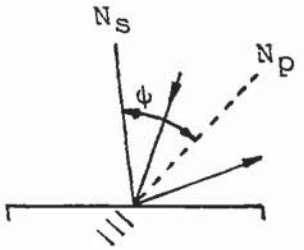

(c) Measurement of d_i

Fig.2.25. Plane-Spacing Diagram and X-Ray Beam Orientation - Relative to the Specimen Surface.

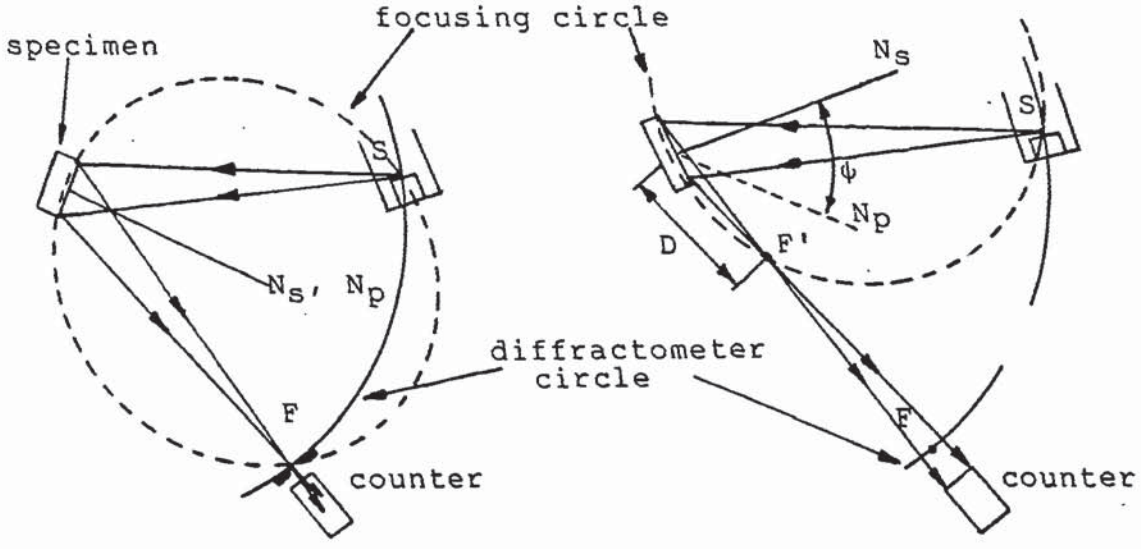

(a) $\psi = 0$

(b) $\psi \neq 0$

Fig.2.26. Use of a Diffractometer for Stress Measurement.

Strain along the direction OB, (Figure 2.24), can be derived from:

$$\varepsilon_\psi = \frac{1}{E}[\sigma_\phi(1 + \nu)\sin^2\psi - \nu(\sigma_1 + \sigma_2)] \quad \ldots\ldots(2.54)$$

Subtracting equation (2.52) yields:

$$\varepsilon_\psi - \varepsilon_3 = \frac{\sigma_\phi}{E}(1 + \nu)\sin^2\psi \quad \ldots\ldots(2.55)$$

ie. the difference between two strains depends only on the stress acting on the plane of those strains. In terms of plane spacings:

$$\frac{d_n - d_o}{d_o} = \frac{\sigma_\phi}{E}(1 + \nu)\sin^2\psi \quad \ldots\ldots(2.56)$$

The approximation is now made - since $(d_i - d_n)$ is small compared to d_o and d_i, d_n and d_o are all nearly equal to one another, d_o can be replaced by d_i or d_n with negligible error. Thus:

$$\sigma_\phi = \frac{E}{(1 + \nu)\sin^2\psi} * \frac{(d_i - d_n)}{d_n} \quad \ldots\ldots(2.57)$$

This equation forms the basis of the X-ray diffraction technique and is valid for uniaxial or biaxial stress systems. Since the angular shift of the diffracted beam is measured, the stress equation is commonly re-written in terms of '2θ' rather than plane spacing.

Differentiating the Bragg law and combining the result with equation 2.57 gives:

$$\sigma_\phi = \frac{E\cot\theta(2\theta_n - 2\theta_i)}{2(1 + \nu)\sin^2\psi} \quad \ldots\ldots(2.58)$$

which is the more usual form of the equation used in XRD residual stress determinations.

2.9.2.1. The Techniques in Common Use

(1) The Double-Exposure Method

Stress parallel to the sample surface is derived from measurements at two orientations of the angle ψ (commonly $\psi=0°$ and $\psi=45°$). For steels, diffraction from the {211} planes is often chosen for measurement since the peaks occur at a suitably high angle of $2\theta \sim 156°$ to allow more easy detection of peak shift, and because this group of planes is common to both the ferrite and martensite phase.

This technique has several variants. The stationary detector method involves no movement of the X-ray detector/receiving slit along the goniometer arm to account for the variation in focussing conditions, as the angle ψ is altered from 0° to $\psi \neq 0°$. The diffracted beam intensity is reduced for angles of $\psi \neq 0°$ and results in extended data acquisition times.

The parafocus method takes account of the change in focussing conditions and the detector/receiving slit is moved to the new focus position for $\psi \neq 0°$. Figure 2.26 shows the incident and diffracted beam geometry with respect to the sample surface.

Since the focussing circle of the diffracted X-ray beam is always tangential to the sample surface, rotation of the specimen alters the focussing circle position and radius (b). It can be shown that:

$$\frac{D}{R} = \frac{\sin(\theta - \psi)}{\sin(\theta + \psi)} \qquad \ldots\ldots(2.59)$$

- where D is the sample-to-focus distance of the diffracted beam and R is the radius of the diffractometer circle of rotation.

When $\psi > 0°$ the focal point of the diffracted beam is less than R and the receiving slit should be moved as appropriate. This re-positioning of the receiving slit preserves the diffracted beam intensity and therefore should not unduly affect the data acquisition period.

Both of these techniques may be used to acquire data by : (a). The constant time procedure, where the number of counts accumulated in a preset period is measured. This process is repeated at several values of the angle 2θ over the peak scanning range (e.g 148 - 158°). (b). The constant count procedure. This is the same as in (a) but here the time taken to accumulate an arbitrary number of counts is measured.

(2) The $Sin^2\psi$ Technique

Inclined measurements are made for a number of angles of ψ rather than only one ($\psi=45°$). The technique is otherwise the same as for the double-exposure method. Values of d_i or $2\theta_i$ accumulated from testing are plotted graphically against $\sin^2\psi$ and the stress is derived from the slope of the line plotted.

2.9.2.2. Corrections and Errors in Data Analysis

Stress measurement depends on angular diffraction-peak differences derived from examination of a sample at different orientations of its surface to the X-ray beam. To detect these angular differences, which are small even for large stresses, location of the peak maximum must be accurate. Because examined materials are frequently heavily strained due to heat treatment or cold-work, the diffraction peaks are broad and make peak centre location difficult.

There is a particular problem here with tool steels, where high alloy contents and structural segregation add to the line broadening phenomenon.

The standard way to find the centre of a diffraction line is to fit a parabola to the top of it and take the parabola axis as the line centre (Figure 2.27). The centre of the diffraction line is given by:

$$h = x_1 + \frac{c(3a + b)}{2(a + b)} \qquad \ldots\ldots(2.60)$$

(where the variables are as described in Figure 2.27). The dependent variable of intensity may be in counts s^{-1}, counts for a fixed time or reciprocal time for a fixed count.

For broad diffraction lines, corrections should be applied to the raw diffraction intensity data prior to line centre determination. This is accomplished by use of the Lorentz-polarisation and absorption factor:

$$L.P.A. = \frac{(1 + \cos^2 2\theta)}{\sin^2\theta}(1 - \tan\phi\cot\theta) \qquad \ldots\ldots(2.61)$$

Measured diffraction intensities are divided by the LPA factor in fixed time procedures. In the Fixed count method diffracted intensity data is multiplied by the LPA factor since the measured time interval is inversely proportional to the intensity. Use of these factors are made to make the line more nearly symmetrical before attempting the line centre determination.

The precision of one's technique is governed by the statistical error in counting and this error has been shown to be proportional to $1/\sqrt{N}$ where N is the number of counts[87].

Accuracy can be affected by errors of two kinds, geometric and physical. The main geometric error is that of displacement of the specimen from the diffractometer axis. This can be minimised by the use of a dial gauge to ensure that the sample surface is accurately located in the plane of the goniometer axis of rotation.

Physical properties of the sample can lead to the largest sources of error in stress analysis. Large grain size, preferred orientation, surface roughness and plastic deformation can all have adverse effects on the accuracy of any measurements made. Variation in the elastic constant 'E' and the Poisson ratio ' ν' can also cause errors in stress calculations. It is best to measure these on the material under test if at all possible, to reduce the errors involved in using quoted estimates from the literature.

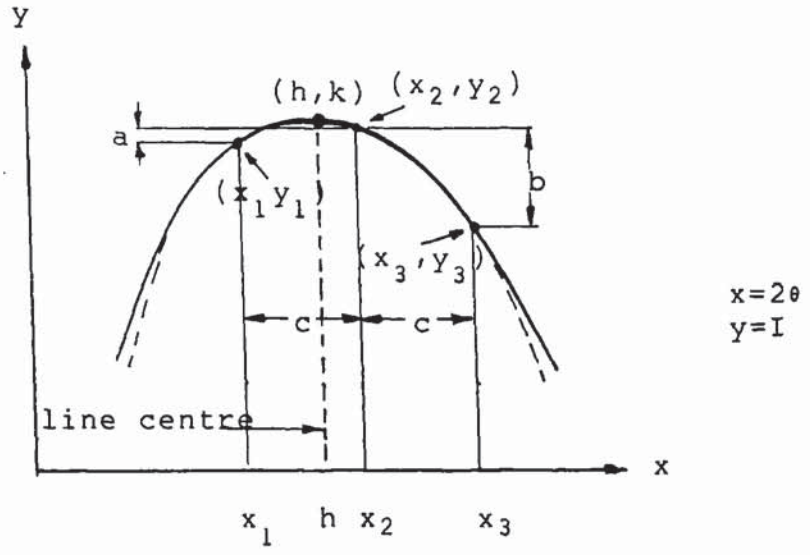

Fig.2.27. Three Point Method for Fitting a Parabola.

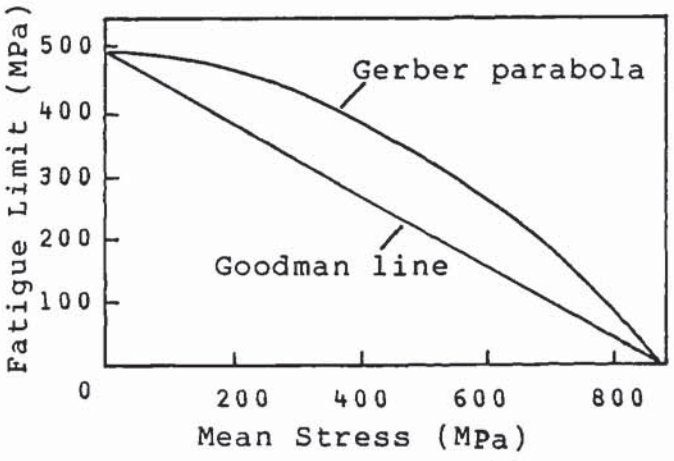

Fig.2.28. Fatigue Strength vs Mean Stress in the Core.

2.10. Fatigue of Case Hardened Steels

The term fatigue refers to the behaviour of a material subjected to cyclic stresses[88,89]. The end result of cyclic stressing is usually fatigue fracture - the number of stress cycles leading to fracture is a function of the applied stress and is known as the fatigue life.

Fatigue cracks usually start at the surface, 'though in the case of higher stress levels they may initiate within the material at subsurface discontinuities such as non-metallic inclusions. However, surface cracking is more common since bending stresses are at a maximum at the surface and stress concentrations, where crack initiation may occur, are a natural feature of the surface finish of a material.

The stress frequency does not radically affect fatigue failure at normal temperatures and so accelerated testing may be carried out without compromising the validity of the data acquired. The mean stress however, can have a marked effect on fatigue life. Tensile mean stresses result in a lowering of the fatigue limit. Several relationships between fatigue limit and mean stress have been proposed and may be illustrated by Figure 2.28 and the equation[90]:

$$S = S_0\left[1 - \left[\frac{\sigma_m}{\sigma_u}\right]^n\right] \qquad \ldots\ldots(2.62)$$

where S_0 is the fatigue strength for zero mean stress

S is the fatigue strength for a mean stress σ_m

σ_u is the ultimate tensile strength

n is 1 for the Goodman line, and 2 for the Gerber parabola.

The surface of a specimen is of prime importance to fatigue for several reasons:

(1) Slip occurs more easily at the surface than within grains.
(2) Environmental factors can play an important role in crack initiation at the surface.
(3) Sample misalignment will accentuate stresses at the surface.

The generally accepted mechanism for fatigue crack formation is that they originate at intrusions formed by surface slip under the applied load. This may occur either by the operation of several slip planes, as proposed in the Cottrell ratchet mechanism[91], or by cross-slip on a single slip system as suggested by Mott[92]. It is therefore reasonable to surmise, that surface hardening treatments could be used to increase the fatigue resistance of treated components, by increasing the resistance of the surface regions to the operation of slip mechanisms. The improvement however, depends to some extent upon the applied stress system.

Scott[5] states that plain surface hardened specimens will show little or no improvement in fatigue strength at 10^7 cycles (over untreated specimens) in push-pull fatigue stressing, but will improve substantially in cyclic bending or torsion where stresses are maximised at the surface. Cowling and Martin[90,93] however state that axial fatigue is improved by surface hardening, but relate this to the residual stresses present in the core and the case/core surface area ratio.

In the case of cyclic bending and torsion all seem to agree that improvements in fatigue are to be had by case hardening. The degree of improvement 'though, is governed by numerous factors such as case depth, surface hardness, core strength and residual stress distribution.

2.10.1. Case and Core Effects

The excellent impact and fatigue fracture properties of case hardened steels is attributable to their composite nature[94] of different toughness, strength and residual stresses present in the case and core.

Case depth effects on fatigue are related to the residual stress patterns developed, the surface hardness and the core strength[46]. Diesburg, Kim and Fairhurst[95] found that the influence of the core on fracture properties is dependent upon the effective case depth. Jones and Martin[96] showed fatigue strength to be related to the ratio of the cross-sectional areas of the case and core. Cowling and Martin[90] also showed a relationship dependent on the case/core area ratio but equated this to the effective modulus of a nitrided sample so that:

$$E_N = Ef_{case} + \left[\frac{d\sigma}{d\varepsilon}\right]f_{core} \qquad \ldots\ldots(2.63)$$

where E is Youngs modulus for the elastic case and $(d\sigma/d\varepsilon)$ is the slope of the stress/strain curve for non-nitrided core material at the strain 'ε'. Also, f_{case} and f_{core} are the area fractions of case and core respectively. The relationship applies when the core yield stress has been exceeded. The core and case strains are equal but the case would carry a greater proportion of the stress.

Accordingly:

$$\sigma_{case} = \sigma_{yc} + E\varepsilon_p \qquad \ldots\ldots(2.64)$$

$$\sigma_{core} = \sigma_{yc} + \left[\frac{\Delta\sigma}{\Delta\varepsilon}\right]\varepsilon_p \qquad \ldots\ldots(2.65)$$

where σ_{yc} is the applied stress to cause yielding in the core, ε_p being the additional strain after yielding and $(\Delta\sigma/\Delta\varepsilon)$ is the stress/strain increment for non-nitrided material corresponding to the strain ε_p.

In the course of their work on Cr-Mo steels, Bell and Loh[97] found failure to occur by the 'fish-eye' phenomenon at non-metallic inclusions. They surmise that the presence of inclusions at the case-core boundary (a region of maximum tensile stress in rotating bending[5]) would be detrimental to the fatigue strength of the material. This is because stress levels local to inclusions would exceed the material yield stress, and initiate fatigue fracture by decohesion of the matrix to the inclusion. Increasing the case depth effectively moves the probable initiation site towards the core. Thus, a greater applied stress would be necessary at the surface, to create stresses capable of failure initiation at the case-core boundary.

Cowling and Martin[90,93] concluded that high cycle fatigue (10^4 to $5*10^5$ cycles) normally resulted in failure at multiple subsurface nuclei. It is therefore reasonable to assume that higher strength core materials would perform better in fatigue situations. Stronger materials would show greater resistance to plastic deformation by virtue of the inherently higher value of yield stress. This would in turn inhibit nucleation of micro-cracks in the core.

However Scott[5] points out that fatigue improvements due to nitriding of these higher strength steels would be more limited.

Fatigue could be improved by better steelmaking techniques (e.g vacuum melting, electro slag refining etc.) where 'cleaner' steels are produced. These should have a lower non-metallic inclusion content on which fatigue micro-cracks could nucleate. Tool steels, although of great strength, have the additional presence of primary carbides at which cracking might initiate. The effect of these can only be reduced by ensuring that their distribution is even thoughout the structure and that they are small and rounded in nature. This can be effected to some extent by good heat treatment practice.

2.10.2. The Influence of Residual Stress

Surface residual stresses induced by thermochemical and local surface hardening treatments are widely held to be compressive in nature and this has been demonstrated many times.

In nitriding, precipitation of alloy nitrides in the surface layers to which nitrogen has diffused, causes localised expansion of the metal lattice structure. However, the adjacent unexpanded core material restricts this expansion, and the surface layers are therefore held in residual compression. Low temperature nitriding treatments should impose high residual stresses since the relatively low plasticity of the commonly treated steels up to about 550°C, should reduce stress relief by plastic flow. Compressive stresses in the surface act in addition to the applied stress of the fatigue situation, and can only be beneficial.

Figure 2.29 shows the situation pertaining to bending fatigue, where the compressive residual stress acts to counteract the applied tensile stress which attains its maximum value at the surface. This effectively increases the capacity of the material to withstand higher loads, without surface yielding and thereby the onset of fatigue failure.

As noted earlier, fatigue crack initiation at the surface is thought to result from slip-induced intrusions into the material and stronger material is more resistant to the onset of this process. Once a crack has formed, if tensile stresses are present then above a critical value that crack will grow and eventually cause failure. Compressive residual stresses at the surface serve to restrict this action and retard the rate of growth of such cracks.

In the core of nitrided materials adjacent to the case/core boundary there exist balancing tensile stresses. These stresses must be equal and opposite in nature to the surface stress to maintain equilibrium. Bell and Loh[97] show a relationship to predict the maximum tensile stress in the core for stress situations above the fatigue limit of the material:

$$\sigma_{max} = (k_n(\sigma_a) + \sigma_c) > \sigma_{H'} \quad \ldots\ldots(2.66)$$

where k_n is the stress intensity factor at the tip of a propagating micro-crack in the core. σ_a is the applied stress and σ_c is the tensile core residual stress. $\sigma_{H'}$ is the effective fatigue strength of the core material adjacent to the case/core interface.

In conclusion of their work Bell and Loh[97] propose a model to predict the fatigue limit of a nitrided component from the case depth measurements such that:

$$\sigma_{LIM} = \left[\frac{D}{(D - 2\delta)}\right]\sigma_h \qquad \ldots\ldots(2.67)$$

where D is the sample thickness (diameter), δ is the case depth, σ_h is the maximum applied stress level in the core at the fatigue limit of the treated specimen and σ_{LIM} is the fatigue limit (Figure 2.30).

The maximum applied stress level in the core is derived from the relationship:

$$\sigma_h + \sigma_c = \sigma_H, \qquad \ldots\ldots(2.68)$$

when $K_n = 1$. This implies that the core residual stress is of great importance to the fatigue process in case hardened steels.

In conclusion then, it can be seen that the case depth and core effects are dependent both upon one another and on the residual stress system existing as a consequence of the thermochemical treatment given.

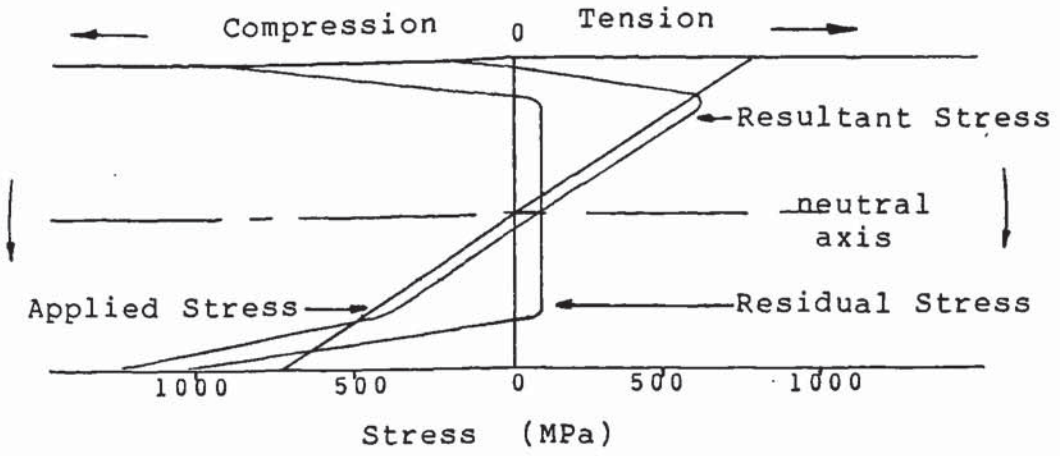

Fig.2.29. Schematic Representation of the Effects of
- Residual Stresses on the Final Stress Pattern
- of a Specimen Loaded in Bending.

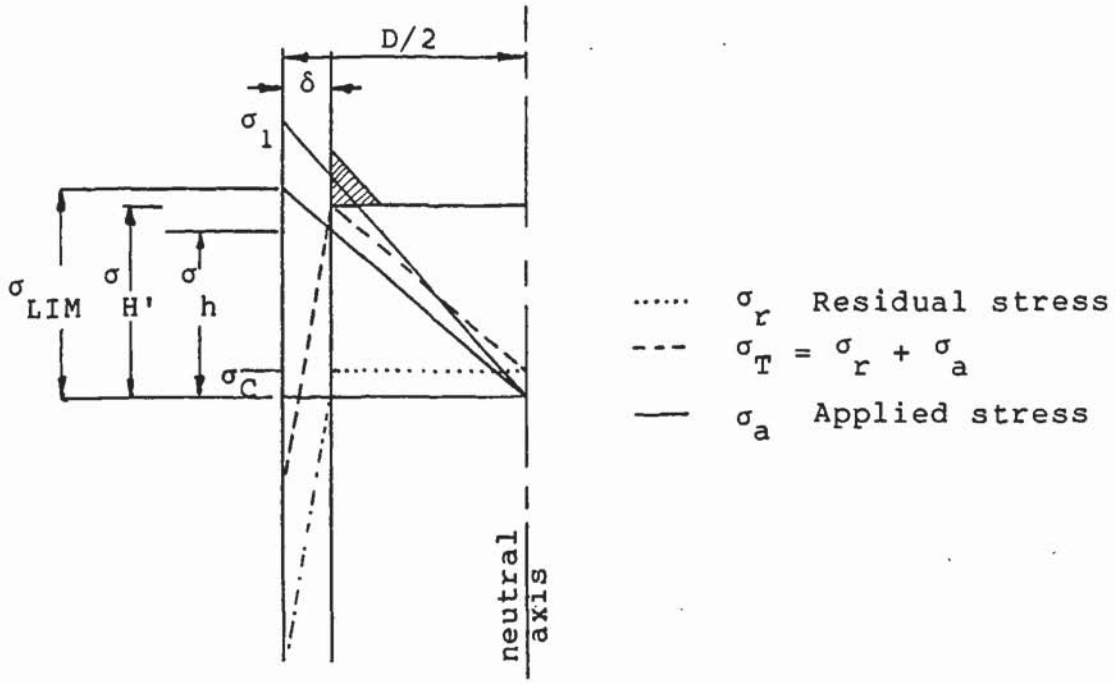

Fig.2.30. Diagram of the Effect of Case Depth on
- Fatigue Limit.

3. Experimental Procedure

3.1. The Materials

Three materials were used in this work; the high speed steels M2, T1 and the semi-high speed steel M50. The T1 was air melted/electroflux remelted steel and the M50 was vacuum induction melted/vacuum arc remelted. Analyses (wt%) for the various bar forms used - all dimensions in mm - are shown below in Table 3.1.

MATERIAL	C	Si	Mn	P	S	Cr	Mo	V	W
M2 17 Ø	0.88	0.26	0.26	0.024	0.008	4.21	4.85	1.76	6.03
22 Ø	0.87	0.23	0.27	0.024	0.012	4.24	4.76	1.80	6.12
M50 16 Ø	0.85	0.23	0.23	0.004	0.006	4.04	4.21	1.03	0.01
16x10	0.85	0.23	0.23	0.004	0.006	4.04	4.21	1.03	0.01
T1 16 Ø	0.78	0.29	0.21	0.016	0.004	4.30	0.08	1.12	18.12
16x10	0.78	0.29	0.21	0.016	0.004	4.30	0.08	1.12	18.12

Table 3.1. Chemical Analysis.

Specimens for unidirectional bending fatigue (Figure 3.1), metallography and residual stress were machined from the various bar stocks to the dimensions shown in Table 3.2. All samples were ground and polished to a fine surface finish of approximately 6μm followed by thorough cleaning and degreasing prior to heat treatment.

MATERIAL	METALLOGRAPHY	FATIGUE	RESIDUAL STRESS
M2	16 Ø x 25	14 Ø x 145	22Øx 9
T1 & M50	5 x 15 x 55	14 Ø x 145	5 x 15 x 55

Table 3.2. Sample Dimensions.(mm)

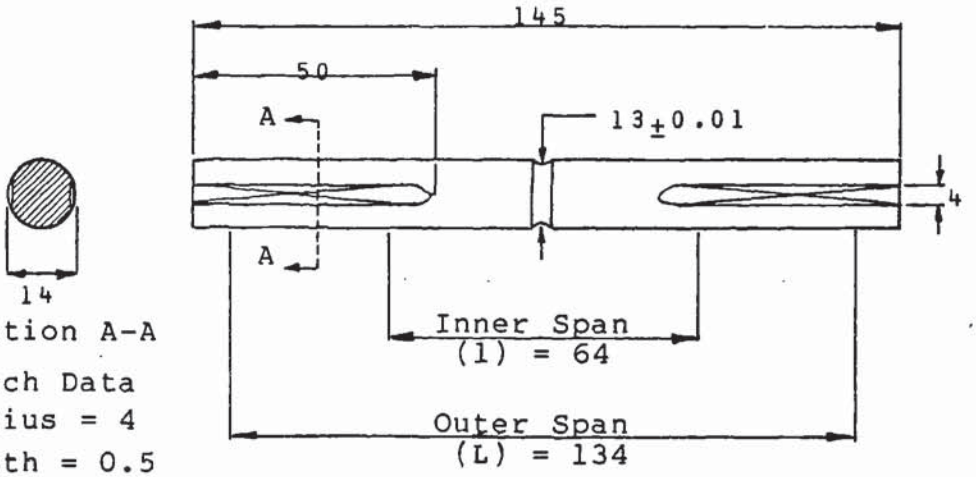

Section A-A

Notch Data
Radius = 4
Depth = 0.5
Kt = 1.16
Circumferential Round

Fatigue Specimens.

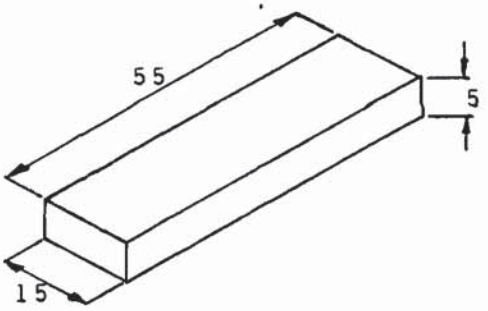

M50 & T1
Metallography,
Acoustic Emission &
Residual Stress Specimens.

M2 Metallography &
Acoustic Emission Specimens.

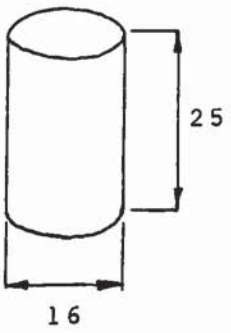

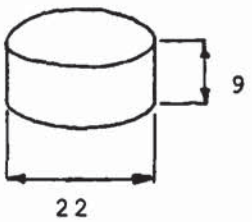

M2 Residual Stress Specimens.

(all dimensions-mm)

Fig.3.1. Specimen geometry and dimensions for the various - tests.

3.2. Heat Treatment

3.2.1. Hardening and Tempering

Hardening was carried out in a vacuum furnace. This consists a cold-walled chamber with rotary and diffusion pumps, for pumping down to operating pressures, a heat exchanger and circulation fan to aid gas quenching and solid graphite resistance heating elements (Figure 3.2).

The specimens were placed, via a top loading door, on a ceramic platform within the furnace chamber hot zone. The chamber was evacuated to approximately 10^{-4} torr before initiating the heating cycle. The samples were held at the hardening temperature for the required time prior to gas quenching to room temperature with high purity nitrogen gas. Tempering was done in an air circulation furnace followed by air cooling to room temperature.

3.2.1.1. M2 (AISI 650 Series)

These samples were divided into three groups and were hardened and tempered according to the schedules described in Table 3.3. In all cases the samples were held at the hardening temperature for 10 minutes. Tempering was a double cycle of 90 minutes duration each time with air cooling to room temperature in between. No protection from oxidation was given during tempering since samples were to be repolished, to recover surface integrity prior to the subsequent plasma nitriding treatment.

TREATMENT	'Full' Harden & Temper	'Full' Harden & Undertemper	Underharden & Full Temper
Austenitising	1180	1180	1030
Tempering	550	500	500

Table 3.3. Hardening and Tempering Temperatures.(°C)

Fig.3.2. The Scot Vac Vacuum Furnace.

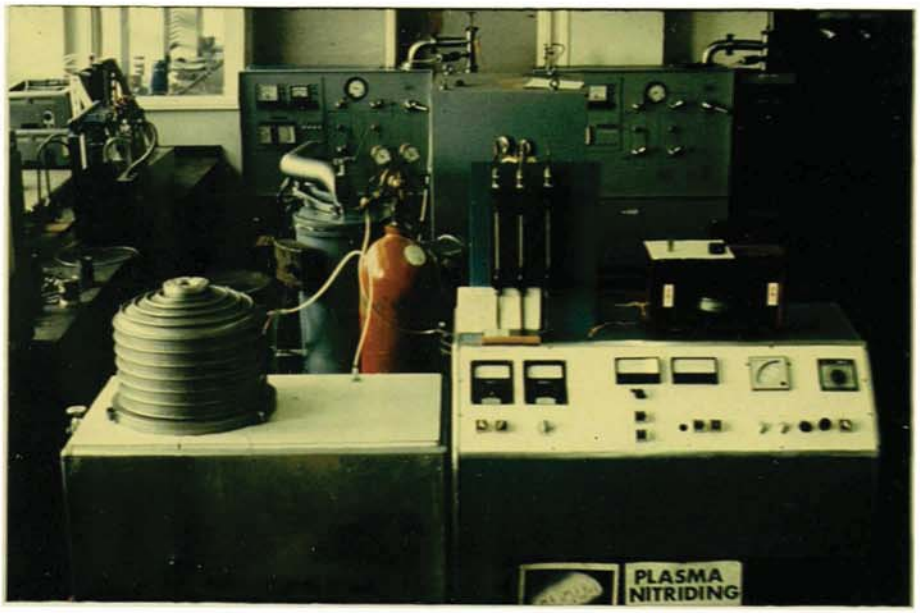

Fig.3.3. The Plasma Nitriding Unit.

The 'Full' Hardening temperature was chosen as the optimum to achieve near maximum hardness together with fair fracture toughness as described in previous work[26]. Also the temperature chosen, although at the bottom of the conventional hardening range for the material, is one finding general acceptance in industry as giving a good 'all round' hardening treatment.

The Underhardening treatment was carried out to improve fracture toughness without undue loss of hardening characteristics, the tempering temperature being chosen to achieve optimum properties for the relevant austenitising temperature with regard to the tempering curves for the material. Undertempering was set at an arbitrary figure to study the effect on the subsequent plasma nitriding treatment.

3.2.1.2. T1 (AISI 610 Series) & M50 (AISI 360 Series).

The prepared test samples were treated according to the desired Rolls Royce specifications for the relevant materials. Details are shown in Table 3.4. below.

TREATMENT	AUSTENITISING TEMP(°C)	TEMPERING TEMP(°C)
T1	1240	550
M50	1100	550

Table 3.4. Hardening and Tempering Temperatures.

The T1 and M50 samples were held at the hardening temperature for 5 and 10 minutes respectively prior to gas quenching to room temperature.

Tempering was divided into three cycles of 2 hours duration each at the specified temperature, the first temper being started less than 1 hour after the samples were removed from the vacuum furnace. Within 1 hour of completion of the first temper, and air cooling to room temperature, the samples were given a sub-zero treatment in liquid nitrogen which lasted for not less than 90 minutes prior to the next temper. This operation was repeated after the second temper and the final temper was followed by a simple air cool to room temperature. Samples were then repolished as was the case with the M2 specimens.

Underhardening and Undertempering treatments were not studied here since materials were not available in sufficient quantity to prepare a useful schedule of tests and also work carried out on the M2 material suggested that the benefits to be achieved from such treatments might not be significant enough to justify the large expenditure of time necessary to complete the work.

3.2.2. Plasma Nitriding

Nitriding was carried out in purpose-built equipment made by personnel at the University. The unit consists of a double-walled, water cooled vacuum chamber fitted with rotary and diffusion pumps, a gas distribution system and a d.c. power supply which included unstable arc-discharge circuitry (Figure 3.3).

The samples were placed in the chamber on the cathode platform, along with a temperature control specimen which had a chromel-alumel thermocouple embedded in it.

The chamber was evacuated to approximately 10^{-4} torr, treatment gas was admitted to purge any remaining air, followed by re-evacuation to 10^{-4} torr. The chamber was backfilled to 1-3 torr with the H_2 - N_2 treatment gas prior to starting the treatment.

With the arc-discharge protection circuitry switched off, potential was applied to the circuit in which the chamber wall was the anode and the samples and platform acted as the cathode. When voltage drop and current flow was established ie. initiation of the plasma glow, the samples were brought up to the treatment temperature using a device which inputs power to the plasma at a controlled rate to ensure steady heating. Sputter cleaning of sample surfaces was achieved during heating to the operating temperature. Once at the desired temperature, the arc-discharge protection circuit was switched back on. Treatment duration was timed from this point. At the end of the cycle, power to the plasma was turned off and the furnace chamber filled with high purity nitrogen gas to accelerate cooling of the samples and chamber.

3.2.2.1. M2 (AISI 650 Series)

The treatment schedule here was based upon the study of process temperature and time utilising an atmosphere of fixed composition. Preliminary tests were carried out using metallography/acoustic emission samples, to determine the best treatment options to use for the fatigue samples. Table 3.5 shows the treatment conditions studied for both the preliminary studies and the fatigue tests.

Atmosphere	75%H_2/25%N_2
gas flow rate.	200*$10^{-6}m^3$.$min.^{-1}$
Chamber Pressure.	4torr (533Pa)
Power Requirements.	0.25 to 1.5kW depending on furnace load and treatment temperature.

Treatment Temperature (°C)	Treatment Times Studied (hrs) Preliminary Tests.	Fatigue Tests.
400	16	16
450	1, 4, 16, 64	16
500	16	16
550	16, 64	16
600	16	—

Table 3.5. Plasma Nitriding Conditions - M2

3.2.2.2. T1 (AISI 610 Series) & M50 (AISI 360 Series)

Since previous work suggested 'white layer' formation might cause problems with the treatment of these steels, and work already completed on the M2 steel showed the optimum treatment temperature range to study, this work was based upon variation of the atmosphere composition using a fixed time and temperature process. Table 3.6 shows the parameters studied.

Treatment Temperature.	450°C.
Treatment time	16 hours
Chamber Pressure	4torr (533Pa)
Power Requirements	(0.5 - 1.1kW) + 0.3kW resistance heating - dependent upon furnace load and gas mixture.
Treatment Atmosphere	75%H_2/25%N_2
	85%H_2 /15%N_2
	95%H_2 /5%N_2
Gas Flow Rate	200*$10^{-6}m^3$. $min.^{-1}$

Table 3.6. Plasma Nitriding Conditions - M50 & T1

Delays in acquisition of test materials necessitated the work schedule being compressed to such an extent that the fatigue samples were treated before the metallography tests had been completed.

Also prior to these materials being treated, considerable modifications were made to the plasma nitrider. Low flow rate meters with fine control needle valves were fitted, together with a gas mixing/expansion chamber to facilitate improved flow control and suppression of flow fluctuation - a problem encountered in the earlier work on the M2 steel.

Additionally, resistance heating elements with an independent electrical supply were fitted to aid heating and temperature control. The diffusion and rotary pumps were removed and replaced by a more powerful rotary pump. This alteration was carried out in anticipation of work to be done, on roller bearing elements, which would have necessitated the use of a 'moving cathode' type of arrangement to ensure total exposure of all surfaces of the samples to the treatment plasma.

3.3. The Tests.

3.3.1. Hardnesses (Bulk and Micro-).

Bulk surface and core hardness (HV_5) values were taken using a Vickers machine. A minimum of four readings were made in each case and average values calculated and reported. Since the plasma-nitrided samples were of good surface finish after treatment, only light polishing was necessary to get a 'bright' surface prior to testing. The microhardness/case depth tests were carried out on a Vickers microscope using a 200gmf load ($HV_{0.2}$), applied for 30 seconds to produce hardness impressions. All precautions as described in the microscope operating instructions were fully observed to ensure consistent and reliable results. Filar eyepiece calibration and test block hardnesses were carried out prior to each period of testing using this equipment.

3.3.2. Metallography

Transverse sections were taken for examination. After sectioning and mounting the metallography specimens in the conventional manner using conducting bakelite, the samples were surface ground prior to final preparation on 6 and 1μm polishing wheels.

A swabbing and immersion technique, using 4% nital, was employed to develop a suitably etched microstructure for metallographic examination. In most cases the etching time was 2 minutes. Microstructures were examined using both optical and scanning electron (SEM) microscopy. The optical study was carried out on both etched and unetched samples, photomicrographs being taken to illustrate structures where necessary.

The SEM was used to study both microstructures and the fracture surfaces of some of the fatigue samples after testing. The Link energy-dispersive X-ray spectroscopy facility was used to establish semi-quantitative analysis of the samples examined and to help in identification of microstructural phases observed.

3.3.3. Acoustic Emission Testing

Dunegan acoustic emission equipment was used in conjunction with a 12.5mm diameter ball bearing indentor and 50 tonne force Instron tensile testing machine to detect cracking of surface layers.

A transducer resonant at 150kHz was used to transmit acoustic emissions to a totaliser (amplifier) of 40dB gain, via a pre-amplifier capable of 60dB gain, to yield a total gain of 100dB. The amplifier output was fed to a twin pen chart recorder calibrated to 10V d.c. full scale deflection on both pens. Full scale deflection on one pen corresponded to 10^5 counts and measured cumulative acoustic output during testing. The other pen simultaneously recorded the test load and was calibrated to 10 tonne force fsd.

Figure 3.4 shows (a). a schematic representation of the test setup and (b). a typical example of the load/acoustic emission data collected on the chart recorder. Oil was smeared over the contacting surfaces of the lower platen and indentor cup and ball in order to reduce external 'noise' from movement and sliding contact at loading points and to aid acoustic coupling to the transducer.

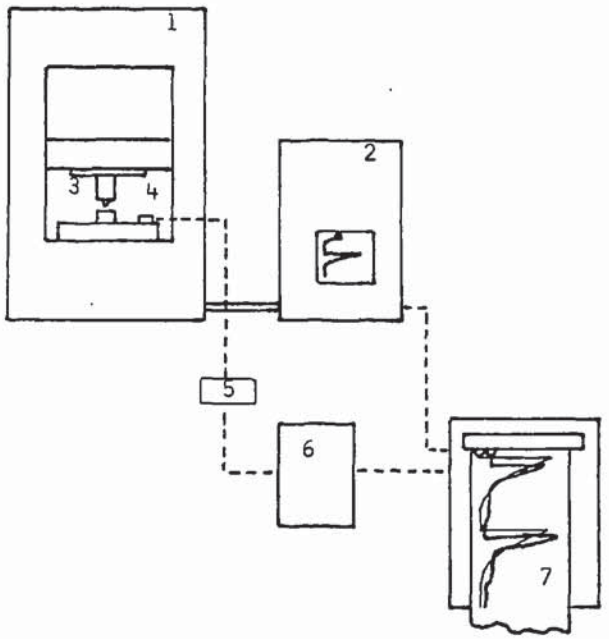

1. Instron 500kN Tensile Test Machine.
2. Instron Control Panel and X-Y Chart Recorder.
3. AE Ball-Bearing Indentor.
4. Transducer (150kHz).
5. Pre-Amplifier.
6. Totaliser (Amplifier).
7. Twin Pen Chart Recorder.

Fig.3.4.(a) Schematic Representation of the Acoustic - Emission Set-up

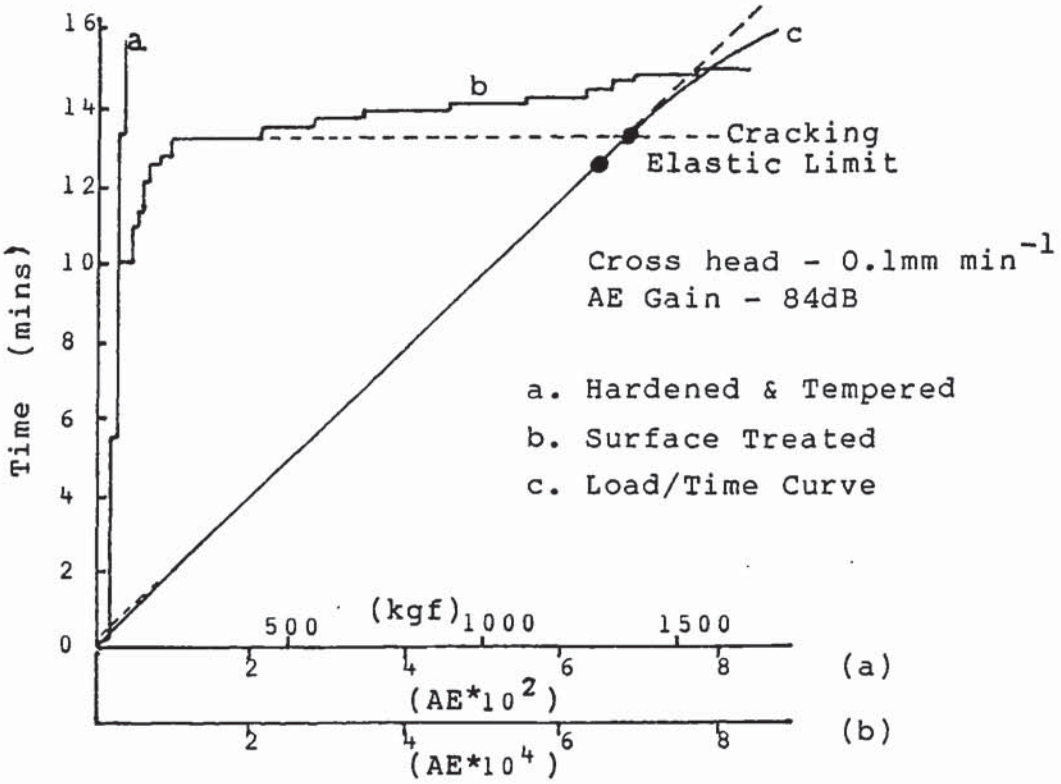

Fig.3.4.(b) A Typical Example of the Output from the Set-up

After initial pre-loading, the load was applied at a crosshead speed of $0.1mm.min^{-1}$. A gain of 84dB was used for the tests since previous work[98] showed cracking would not be easily detected at this level in untreated samples but would be in nitrided specimens. Analysis of the graphical data generated in testing gave the load to first cracking of the case for each treatment tested.

3.3.4. Residual Stress Determination

The Philips X-ray diffraction equipment in standard form cannot be readily applied to residual stress determination. This is due primarily to the difficulty in re-orienting the specimen to the incident X-ray beam so that diffraction data for different ψ angles may be collected. Figure 3.5 shows a schematic representation of the equipment set-up and X-ray beam paths.

After preliminary equipment modifications and residual stress determinations had been carried out, a metallurgical stage attachment was purchased and fitted to the goniometer. This stage allows rotation of the specimen, along the goniometer axis, through the angle ψ, independently of the 2θ movement of the receiving slit and radiation detector. Also, a natural consequence of the alteration of specimen 'attitude' to the incident X-rays, is a change in the focussing conditions of the diffracted beam. The metallurgical kit allowed greater flexibility of radial movement, of the receiving slit/detector to accommodate this change, than was previously possible. Figure 3.6 shows the equipment in its present form.

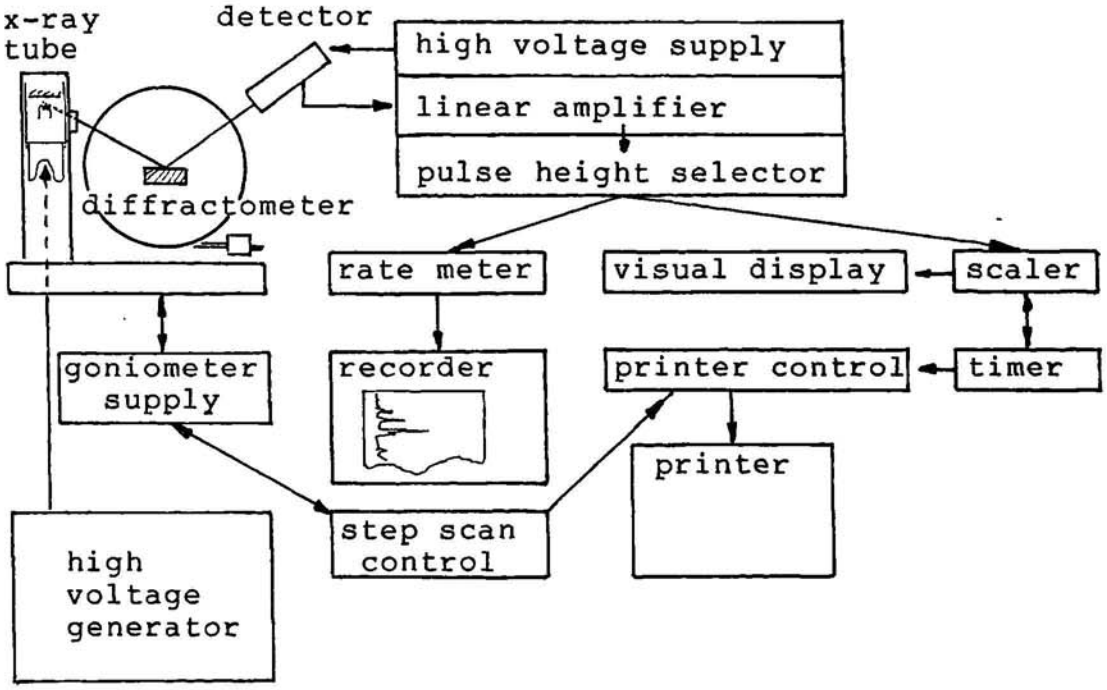

Fig.3.5. Schematic Representation of the XRD Equipment.

Fig.3.6. The Phillips X-Ray Diffractometer with - Metallurgical Stage Attachment.

Several techniques have been used in the course of this work; all of them based upon the determination of the {211} ferrite peak occuring at a Bragg angle of approximately 156° 2θ in steels. The general operating conditions for the equipment are described in Table 3.7.

X-Ray Tube	Chromium
Radiation	Cr K_α
Wavelength	2.2897 Å
Potential	36kV
Current	42mA
Beta Filter	Vanadium (at receiving slit)
2θ Scanning Range	148 to 158 degrees
Divergence Slit	2°
Receiving Slit	0.2mm
Scatter slit	4°
Detector	Proportional counter

Table 3.7. General Operating Conditions for the X-Ray Set.

3.3.4.1. Double Exposure - Fixed Time Counting

Determination depended on step scanning for a small 2θ interval in the vicinity of the {211} ferrite peak (156°2θ). Diffraction data was collected as the number of counts accumulated during measurement for a fixed time (in this case 10 minutes) for each step - peak location being indicated by an increase in the number of counts gathered. This sequence was performed for two ψ values ie. 0° and 45°.

The lateral peak shift, as determined by computation of the accumulated data, yields a value of lattice strain which may be used to calculate residual stresses within the sample surface. Tests were repeated several times on each sample to validate the results obtained and assess the accuracy.

3.3.4.2. Double Exposure - Fixed Count Method

This technique is basically the same as for that described above, but here the time taken to accumulate a pre-determined number of counts is measured for each step; peak location being indicated by a fall in count time.

Again the procedure was repeated for two values of the angle ψ (0 and 45°). Modification of the computation was made to account for the different type of data acquired (discussed later) but the basis of the stress determination was the same. In most cases the count rate interval was restricted to 10^4 to $3*10^4$ counts due to low count rates being achieved on these materials.

3.3.4.3. Multiple Exposure Technique - $Sin^2\psi$.

This is the same procedure as in 3.3.4.2. but with one important difference. Instead of carrying out step scanning for two angles of ψ, additional scans at ψ =15° and ψ =30° were also carried out.

The additional data generated after computation of peak shift was used to construct graphs of lattice strain ($\Delta 2\theta$) vs. $\sin^2\psi$.

Prior to these tests calculations were made for depth of X-ray penetration and absorption by the sample surface. Accordingly, some problems were expected due to the presence and thickness of surface white layer formed during some of the nitriding treatments. This proved to be the case during testing and so electrolytic polishing was carried out on each sample prior to testing. This removed a fixed amount of the surface and it was hoped that this would reduce the problems experienced in peak identification.

Table 3.8 shows the conditions for electrolytic polishing together with the solution used and depth of material removed.

Additionally, set-up errors during testing were expected due to sample location on the goniometer axis. This was more of a problem with the original setup than with the metallurgical stage facility, which has a dial gauge for accurate sample height location. Consequently tests were carried out on a fully-annealed mild steel sample to determine errors generated by sample location in the X-ray beam. At this stage, no work has been carried out to determine the materials' Poisson ratio and modulus of elasticity due in part to the need for additional test equipment and also due to the fact that stress sign and magnitude are of more importance at this time rather than precise values of stress.

Solution	95% Glacial Acetic Acid +5% Perchloric Acid
Temperature	14 to 20°C. (maintained by a cooling coil immersed in the etchant)
Voltage	50 V
Current Density	1.0 A $cm.^{-2}$
Time	1.75 mins
Material Removed	20μm ± 3μm

Table 3.8. Electropolishing Conditions

3.3.5. Surface Phase Analysis

The x-ray diffractometer as described for the residual stress determination was used.

Prior to electropolishing the specimens for residual stress determination, surface phase analysis was carried out on each sample to identify the presence or absence of any white layer formed during plasma nitriding.

Continuous scanning over 40° - 140° 2θ was used for these tests, with operating conditions as described in Table 3.9 below.

The data output of count rate vs 2θ angle was collected in graphical form on the chart recorder for each sample examined.

X-Ray Tube	Chromium
Radiation	Cr K_α
Wavelength	2.2897 Å
Potential	36kV
Current	42mA
Beta Filter	Vanadium (at receiving slit)
2θ Scanning Range	40 to 140 degrees
Scan speed	1° min^{-1}
Divergence Slit	1°
Receiving Slit	0.1mm
Scatter slit	2°
Detector	Proportional counter
Chart Speed	10mm min^{-1}

Table 3.9. X.R.D. Operating Conditions for Phase Analysis.

3.3.6. Fatigue Tests

A cylindrical notched bar was used with machined flats to accommodate the loading points. The geometry and dimensions of the test set-up and specimen are shown in Figure 3.1.

An Amsler Vibrophore electro-magnetic resonance machine was used with a 50kN dynamometer fitted. The samples were tested in unidirectional bending fatigue at a frequency of 100Hz ± 10, using a purpose built four-point loading system with an inner span (l) of 64mm and an outer span (L) of 134mm.

Using this test geometry:

$$\sigma_{nominal} = \frac{8P(L - l)}{\pi D^3} \qquad \ldots\ldots(3.1)$$

where D is the specimen diameter at the notch root and P is the load.

For D = 13mm this reduces to:

$$\sigma_{nominal} = (8.11*10^{-2}).P \quad (mm^{-2}) \qquad \ldots\ldots(3.2)$$

The first tests carried out suffered from severe fretting wear of the loading points, causing some load instability during testing. In addition to this problem, the high loads used caused the loading points of the test jigs (adjustable for variation of the span width) to work themselves loose, causing loss of control of the load oscillation and excessive vibration.

New test jigs with loading points, of 8mm diameter BM2 high speed steel inserts, cemented into mild steel blocks with Truloc Superfit 211 bearing cement were made. Molybdenum disulphide grease was used as a loading point lubricant. Steel inserts were used to facilitate rotation or replacement of the loading points, if evidence of damage was seen, prior to starting a test. Each insert was hardened, tempered and plasma nitrided for 4hrs at 450°C to further reduce the fretting damage problem.

The theoretical stress concentration factor for the notch dimensions used ie. radius 'R' = 4mm and depth 'a' = 0.5mm, was k_T = 1.16. Use of such a low k_T value required the removal of all sharp edges from the load bearing flats to ensure that samples failed within the notched region.

A step testing technique was used where, if the specimen survived 10^5 cycles at the applied stress level, the load was increased by 5% and the test was re-run at the new value. This procedure was repeated to sample failure. The cycles survived at the failure load was recorded.

A stress ratio of approximately R = 0.25 was used ie.

$$R = \frac{\sigma_{min}}{\sigma_{max}} = 0.25 \qquad \ldots\ldots(3.3)$$

and since:

$$\sigma_{mean} = \frac{(\sigma_{max} + \sigma_{min})}{2} \qquad \ldots\ldots(3.4)$$

the maximum stress is given by:

$$\sigma_{max} = 1.6\sigma_{mean} \qquad \ldots\ldots(3.5)$$

Testing was carried out in accordance with the Vibrophore manual for Type 10HFP 422 machines. A sample was centralised on the loading points of the lower jig and the mean load was applied with the cross-head screw. The magnet gap was set to 1.3mm (12 teeth) and the machine was started. Maximum load was set using the dynamometer light scale ensuring, that this was not exceeded during adjustment. Fine tuning of the machine controls was carried out for running at approximately 100Hz and the overload and failure relays were activated.

Five bars were tested for each heat treatment condition. However, some non-valid results were obtained due to failure prior to achieving the test load ie. during set-up. Additionally, several output valves failed causing imbalance between the output stage amplifiers, and the dynamometer photocell (which is used to control the load amplitude) also failed resulting in overload and fracture of a number of specimens.

The test geometry used was taken from work carried out by Child, Plumb and Reeves[98]. Testing to 10^5 cycles was also derived from this work since, it was observed that, these materials predominantly failed within 10^5 cycles of testing at the fracture load.

4. Results

4.1. Heat Treatment Identification

Table 4.1 shows the identification codes for the various plasma nitriding treatments carried out. For the M2 steels these labels are made-up from the treatment temperature, prior heat treatment condition and the treatment duration. The prior heat treatment condition is signified by a letter according to the following :

(i) F - Hardened @ 1180°C and double tempered @ 550°C (fully hardened)

(ii) U - Hardened @ 1180°C and double tempered @ 500°C (under-tempered)

(iii) H - Hardened @ 1030°C and double tempered @ 500°C (under-hardened)

The treatment atmosphere is not identified since this was the same in all cases ie. 75%H_2/25%N_2 at a pressure of 4torr (5.3mbar or 533Pa).

T1 and M50 steels are signified by the letters T and M respectively. Additionally, the treatment atmosphere used in the plasma nitriding of these steels has been appended (in parentheses) to the relevant label and is identified by the atmosphere nitrogen content.

Treatment	Material & Condition	Atmosphere	Identification
Hardened & Tempered	M2 (F)	vacuum	0F0
	(U)		0U0
	(H)		0H0
16hrs @ 400°C	M2 (F)	$75\%H_2/25\%N_2$	400F16
"	(U)	"	400U16
"	(H)	"	400H16
1hr @ 450°C	M2 (F)	"	450F1
"	(U)	"	450U1
"	(H)	"	450H1
4hrs @ 450°C	M2 (F)	"	450F4
"	(U)	"	450U4
"	(H)	"	450H4
16hrs @ 450°C	M2 (F)	"	450F16
"	(U)	"	450U16
"	(H)	"	450H16
64hrs @ 450°C	M2 (F)	"	450F64
"	(U)	"	450U64
"	(H)	"	450H64
4hrs @ 500°C	M2 (F)	"	500F4
16hrs @ 500°C	M2 (F)	"	500F16
"	(U)	"	500U16
"	(H)	"	500H16
4hrs @ 550°C	M2 (F)	"	550F4
16hrs @ 550°C	M2 (F)	"	550F16
"	(U)	"	550U16
"	(H)	"	550H16
64hrs @ 550°C	M2 (F)	"	550F64
"	(U)	"	550U64
"	(H)	"	550H64
4hrs @ 600°C	M2 (F)	"	600F4
16hrs @ 600°C	M2 (F)	"	600F16
"	(U)	"	600U16
"	(H)	"	600H16
Hardened & Tempered	M50	vacuum	0M0
	T1	"	0T0
16hrs @ 450°C	M50	$75\%H_2/25\%N_2$	450M16(25)
"	T1	"	450T16(25)
"	M50	$85\%H_2/15\%N_2$	450M16(15)
"	T1	"	450T16(15)
"	M50	$95\%H_2/\ 5\%N_2$	450M16(5)
"	T1	"	450T16(5)

Table 4.1. Identification of Plasma Nitriding Treatments

4.2. Surface/Core Hardness and Case Hardness Profiles

Table 4.2 is a summary of the data collected from the various bulk and micro-hardness surveys carried out for each plasma treatment. The case depths described have been determined from graphs of micro-hardness vs depth as shown by Figures 4.1(a) - (o).

The most common practice when determining case depths is to take the depth to 550Hv as contituting the case. This is normal for work on case hardened plain carbon and low alloy steels.

However, tool steels generally have core hardnesses greater than 550Hv and this criterion is therefore of less value here. Accordingly, the case depth determination has been based upon the extent of hardening to the core value + 50Hv. This alternative criterion is used by the tool heat treatment industry for harder materials.

Identification	Case Hv_5	Core $Hv_{0.2}$	Case Depth (μm)	
			White Layer	(core+50Hv)
0F0	910	907		
0U0	805	817	0	0
0H0	720	718		
400F16	1335	896		85
400U16	1211	865	2.0	84
400H16	1259	740		80
450F1	992	922		35
450U1	946	865	0	0
450H1	852	766		0
450F4	1146	899		84
450U4	1006	915	<1.0	0
450H4	992	795		45
450F16	1413	920	5.5	155
450U16	1304	937	7.5	170
450H16	1325	840	6.5	165
450F64	1413	895	10.0	270
450U64	1405	856	8.0	270
450H64	1436	742	11.0	290
500F4	1375	957	<1.0	90
500F16	1299	922		150
500U16	1235	950	<1.0	160
500H16	1207	840		170
550F4	1314	926	<1.0	125
550F16	1096	707	10.0	315
550U16	1049	704	11.0	290
550H16	1116	586	9.0	335
550F64	1210	809	11.5	510
550U64	1104	811	11.5	490
550H64	1137	646	12.0	510
600F4	1120	761	<1.0	215
600F16	1080	443	8.0	285
600U16	1034	545	10.0	265
600H16	1006	549	9.0	270
0M0	906	873	0	0
0T0	932	927	0	0
450M16(25)	1028	878	<1.0	280
450T16(25)	1045	925	<1.0	200
450M16(15)	1315	871	<1.0	270
450T16(15)	1371	937	<1.0	150
450M16(5)	1284	888	<1.0	210
450T16(5)	1339	950	<1.0	140

Table 4.2. Hardness and Case Depth Data for M2, M50 and T1

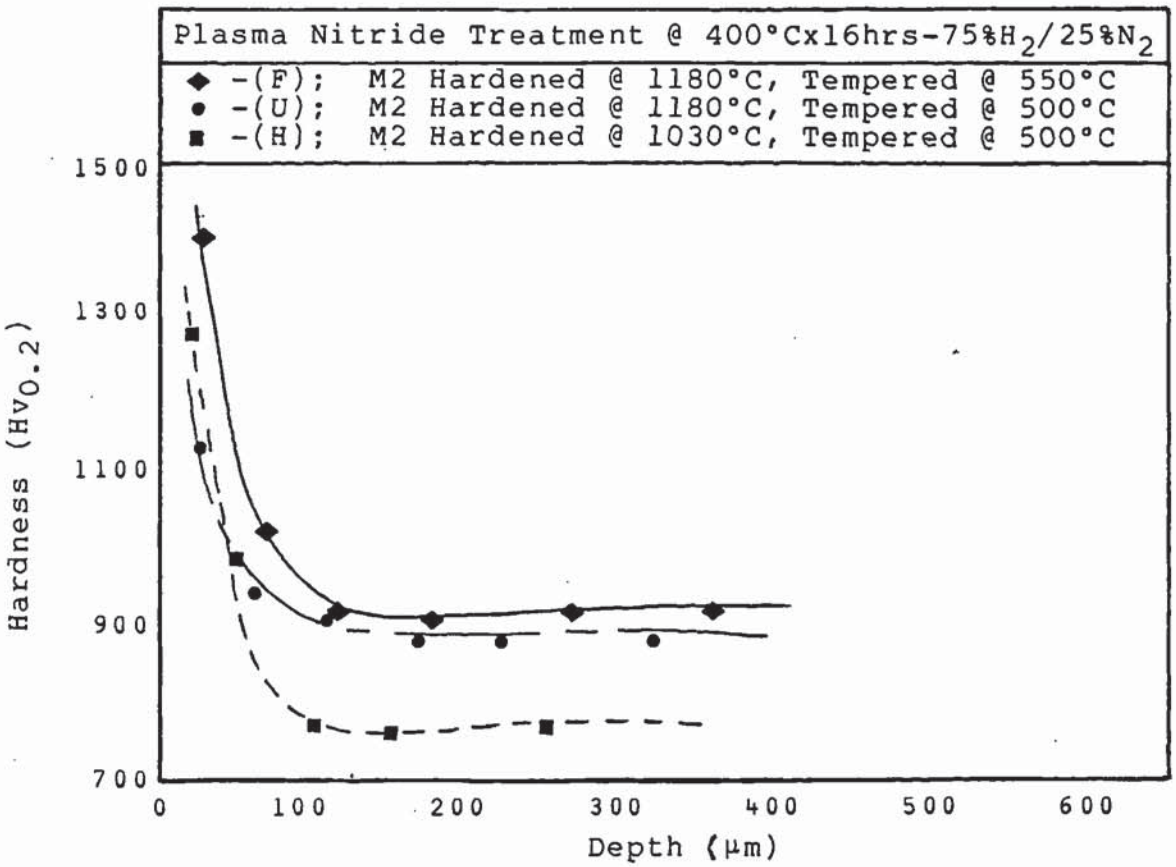

Fig.4.1 (a) Case Hardness Profiles for Plasma Nitrided M2.

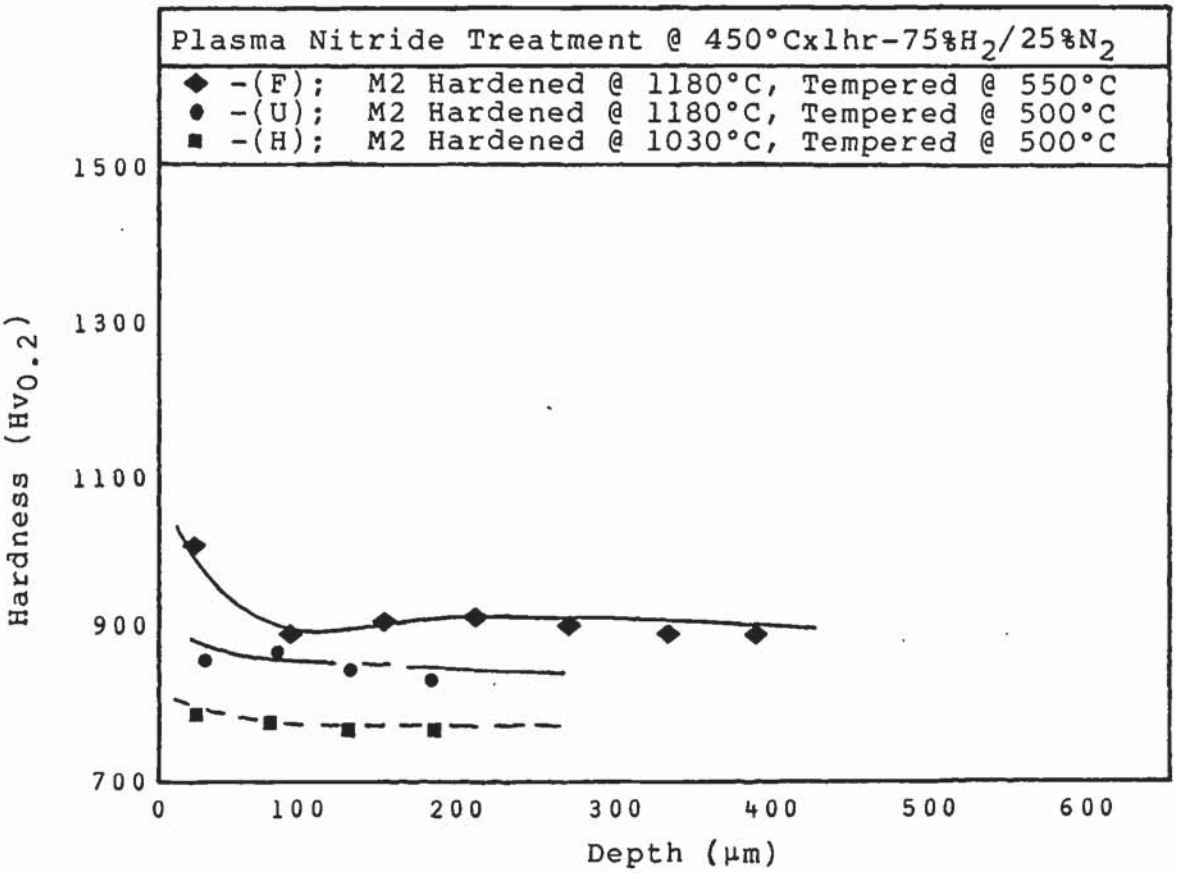

Fig.4.1 (b) Case Hardness Profiles for Plasma Nitrided M2.

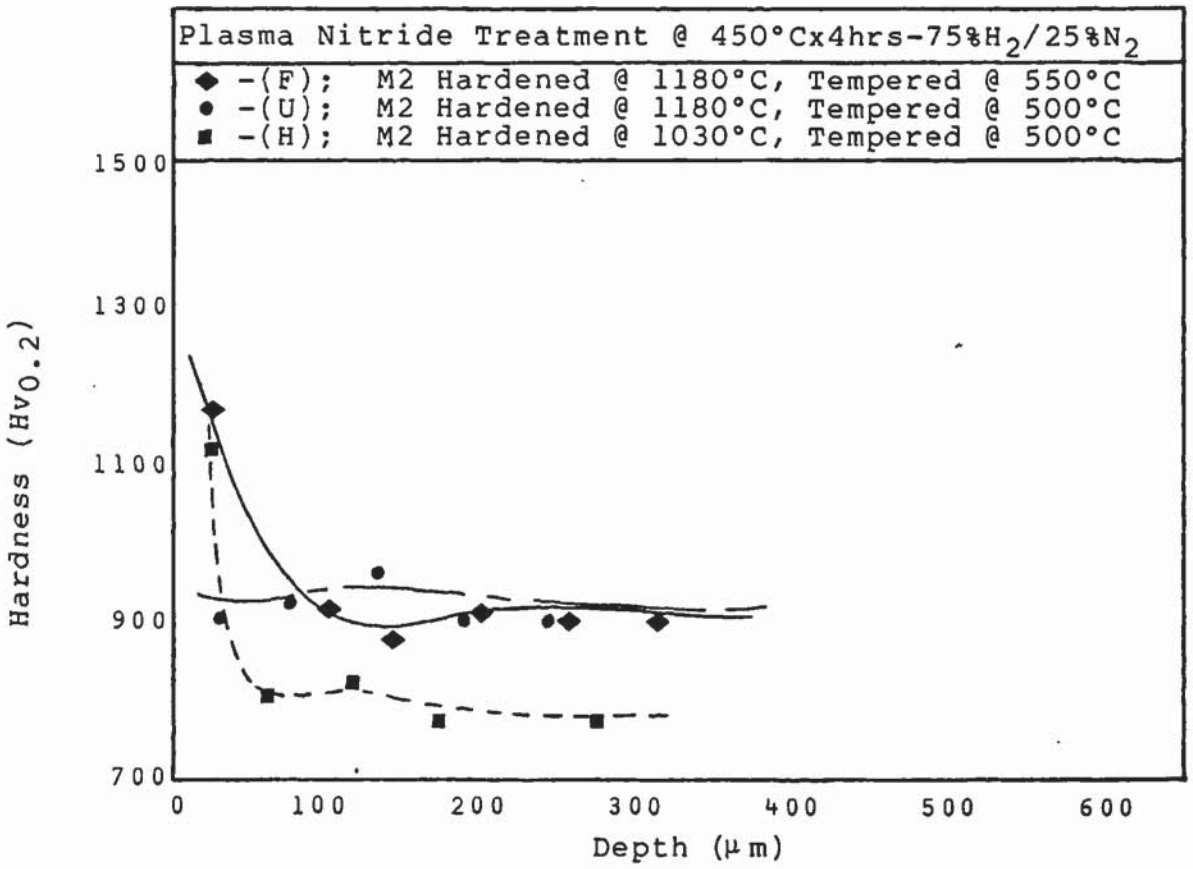

Fig.4.1 (c) Case Hardness Profiles for Plasma Nitrided M2.

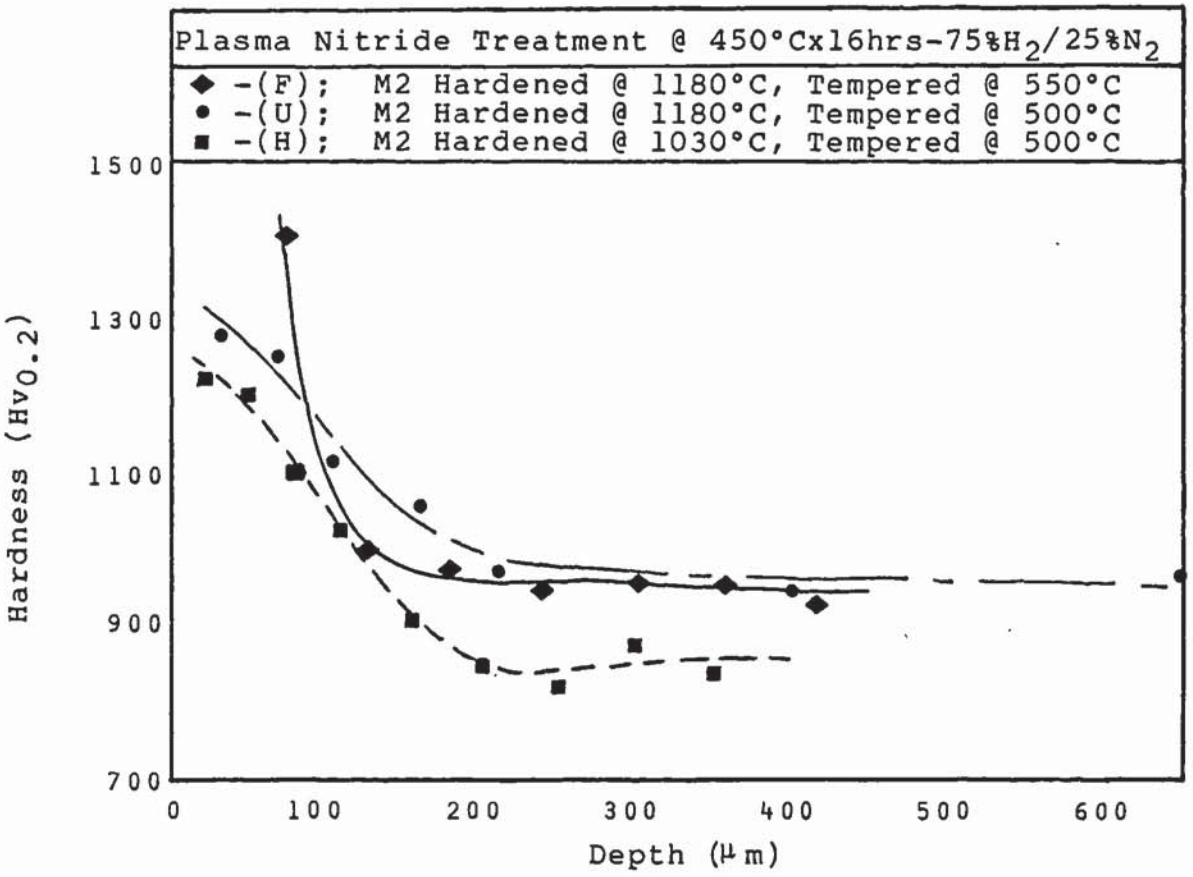

Fig.4.1 (d) Case Hardness Profiles for Plasma Nitrided M2.

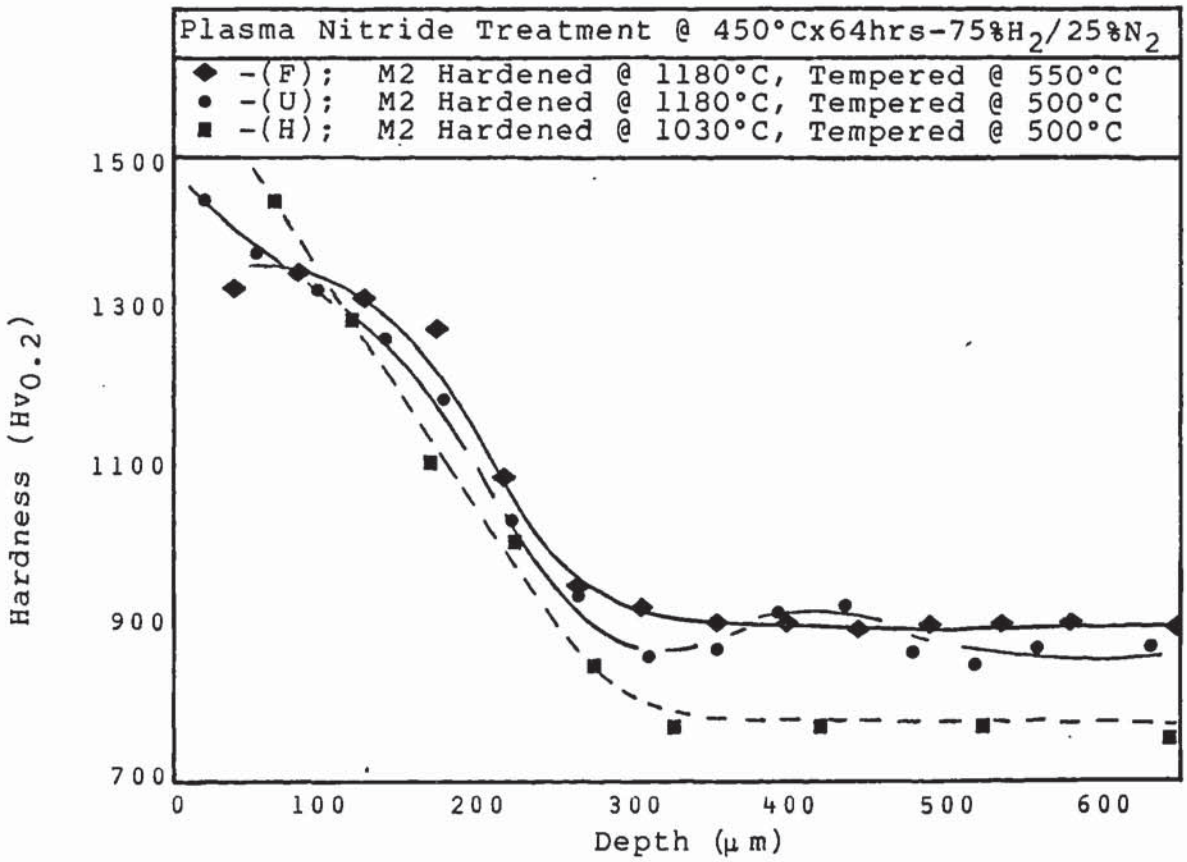

Fig.4.1 (e) Case Hardness Profiles for Plasma Nitrided M2.

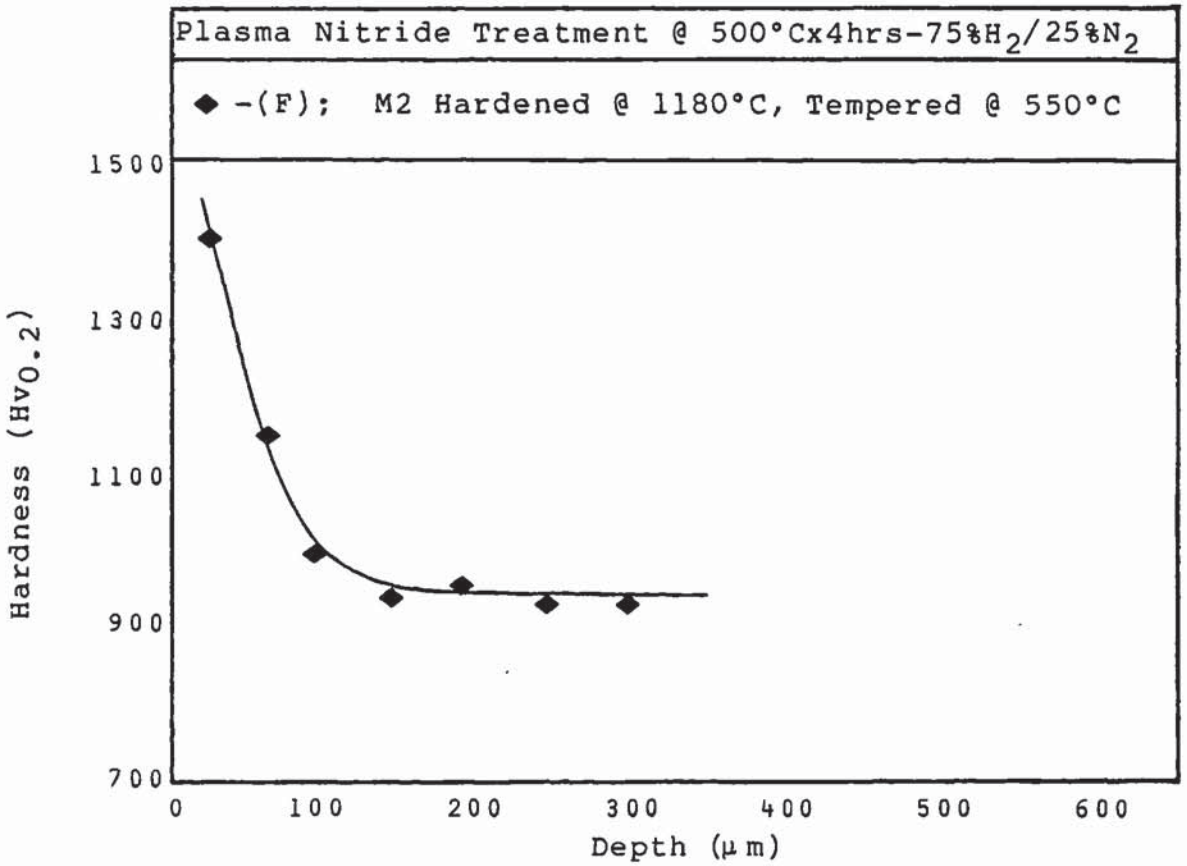

Fig.4.1 (f) Case Hardness Profile for Plasma Nitrided M2.

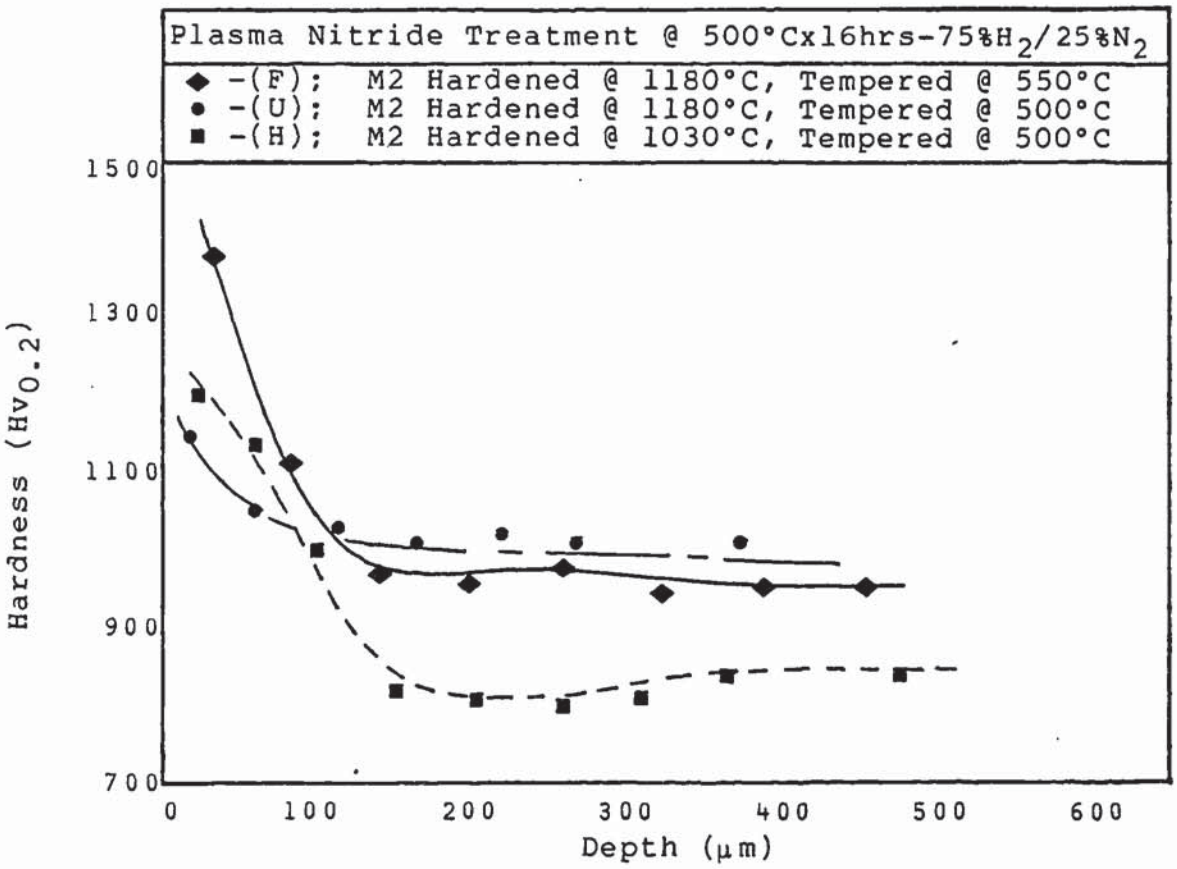

Fig.4.1 (g) Case Hardness Profiles for Plasma Nitrided M2.

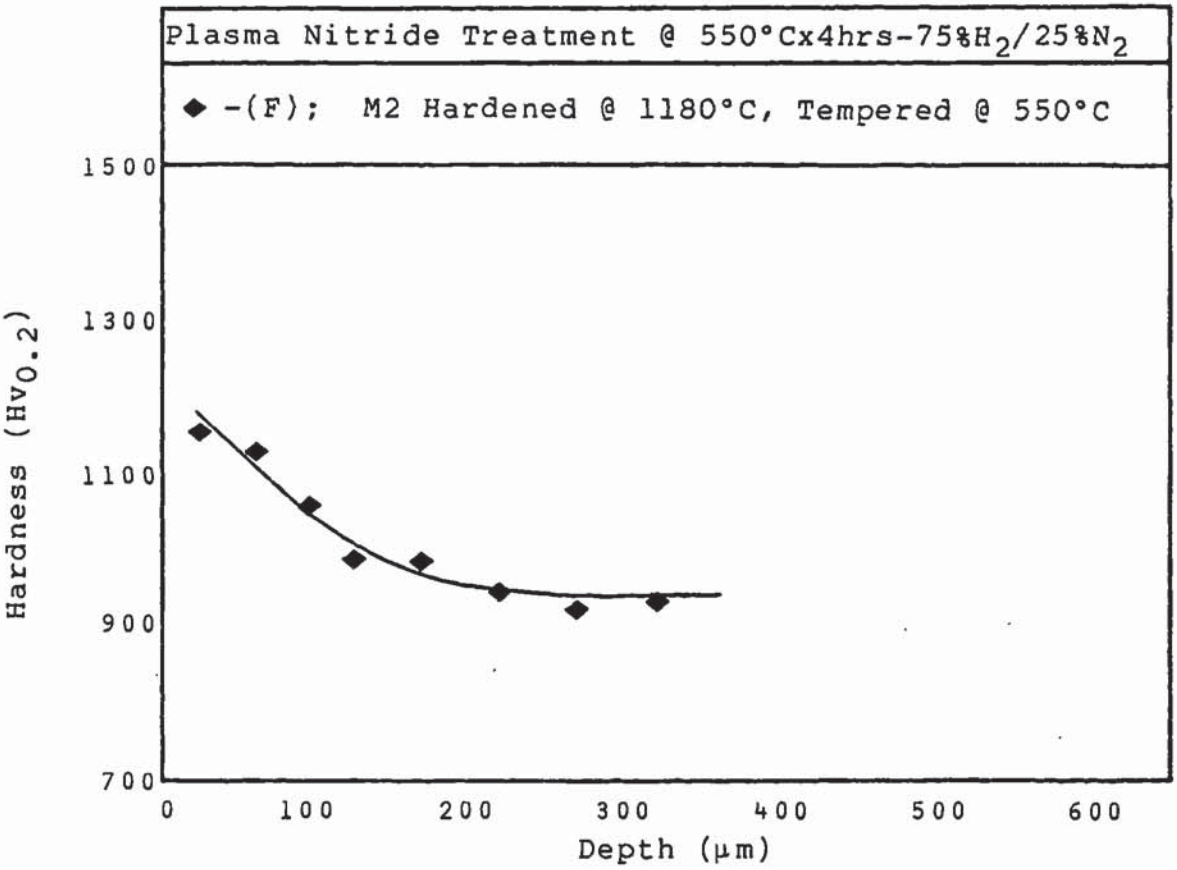

Fig.4.1 (h) Case Hardness Profile for Plasma Nitrided M2.

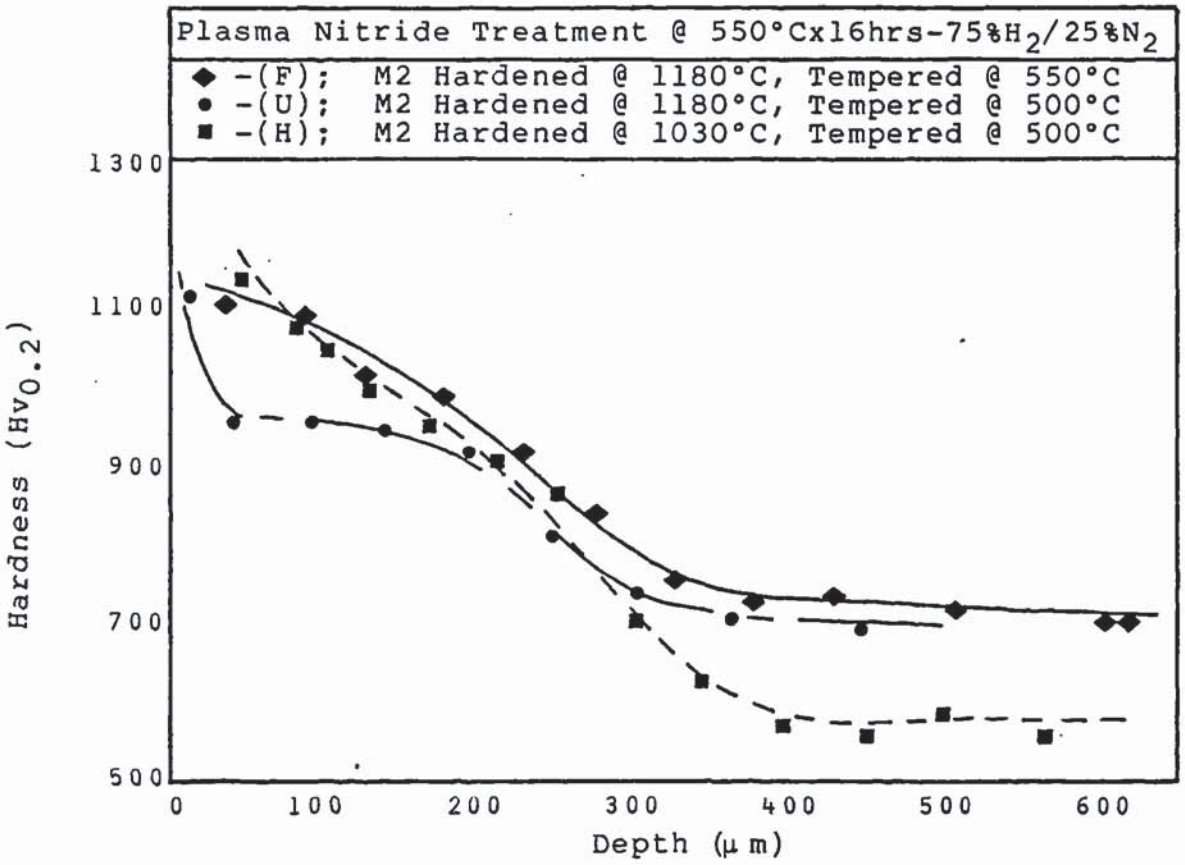

Fig.4.1 (i) Case Hardness Profiles for Plasma Nitrided M2.

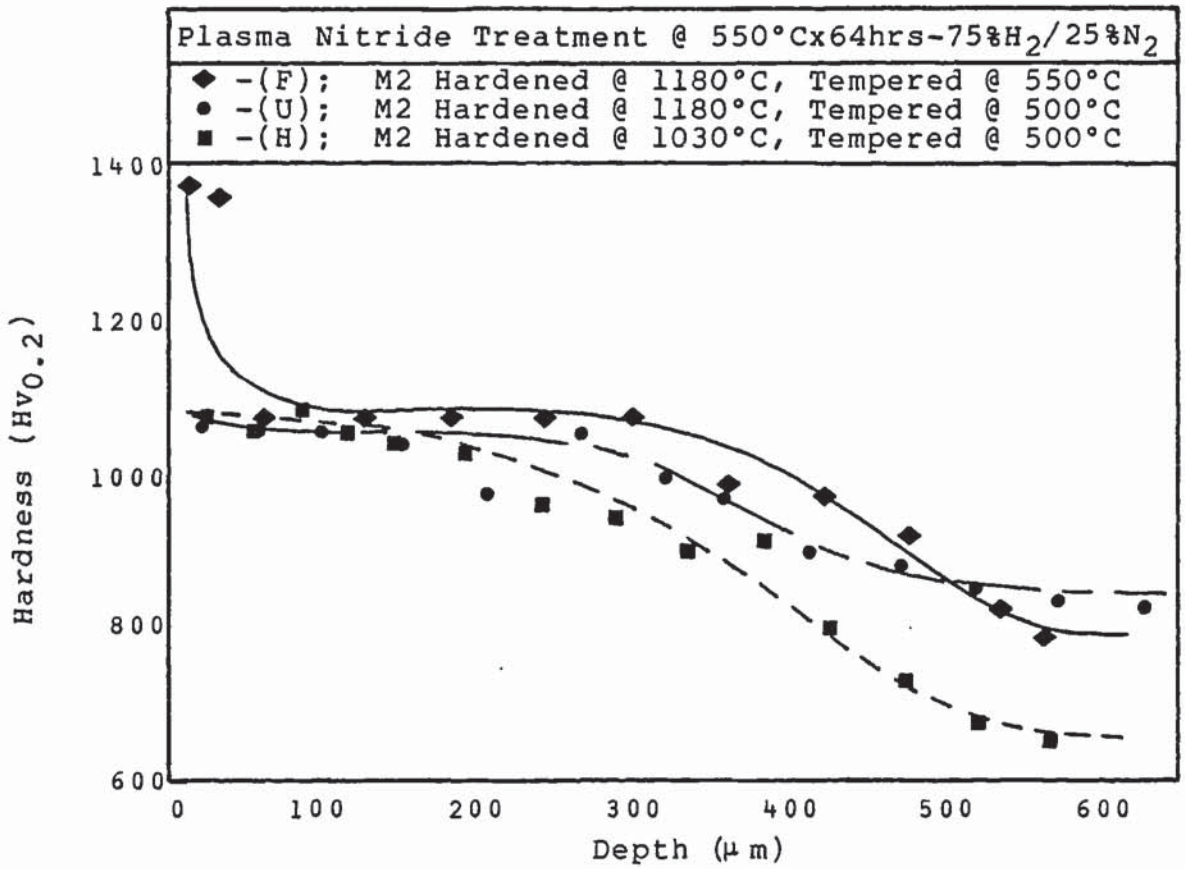

Fig.4.1 (j) Case Hardness Profiles for Plasma Nitrided M2.

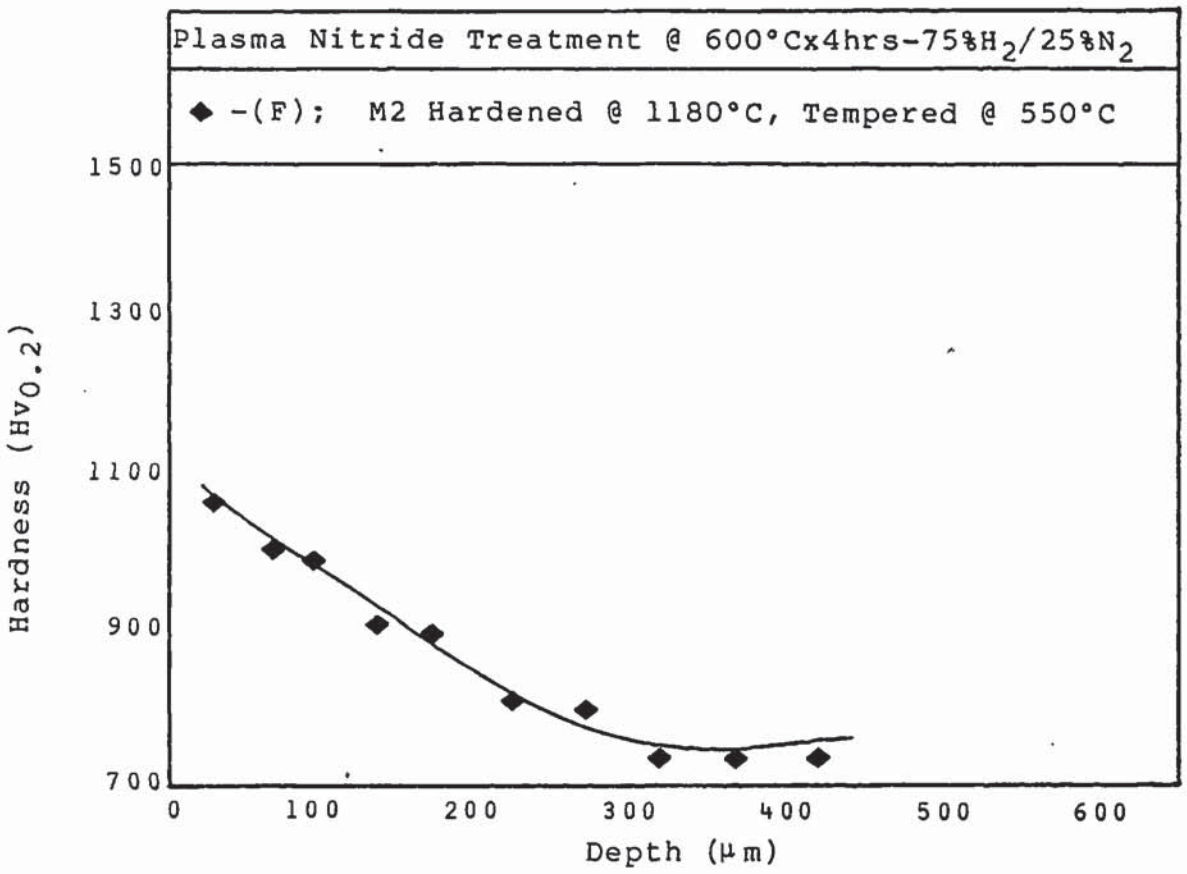

Fig. 4.1 (k) Case Hardness Profile for Plasma Nitrided M2.

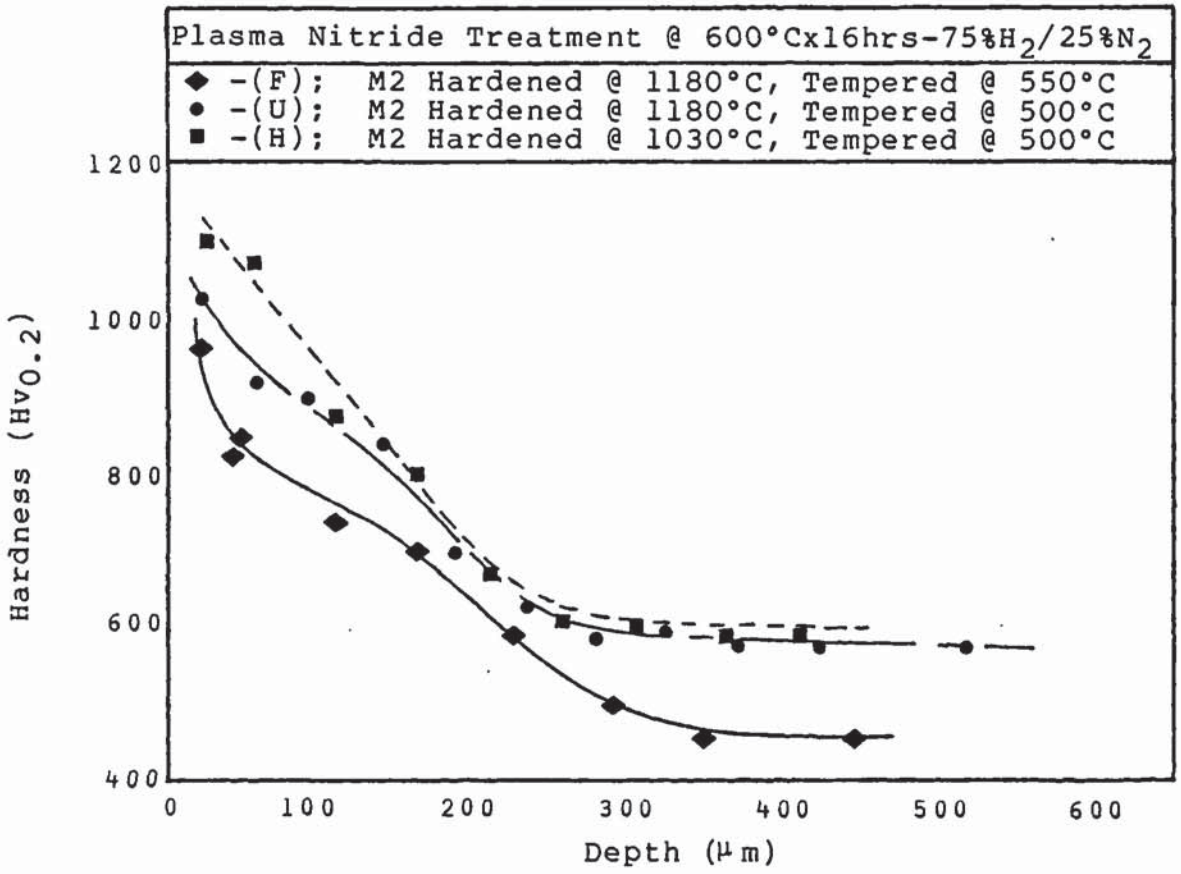

Fig. 4.1 (l) Case Hardness Profiles for Plasma Nitrided M2.

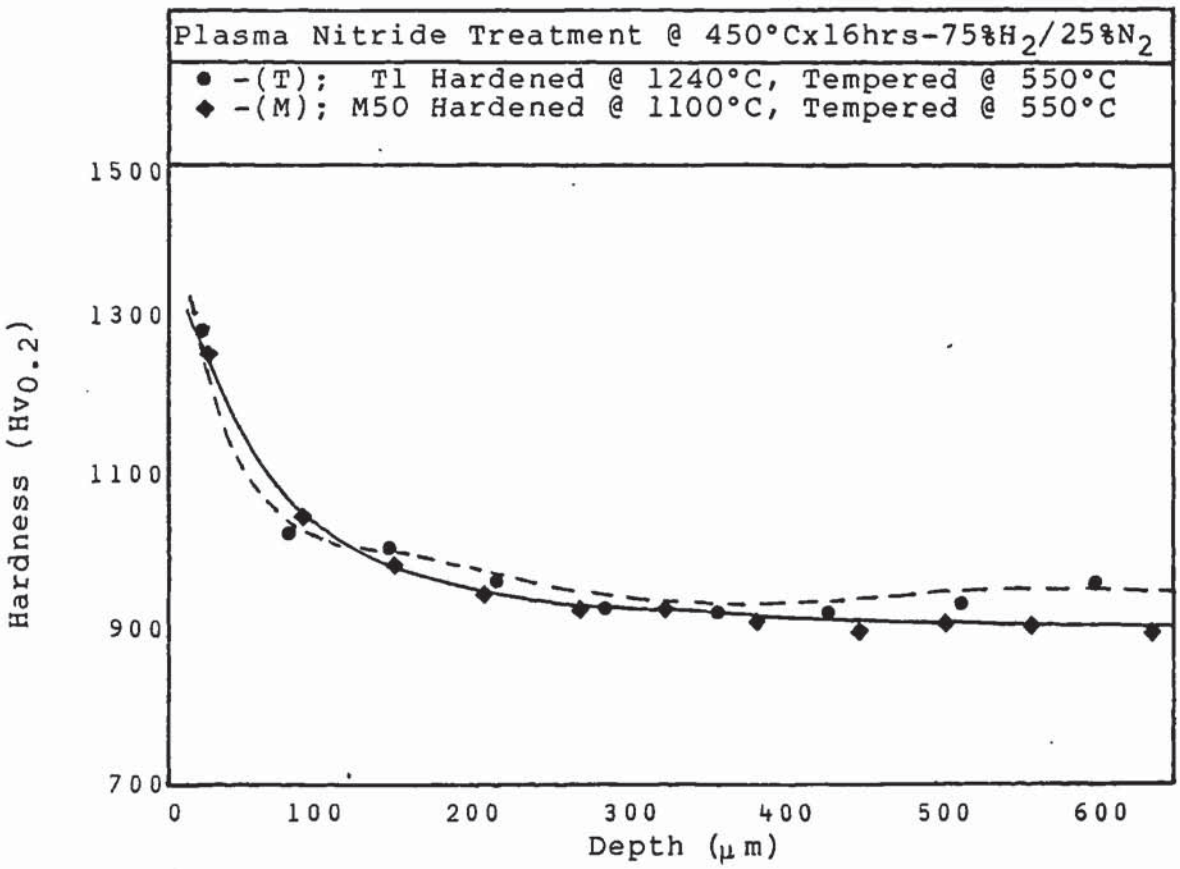

Fig.4.1 (m) Case Hardness Profile for Plasma Nitrided T1/M50

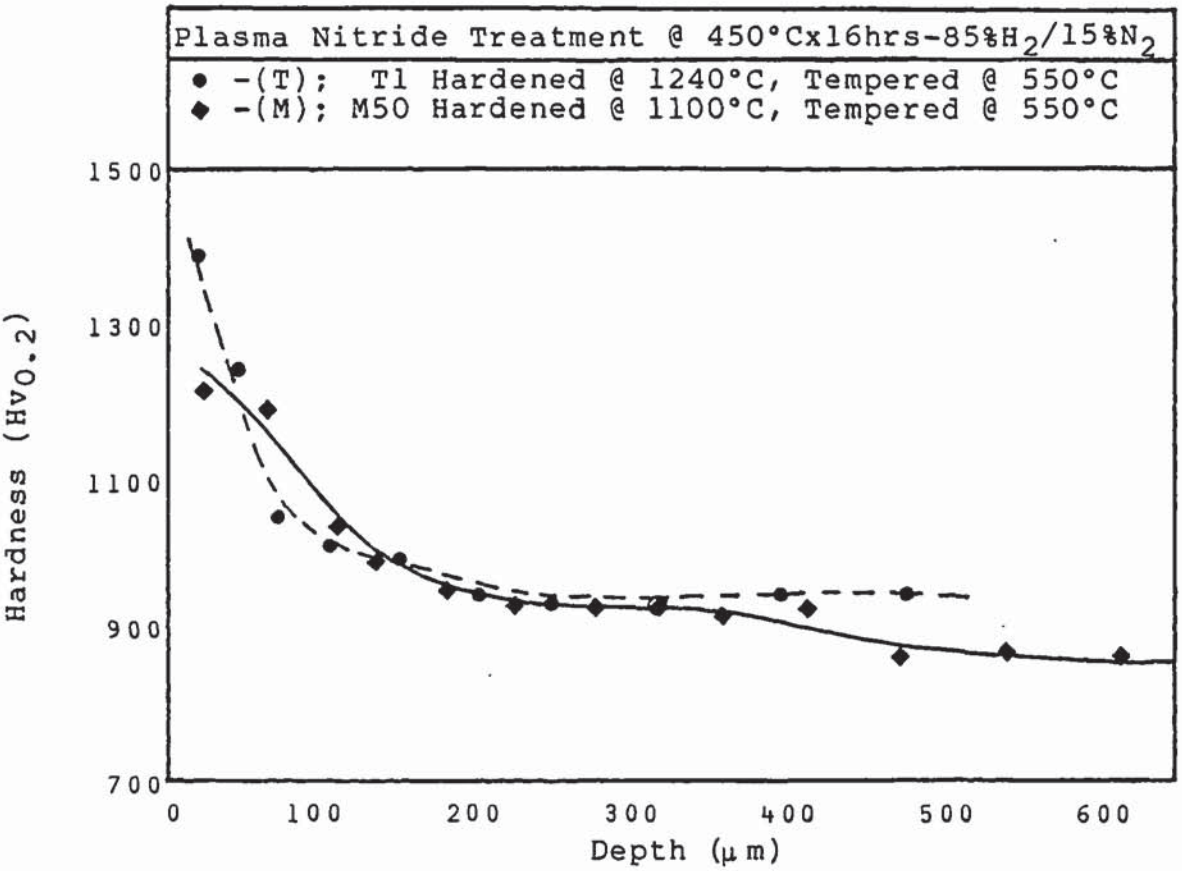

Fig.4.1 (n) Case Hardness Profile for Plasma Nitrided T1/M50

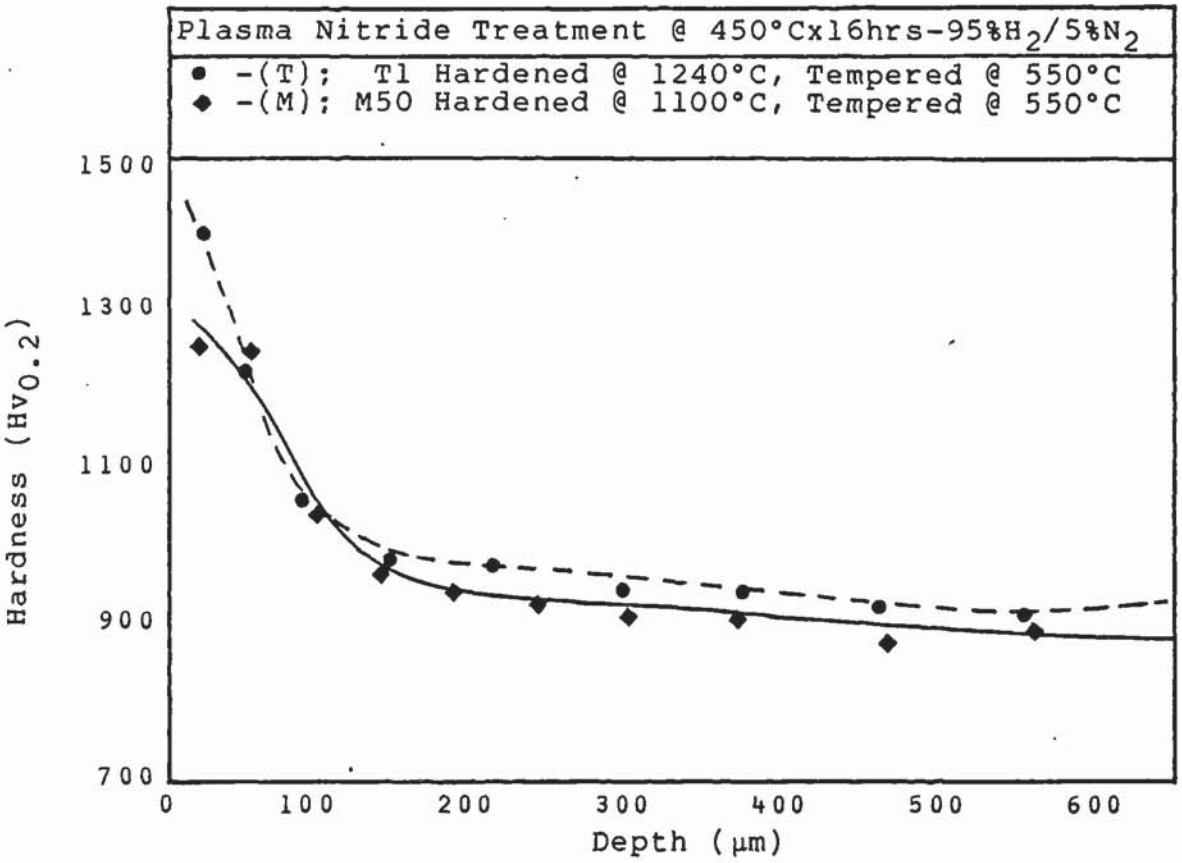

Fig.4.1 (o) Case Hardness Profile for Plasma Nitrided T1/M50

Overall, a prior treatment of fully hardening and tempering of M2 produces better case hardening profiles after plasma nitriding. Underhardening and undertempering treatments show a tendency to develop hardness 'troughs' in the case at or near to the case/core interface.

Low temperature treatments develop steep hardness profiles while higher temperatures and longer times reduce the severity of the gradient produced. Long treatment times also favour lower surface hardnesses and the development of a pronounced hardness 'plateau' below the sample surface.

M50 and T1 steels show similar hardness profiles to one another independent of the treatment atmosphere. T1 displays a slight tendency towards the formation of hardness troughs near the case/core interface while M50 shows evidence of forming small hardness plateaux ('though less pronouced than those developed in M2 steel). It is apparent that any case depth differences for M50 and T1 steels subjected to similar plasma treatments will be due primarily to the difference in core hardnesses.

4.2.1. Surface/Core Hardness and Case Depth Trends

Figures 4.2(a) - (f) show the general trends in hardness and case depth variation measured against plasma nitriding temperature and time for the M2 steel. These summary graphs are derived from the data presented in Table 4.2.

Figures 4.2(g) and (h) show the trends of hardness and case depth development against the nitrogen content in the treatment atmosphere for the steels M50 and T1.

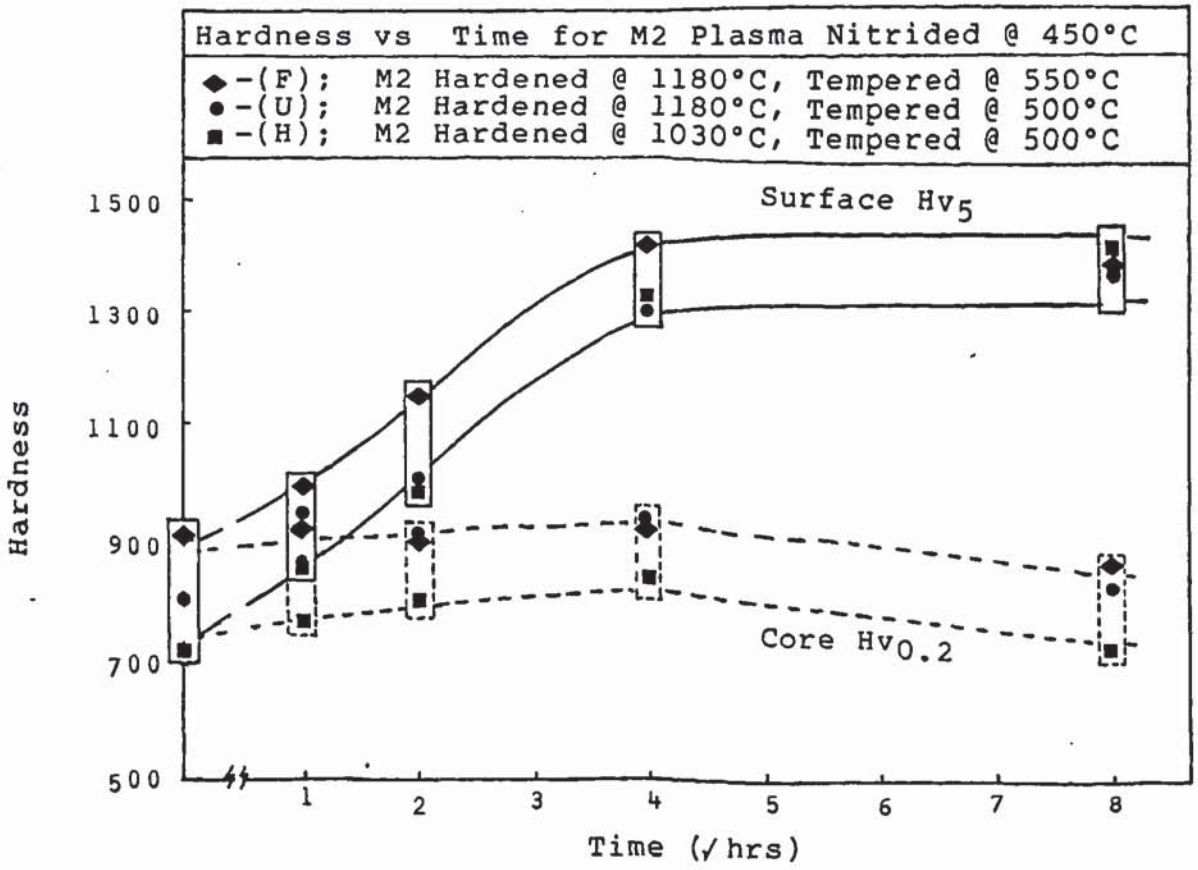

Fig.4.2 (a) Effect of Time at 450°C on the Hardness of M2

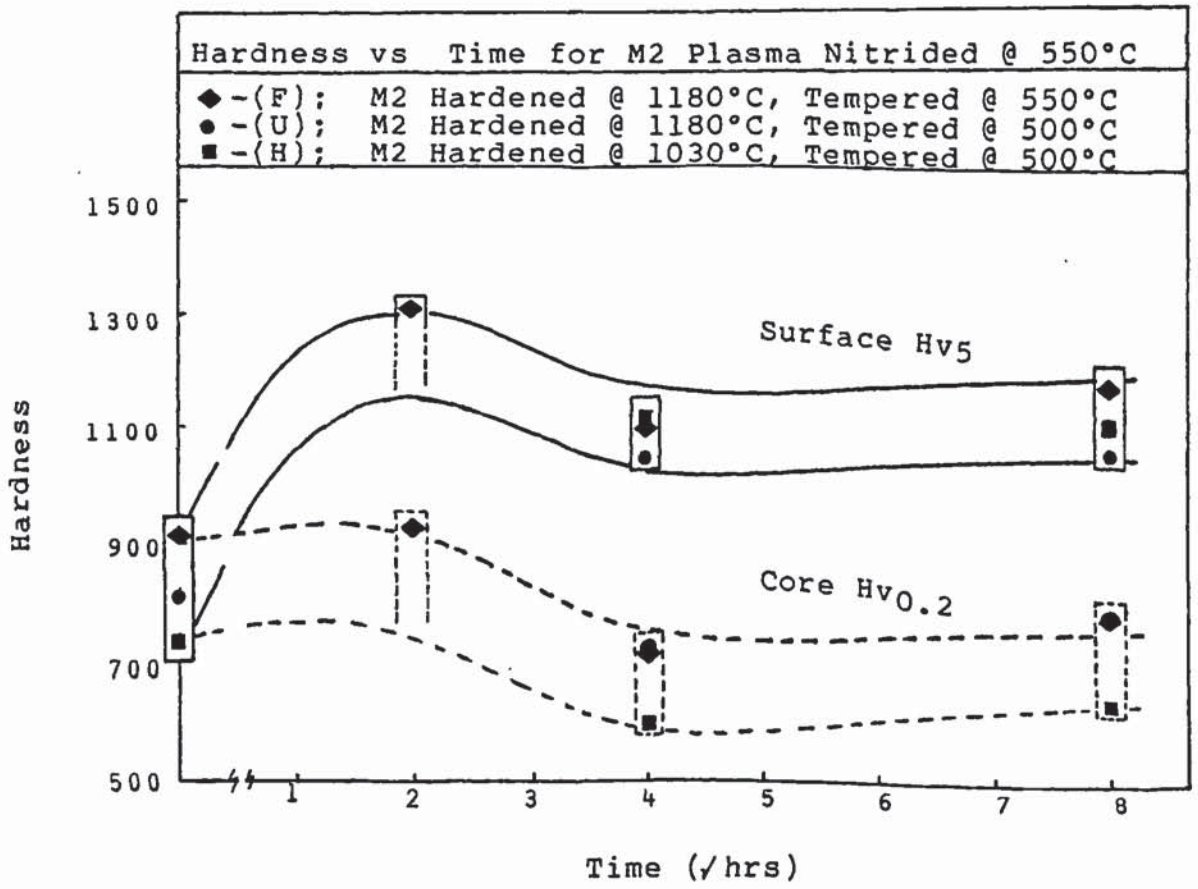

Fig.4.2 (b) Effect of Time at 550°C on the Hardness of M2.

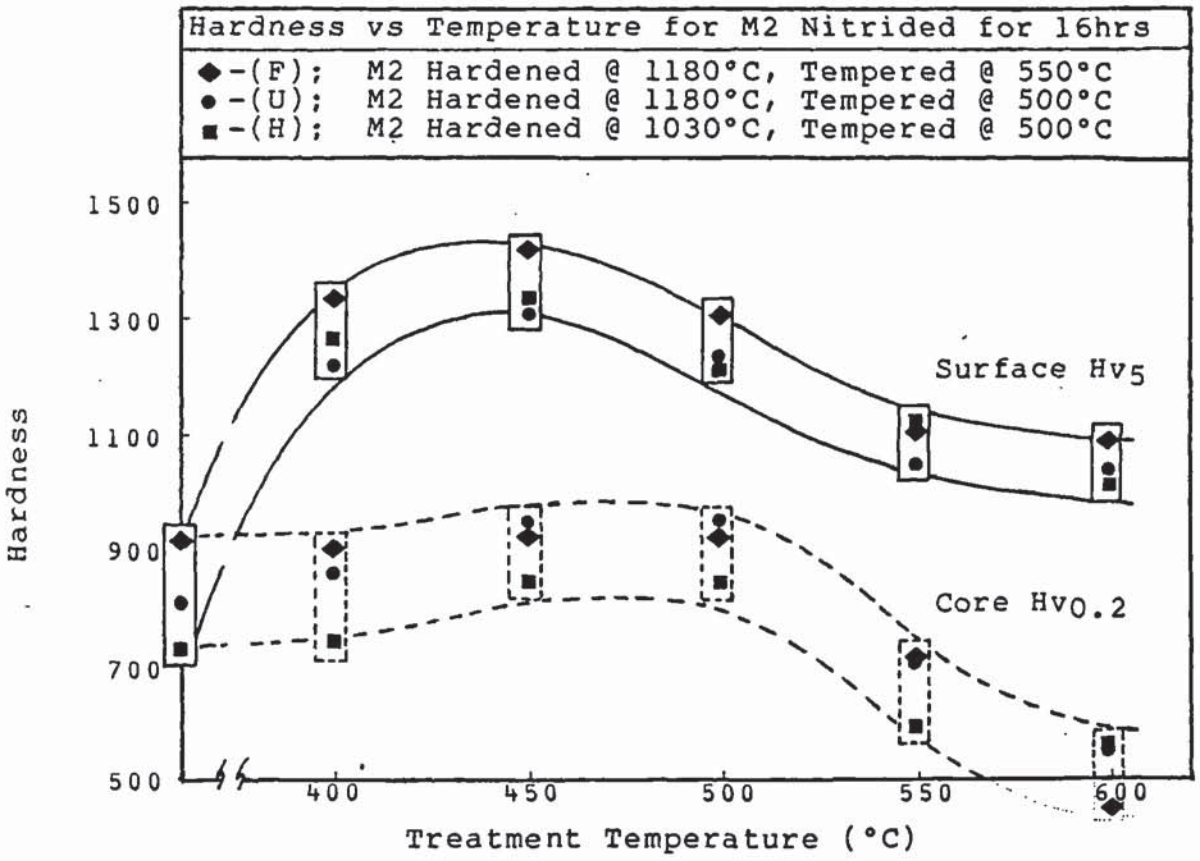

Fig.4.2 (c) The effect of 16hrs @ Temperature on M2 Hardness

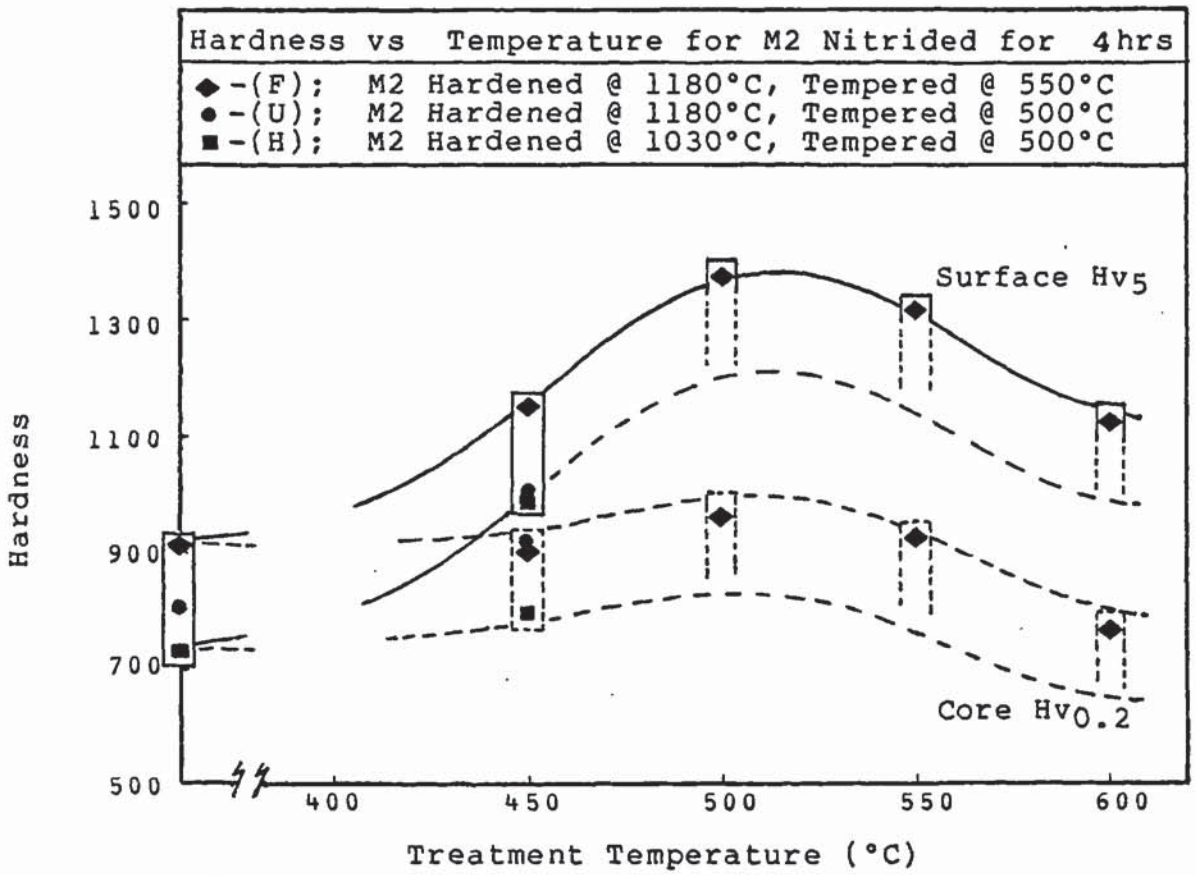

Fig.4.2 (d) The effect of 4hrs @ Temperature on M2 Hardness

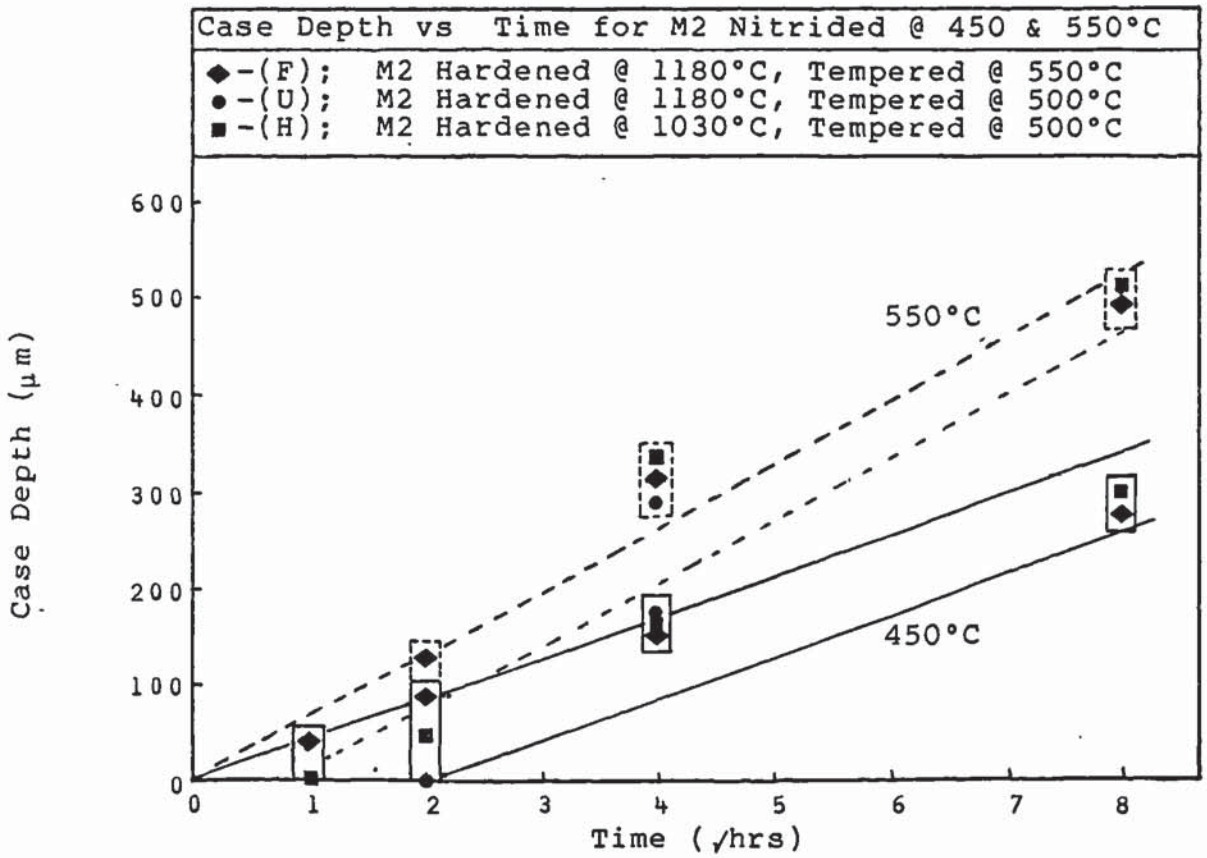

Fig.4.2 (e) The Effect of Time on the Case Development of M2

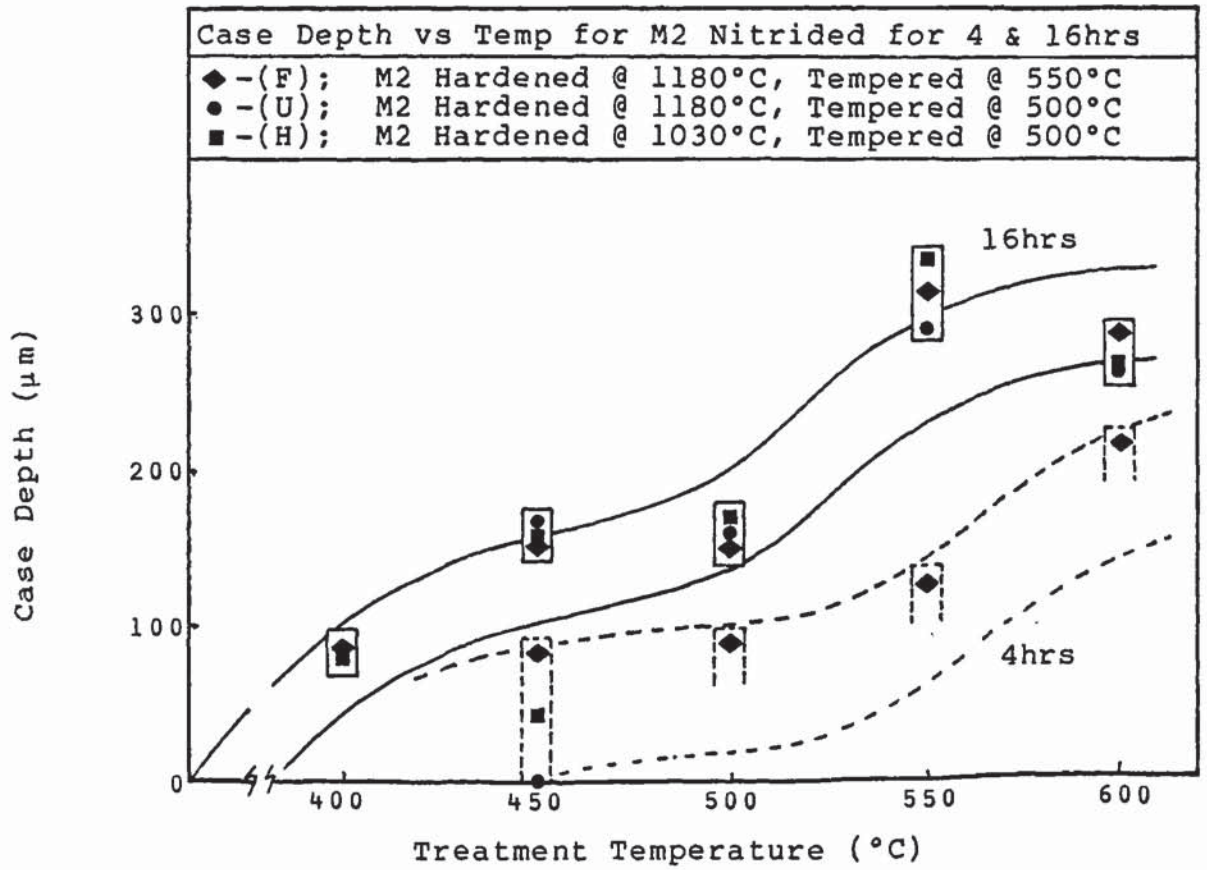

Fig.4.2 (f) The Effect of Temperature on M2 Case Development

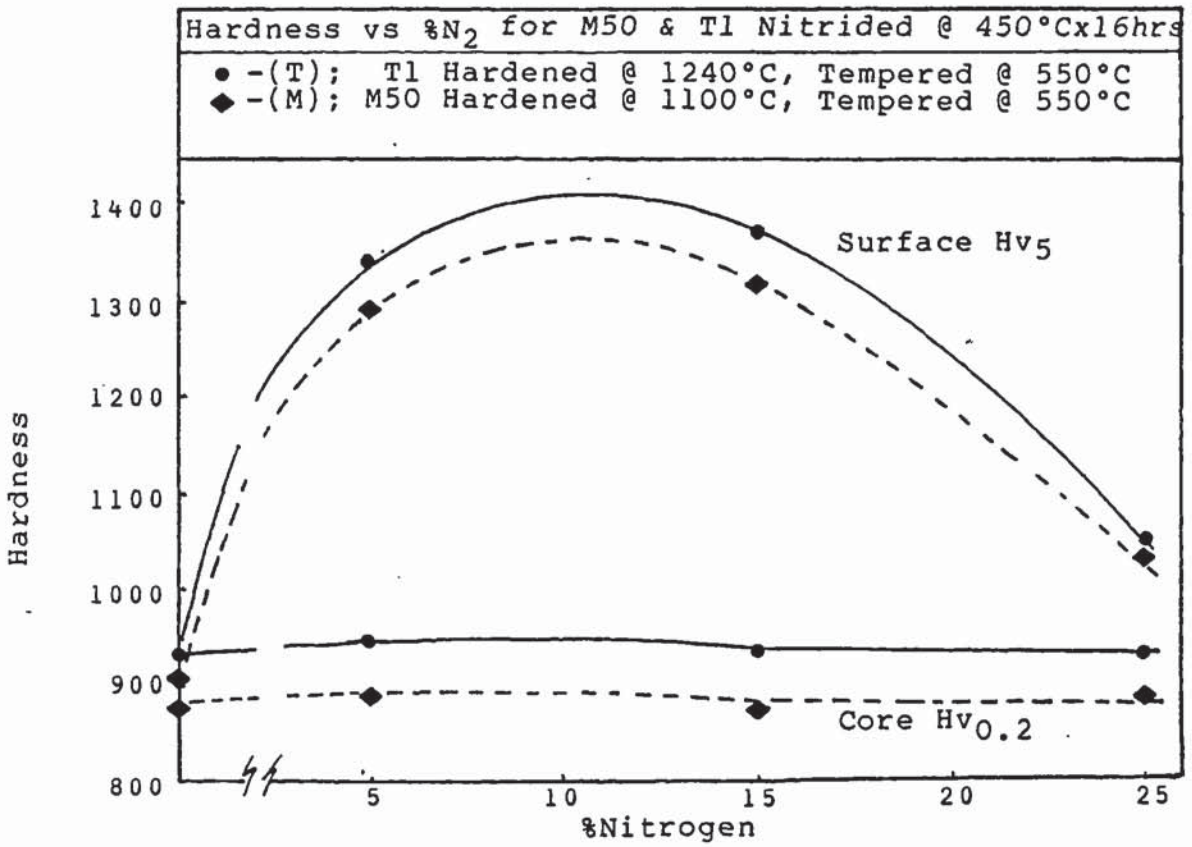

Fig.4.2 (g) The Effect of Atmosphere N_2 Content on Hardness - of Plasma Nitrided M50 & T1

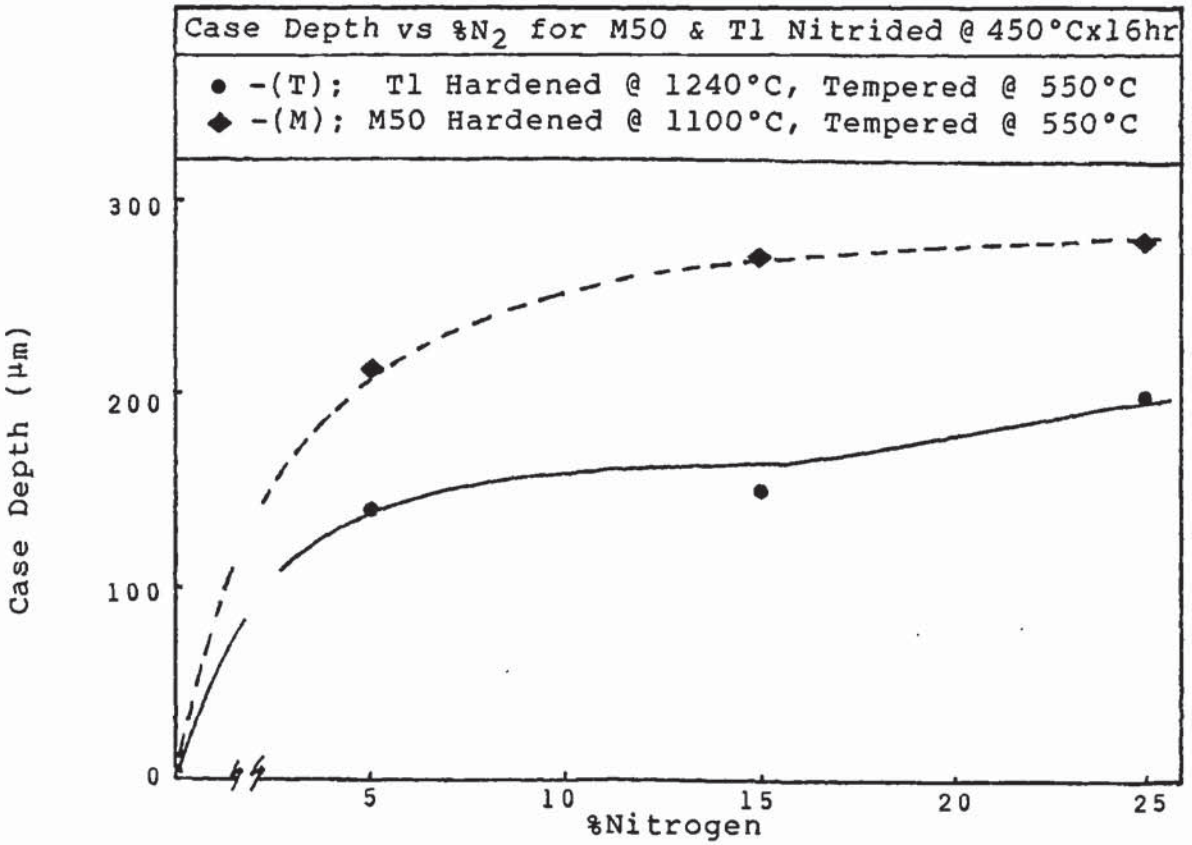

Fig.4.2 (h) Effect of Atmosphere N_2 Content on Case Depth - of Plasma Nitrided M50 & T1

Figures 4.2(a) - (d) relevant to M2 steel, show maximum surface hardening to be developed by plasma nitriding at 450°C for periods of at least 16 hours duration. Core hardness is not unduly affected by these treatments.

Treatments at 550°C or higher effect lower surface hardnesses together with considerable core softening. High surface hardness with no detriment to the core strength can be achieved by short duration treatments of approximately 4 hours at 500°C. Higher temperatures and/or longer times effect a decline in both case and core hardnesses.

Figure 4.2(e) shows the relationship of case development to the square root of the treatment time for 450°C and 550°C. Linear regression analysis of the data presented for 450°C treatments yields an equation of the form:

$$CD = -21 + 38.6\sqrt{t} \qquad \ldots\ldots(4.1)$$

where time (t) is in hours and case depth (CD) is in μm. The correlation coefficient (r) is 0.968 indicating a good degree of linearity in the data presented.

Analysis of the 550°C data again yields a relationship predicting linearity, this time with r = 0.975. However, observation of the graphical presentation of the data implies that the 16hr treatment has produced unduly high values of case depth. This is supported by Figure 4.2(f), and examination of the core hardness values presented in Table 4.2 imply that measured case depths may be high due to lower than expected core hardness values for this treatment. Lower than expected case and core hardnesses are also highlighted by Figure 4.2(b).

Figures 4.2(g) and (h) show the trends of hardness and case development for the M50 and T1 steels plasma nitrided in progressively lower nitrogen potential atmospheres. Both materials follow the same hardening trend. Optimum hardening appears to be obtained in an atmosphere of about $10\%N_2/90\%H_2$. Neither material's core hardness is affected detrimentally by treating in high or low nitrogen potential atmospheres at 450°C for 16hrs.

Optimum case development for M50 would appear to occur in atmospheres containing more than $15\%N_2$. T1 develops a smaller case depth at all N_2 potentials but has higher surface hardness values.

The relationships of hardness and case depth development to atmosphere nitrogen potential are not simple ones even though case development bears some resemblance to a logarithmic type law.

4.3. Metallography

4.3.1. Optical Examination

Figures 4.3(a) - (j) show optical micrographs to illustrate the core and case structures of the specimens after heat treatment.

The samples are all shown in the etched condition, having been given the same etching treatment as described in Section 3.3.2. ie. immersion and swabbing for approximately 2 minutes in 4% nital.

Examination of longitudinal sections of the materials after hardening and tempering showed the M2 steel to have a small degree of carbide banding - carbides being generally small and rounded, with a small proportion of larger primary carbides interspersed throughout the structure. M50 & T1 were shown to have less banding present, carbides again being small and rounded with larger primary carbides being well distributed throughout the structure.

In view of the relatively low preponderance of carbide banding found in the steels used for this work, it was deemed acceptable to dispense with the necessity for examination of longitudinal sections for each treatment. Therefore all microstructures presented are of transverse sections.

400F16

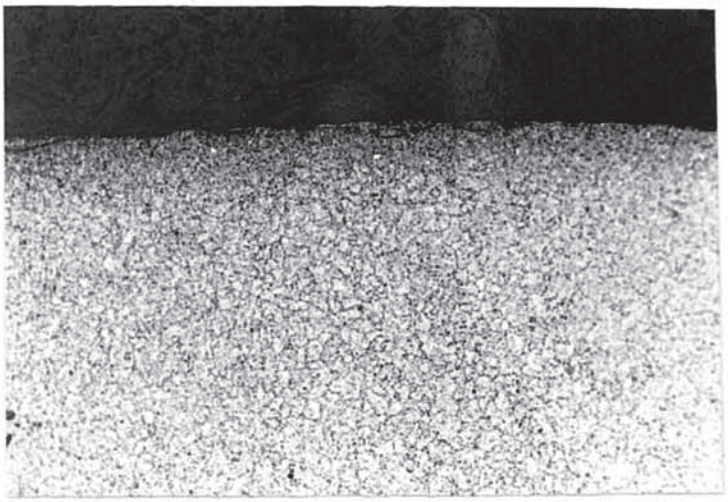

400U16

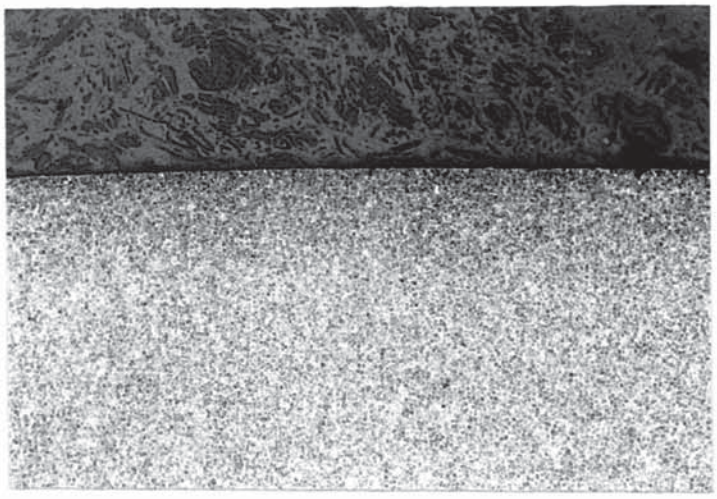

400H16

Fig.4.3 (a) 400°C x 16hrs - M2 Case Structures - Mag'n X168

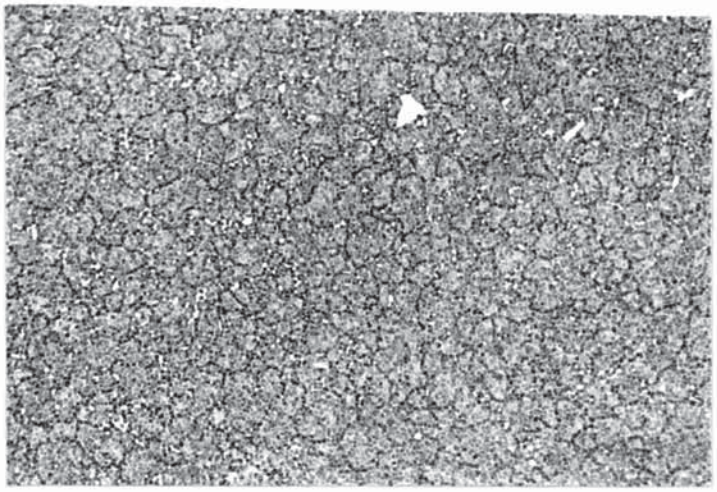

450F16

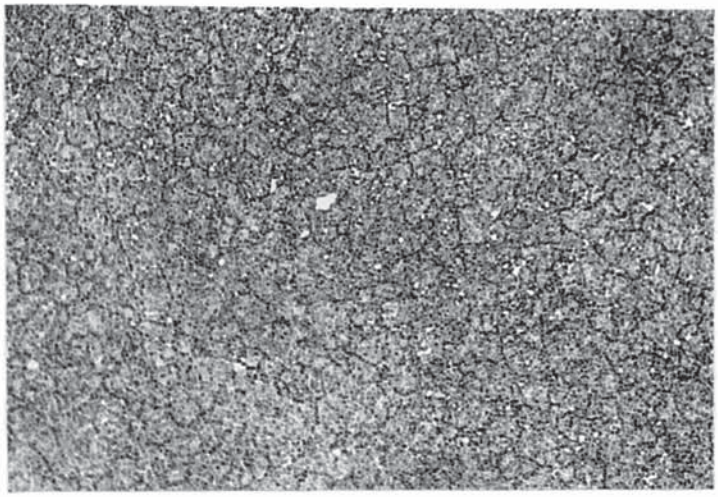

450U16

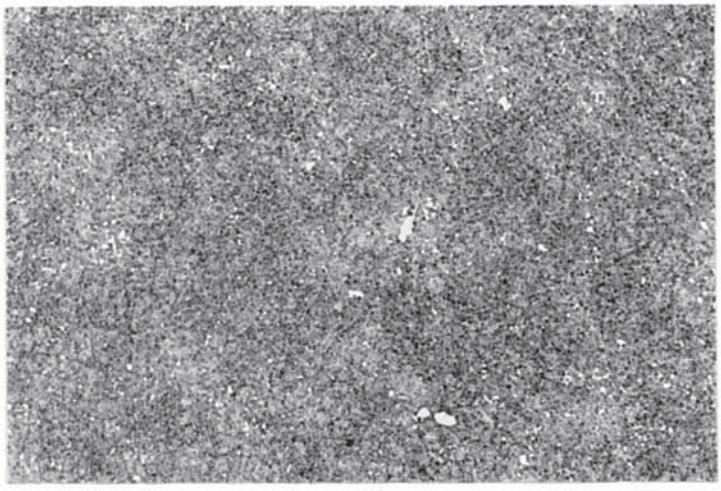

450H16

Fig.4.3 (b) 450°C x 16hrs - M2 Core Structures - Mag'n X420

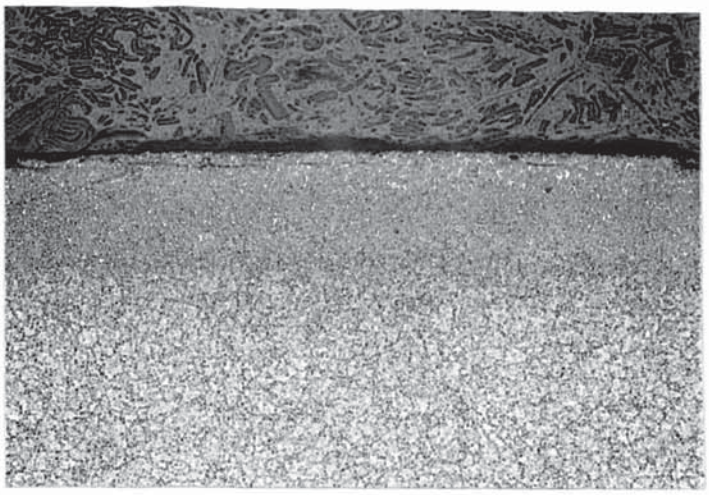

450F16

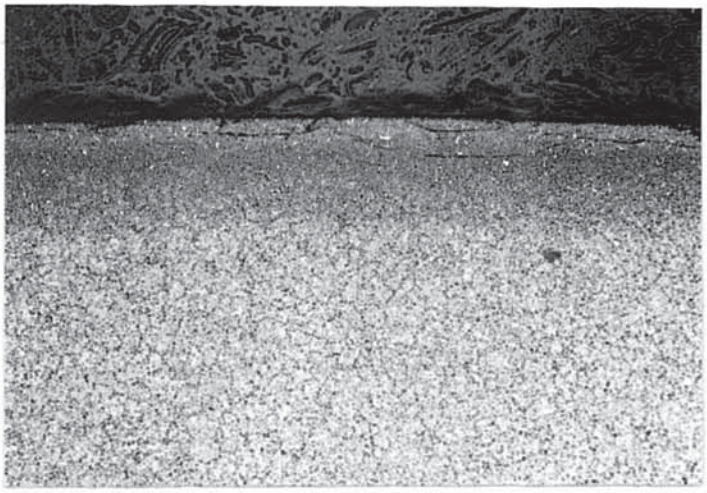

450U16

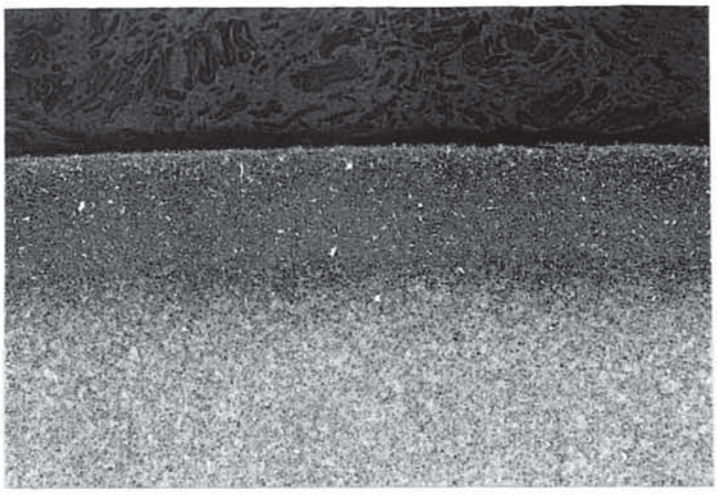

450H16

Fig.4.3 (c) 450°C x 16hrs - M2 Case Structures - Mag'n X168

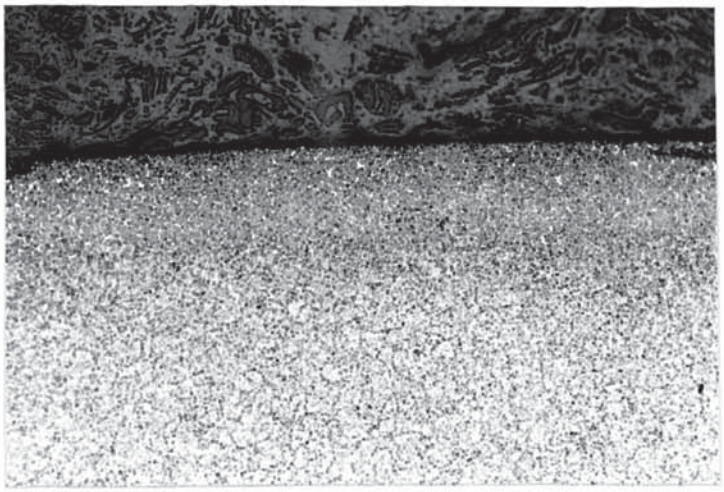

500F16

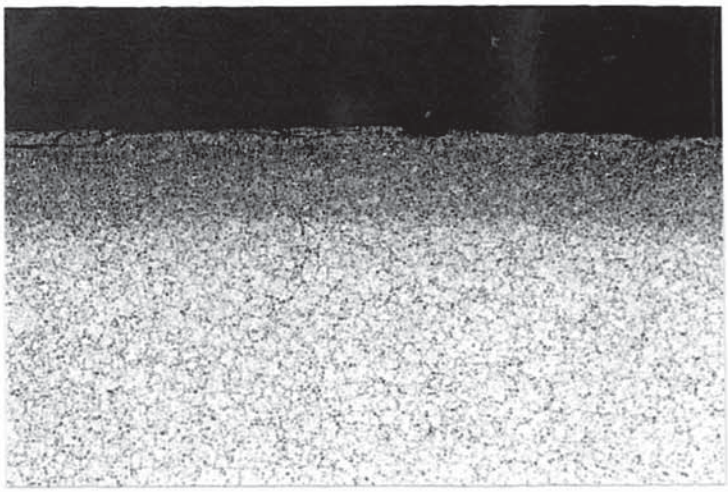

500U16

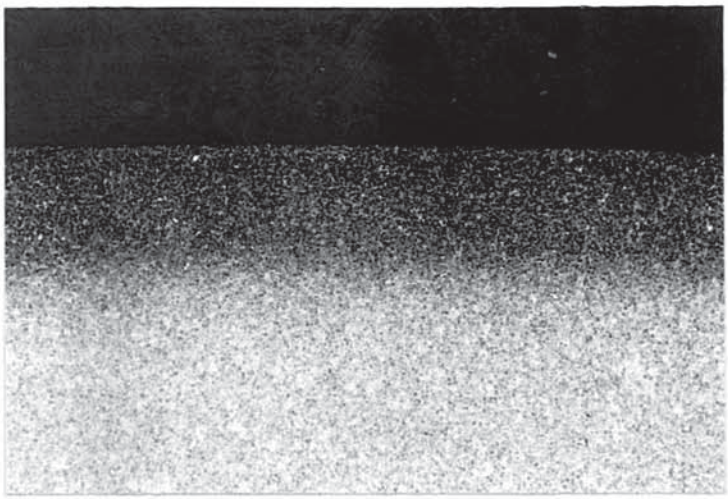

500H16

Fig.4.3 (d) 500°C x 16hrs - M2 Case Structures - Mag'n X168

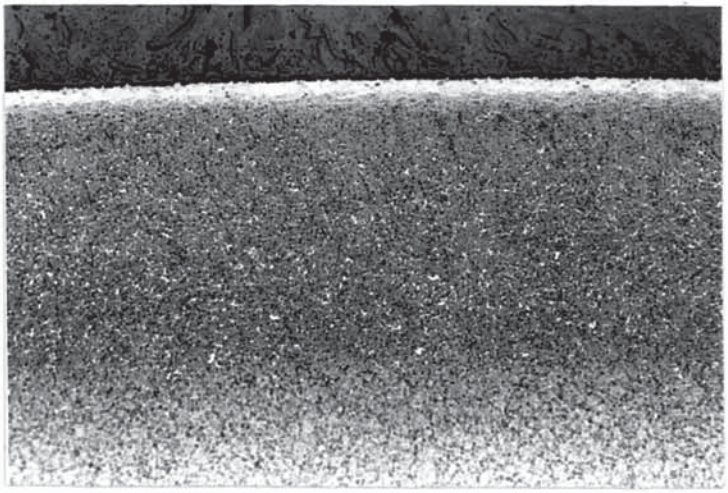

550F16

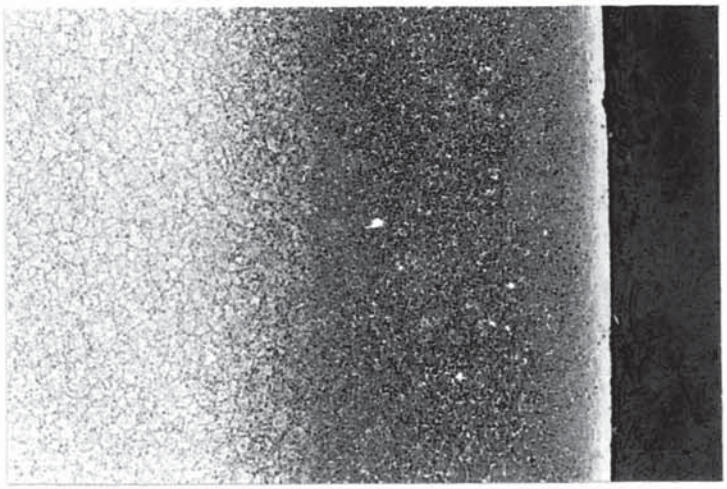

550U16

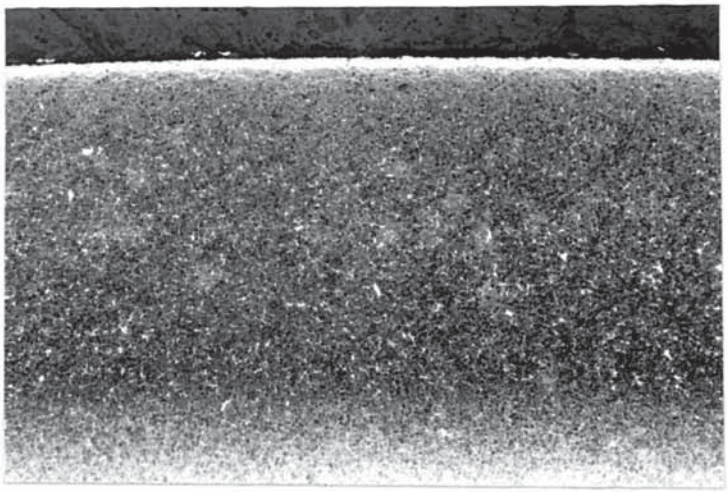

550H16

Fig.4.3 (e) 550°C x 16hrs - M2 Case Structures - Mag'n X168

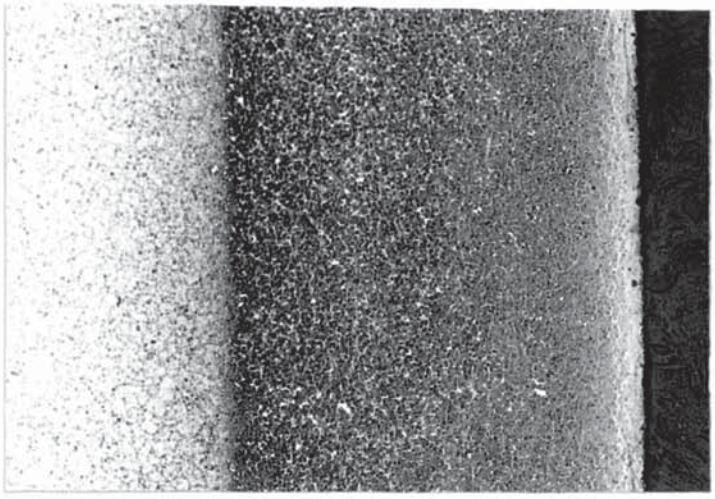

550F64

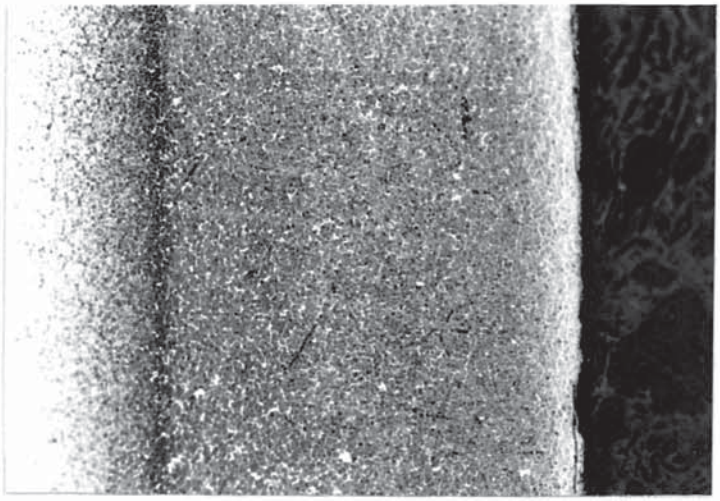

550U64

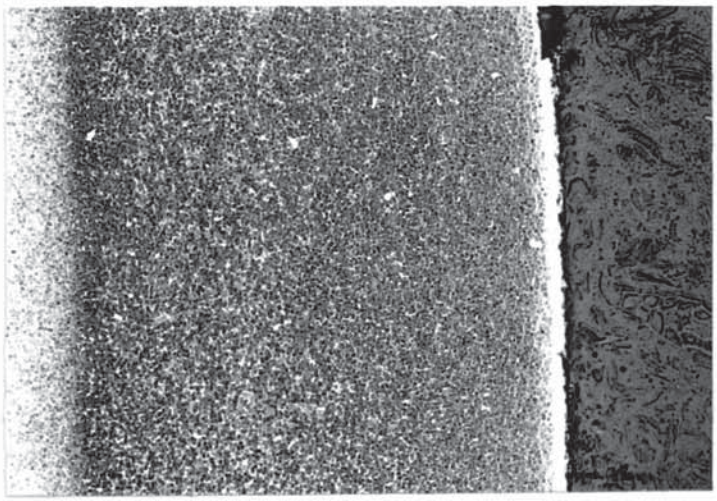

550H64

Fig.4.3 (f) 550°C x 64hrs - M2 Case Structures - Mag'n X168

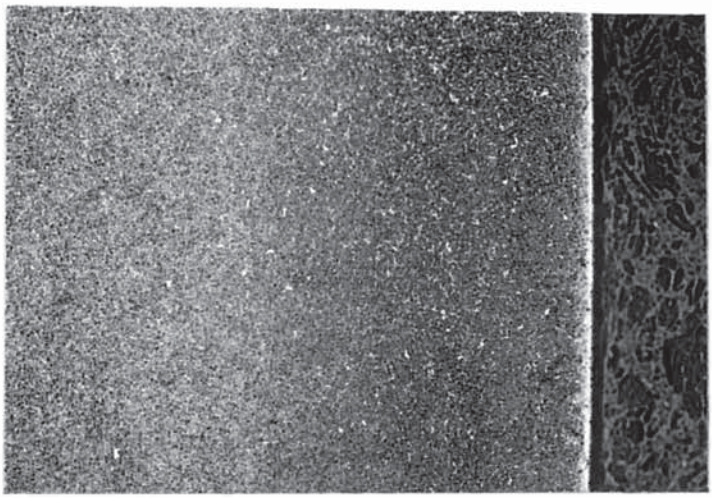

600F16

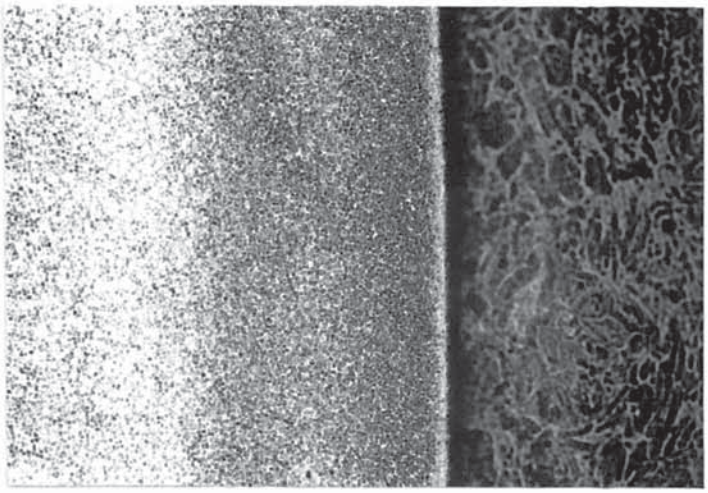

600U16

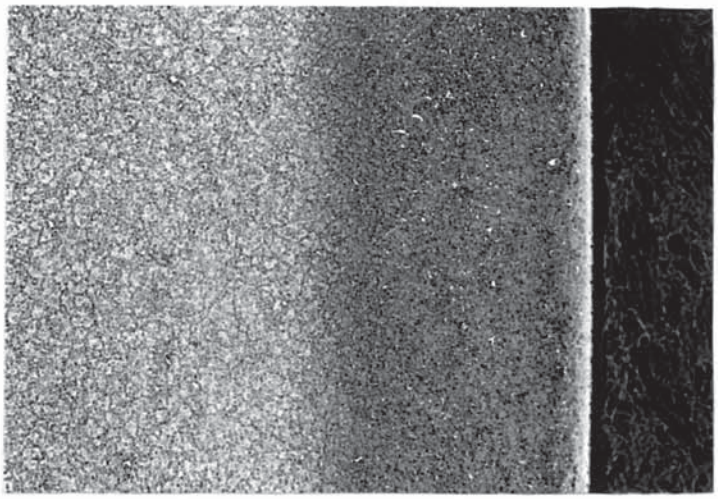

600H16

Fig.4.3 (g) 600°C x 16hrs - M2 Case Structures - Mag'n X168

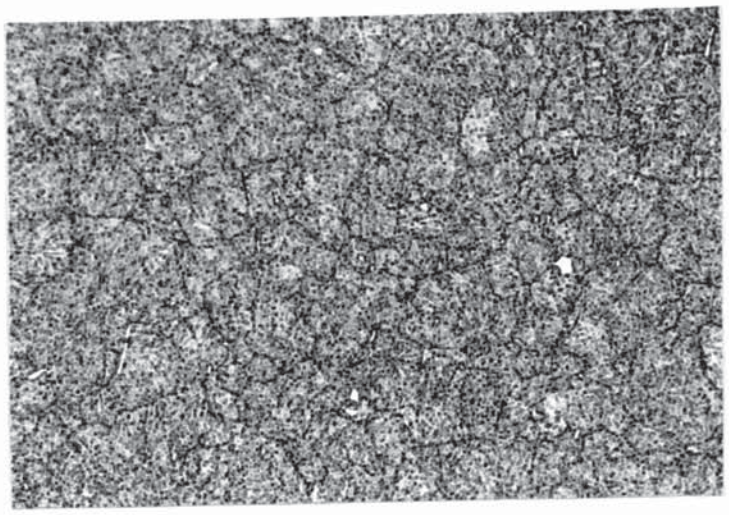

OMO

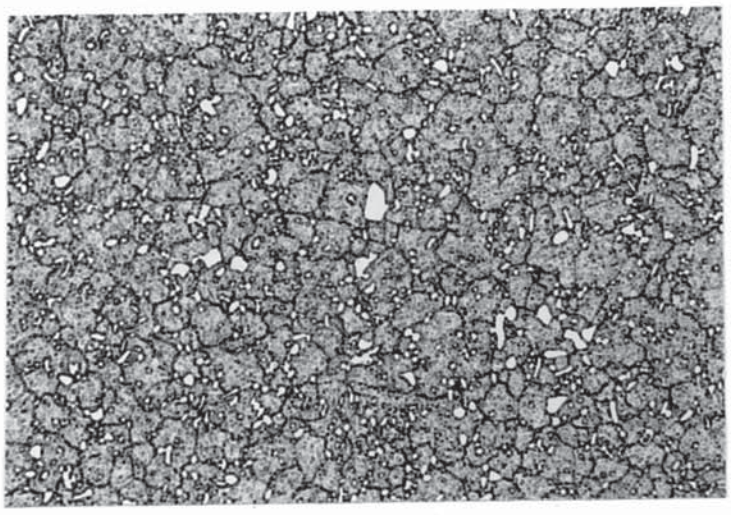

OTO

Fig.4.3 (h) Hardened & Tempered Core Structures - Mag'n X420

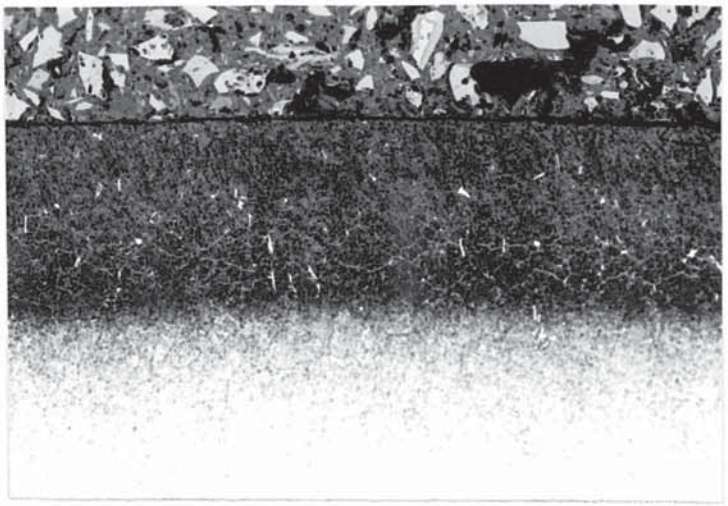

450M16(25)

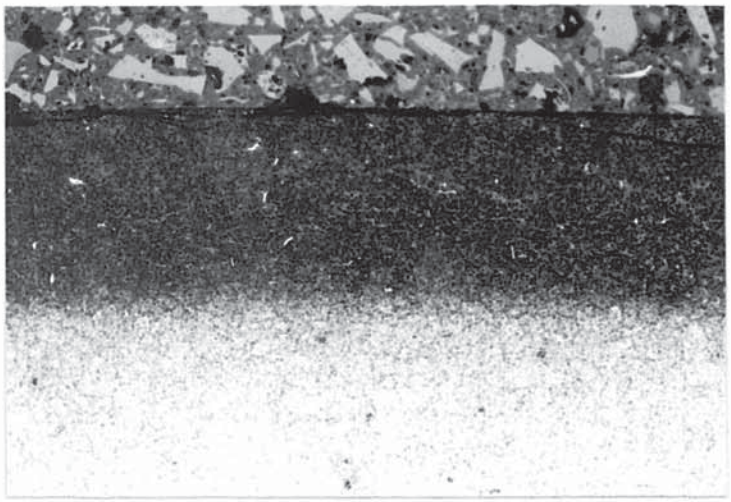

450M16(15)

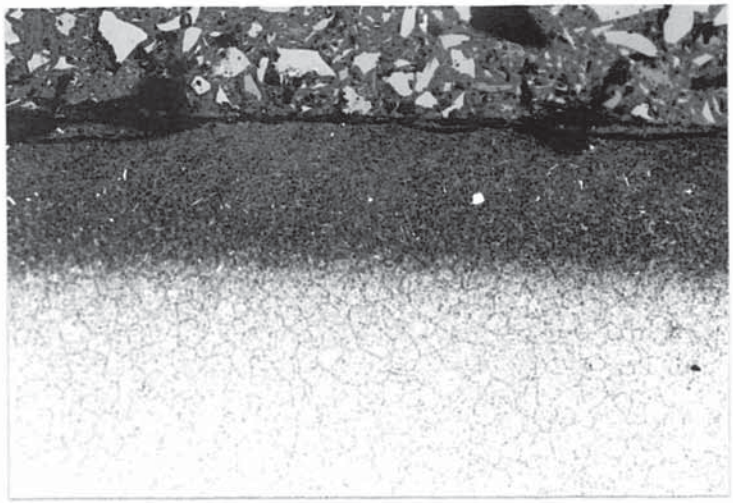

450M16(5)

Fig.4.3 (i) 450°C x 16hrs - M50 Case Structures - Mag'n X168

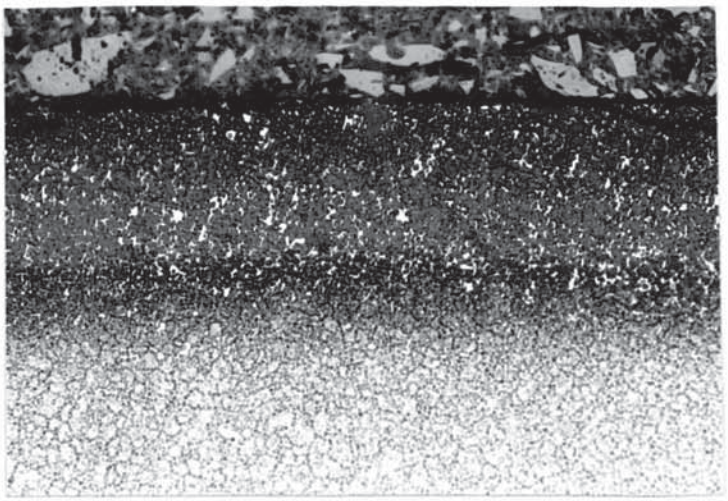

450T16(25)

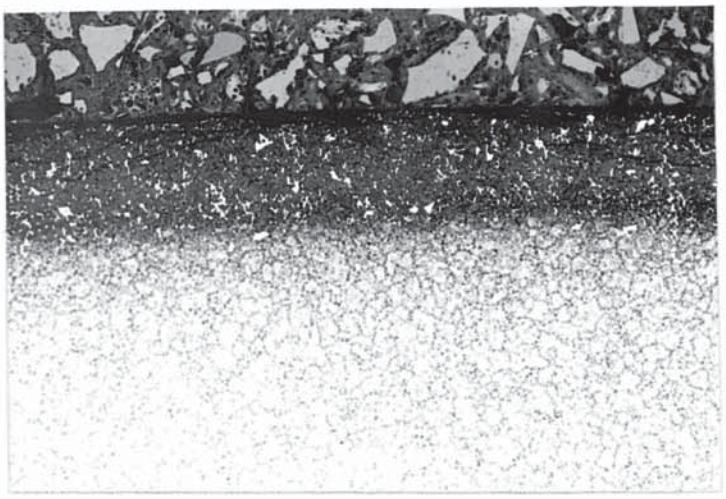

450T16(15)

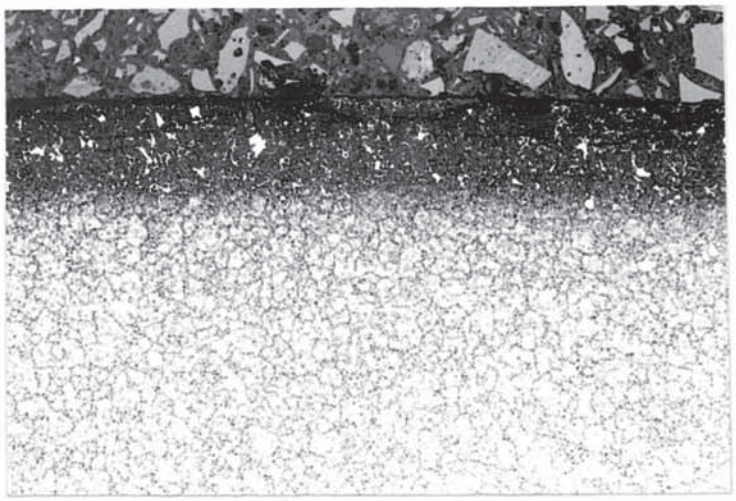

450T16(5)

Fig.4.3 (j) 450°C x 16hrs - T1 Case Structures - Mag'n X168

Figures 4.3(a) - (g) show the case and core structures of M2 after plasma nitriding at the various temperatures and times described.

The core structures were relatively similar for all plasma treatments studied. Figure 4.3(b) shows the underhardened structure to be arguably finer in nature than either the fully hardened or undertempered treatments, with the secondary hardening carbides being very fine and well distributed in nature.

The low temperature and short duration treatments show virtually no evidence of a case in the etched condition - higher temperature and longer time treatments showing progressively more well defined case structures. Evidence of preparation damage to the surface of the specimens is apparent in most cases, being particularly pronounced in the undertempered structures (at higher temperature and/or longer time treatments).

Figures 4.3(e) - (g) show clear evidence of white layer formation on the sample surface - the 550°C treatments (Figures 4.3(e) & (f)) seemingly particularly prone to layer formation. These treatments also display evidence of intergranular penetration of the surface compound layer and a dark inner band at the case-core interface.

In all cases the etch case depth is less than that determined by microhardness profile.

Figures 4.3(h) - (j) illustrate the case and core structures of the heat treated M50 and T1 steels.

Figure 4.3(h) shows the main differences in the structures of M50 and T1; M50 essentially having a fine tempered martensite matrix with only a small amount of primary and secondary alloy carbide dispersed within it. In contrast the T1 has a more well defined grain structure and very much more primary and secondary carbide distributed throughout the structure.

The M50 micrographs show no evidence of white layer formation but do display very definite case structures. This trend is repeated in the T1 specimens. Surface damage due to micro-specimen preparation is again apparent in all of the plasma nitrided samples with the exception of 450M16(25).

As with the M2 specimens, the etch case depths tended to be less than that determined by hardness profile.

4.3.2. Electron Microscopy

Figures 4.4(a) - (e) illustrate some of the case and core structures of the M2 steel at the higher magnifications available with scanning electron microscopy. Figure 4.4(f) shows the case of T1 after plasma nitriding in a low nitrogen potential atmosphere.

Semi-quantitative analysis, carried out on some of the specimens, indicated the approximate distribution of the alloying elements in the phases seen. Examples of the kind of data acquired are shown in Table 4.3. Since semi-quantitative analysis was used no data was gained on the carbon distribution in the constituent phases. Therefore it was only possible to infer the approximate composition of carbides examined. This has been done by

observation of the ratio of alloying elements present and comparison with the published information on the morphology of the various carbides present in tool and carbon steels.

Treatment	Steel	Analysis (wt%)					Phase
		W	Mo	V	Cr	Fe	
400F16	M2	4.21	1.79	0.76	4.28	88.55	matrix
500F16	M2	4.19	2.85	1.73	4.99	86.28	matrix
550F16	M2	4.36	1.87	1.35	4.84	87.58	matrix
450M16(25)	M50	-	3.03	0.98	4.99	91.00	matrix
450M16(25) (fatigue sample)	M50	-	3.99	2.27	5.92	87.82	matrix
450T16(5)	T1	12.67	-	1.03	5.01	81.29	matrix
450T16(15)	T1	11.26	-	1.07	5.28	82.40	matrix
450M16(25)	M50	-	68.89	12.64	10.56	7.91	M_6C
OTO (hardened & tempered)	T1	62.14	-	2.33	3.73	31.80	M_6C
450T16(5) (fatigue sample)	T1	61.79	-	2.11	3.66	32.43	M_6C

Table 4.3. Semi-Quantitative Analysis of Microstructural - Phases in M2, M50 & T1

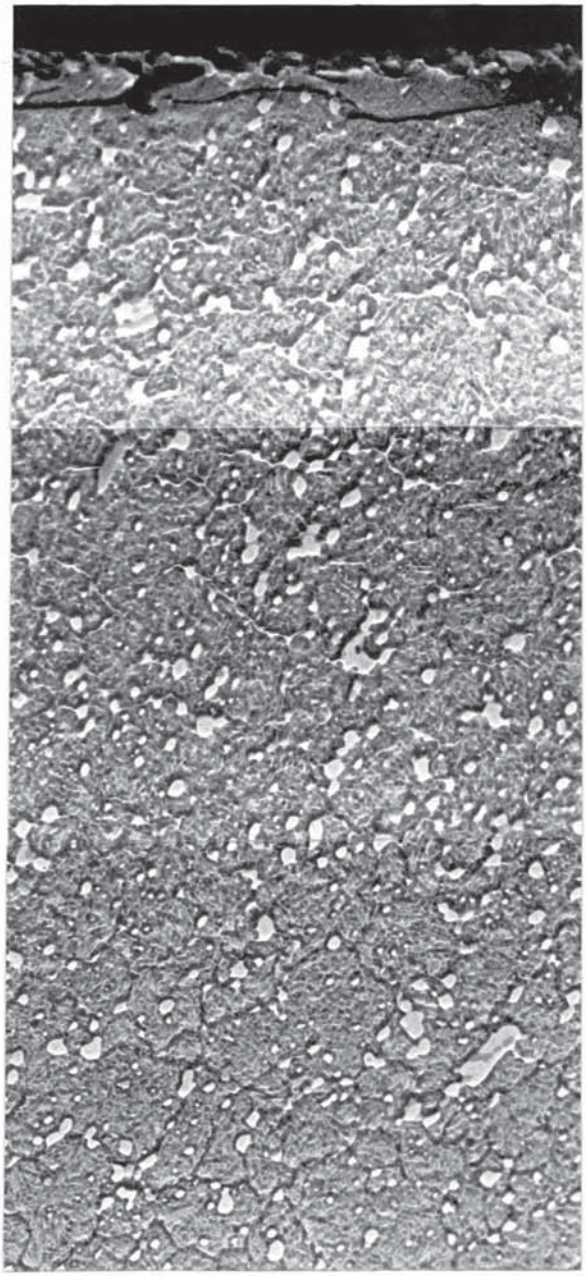

450F16

Mag'n x1500

10μm

Fig.4.4 (a) 450°Cx16hrs - M2 Case Structure

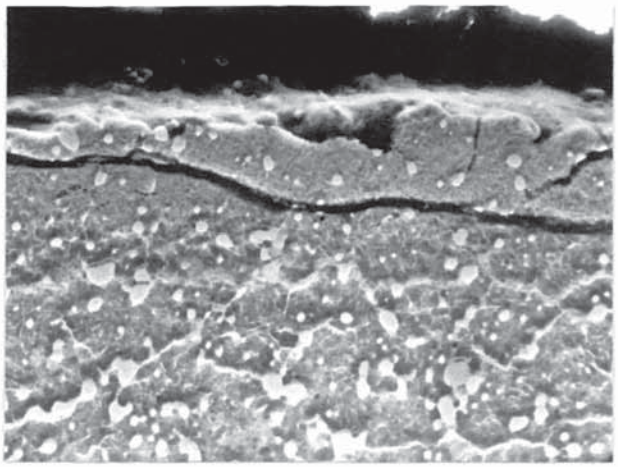

450F64

Case

Mag'n x1500

10μm

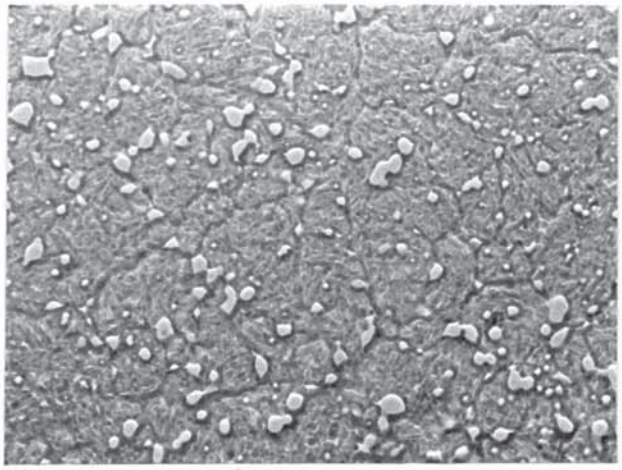

450F64

Core

Fig.4.4 (b) 450°Cx64hrs - M2 Case/Core Structure

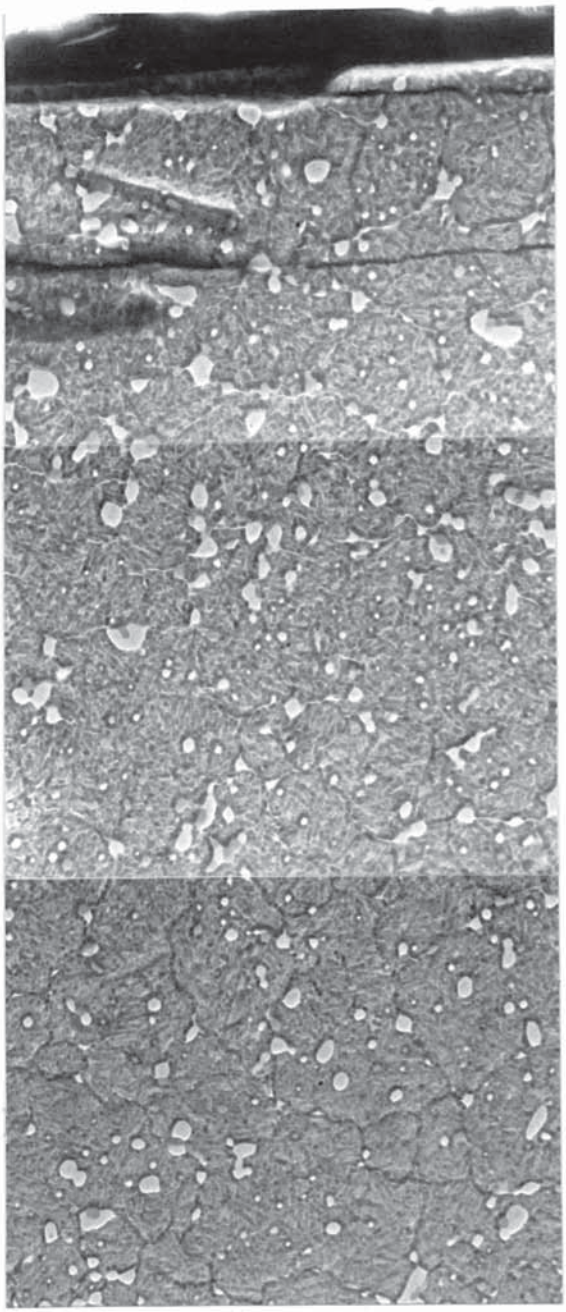

500F16

Mag'n x 1650

10μm

Fig.4.4 (c) 500°Cx16hrs - M2 Case Structure

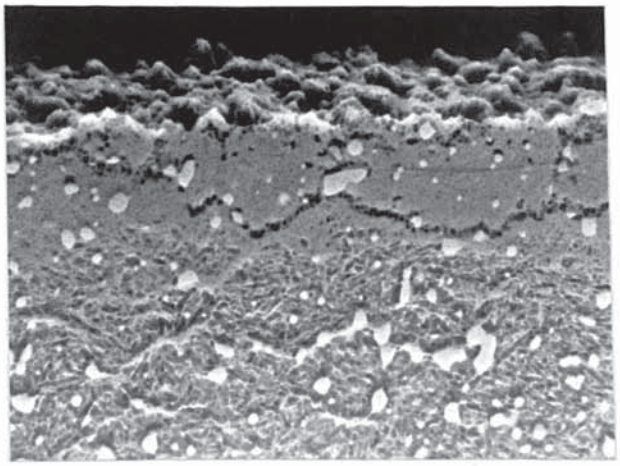

550F16

Case

Mag'n x1650

10μm

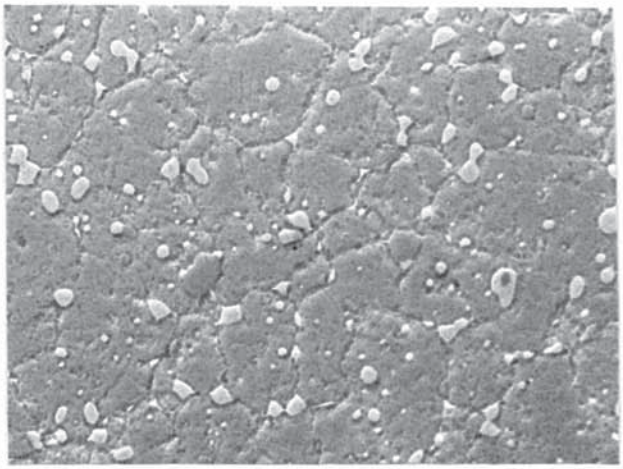

550F16

Core

Fig.4.4 (d) 550°Cx16hrs - M2 Case/Core Structure

550F64

Mag'n x1100

10μm

Fig.4.4 (e) 550°Cx64hrs - M2 Case Structure

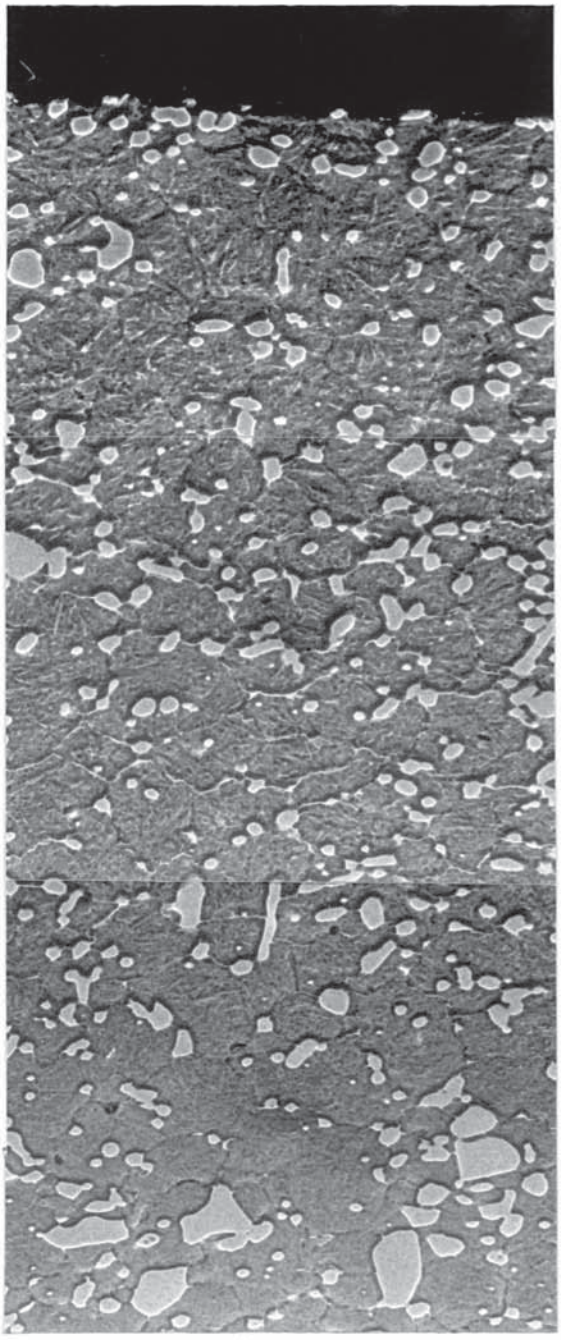

450T16(5)

Mag'n x1300

10μm

Fig.4.4 (f) 450°Cx16hrs(5) T1 Case Structure

Both Figure 4.4(c) - M2 treated at 500°C for 16hours, and Figure 4.4(f) - T1 treated at 450°C in 95%H_2/5%N_2 show an absence of intermetallic compound white layer at the surface.

All of the micrographs show evidence of an intergranular nitride/carbonitride network in the regions immediately below the surface. Also, some of the larger carbides can be seen to be duplex in nature - Figures 4.4(a), (c), (e).

Figures 4.4(d) and (e) illustrate how 'white layer' has grown inwards from the surface and show both embedded carbides and the 'skeleton' of prior austenite grain boundaries within the layer.

4.3.3. Fatigue Fracture Surfaces

Macro-photographs and scanning electron micrographs of some of the fatigue specimens' fracture surfaces are shown in Figures 4.5(a) - (f). M2, M50 and T1 steels are all illustrated.

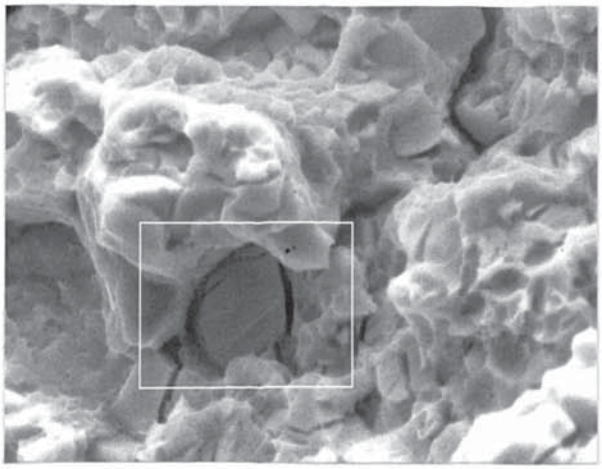

(a) In proximity to Specimen centre

Mag'n x4K

4 μm

(b) Mag'n x3.6

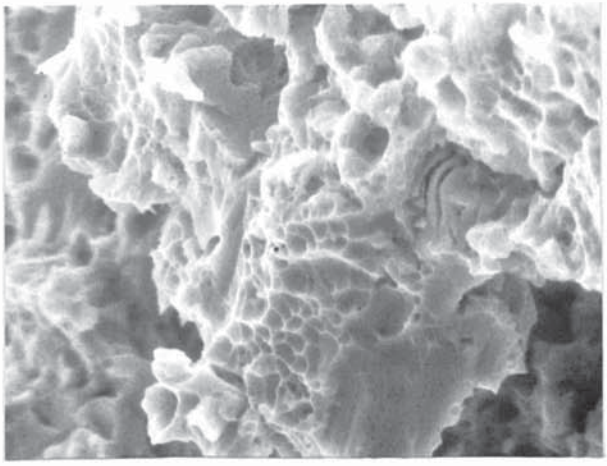

(c) In proximity to Initiation site

Mag'n x4K

4 μm

Fig.4.5 (a) 400°Cx16hours - M2 Fatigue Fracture Surface

(a) In proximity to Initiation Site

Mag'n x 170

100μm

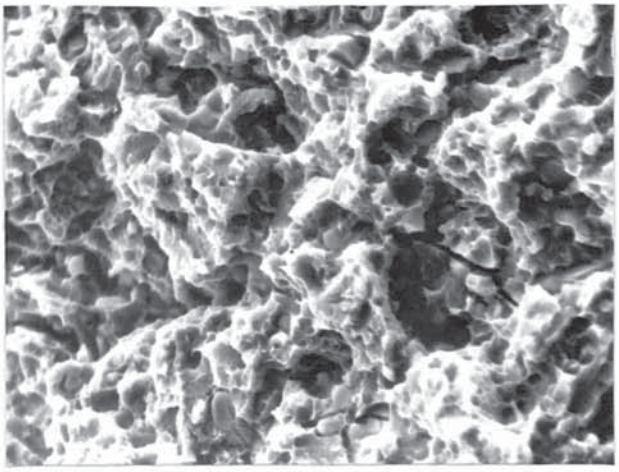

(b) In proximity to Initiation Site

Mag'n x2K

10μm

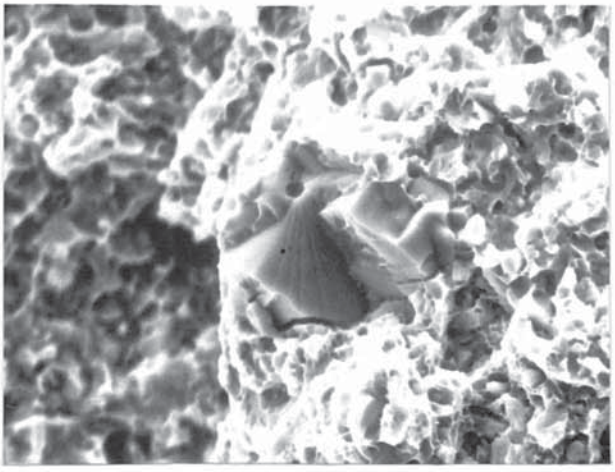

(c) Centre of Specimen

Mag'n x2K

10μm

Fig.4.5 (b) 550°Cx16hours - M2 Fatigue Fracture Surface

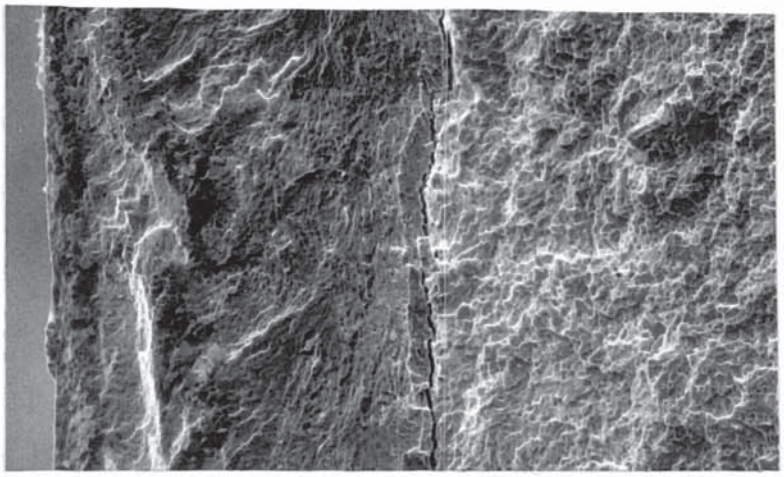

(a) End of failure

Mag'n x550

20 μm

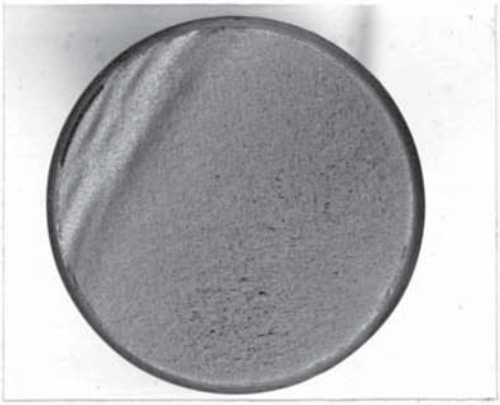

(b) Mag'n x3.6

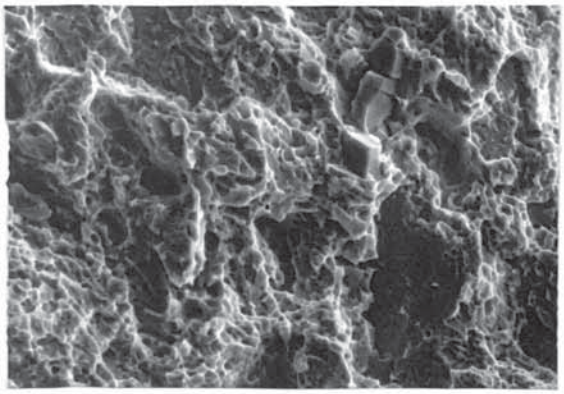

(c) Centre of Specimen

Mag'n x1300

10 μm

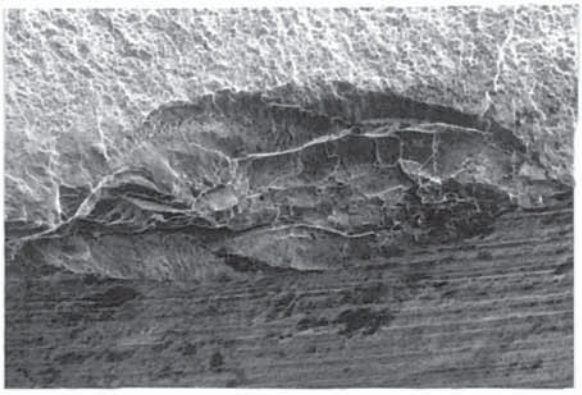

(d) Initiation Site

Mag'n x140

100 μm

Fig.4.5 (c) 450°Cx16hours - (75%H_2/25%N_2) - M50 Fatigue - Fracture Surface

(a) In proximity to Initiation Site

Mag'n x130

100μm

(b) Mag'n x3.6

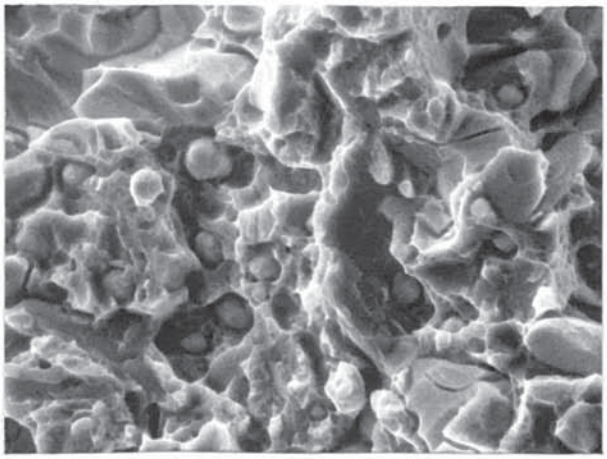

(c) Below the Initiation Site

Mag'n x3250

4μm

Fig.4.5 (d) 450°Cx16hrs - (75%H_2/25%N_2) - T1 Fatigue - Fracture Surface

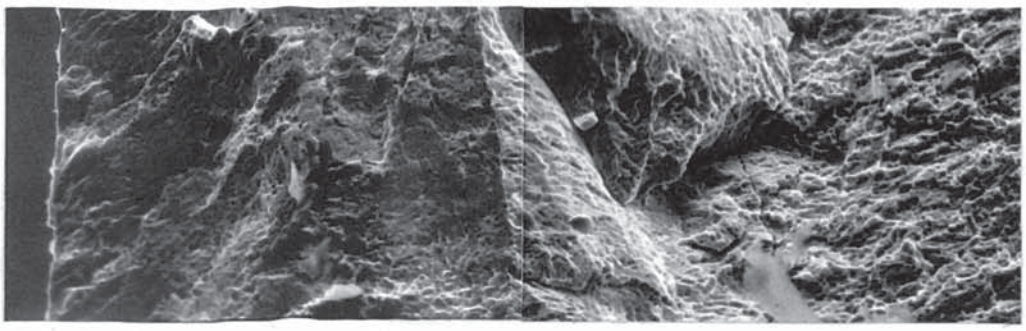

(a) Adjacent to end of failure

Mag'n x675

40μm

(b) Mag'n x3.6

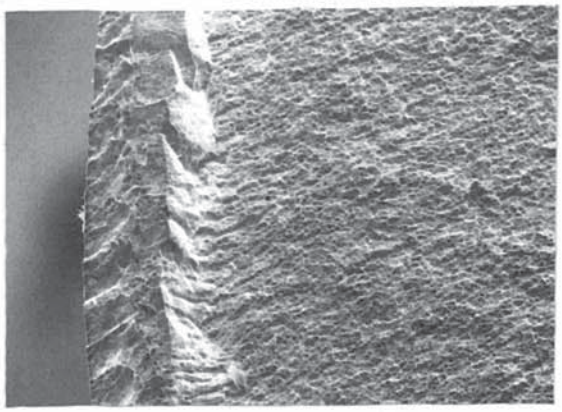

(c) Near end of failure

Mag'n x125

100μm

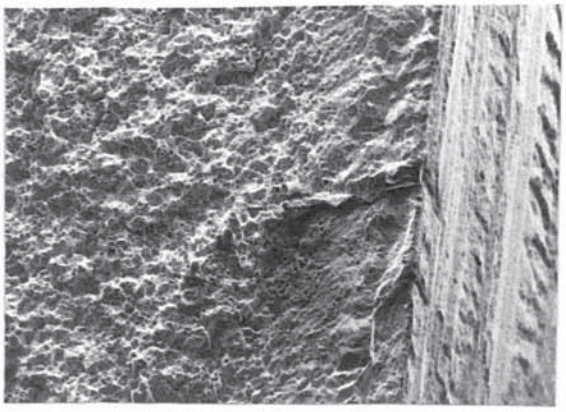

(d) Near initiation Site

Mag'n x140

100μm

Fig.4.5 (e) 450°Cx16hours - (85%H_2/15%N_2) - M50 Fatigue - Fracture Surface

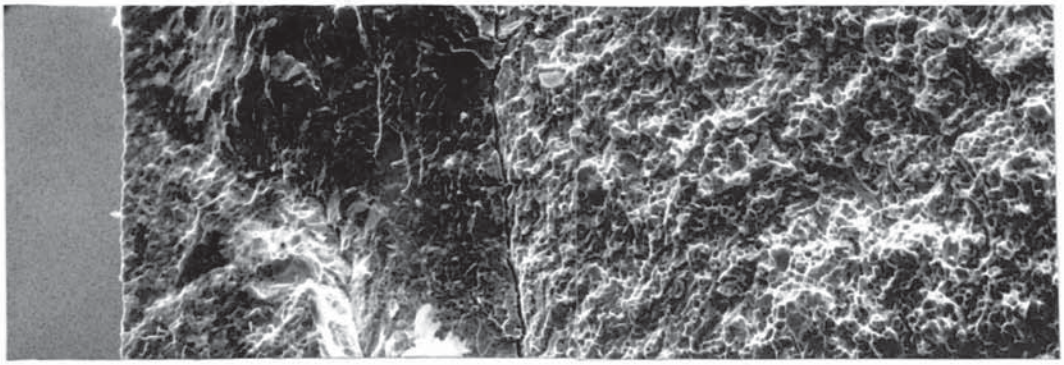

(a) Adjacent to end of failure

Mag'n x650

40 μm

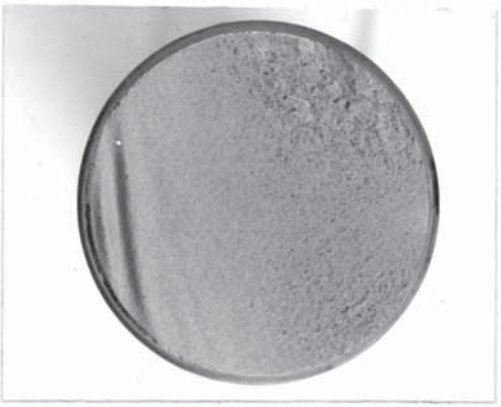

(b) Mag'n x3.6

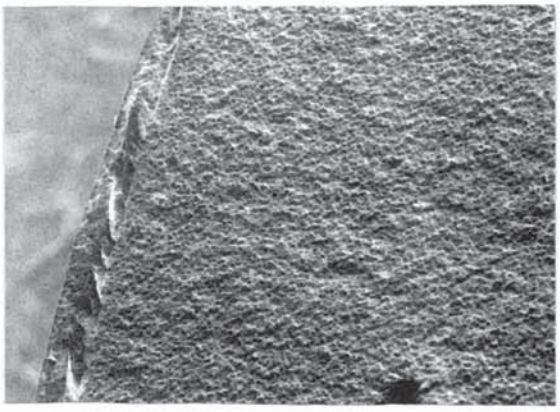

(c) Near end of failure

Mag'n x60

200 μm

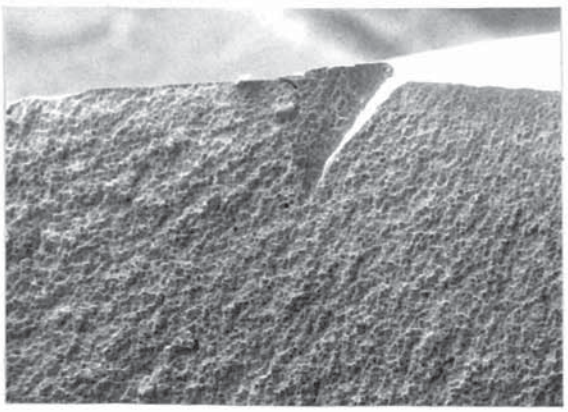

(d) Near initiation Site

Mag'n x60

200 μm

Fig.4.5 (f) 450°Cx16hours - (85%H_2/15%N_2) - T1 Fatigue - Fracture Surface

The M2 fatigue specimens, Figures 4.5(a) and (b), illustrate how fatigue cracks have propagated through the structure in an intergranular manner. Carbides have decohered from the rest of the structure where a crack has passed around their periphery, and show a cleavage type of failure.

Figures 4.5(c) and (e) show examples of failure in the M50 steel. Both display a distinct transition of fracture appearance bounded by cracks in the regions close to the end of failure. Both also show thumbnail type initiation sites which are similar in appearance to the end of failure fractures.

The T1 steels, Figures 4.5(d) and (f) have similar fractures to those in the M50. Again a transition of fracture appearance bounded by a crack is evident at the end of failure (Fig.4.5(f)). Figure 4.5(d) displays two thumbnail initiation sites while Figure 4.5(f) shows a distinct notch in the vicinity of initiation. This is very likely not the start of failure, but damage incurred at the end of failure due to the specimen impacting with the upper jig of the fatigue test rig.

4.4. Case Cracking Tendency and Stress Analysis

Data from the acoustic emission tests is presented in Table 4.6. Also shown in this table are equivalent Hertz and shear stresses together with the depth to maximum shear stress. These values have been derived from stress analysis calculations as outlined in section 2.2 and Appendix 1.

The graphical output (Figure.3.4(b)) from these tests was difficult to assess. Therefore, the acoustic output for each test was re-plotted against load to give a more clear indication of the load to cause the first cracks in the plasma nitrided case. This value was taken as the point at which the first change in slope of the line occurred. This is shown in an example of the collated data - Figure 4.6(a).

The values of Youngs modulus and Poisson ratio used in the calculations were taken from published literature. A value of 0.29 was taken as the Poisson ratio for all three steels. The Youngs modulus figures used are as follows:

M2	206850MPa
M50	208510MPa
T1	227450MPa

Figures 4.6(b) - (d) are compilations of the data presented in Table 4.4. and Table 4.2.

Identification	Load for 1st Crack (kN)	Hertz Stress σ_{max} (GPa)	Max Shear Stress $\tau_{(1)max}$ (GPa)	Max Shear Depth $Z_{(1)max}$ (mm)
400F16	40.00	13.54	2.19	0.550
400H16	1.50	4.53	0.73	0.184
450F1	30.00	12.30	1.99	0.500
450U1	34.00	12.82	2.07	0.521
450H1	6.00	7.19	1.16	0.292
450F4	52.00	14.77	2.39	0.600
450U4	7.00	7.57	1.22	0.308
450H4	3.00	5.71	0.92	0.232
450F16	16.00	9.97	1.61	0.405
450U16	17.00	10.18	1.65	0.414
450H16	2.50	5.37	0.87	0.218
450F64	48.00	14.38	2.33	0.584
450U64	40.00	13.54	2.19	0.550
450H64	35.00	12.95	2.09	0.526
500F4	19.00	10.56	1.71	0.429
500F16	12.50	9.18	1.49	0.373
500U16	5.00	6.77	1.09	0.275
500H16	2.00	4.99	0.81	0.203
550F4	6.20	7.27	1.18	0.295
550F16	14.00	9.54	1.54	0.388
550U16	10.00	8.53	1.38	0.347
550H16	10.00	8.53	1.38	0.347
550F64	7.50	7.75	1.25	0.315
550U64	8.00	7.91	1.28	0.322
550H64	10.00	8.53	1.38	0.347
600F4	26.00	11.72	1.90	0.476
600F16	7.00	7.57	1.22	0.308
450M16(25)	27.00	11.90	1.93	0.482
450M16(15)	25.50	11.70	1.89	0.473
450M16(5)	55.75	15.16	2.45	0.614
450T16(25)	41.00	14.08	2.28	0.546
450T16(15)	40.25	13.99	2.26	0.543
450T16(5)	57.25	15.73	2.54	0.610

Table 4.4. Load and Equivalent Stress to cause Case Cracking

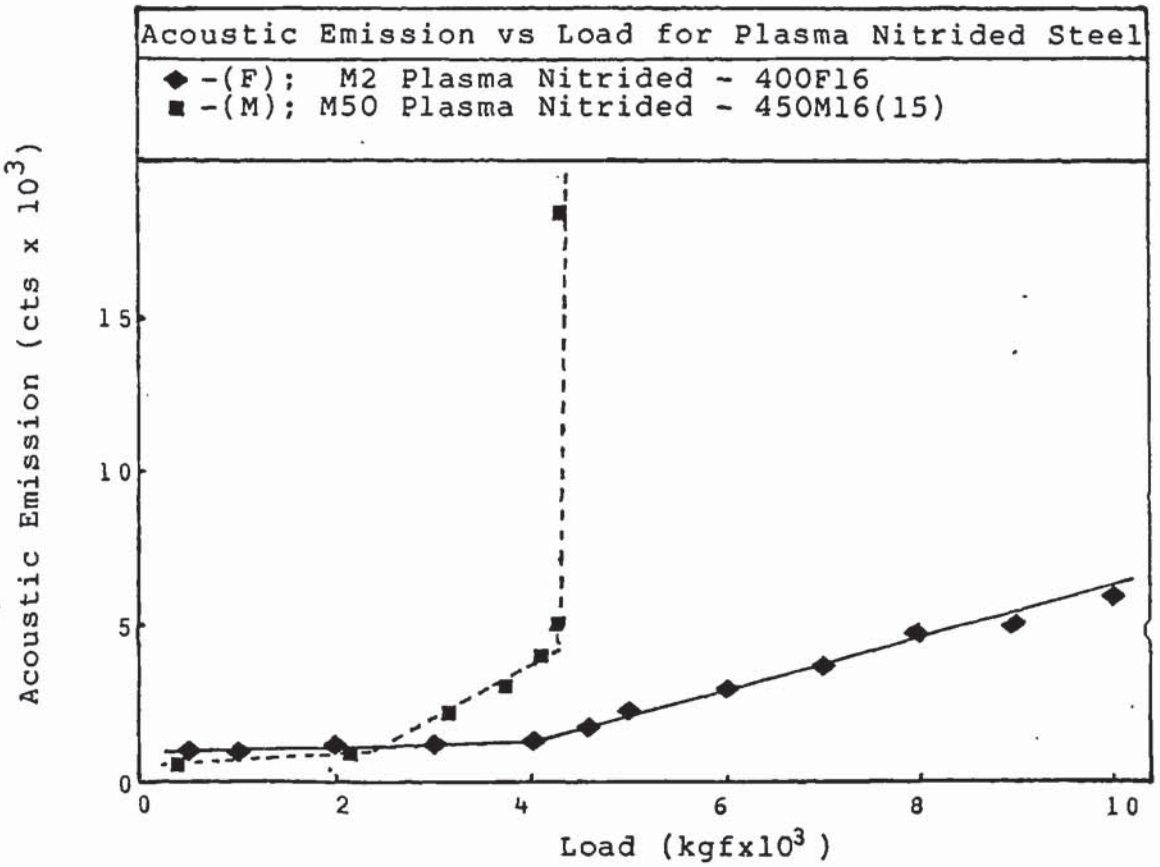

Fig.4.6 (a) Example of Compiled Acoustic Emission Test Data

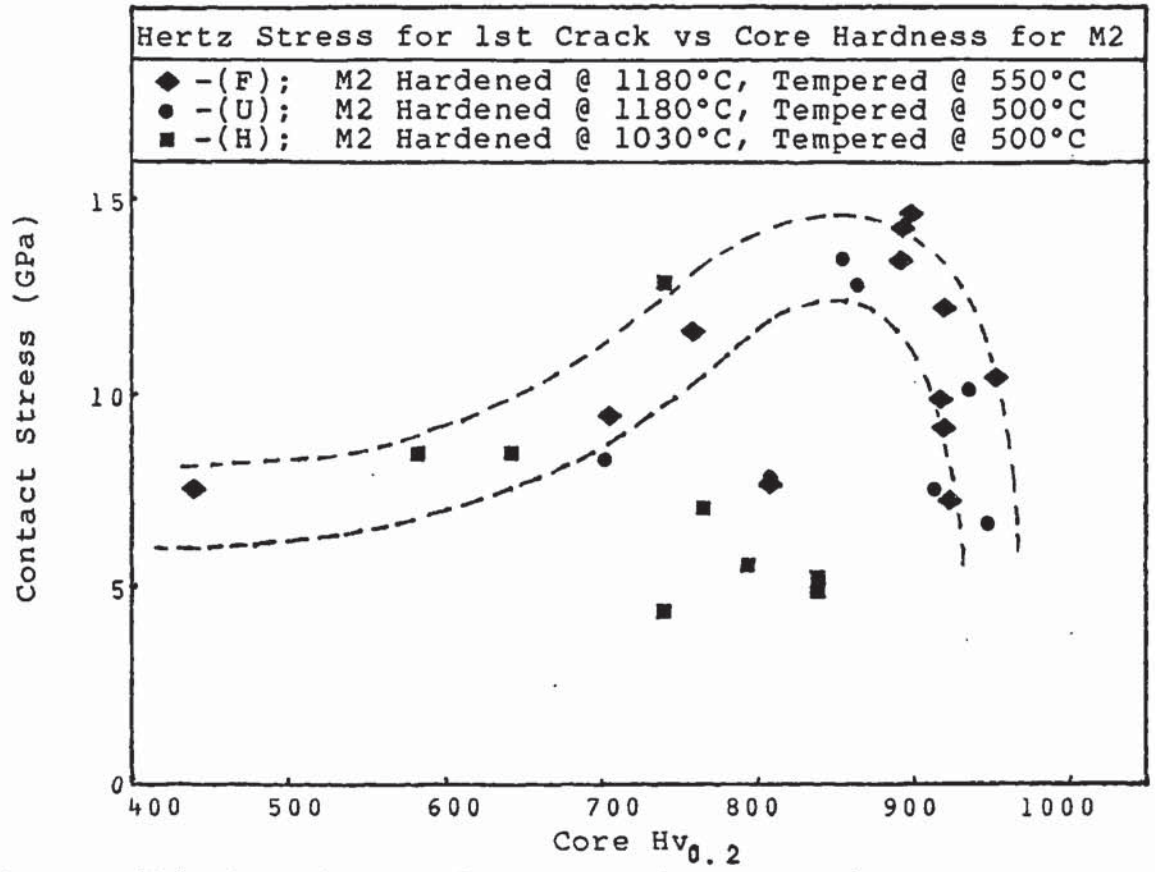

Fig.4.6 (b) The Effect of Core Hardness on the Stress to - Initiate Case Cracks in Plasma Nitrided M2

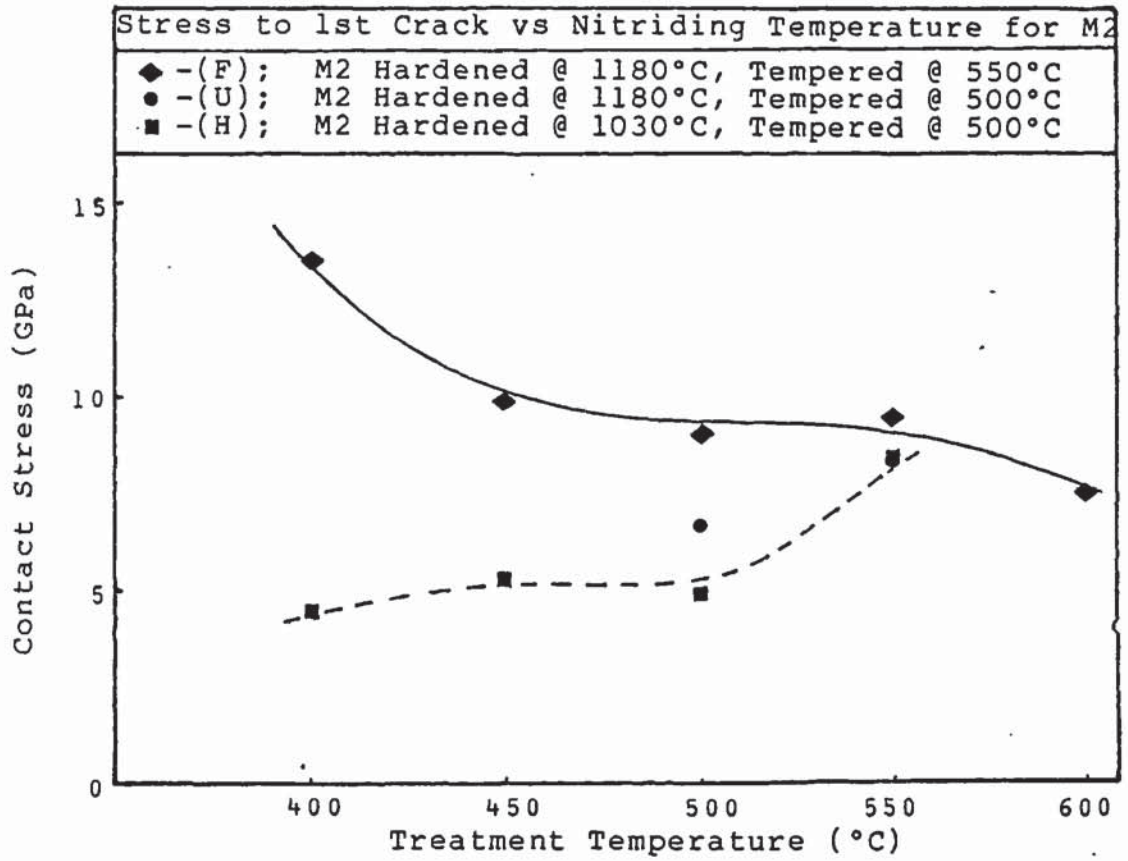

Fig.4.6 (c) Effect of Plasma Nitriding Temperature for 16hr - Treatments on the Case Cracking Tendency of M2

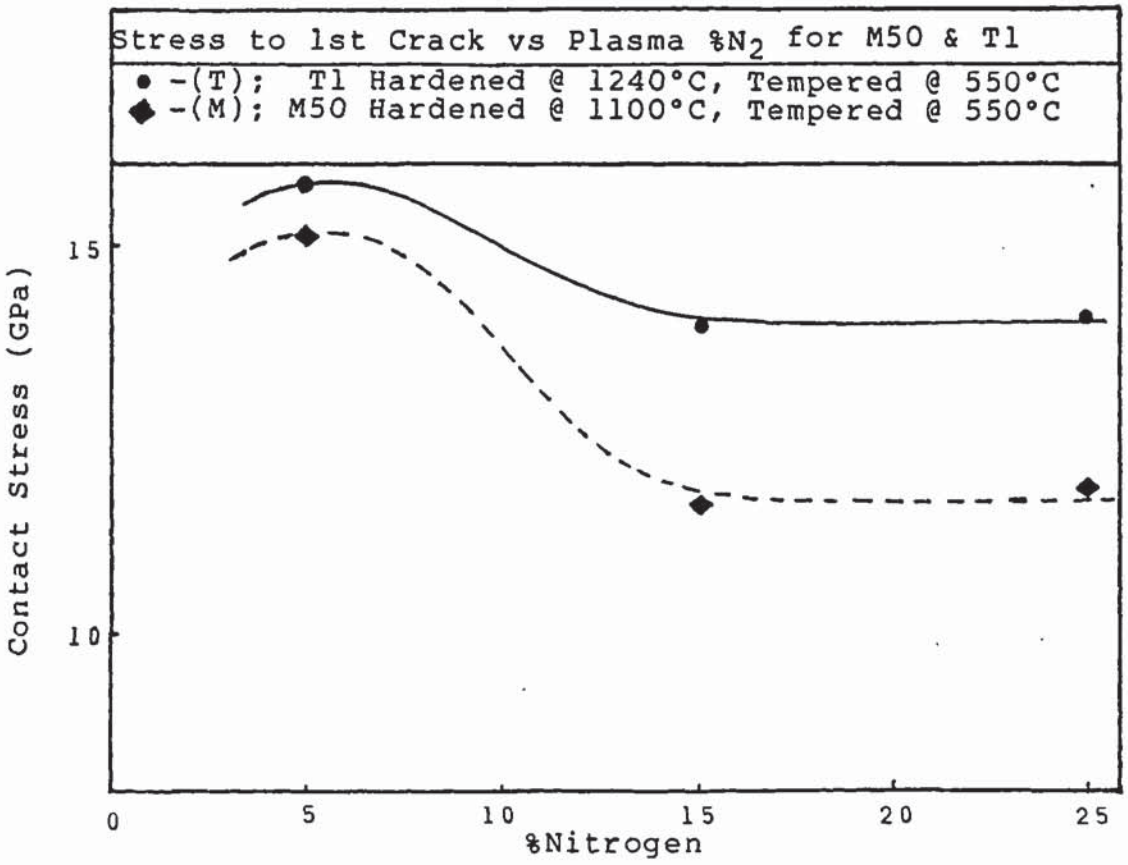

Fig.4.6 (d) Effect of Plasma N_2 Content on the Case Cracking - Tendency of M50 & T1 Plasma Nitrided 450°Cx16hrs

Figure 4.6(b) shows the relationship of case cracking tendency to core hardness of plasma nitrided M2 in the three hardened and tempered conditions used. An optimum level of core hardness to maximise resistance to case cracking is apparent. Also shown are a group of results which do not conform to this general trend.

Figure 4.6(c) illustrates case cracking tendency as measured against treatment temperature for 16hour treatments. Curves have been drawn here, but regression analysis yields a linear relationship of reasonably good fit, correlation coefficient (r) = -0.89, for the fully hardened and tempered data. The equation derived from the analysis is:

$$H = 22.33 - 0.0247(T) \qquad \ldots\ldots(4.2)$$

- where H is the contact (or Hertz) stress in GPa and T is the treatment Temperature in °C.

The underhardened and tempered data also yields a linear relationship on examination, but of slightly lower correlation ie. r = 0.87. The predicted equation here is:

$$H = -6.61 + 0.0265(T) \qquad \ldots\ldots(4.3)$$

Figure 4.6(d) shows the contact stress to cause case cracking measured against the nitrogen content of the plasma treatment atmosphere for M50 and T1. There is not enough data here to come to any firm conclusions, but it does appear that lower nitrogen content atmospheres might improve resistance to case cracking tendency.

4.5. Residual Stress Analysis

The results of the residual stress tests are presented in Table 4.5. The table shows data from all three x-ray diffraction techniques used on samples in the as-treated and electropolished conditions.

The tests carried out to determine 'set-up' errors in the equipment are related to data acquired prior to fitting of the metallurgical stage to the x-ray goniometer. Peak shift in a low stress mild steel sample due to sample misalignment on the goniometer axis ie. test repeatability, was found to be $\pm 0.015^{\circ} 2\theta$ ie. equivalent to a stress of ±8.93MPa. Therefore there is an instrumental error in these results making the quoted values up to 17.86MPa out.

Fitting of the Metallurgical stage reduced this sample alignment error to negligible levels ie. ±1.12MPa. Peak location and stress calculations were carried out by computer analysis of the acquired data. The program used is listed in Appendix 2 and is based upon a program by Kirk[99,100]. The stress values, for the double-exposure techniques, were calculated using the equation:

$$\sigma_{\phi} = \frac{E}{(1+\nu)\sin^2\psi}\left[\frac{\sin\theta_n}{\sin\theta_i} - 1\right] \qquad \ldots\ldots(4.4)$$

where θ_n = peak location for $\psi=0^{\circ}$

θ_i = peak location for $\psi=45^{\circ}$

E = Youngs modulus for the test material

ν = Poissons ratio for the test material

$\psi = 45^{\circ}$

Treatment	Double Exposure MPa	$Sin^2\psi$ MPa	Average Stress MPa	Notes
Fe Powder Std	- 132.26	-		
"	- 133.38	-	- 132.79	
Vacuum Annealed	+ 326.80	-		
"	+ 367.45	-		
"	+ 412.12	-		6
"	+ 310.06	+ 302.89	+ 343.86	
"	+ 212.44	+ 216.64	+ 214.54	1
OFO (H&T)	+ 351.34	-		
"	+ 240.01	+ 228.13	+ 273.16	6
"	+ 160.26	+ 147.94	+ 154.10	1
"	+ 413.24	-		2,4
"	+ 193.07	-	+ 303.15	2
400F16	- 364.68	-		2,6
"	- 211.38	-		2
"	- 134.42	-	- 236.82	2
450F4	- 747.50	-		
"	- 758.79	-		
"	- 648.55	-	- 718.28	6
"	- 705.38	- 729.54	- 717.46	1
450F16	- 671.12	-		4,5,6
"	- 703.93	-		4,5,6
"	- 693.42	-	- 689.49	
"	- 286.12	- 247.91	- 267.01	1
"	- 377.45	-		2
"	- 301.71	-		2
"	- 248.69	-	- 309.28	2
450H16	- 391.24	- 407.31	- 399.27	1
450U16	- 280.98	- 233.99	- 257.48	1
450F64	- 192.38	- 180.95	- 186.66	1
450H64	+ 0.99	+ 3.73	+ 2.36	1,3
450U64	- 74.29	- 87.30	- 80.79	1,3
500F16	- 813.85	-	- 813.85	6
"	- 643.60	- 642.81	- 643.20	1
"	- 466.93	-		2
"	- 348.19	-	- 407.56	2
500U16	- 749.16	-	- 749.16	5,6
550F16	- 285.83	- 283.13	- 284.48	1
"	- 312.19	-	-312.19	2
550H16	- 256.22	- 258.12	- 257.17	1
550U16	- 245.76	- 248.14	- 246.95	1
600F16	- 327.70	- 327.63	- 327.66	1

Notes
1. Electropolished
2. Fatigue samples
3. Poor straight line fit for $Sin^2\psi$
4. Poor std deviation for peak fitting in double exposure
5. Double exposure by fixed-time method
6. Error of ±8.93MPa on double exposure result

Table 4.5. Residual Stress Results for M2

Treatment	Double Exposure MPa	$Sin^2\psi$ MPa	Average Stress MPa	Notes
M50				
Vacuum Annealed	+ 82.67	+ 78.03	+ 80.35	
OMO (H&T)	+ 140.53	-		
"	+ 128.14	-		
"	+ 112.79	-	+ 127.15	4
"	+ 80.10	-		
"	+ 100.53	+ 106.34	+ 103.43	1
450M16(25)	- 311.22	-	- 311.22	4
"	- 467.83	- 459.68	- 463.75	1
450M16(15)	-1279.71	-1267.70	-1273.70	1
450M16(5)	-1115.75	-1112.90	-1114.32	1
T1				
Vacuum Annealed	+ 360.12	+ 358.93	+ 359.52	
OTO (H&T)	+ 271.35	-	+ 271.35	
"	- 8.78	- 2.64	- 5.71	1,3,4
450T16(25)	- 402.42	- 407.62	- 405.02	1
450T16(15)	- 702.29	- 688.20	- 695.24	1,3
450T16(5)	-1087.04	-1091.10	-1089.07	1

Table 4.5.cont'd Residual Stress Results for M50 & T1

Identification	Peak Location				Stress MPa
	$\psi=0°$	std dev	$\psi=45°$	std dev	
400F16	156.464	0.044	156.696	0.068	-134.427
450M16(25)	155.557	0.223	156.072	0.312	-311.222
OTO	153.429	0.033	153.058	0.032	+271.352

	ψ	$Sin^2\psi$	d	$\Delta d/d_\perp$	Stress MPa
550H16	0	0	1.1737	0	
	15	0.0698	1.1736	$-5.031*10^{-5}$	
	30	0.2500	1.1733	$-3.684*10^{-4}$	-258.12
	45	0.5000	1.1728	$-7.989*10^{-4}$	
	Equation: $A=3.060*10^{-5}$; $B=-1.640*10^{-3}$; r=0.997				
450M16(25)	0	0	1.1782	0	
	15	0.0698	1.1779	$-2.588*10^{-4}$	
	30	0.2500	1.1774	$-6.841*10^{-4}$	-459.68
	45	0.5000	1.1765	$-1.447*10^{-3}$	
	Equation: $A=-2.098*10^{-5}$; $B=-2.822*10^{-3}$; r=0.997				
450T16(5)	0	0	1.1830	0	
	15	0.0698	1.1827	$-2.937*10^{-4}$	
	30	0.2500	1.1813	$-1.472*10^{-3}$	-1091.1
	45	0.5000	1.1794	$-3.082*10^{-3}$	
	Equation: $A=6.500*10^{-5}$; $B=-6.253*10^{-3}$; r=0.999				

Table 4.6 Examples of Data from the Stress Programs

$Sin^2\psi$ results were computed using a second program (Appendix 2) rather than by the conventional graphical technique. The stress is calculated from the equation:

$$\sigma_\phi = m \left[\frac{E}{1+\nu}\right] \qquad \ldots\ldots(4.5)$$

where m is the slope of the graph of ε vs $Sin^2\psi$, the other terms 'E' and 'ν' being as described earlier.

Examples of data generated by computation for both the double exposure and $Sin^2\psi$ techniques are given in Table 4.6.

Figures 4.7(a)-(c) are compilations of the data presented in Tables 4.5 and 4.2.

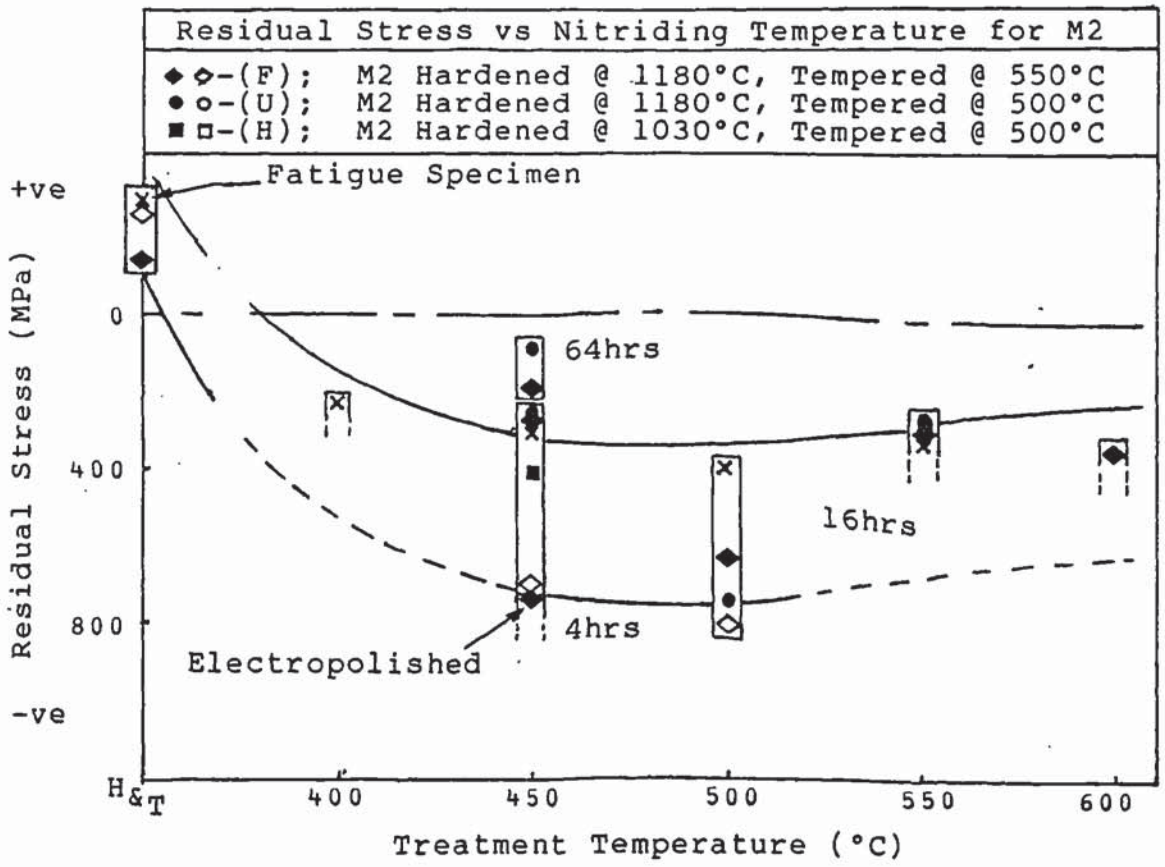

Fig.4.7 (a) The Effect of Treatment Temperature on Residual - Stress of Plasma Nitrided M2.

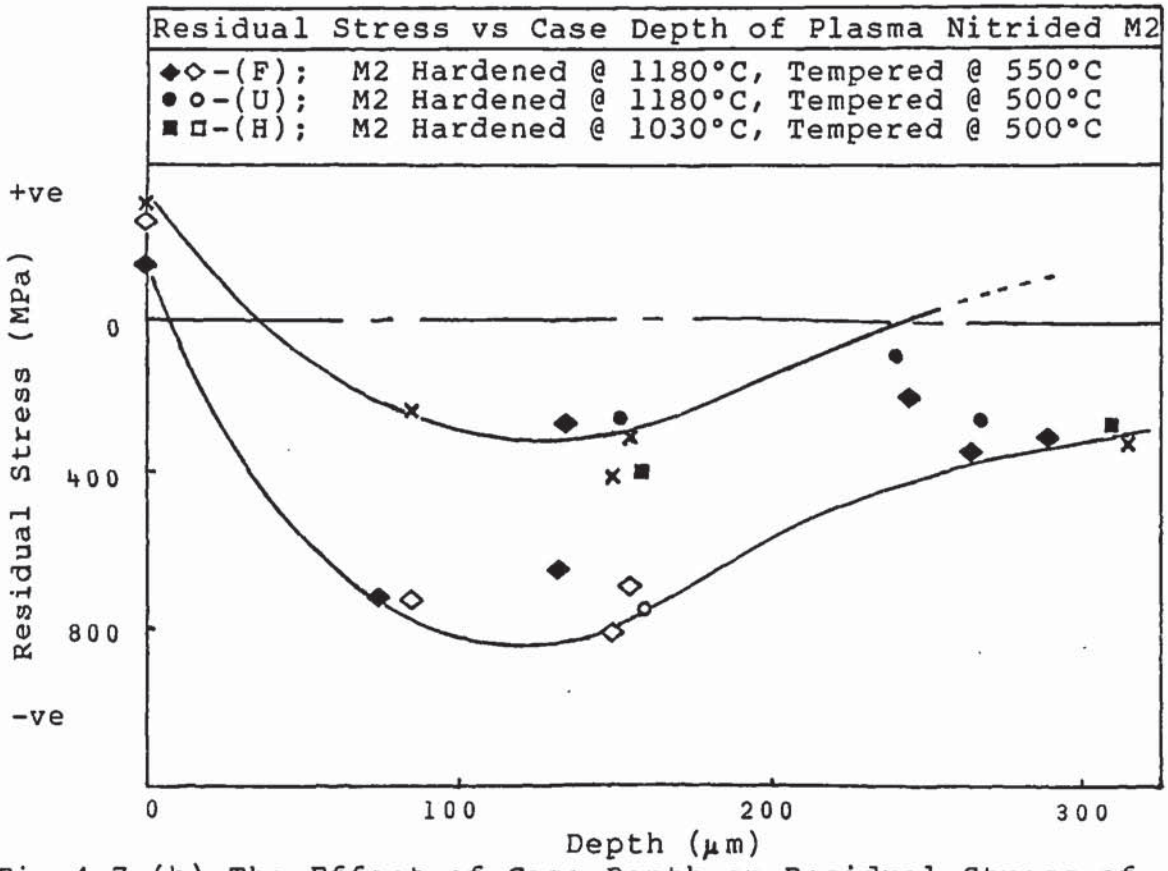

Fig.4.7 (b) The Effect of Case Depth on Residual Stress of - Plasma Nitrided M2

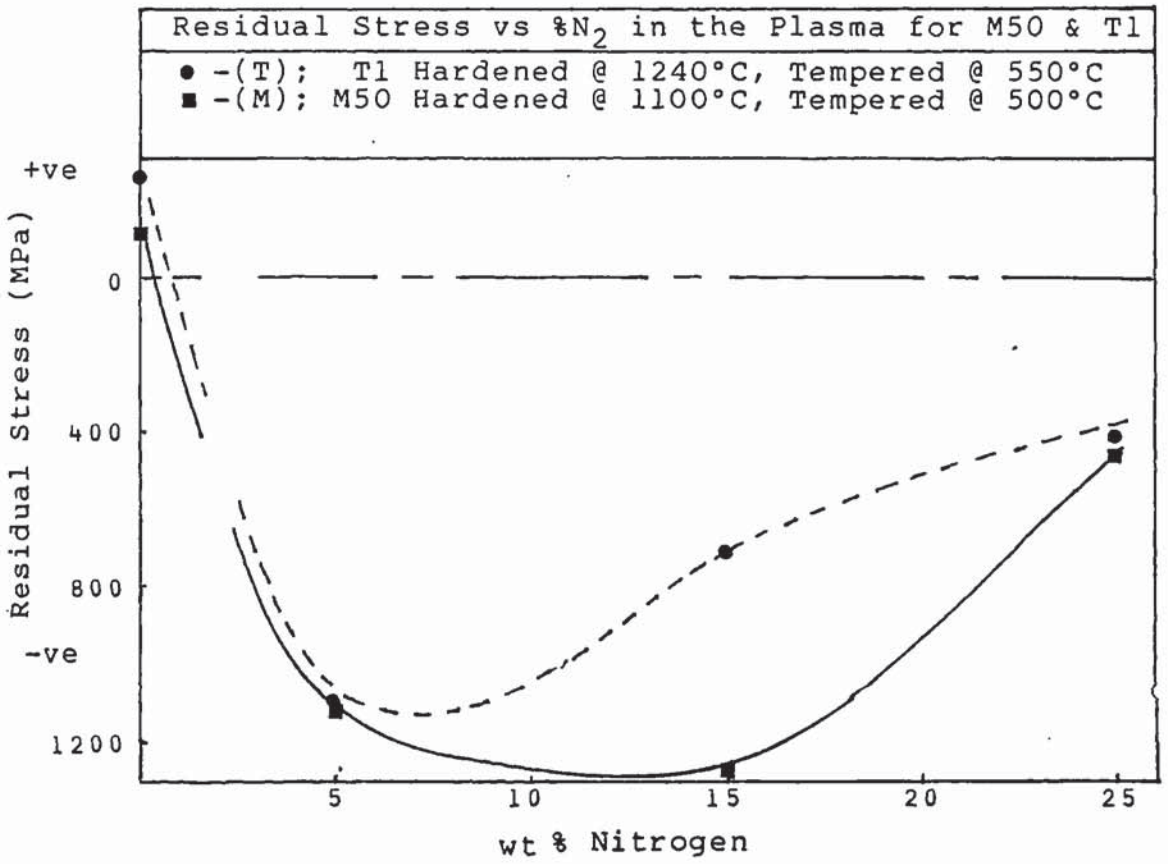

Fig.4.7 (c) The Effect of Plasma N_2 Content on the Residual - Stress in Plasma Nitrided M50 & T1

Figure 4.7(a) shows residual stress as a function of treatment temperature for M2. Values for the unpolished and electropolished conditions are shown together with results obtained from fatigue specimens. The general trend obtained from Figures 4.7(a) and (b) is that largest residual stresses are produced by 450°C to 500°C treatments - shorter times giving the larger stresses although this is substantiated by only one set of results.

Figure 4.7(b) implies an optimum case depth to generate peak residual stresses in the specimen. The data points plotted here take account of the layer removed during electropolishing. No corrections to the residual stress values have been applied since only a very small amount of the case has been removed in specimen preparation. This is in accordance with published information[101,102].

Figure 4.7(c) shows the relationship of residual stress to treatment atmosphere nitrogen content for the M50 and T1 steels. There are not enough data points for conclusive evidence, but the trend implies that lower nitrogen potential atmospheres lead to larger residual stresses in the case. It is also apparent that much larger compressive stresses are generated in these steels than in M2 during the plasma nitriding process.

4.6. Surface Phase Analysis

Detailed phase analysis has not been carried out and was not the purpose of this study. It was only necessary to determine the presence or absence of a surface intermetallic compound layer on the specimens to be used for the residual stress analysis.

Table 4.7 shows the presence or absence of white layer on the samples tested by x-ray diffraction. Also shown are the results of a very simple test, used in many metallurgical laboratories, for the detection of white layer. The basis of this test is the deposition of copper on the specimen surface from a solution of 10% cupric ammonium chloride. Deposition of copper indicates the absence of white layer and has been designated in the table as a positive response to the test. Where deposition is patchy, the implication is that a discontinuous surface compound layer is present. A negative response (no copper deposition) indicates the presence of a continuous surface compound layer of iron nitride.

Identification	White Layer Presence		
	XRD[1]	$Cu(NH_4)Cl$ Test[2]	Metallography[3]
400F16	-	-ve, present	yes, 2μm
450F1	-	+ve, traces	no, ≤1μm
450F4	-ve	+ve, traces	no, ≤1μm
450F16	$\varepsilon+\gamma'$	-ve, present	yes, 6μm
450F64	ε	-	yes, 10μm
500F4	-	+ve, traces	no, ≤1μm
500F16	ε	+ve, traces	no, ≤1μm
550F4	-	+ve, traces	no, ≤1μm
550F16	ε	-ve, present	yes, 10μm
550F64	-	-ve, present	yes, 12μm
600F4	-	-ve, present	no, ≤1μm
600F16	ε	-ve, present	yes, 8μm
450M16(25)	-ve	-	no
450M16(15)	-ve	-	no
450M16(5)	-ve	-	no
450T16(25)	-ve	-	no
450T16(15)	-ve	-	no
450T16(5)	-ve	-	no

Notes

(1) XRD test:
- \- signifies no test carried out
- -ve not enough peaks for positive identification

(2) $Cu(NH_4)Cl$ Test:
- \- signifies no test
- +ve white layer absent
- -ve white layer present

(3) metallography: yes/no white layer observed or not observed

Table 4.7. Surface Phase-Analysis Results

4.7. Fatigue Testing

Data derived from the unidirectional bending fatigue tests is presented in Table 4.8 . The table shows mean, maximum and minimum stresses together with the number of cycles to failure at the failure load. The maximum and minimum loads were chosen to give an 'r' value of 0.25. However, in practice the value was much closer to 0.3 for most of the tests. The footnotes to the table itemize some of the experimental problems encountered during testing.

Figures 4.8(a) - (d) are compilations of the data presented in Tables 4.8 and 4.2.

Identity	Stress at Failure (MPa)			Stress Ratio r	Cycles to Failure ($x10^3$)	Notes
	σ_{max}	σ_{mean}	σ_{min}			
0F0	709	443	177	0.25	7	
	676	422	169	"	23	
	709	443	177	"	81	
	676	422	169	"	56	
averages	693	433	173	-	-	
400F16	2054	1326	597	0.29	2	
	1774	1146	517	"	6	1,2
	-	-	-	-	-	4
	-	-	-	-	-	3,9
averages	1914	1236	557	-	-	
450F16	1610	1059	509	0.32	11	
	1261	829	398	"	81	
	1201	791	382	"	42	
	-	-	-	-	-	2,9
	-	-	-	-	-	5,9
averages	1357	893	430	-	-	
500F16	1201	789	378	0.31	19	
	1390	914	438	"	3	
	1144	771	398	0.35	16	
	-	-	-	-	-	6,9
	-	-	-	-	-	2,9
averages	1245	825	405	-	-	
550F16	1144	771	398	0.35	92	
	1460	959	458	0.31	7	
	1460	969	477	0.33	44	
	1532	1025	517	0.34	4	
	-	-	-	-	-	2,9
averages	1399	931	463	-	-	

Notes

(1) Sample failed outside notch at prior loading point marks
(2) Failed before reaching set maximum load
(3) Failed in setup due to gross overload
(4) Specimen not tested - Sent for independent residual stress analysis
(5) Failed before reaching maximum load - excessive fretting - jigs worked loose
(6) Failed in setup - gross overload due to m/c failure - output valves 'blown'
(7) Failed to achieve set maximum load - m/c instability - sample plastically deformed
(8) Failed in setup - photocell and fuses 'blown' in m/c
(9) Data not collated for use in these results

Table 4.8 . Unidirectional Bending Fatigue Test Results

Identity	Stress at Failure (MPa)			Stress Ratio	Cycles to Failure	Notes
	σ_{max}	σ_{mean}	σ_{min}	r	($\times 10^3$)	
0M0	1201	799	398	0.33	88	
	1089	714	338	0.31	33	
	1089	714	338	"	54	
	1089	714	338	"	45	
	-	-	-	-	-	8,9
averages	1117	735	353	-	-	
450M16(5)	1089	704	318	0.29	72	
	1089	704	318	"	32	
	1089	712	334	0.31	54	
	-	-	-	-	-	2,9
	-	-	-	-	-	2,9
averages	1089	707	323	-	-	
450M16(15)	1144	741	338	0.30	18	
	1144	739	334	0.29	33	
	1201	789	378	0.31	49	
	1089	694	298	0.27	95	
	-	-	-	-	-	6,9
averages	1145	741	337	-	-	
450M16(25)	1324	861	398	0.30	7	
	1261	829	398	0.32	17	
	1324	841	358	0.27	15	
	-	-	-	-	-	2,9
	-	-	-	-	-	2,9
averages	1303	844	385	-	-	
0T0	1261	810	358	0.28	40	
	1201	799	398	0.33	13	
	1144	761	378	"	29	
	1089	680	271	0.25	36	
	-	-	-	-	-	2,9
averages	1174	763	351	-	-	
450T16(5)	1144	739	334	0.29	23	
	1089	704	318	"	14	
	1089	724	358	0.33	80	
	-	-	-	-	-	2,9
	-	-	-	-	-	3,9
averages	1107	722	337	-	-	
450T16(15)	1089	694	298	0.27	68	
	1089	704	318	0.29	67	
	1390	894	398	"	29	
	-	-	-	-	-	8
	-	-	-	-	-	2,9
averages	1189	764	338	-	-	
450T16(25)	1390	894	398	0.29	38	
	1460	959	457	0.31	35	
	1261	819	378	0.30	3	
	-	-	-	-	-	7,9
	-	-	-	-	-	2,9
averages	1370	891	411	-	-	

Table 4.8. cont'd. Unidirectional Bending Fatigue Test - Results

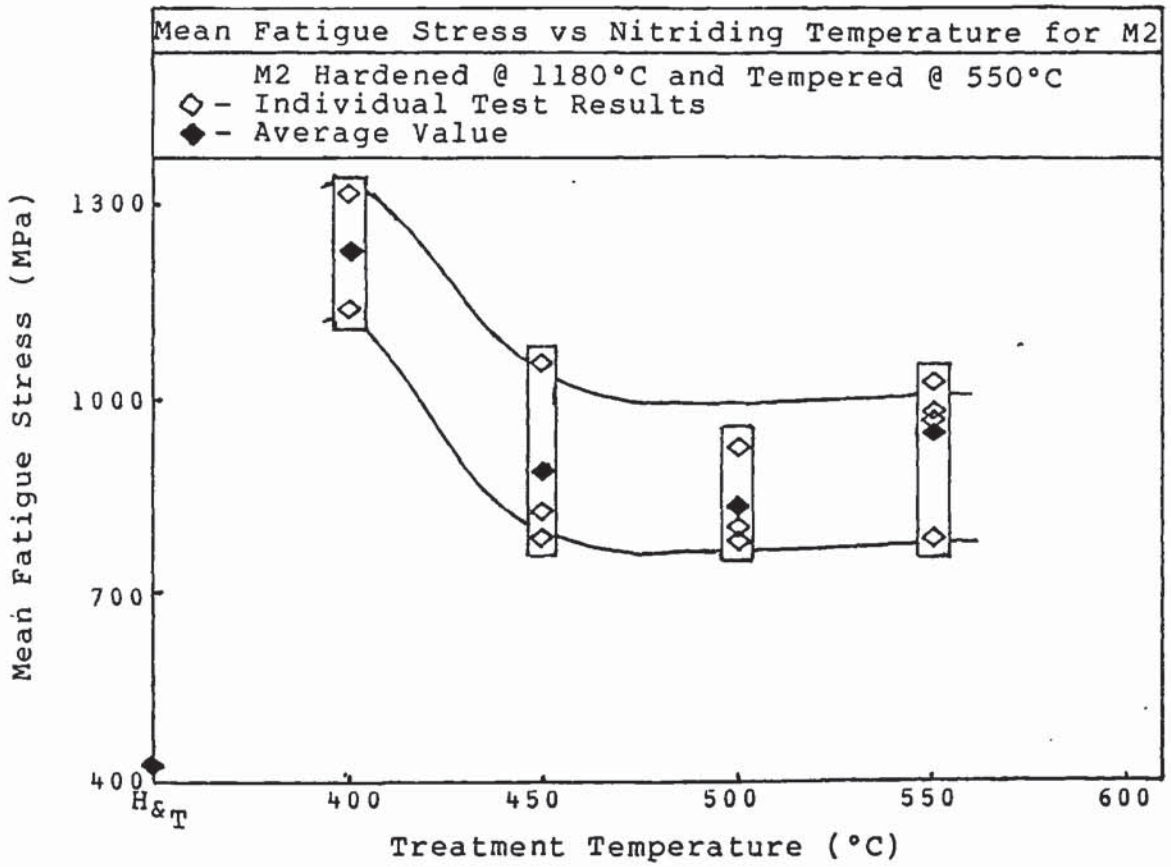

Fig.4.8 (a) The Effect of Treatment Temperature on the Mean - Fatigue Strength of M2 Plasma Nitrided for 16hrs

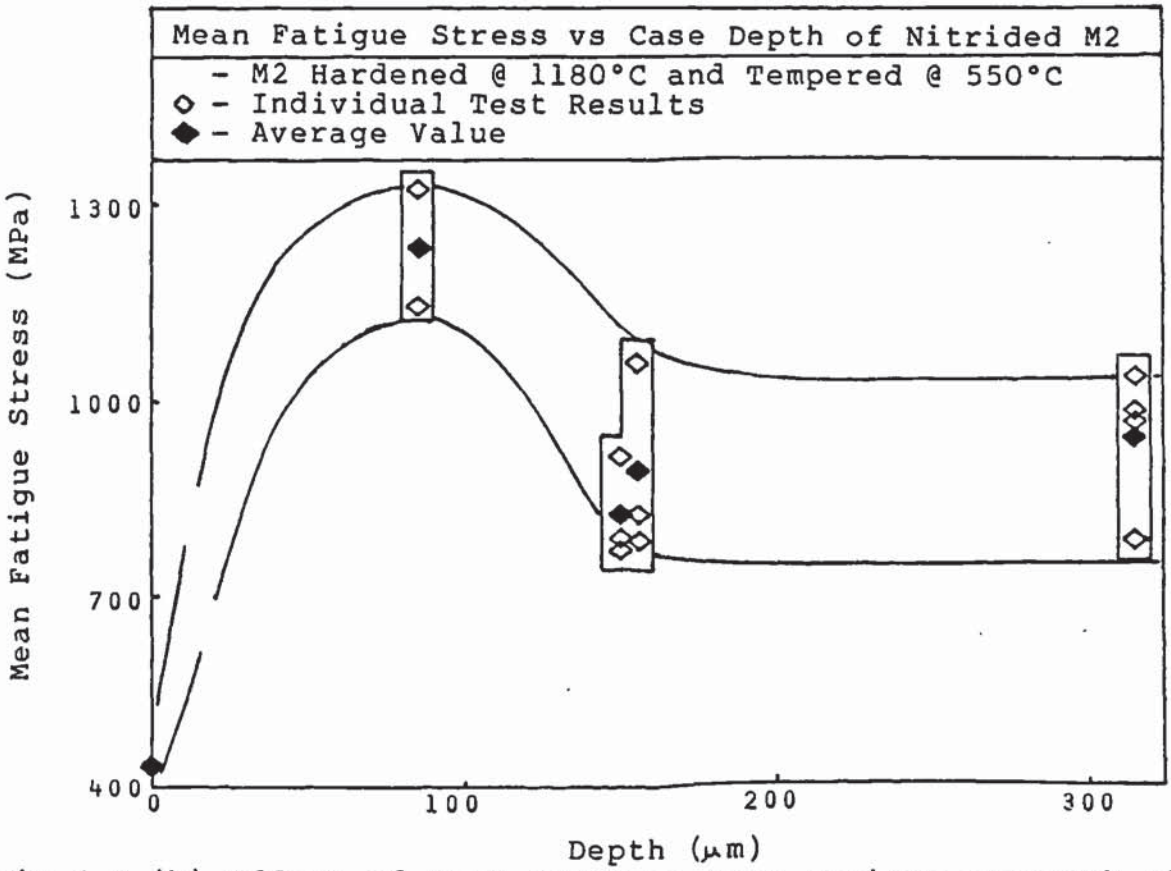

Fig.4.8 (b) Effect of Case Depth on Mean Fatigue Strength of - M2 Plasma Nitrided for 16hrs

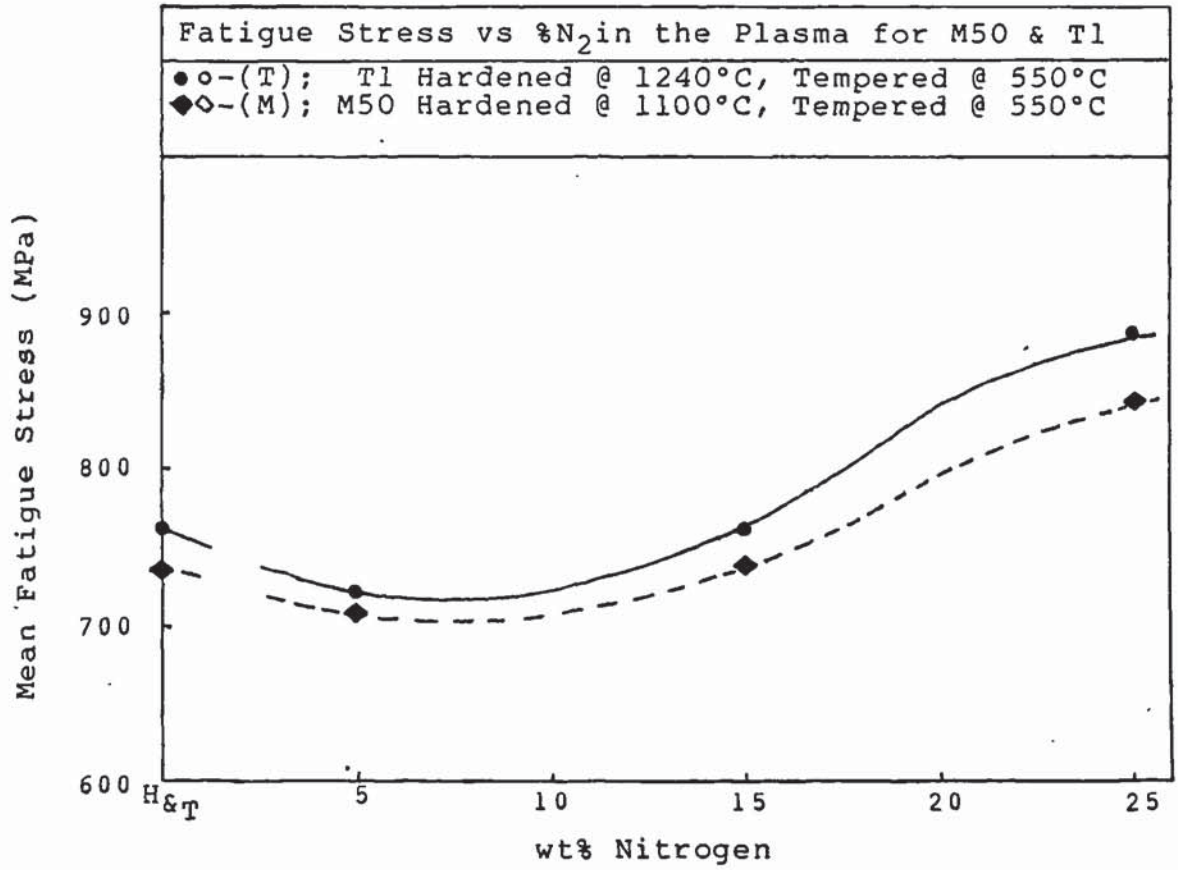

Fig.4.8 (c) Effect of Plasma N_2 Content on The Mean Fatigue - Strength of M50 & T1 Plasma Nitrided - 450x16hrs

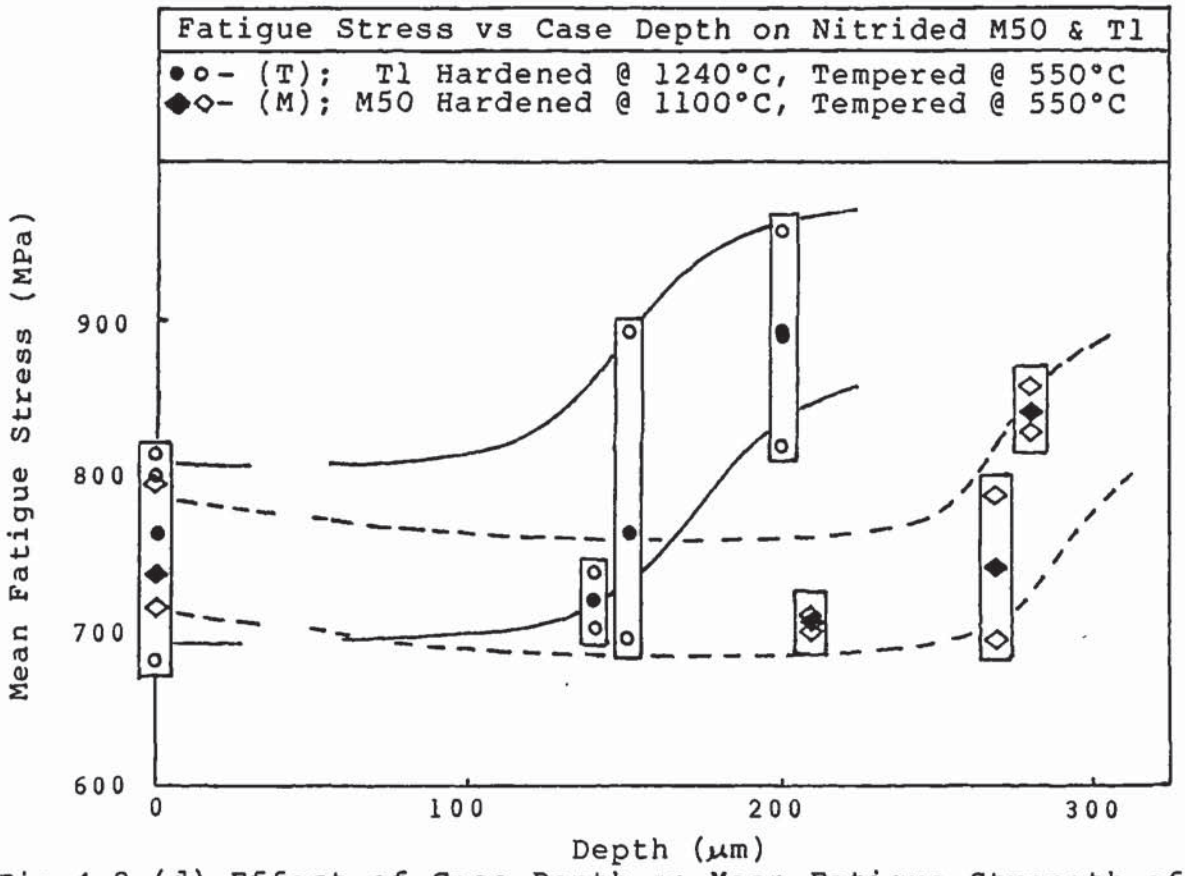

Fig.4.8 (d) Effect of Case Depth on Mean Fatigue Strength of - M50 & T1 Plasma Nitrided for 16hrs @ 450°C

Figure 4.8(a) shows the mean fatigue strength of M2 as a function of treatment temperature for 16hour plasma nitriding treatments. All of the treatments give a significant improvement over the hardened and tempered bend fatigue strength. Temperatures in excess of 450°C appear to give essentially the same level of fatigue improvement while treating at 400°C gives a much greater increase in strength.

Figure 4.8(b) shows fatigue strength variation with increasing case depth. The marked fatigue improvement from treating at 400°C is again well displayed here at a case depth of 80 - 100μm. Larger cases as displayed by higher temperature treatments give similar bend fatigue strengths to one another but yield a lower level of improvement over the hardened and tempered condition.

Figures 4.8(c) and (d) refer to the M50 and T1 steels and show the relationship of bending fatigue strength to the treatment atmosphere nitrogen content and the case depth developed for 16hrsx450°C plasma nitriding treatments. Figure 4.8(c) points to no overall fatigue improvement being gained from lower nitrogen potential atmospheres with respect to the hardened and tempered materials. A good improvement in fatigue strength is shown for treatments in a 75%H_2/25%N_2 plasma atmosphere. This is confirmed in Figure 4.8(d) where a marked improvement is noted for each steel once an apparent critical case depth has been achieved. This contrasts with the data for M2 which implies an optimum case depth for maximum fatigue strength improvement.

5. Discussion

5.1. Introduction

The strength of steels is of fundamental importance to the engineer. By careful use of steel strengthening mechanisms he can produce components or structures which are stronger and of greater reliability.

However strength is limited in usefulness by plastic yielding and fracture, and these are not mutually compatible. Greater strength (or resistance to plastic flow) leads to a reduction in ductility and toughness. One can see that it is necessary to optimise these properties for a particular application and this is primarily achieved by heat treatment.

The most common treatment applied to steels is to harden to achieve strength, and then temper to gain some measure of toughness. But, for some applications the bulk properties achieved need to be supplemented to improve the strength and wear resistance of the surface layers. This may by accomplished by thermochemical surface heat treatments such as plasma nitriding.

In general surface treatments depend upon the diffusion of an element into the surface, where a chemical reaction takes place and causes a structural change in the steel. By virtue of their dependence upon diffusion mechanisms, these treatments are carried out at moderate temperature and therefore pose problems due to degradation of the pre-existing properties of the material. Although plasma nitriding is less susceptible to this drawback, because it can be carried out at lower temperatures, there is still some risk at extended treatment times.

The case and core hardness of plasma nitrided steels is dependent not only on the nitriding treatment itself but also on the prior condition of the steel. The hardening and tempering pre-treatments are of major importance to the subsequent response of the steel to the plasma process.

The Holloman equation predicts, and practical experience shows, that extended treatment times and/or higher temperatures lead to a 'softening back' of the bulk hardness of treated steels.

It was hoped that this effect could be delayed during nitriding by selection of suitable hardening and tempering treatments.

5.2. The Hardness, Depth and Structure of Nitrided Cases

5.2.1. Effect of Time and Temperature

Manufacturing industry is currently hardening BM2 high speed steel at about 1180°C, the lower end of the hardening range. This ensures that, although sufficient of the carbides are dissolved to ensure full hardening, excessive grain growth or incipient fusion at grain boundaries is not a problem.

It was anticipated that fully hardened and tempered specimens would show some core softening at extended plasma nitriding times and at temperatures equivalent to or higher than the tempering temperature. However only higher temperature treatments were found to show any marked degree of core softening.

Underhardening and fully tempering at 500°C was carried out to assess the core strengthening characteristics of the subsequent plasma nitriding process. Higher temperature and longer time treatments did benefit from a developing core strength but this was at the expense of a considerable loss of core hardness.

Treatments carried out at 400°C gave shallow case depths with steep hardness gradients near to the surface [Figure 4.1(a)]. There was a good degree of surface hardening and core hardness was not affected detrimentally. Figure 4.3(a) shows no evidence of an etch case. Underhardened specimens had a fine aggregate of tempered martensite and small secondary hardening and larger primary carbides. The grain structure was not well defined. This is in contrast to the other pre-treatments where the structure was less aggregated and showed a much more definite grain structure.

400F16, 400U16 and 400H16 all had similar case hardness profiles to one another but 400H16 was much softer as expected. Optical metallography gave no evidence of surface compound white layer on these specimens but the chemical test (Table 4.7) and scanning electron microscopy indicated the presence of a continuous layer of up to 2 μm in thickness.

Short treatments at 450°C gave shallow cases [Figures 4.1(b) and (c)] implying that an incubation period is necessary to initiate case development. This is in agreement with the current understanding of the mechanisms operating in other nitriding techniques. Case development was initiated first on 450F1 followed by 450H4. At these treatment times case development had not started on the undertempered specimens. Surface hardness was not developed to the same extent as in the 400°C treatment but core hardness of the undertempered and underhardened conditions did show some improvement. A surface white layer was not formed by these treatments.

Deeper cases were produced at longer times [Figures 4.1(d) and (e)] and surface hardness was developed to a maximum for these treatments. Core hardness was also seen to benefit from times up to 16hrs for the undertempered and underhardened pre-treatments. Longer treatments still gave a core hardness improvement but to a lesser degree. The underhardened condition was still much softer than the other two pre-treatments for these plasma treatments and this is reflected in the microstructures as illustrated by Figure 4.3(b) where the core is still of the finely aggregated structure seen in the 400°C treatment.

Figure 4.3(c) shows an etch case for all three hardened conditions but there is no evidence of surface compound layer. There is evidence of surface cracking - more in 450U16 than in either 450F16 or 450H16. This surface damage is thought to be due to the technique used in specimen preparation for metallographic examination.

Figure 4.4(a) shows 450F16 in more detail and confirms the data provided in Table 4.7 that surface compound layer is present. There is also evidence of intergranular penetration of this compound layer into the diffusion case. Cracking is apparent in the surface layer. Figure 4.4(b) shows the surface compound layer present on 450F64. Cracking is apparent together with intergranular penetration of the compound layer and embedded carbides in the compound layer.

Steep hardness profiles were developed in 500°C plasma treatments [Figures 4.1(f) and (g)]. 500H16 [Figure 4.1(g)] showed a hardness trough at the case/core interface and 500U16 displayed a very hard core. This latter point could be due to the secondary hardening peak. The maximum secondary hardening effect would take much longer to achieve at the lower tempering temperature used for this pre-treatment and would therefore not be completed within the time used in tempering. This then could be used to offset the effects of of an extended plasma treatment at this temperature.

Figure 4.3(d) shows an etch case on all samples and surface cracking on 500F16 and 500U16. Again the underhardened treatment shows a less well defined grain structure consistent with treatments carried out on this steel condition at lower temperatures. Table 4.7 shows a mixed response to the various tests, on this plasma treatment, for white layer presence. However, Figure 4.4(c) shows 500F16 at higher magnification and there is no real evidence of surface compound layer present. Examination of the parameters used during plasma nitriding show that a gas flow rate of only 100cc min^{-1} was used in this treatment due to instability in temperature and pressure control. This could account for the absence of a continuous surface compound layer. Figure 4.4(c) also shows cracking of the diffusion case and the presence of a very small amount of intergranular nitride penetration.

550F4 [Figure 4.1(h)] showed a good well developed case with no real evidence of surface compound layer being present. Surface hardness developed to a lesser degree than in the 450°C treatments but the core hardness was unaffected by the treatment. Deeper than expected case depths were produced by the 16hr treatment [Figure 4.1(i)], surface hardness was not developed very well and core hardness was drastically reduced. The deeper cases would result from the lower than expected core hardnesses and these would appear to be a direct result of lack of temperature control during this plasma treatment where it is noted that a higher than desired temperature prevailed during the later stages of the treatment. This was due to imminent breakdown of the control thermocouple.

A substantial surface compound layer has been formed by this treatment - Figure 4.3(e). A small amount of intergranular penetration of the layer is evident and this is confirmed, for 550F16, by Figure 4.4(d). One can also see here the 'skeleton' of a prior austenite grain boundary within the surface compound layer, manifested as a line of porosity. (These skeleton defects are regions through which surface spalling or cracking could progress more readily) There are carbides embedded in the white layer and the acicular nature of the diffusion layer is also apparent.

After 64hrs, very heavy cases have developed and surface hardness was higher than after the 16hr treatment at this temperature [Figure 4.1(j) and Table 4.2]. (This was unexpected and is another manifestation of the poor temperature control in the 550°Cx16hr treatment) A hardness plateau extending for most of the effective case depth was apparent on these specimens. 550F64 also had a very steep hardness gradient immediately below the surface which tapered off into the plateau. This corresponds to the location of surface compound layer and intergranular penetration of the layer into the diffusion case.

The extent of surface compound layer can be seen in Figure 4.3(f), together with an inner dark band at the etch case/core interface. Intergranular penetration is apparent as is spalling and cracking of the surface compound layer. Figure 4.4(e) is a montage of the outer part of the case on 550F64 and shows more clearly the intergranular penetration of the compound layer, together with the surface compound layer containing both embedded carbides and prior austenite grain boundaries.

At 600°C, deep cases were produced by both 4hr and 16hr treatments [Figures 4.1(k) and (l)]. There was no real evidence of surface white layer after 4hrs but there did appear to be some intergranular penetration. After 16hrs at 600°C the fully hardened condition had a softer core than either of the other two pre-treatment conditions [Figure 4.1(l)]. The case profiles were not steep in gradient but did show a small surface hardness improvement over the untreated steel conditions.

A substantial surface compound layer was formed after 16hrs as shown by Figure 4.3(g). No surface spalling is apparent, nor is intergranular penetration of the surface compound layer. However scanning electron microscopy on 600F16 did show a substantial presence of intergranular penetration, near the surface and that this was formed in a planar manner. Figure 4.3(g) shows that the core structure has been affected by this high temperature treatment. 600F16 had an aggregated structure of fine, spherical and well distributed carbides embedded in the matrix. In contrast 600H16 has lost its fine aggregate nature and shows a more well defined grain structure. 600U16 was essentially unchanged with reference to the lower temperature treatments.

Figure 4.2(a) shows the effect, on hardness, of plasma nitriding at 450°C. A maximum surface hardness is apparent after 16hrs while the core hardness is essentially unchanged at all of the times shown. In general, the fully hardened condition has responded best to surface hardening and showed the least variance in core hardness for this treatment temperature.

At 550°C, surface hardness has developed more quickly [Figure 4.2(b)] and achieved a maximum value after a 4hr treatment. Longer times are seen to effect both case and core softening at this temperature. However hardness after 16hrs was lower than it was after 64hrs (an unreasonable result) and this is quite inconsistent with the trend seen for 450°C treatments. This anomaly, as already stated, is due to temperature fluctuation (in effect higher than set temperature was experienced by the samples) at the end of the treatment and has resulted in undue softening of the core structures.

Figure 4.2(c) shows the hardening response for 16hr treatments at various plasma nitriding temperatures. Again the maximum surface hardening effect is shown to occur at about 450°C. This is a confirmation of conclusions drawn by previous workers[54,77,78].

Core hardness is reduced sharply by treatments in excess of 500°C. This is to be expected since higher temperatures at this time would facilitate alloy element diffusion and consequent carbide growth, leading to an overageing effect in the core material. Similarly, surface hardness would be affected by growth of the nucleated nitrides in the diffusion case, but to a much lesser degree than for carbide growth in the core - alloy elements in solution would already be depleted in the case by the initial nucleation and precipitation of the alloy nitrides.

The undertempered condition has been ineffective in delaying core softening at this treatment time except at 600°C where some benefit in core hardness has resulted.

In general, underhardening and undertempering have offered no benefit to surface hardening at any treatment temperature. However underhardening does offer a much tougher core without too much detriment to the surface hardenability offered by plasma nitriding.

Figure 4.2(d) records the effect of nitriding temperature on hardness for 4hr treatments. Confirmation of maximum surface hardening being achieved at approximately 500°C, for this treatment time, is shown as is the less severe decline in core hardness as treatment temperature is elevated.

The relationship of case development to nitriding time is well known for most nitriding processes. This relationship for plasma nitriding is shown in Figure 4.2(e) for two different treatment temperatures. As can be seen, a linear response exists implying a parabolic relationship with case depth proportional to the square root of the treatment time. As reported:

$$CD = -21 + 38.6\sqrt{t} \qquad \ldots\ldots(4.1)$$

for treatments at 450°C, and:

$$CD = -33.2 + 60.8\sqrt{t} \qquad \ldots\ldots(5.1)$$

for treatments at 550°C.

Both of these relationships imply an incubation period for case development of approximately 18 minutes. This is not completely understood since one might expect a higher temperature treatment to initiate more quickly. It is possibly due to the high degree of sputtering which occurs in the initial stages of the process.

Sputtered material in the first part of nitriding would contain a high proportion of surface oxide and would therefore yield less FeN to back diffuse and adsorb onto the workpiece surface. The nitrogen potential would therefore build up more gradually at the surface as suggested by Rozendaal et al[76] and not immediately as propounded by Edenhofer[49].

Figure 4.2(f) demonstrates the development of case depth as a function of plasma nitriding temperature for two treatment times. The relationship has been represented by curves. However, regression analysis of the data presented indicates that a reasonable degree of linearity exists in the relationship. For 16hr treatments:

$$CD = -332.1 + 1.061(T) \quad \ldots\ldots(5.2)$$

where C_D is case depth in μm and T is the plasma nitriding temperature in °C. The correlation coefficient (r) is 0.892 and this relationship must therefore be regarded as only tentative. For 4hr treatments:

$$CD = -439.3 + 1.065(T) \quad \ldots\ldots(5.3)$$

Correlation of data to the equation here is r = 0.917 ie. a slightly better correlation than for the 16hr data, but the relationship must still be regarded with suspicion until confirmed or denied by further experimentation.

Equations 5.2 and 5.3 predict threshold temperatures of approximately 313°C and 413°C respectively for case development at the stated times ie. at about 320°C, at least 16hrs at temperature would be necessary to initiate case development.

This is not an unreasonable time since this threshold is approximately the lowest conceivable temperature at which plasma nitriding is possible. Similarly, at about 400°C at least 4hrs at the nitriding temperature would be necessary to effect case development. This is to be expected since a higher temperature treatment would be needed to initiate case development more quickly.

These equations give greater errors of prediction at lower temperatures and this could again be a manifestation of the sputtering effect prevalent in the early stages of treatment and/or the lower power plasma, used for low temperature processing, giving a smaller amount of sputtering due to the inherently lower energy of impacting ions.

Both of these features can be controlled to some extent by treatment pressure in that a higher chamber pressure increases the tendency for back diffusion of sputtered material from the plasma to the workpiece. Conversely, low pressure enhances sputtering and surface cleaning.

5.2.2. Effect of Treatment Atmosphere Nitrogen Content

The M50 and T1 steels were plasma nitrided after examination of the tests carried out on M2, and in consideration of the results collated were treated for 16hrs at 450°C. In order to achieve different properties and case depth, the treatment atmosphere was varied for this series of tests.

Both steels exhibit similar case hardness profiles when treated in a 75%H_2/25%N_2 atmosphere [Figure 4.1(m)]. Surface hardening was not drastically improved and the core hardness was unaffected by this treatment. Examination of the surface hardnesses in Table 4.2 and the profiles of

Figure 4.1(m) show that case hardness peaks not at the surface but just below it on both steels.

Figures 4.3(i) and (j) show the case structures 450M16(25) and 450T16(25) relevant to this treatment. No surface compound layer was apparent on either steel but 450M16(25) had a very marked presence of intergranular nitride/carbonitride within the diffusion layer and close to the case/core interface. 450T16(25) also shows intergranular penetration but it is not as readily identifiable due to the high incidence of primary and secondary hardening carbides within the structure. An inner dark band, corresponding to an observed plateau in the case hardness profile of 450T16(25), was also apparent in Figure 4.3(j) at the etch case/core interface.

The T1 steel from 450T16(15) exhibited a sharper hardness gradient at the surface than in the equivalent M50 steel [Figure 4.1(n)]. The M50 steel from 450M16(15) had a pronounced hardness plateau extending over a large part of the effective case depth. Surface hardness has benefitted greatly from treatment in this 'leaner' plasma atmosphere (ie. 15%N_2) - T1 gaining the most improvement.

Figure 4.3(i) 450M16(15) shows a lower preponderance of intergranular nitride than in 450M16(25). There was no surface compound layer but there was evidence of some surface cracking. 450T16(15), Figure 4.3(j) shows a thinner etch case with no evidence of intergranular nitride or surface compound layer, but slight surface cracking is apparent.

Similar case profiles were shown by both steels for the lean atmosphere (5%N_2) as can be seen from Figure 4.1(o). Surface hardening benefits here were only marginally less than for the 85%H_2/15%N_2 treatment atmosphere but surface spalling was much worse - Figures 4.3(i) and (j). There was intergranular nitride within the case of 450M16(5) but it was spread throughout the case and was not concentrated near the case/core interface as it was in the other treatments. The T1 steel of 450T16(5) showed no real evidence of intergranular penetration but closer examination using the scanning electron microscope revealed a substantial presence of intergranular nitride developing close to the case/core interface [Figure 4.4(f)].

Figure 4.2(g) shows the effect of treatment atmosphere nitrogen content on the case and core hardness of M50 and T1. Maximum surface hardness was achieved on both steels at 15%N_2 and an optimum is implied for approximately 10 to 12%N_2 in the treatment atmosphere. Core hardness was practically unchanged for this treatment temperature and time.

The relationship of case development to treatment atmosphere is shown in Figure 4.2(h). M50 has clearly developed a heavier case for all nitrogen contents in the treatment atmosphere and appears to follow a logarithmic rule such as:

$$CD = 139.6 + 45.3Ln(\%N_2) \qquad .....(5.4)$$

Regression analysis of the data yields a coefficient (r) of 0.983 indicating that the data follows the predicted trend quite well. However there are not enough data points to be sure of the validity of this equation. The T1 steel developed smaller cases but not as predictably as the M50.

5.3. Contact Stress and Case-Cracking Tendency

Use of steels or any other material in high load-bearing applications, such as roller bearings in aero engines, places an onerous task on the working surfaces of the component, since this is where most of the load is carried. Consequently fatigue failure occurs predominantly at the surface. High speed steels are often used in these cases since they have been shown to have high hardness and fatigue strength. There is some argument about whether or not a high core hardness is desirable since this could improve 'case crushing' resistance. However in the case of tool steels, where the hardness difference between case and core rarely exceeds 150Hv, it is usual to treat to achieve maximum hardness and wear resistance at the expense of core toughness to obtain maximum surface fatigue strength.

The test carried out was primarily seen as a grading exercise since it makes no account of the complex stress system pertaining to the rolling bearing situation ie. centrifugal forces are not considered and since this was a static test, the effects of the alternating orthogonal shear stress in assisting surface spalling could not be studied other than by predicting its magnitude relevant to the contact loading. Nevertheless, an indication is given of the ability of a plasma nitrided case to withstand load without cracking.

5.3.1. M2 - The Effect of Treatment Temperature and Time

Figure 4.6(b) shows the stress to cause case cracking with respect to core strength. The maximum stress withstood prior to case cracking apparently depends upon a minimum core hardness of approximately 850 - 900Hv and exceeding this hardness is detrimental to case cracking resistance.

An optimum hardness condition for contact stress resistance of other steels has been reported before[103,104] but it is generally thought that rolling contact fatigue life should increase progressively with hardness[105].

A group of results is shown, primarily for underhardened treatments, which do not conform to the general trend of the graph. The underhardened samples in this group all have case depth less than 170μm, but the undertempered and fully hardened specimens have very heavy cases. There is therefore no common factor, with respect to case depth, for these 'anomalous' results; nor is surface hardness a controlling factor.

It is important to note that, the data presented here has been derived from calculations based on the general assumptions, made by Hertz[12], of elastic conditions prevailing. However, loads measured for first cracking of the case during testing are in excess of that necessary to cause yielding in compression.

With a compressive yield stress of approximately 2.8GPa, plastic flow will be manifest on the surface at a contact stress of about 4.2GPa - indicating that all of the tests completed here would show substantial plastic flow. Additionally, the ball bearing indentor would also deform considerably at the loads measured. In fact some of the tests resulted in ball bearing failure. Due to plastic deformation of the ball and test piece, contact surface areas would be different to those calculated and would result in lower than predicted contact stresses.

The harder core materials would deform to a lesser degree and would thus be experiencing a contact stress closer to the values predicted here. No correction for this error has been made here but it is expected that with suitable mathematical analysis a trend relating case depth, hardness and contact stress might become more apparent. In the interim however, Table 4.4 describes the load to first cracking of the case and this value is quite independent of the problems of plastic flow in the tested materials.

Figure 4.6(c) shows the effect of increasing plasma nitriding temperature on contact stress necessary to cause case cracking. For the fully hardened and tempered condition an increase in treatment temperature has detracted from performance and lower temperature treatments have yielded the higher stress to first crack results. Steels in the underhardened condition benefit by an increase in treatment temperature - probably due to the gradually developing core hardness at higher temperatures. The fully hardened steel data follows a relatively linear trend and regression analysis predicts:

$$\sigma_H = 22.3 - 0.025(T) \qquad \ldots\ldots(5.5)$$

where σ_H is the contact (or Hertz) stress in GPa and T is the plasma nitriding temperature in °C. The correlation coefficient (r) is -0.89 which indicates a reasonable degree of conformity of the data to the predicted trend.

5.3.2. T1 & M50 - The Effect of Nitriding Atmosphere

Figure 4.6(d) shows the contact stress as a function of nitrogen content in the nitriding atmosphere. It is difficult to draw any real conclusions from the presented data. However, the specimens treated in the low nitrogen

potential atmosphere (5%N_2) have performed better in this test. This was not a direct result of core hardness since all of the treatments tested had similar core hardness values. The low nitrogen atmospheres do give thinner cases and high surface hardness. The contact stresses calculated for these steels are generally higher than those quoted for M2 and the limitations of the accuracy of the data apply here also.

Rolling contact fatigue tests carried out by other workers[4,106-9] have been carried out on various test rigs at Hertzian stress levels varying from 4.17 to 5.88GPa. These stresses are close to the threshold to cause surface plastic deformation. Case cracking in the current work has been seen to occur at stresses higher than those used in other work and far in excess of the stress experienced by rolling bearings in the current range of jet engines - Day[107] in his work states that a stress of 4.5GPa is approximately 2.5 times that normally experienced in service. It is suggested therefore that failure of plasma nitrided rolling bearing elements by case cracking or spalling would be less of a problem than is currently anticipated.

Current bearing design criteria specify that case hardened components need case depths at least three times the depth to maximum shear stress. This implies, for example in Day's work[107], that a minimum case depth of 228 μm would be necessary to exceed safely the depth to maximum shear stress developed by normal service conditions. Work carried out by Cotterill[110] indicates that this safety factor is over conservative when applied to the hard tool steels.

The current work has resulted in case failure at loads where, in the majority of cases, the depth to maximum shear stress is greater than the case depth. The load to cause cracking was still far in excess of those normally experienced by engine bearings. It is suggested therefore that a more reasonable case depth criterion might be 1.5 times the depth to maximum shear stress when applied to the tool steels used in bearing manufacture. This would correspond to a case depth of about 115μm for normal service conditions and this depth is well within the capabilties of a 450°Cx16hrs plasma nitriding treatment for all three of the steels examined here.

It was planned to supplement the currently completed tests on M50 and T1 by cone and ball roll contact fatigue tests, at Rolls-Royce, on the best treatment option determined from this work. This would correspond to a treatment of 16hrs duration at 450°C in a plasma nitriding atmosphere of 85 - 90%H_2/10 - 15%N_2 and controlled at 4torr chamber pressure.

With this in mind, considerable modifications were made to the plasma nitriding unit. The gas flow control system was replaced with fine needle valve flow meters and a mixing chamber for gas supply to the treatment chamber. This modification eliminated a problem, experienced in the early work carried out on the M2 steel, of gas pressure fluctuation due to back pressure in the individual gas supply lines. Resistance heating elements were also fitted to the chamber heat shield to facilitate more precise temperature control. This was seen to be a problem in that pressure fluctuations could radically alter the heat input to the workpiece.

By use of resistance heating it was not necessary to apply full power to the plasma to achieve higher treatment temperatures. This is a prime necessity for the treatment of other materials such as titanium and its alloys. Without resistance heating an increase in chamber pressure is necessary to gain the required heat input to the workpiece to achieve high temperatures. A consequence of separate resistance heating was that lower pressures were feasible during treatment without temperature instability. Also lower pressure/power plasmas enabled greater control over surface compound layer formation.

These modifications were carried out before work on the M50 and T1 steels was started and indications are that surface white layer formation has been suppressed to insignificant levels.

5.4. Residual Stress - Its Trends and Effects

Residual stress may be harmful or beneficial, and fatigue resistance is thought to be highly influenced by it. Residual compressive stress at the surface of an object is widely thought to confer good fatigue resistance[94], the opposite being true for tensile residual stresses. Rolling contact fatigue is also thought to benefit from the presence of compressive residual stress.

5.4.1. M2 - Treatment Time and Temperature Effects

On examination of Figure 4.7(a) it is apparent that, in the hardened and tempered condition, these steels have tensile surface residual stresses present. This was expected and a simple 'though inaccurate calculation (shown later) can be carried out to predict this.

The graph shows a general trend which predicts maximum residual stress to be produced by plasma nitriding at 450°C to 500°C. Surface hardening is also seen to be maximum at 450°C [Figures 4.2(a) and (c)]. This implies an optimum temperature to produce maximum surface compressive residual stress - a not unexpected result since higher temperatures would result in considerable stress relief for the treatment times used. Mittemeijer[111] has previously reported that a linear relationship exists between hardness and average microstrain during case hardening but shows no such correlation with respect to macrostrain. Although microstrain has not been investigated in the present work, the effect of hardness on macrostrain does not show a linear correlation and this is in agreement with Mittemeijer's findings.

The time at temperature during nitriding is also of importance since longer treatments yield lower values of compressive residual stress while shorter times give correspondingly higher stresses. This confirms work done by Rozedaal et al[76] who assert that there is an optimum treatment time to develop maximum compressive residual stresses and propose an equation to predict the stress and indirectly the time:

$$\sigma_s = \frac{\beta . E}{1 - \nu} (\bar{C} - C_s) \qquad \ldots\ldots(5.6)$$

where σ_s = surface residual stress

β = Vegards constant

$\bar{C}$ = average nitrogen concentration of the specimen

C_s = surface nitrogen concentration.

Prolonged nitriding then leads to a decrease in the magnitude of the surface compressive residual stresses. Mittemeijer[111] explains that initially microstresses increase as the surface layers are saturated with nitrogen to form precipitates and then decrease as precipitated particles coarsen and grow at extended times. This would correspond to the situation of coherency strains declining as a particle grows and gradually loses coherency with the matrix lattice structure.

The core of a treated component also undergoes structural degradation, during extended plasma nitriding, as carbon is rejected from solution to either facilitate further carbide precipitation or more likely carbide growth. This then would also contribute to the decline of the residual stress system towards equilibrium.

It is noted that stresses at the surface are much larger than those immediately below the surface (after electropolishing) - (Table 4.5). The first tests carried out showed much higher stresses than those reported here. Stresses up to -1500MPa were recorded but the reliability of peak location was so low that these results have been discounted for the purpose of this work.

The fatigue specimens showed stresses much nearer to the electropolished values of the residual stress samples. This could be due to the fatigue specimens being plasma nitrided after the resistance heating was fitted and the gas flow system was modified on the plasma nitriding unit. Metallographic examination of some of the tested fatigue samples showed a markedly reduced presence of surface intermetallic compound layer, - residual stress is likely to be larger in the compound layer than in the diffusion zone due to the greater degree of lattice misfit with the original ferrite matrix. According to Rozendaal et al[63] the sign of the stress at the immediate surface may even change from negative to positive in thick layers.

Figure 4.7(b) shows peak residual stress to occur at a case depth of approximately 130 - 150 μm and the larger case depths are clearly much less compressive in nature and may eventually become tensile[111]. These deeper cases are formed at extended treatment times and/or high treatment temperatures.

5.4.2. T1 & M50 - Effects of the Nitriding Atmosphere

Figure 4.7(c) shows the effect of plasma nitrogen potential on the surface residual stress of M50 and T1. M50 displayed its maximum stress over a range of atmosphere concentration

and T1 has a lower level of stress present. Both have larger compressive stresses than in M2 after an equivalent plasma treatment. There is not enough data to clarify the situation pertaining to these steels. However, maximum stresses have been produced, for 450°Cx16hr treatments, at approximately 12 - 15%N_2 for M50 and 8 - 10%N_2 for the T1 steel.

As with M2 there appears to be an optimum case depth at which maximum surface compressive residual stress is generated and cases greater than this sharply reduce the magnitude of the stress present. For M50 this case depth approximates to 250 - 270μm and for T1 it is about 140 μm. This result cannot be taken as a real effect without much additional work to verify the current work.

It has already been stated (section 2.9) that on hardening a steel like M2 one might reasonably expect a net volume expansion of 2.75%. Assuming full transformation to martensite and ignoring the tetragonality of the martensitic structure (this will only result in an error of about 5%), then if the lattice parameter a = 2.866Å (Cullity[87]) and Δa is the increase in the lattice parameter due to hardening then

$$0.0275 = (a + \Delta a)^3 - a^3 \qquad \text{.....(5.7)}$$
$$= 3a^2\Delta a + 3a\Delta a^2 + \Delta a^3$$

Now, assuming that Δa is very small with respect to 'a' then Δa^2 and $\Delta a^3 \ll a$ and may be discounted for simplicity. Thus

$$\Delta a = 1.116 * 10^{-3} \text{ Å}$$

Lattice strain $\varepsilon = \Delta a/a$ and the consequent stress is related to ε by:

$$\sigma_y = \varepsilon_y . E \qquad \ldots\ldots(2.48)$$

So that the stress due to hardening would be approximately +80MPa. Tempering at low temperature would only reduce this by a very small amount, say up to 5MPa.

This value is clearly much smaller than that reported in Table 4.5 but the general manner in which the stress is generated is shown. The calculation is a gross oversimplification of the real situation and this is the cause of the dissimilarity between the measured and calculated values for hardened and tempered residual stress.

Reference to the work of Ericsson[112] on the prediction of stresses in case carburised steels gives an indication of the complexity of the subject and shows the necessity for quite involved computer analysis to derive reasonable values of stress in case hardening situations.

Residual stress is algebraically additive to the stress system prevailing in a situation eg. rolling contact or bending fatigue. It can therefore have a profound effect upon the material response to a particular stress system.

Consider a rolling contact situation between a ball of radius 6.25mm and a flat plate. Assuming both elements to have the same elastic modulus E = 207GPa and Poisson ratio $\nu = 0.29$, a circular contact area will be formed and application of the equations in section 2.2.1 will yield a contact radius - a = b = 0.366mm and a contact pressure of 4.21GPa.

(The calculation is shown in Appendix 1). Also the maximum shear stress τ_{max} = 0.689GPa and the depth to maximum shear z_1 = 171μm.

At the surface and in the centre of the circular contact area $\sigma_x = \sigma_y = -0.79\sigma_{max}$ and $\sigma_z = -\sigma_{max}$ (equations 2.13 to 15, section 2.2.2).

$$\tau_{max} = \frac{1}{2}(\sigma_z - \sigma_y) \qquad \text{.....(2.16)}$$

ie. $$\tau_{max} = \frac{1}{2}(-\sigma_{max} + 0.79\sigma_{max})$$

and so $$\tau_{max} = -0.442\text{GPa}$$

Now if compressive residual stress prevails in and parallel to the surface, τ_{max} will be reduced in magnitude since σ_y will increase in size. A similar situation will exist at all depths below the contact surface where residual stress is compressive in nature. In a case hardened component the compressive stress at the surface generally declines with depth and therefore its beneficial influence on shear stress will also decline. Near the case/core interface this stress may well become tensile and could serve to exacerbate the shear stress. It is partly for this reason that the established criterion of producing a case depth three times the depth to maximum shear stress still prevails in the bearing and aerospace industries for rolling bearing applications.

The situation in bending fatigue can be treated in a similar manner. Compressive surface residual stress reduces the effective tensile stress generated at the surface of the specimen by the prevailing stress system as discussed in section 2.10.2 and shown by Fig. 2.29.

5.5. Surface Intermetallic Compound - White Layer

As reported in section 4.6, detailed surface phase analysis has not been studied. However, Table 4.7 shows the results of the tests used to detect the presence of white layer. As can be seen short treatment times do not yield a white layer at any of the plasma nitriding temperatures used in this work whereas longer times do. It is also noted that the longest treatment times used on the M2 steels do not radically increase the layer thickness beyond that for a 16hr treatment time and white layer thickness overall is less than might be expected from an equivalent gaseous nitriding process.

The 16hr treatment at 500°C on M2 gave an anomalous result in that only traces of white layer were found to be present. This was unexpected and does not fit the general trend of white layer formation ie. $CD \propto \sqrt{t}$, followed by the other treatments. The reason for this anomaly has already been discussed in section 5.2.1.

The x-ray diffraction results corresponded reasonably well with the observations made by metallography. The tests carried out on M50 and T1 produced diffraction traces which were inconclusive for phase analysis ie. not enough peaks were found to make phase identification definite. This may have been due to the use of chromium radiation on these steels to restrict the data gathered in analysis to the very surface regions of the specimens, whereas the M2 steels were examined using molybdenum radiation which penetrates to a much greater depth. However, metallography failed to identify the presence of surface white layer on any of the M50 or T1 samples either. This was unexpected.

This could point more to the success of using lower power plasmas in restricting white layer formation rather than the originally conceived idea of restricting layer formation by lowering the nitriding potential of the treatment atmosphere.

The cupric ammonium chloride test proved, in most cases, to be in reasonable agreement with the metallography and x-ray diffraction tests and without doubt is a very fast and simple test to perform. Also, by weakening the solution (by adding ethyl alcohol) to approximately 1% solution, one can use the mixture as an etchant for ferrous microspecimens. Intermetallic compound layer within a structure is not attacked and shows up white whereas the main matrix is covered by a deposit of copper. This is not a precise technique and requires much trial and error to get the solution strength, etching time and technique just right for the steel under examination.

5.6. Unidirectional Bending Fatigue

It is well established that most fatigue failures originate at the surface of the specimen and there are several important reasons why this should be so.

1. Slip occurs more easily at the surface than within grains.
2. The operating environment is in contact with the surface, and
3. Specimen misalignment gives larger stresses at the surface than within.

It is apparent then that any alteration of the surface properties will affect fatigue performance either adversely or beneficially. So, thermochemical heat treatments such as nitriding and carburising, which confer compressive surface residual stresses on a treated component, should be beneficial to fatigue resistance.

5.6.1. M2 - Treatment Temperature and Case Depth Effects

Plasma nitriding is beneficial to the fatigue strength of treated M2. This is apparent from consideration of Figures 4.8(a) and (b) where the hardened and tempered strength is improved by up to three times by nitriding for 16hrs at 400°C. Figure 4.5(a) shows the fracture surface of one of the bending fatigue specimens after testing. The photo-macrograph (b) shows a quite tough fracture for the initial stages of failure (the top of the photograph) which changes to a more brittle mode of fracture at approximately half the specimen thickness. Failure has initiated on the tension side of the specimen and initially exhibits a ductile failure mode as shown by the SEM micrograph (c).

The structure, although basically intergranular also shows the 'cup and cone' feature characteristic of ductile failure. This ductile characteristic is evidence of plastic deformation prior to fracture, but is only a tiny proportion of the complete fracture surface and is not indicative of the rapid propagation of the fracture through the structure.

Near to the centre of the sample - (a), the fracture surface shows little evidence of ductile fracture. The structure is almost completely intergranular with cleaved carbides embedded in the matrix. A large crack is also seen propagating through the structure and the carbide is decohered from the matrix where the crack has passed around its periphery.

It is probable that failure has initiated not at the surface but at some depth close to the case/core interface where the residual stress, conferred by the plasma nitriding treatment, has become tensile in nature as proposed by several researchers[97,111]. This would almost certainly be the case if the yield stress of the core material has been exceeded[90]. Since the mean stress at failure for this treatment is already close to the yield stress of the material, additional tensile residual stress at the case/core interface could cause plastic deformation to occur as confirmed by Figure 4.5(a) - micrograph (c).

Higher temperature plasma treatments give up to twice the fatigue strength of the fully hardened and tempered condition for the steel, as shown by Figure 4.8(a). This is also implied by Figure 4.8(b) where the larger case depths are indicative of the higher nitriding temperatures used to produce them.

This graph indicates an optimum case depth to produce maximum fatigue strength in plasma nitrided M2. This trend has been reported before by Harris[113] and by Frith[114], who showed quite thin cases of about 75μm thickness to maximise fatigue strength in rotating bend fatigue testing of 3%Cr-Mo steel. However this trend towards optimum case depth for maximum improvement in fatigue strength makes no account of the change in case and core hardness.

Several workers[46,90,97] have found that an increase in the ratio of case depth to core thickness also increases the fatigue strength and the relationship tends to be linear in nature. Also it has been noted[105] that increasing the surface hardness gives an increase in fatigue strength. In high load fatigue situations the core strength is also paramount to performance since crack nucleation is most likely to occur subcutaeneously in case hardened steels and stronger core material would therefore resist fatigue crack nucleation more effectively.

So, the effect of case depth on fatigue strength for plasma nitrided M2 steel cannot be fully assessed from the present work since other variables are also operative in the results obtained. This precludes the use of the results to test the relationship proposed by Bell and Loh[97], of the fatigue limit being a function of the case/core thickness ratio (equation 2.67 in section 2.10.2).

It should be noted that the best treatment has neither maximum compressive residual stress, case depth or case and core hardness and it might be inferred therefore that an optimum value does exist for these parameters.

The treatments 450F16 and 500F16 have similar case depths and core hardnesses and give similar fatigue strengths, but their case hardnesses are quite different. The possibility arises then, that surface hardness is less important in this instance, than either the case depth or the core strength in controlling the fatigue response of the treated material.

For 550F16 both case and core hardness have fallen substantially and the case depth is almost doubled, but the fatigue response is about the same as at 450°C and 500°C. The deeper case depth must be compensating for the deterioration in case and core hardness and therefore could be thought of as the dominant factor in fatigue response for these treatments.

Therefore when the case depth is small the hardness of both case and core are of greater importance and vice versa. The 400F16 treatment then, appears to be the best compromise between case depth, core and case hardness and gives the best improvement in fatigue strength over the hardened and tempered condition.

Figure 4.5(b) shows the difference in fracture structure as compared to the 400F16 treatment [Figure 4.5(a)]. The case, photomicrograph (a), is manifested by a change in fracture morphology between the surface and core structures and has a less granular appearance. The core material adjacent to the fracture initiation site (b) shows an intergranular type of failure with very small embedded carbides, some of which are cleaved and decohered from the matrix structure. The centre of the specimen (c) is essentially the same fracture structure but also has larger primary carbides which have again cleaved and partially decohered from the matrix.

5.6.2. T1 and M50 - Atmosphere and Case Depth Effects

Figure 4.8(c) shows the improvement in fatigue strength to be gained by plasma nitriding M50 and T1 in atmospheres containing greater proportions of nitrogen. The fatigue improvements are markedly smaller for these steels than those for M2. This is not unexpected because these steels have undergone a more sophisticated processing route in their manufacture. The M2 steel was normal air melt quality and stood to gain more from plasma nitriding. The T1 and M50 steels were EFR and VIM-VAR steels respectively and have a much cleaner and refined structure with low carbide segregation. Improvements in fatigue strength, of 15 to 20% for M50 and up to 30% for T1, have been achieved by plasma nitriding these steels.

Figure 4.8(d) indicates a threshold case depth for both steels, to achieve a marked improvement in fatigue performance. The core hardness of M50 was essentially constant for all of the treatments and has therefore not exerted undue influence on the results shown. T1 core hardness did show some variation and may have had a small effect on the results.

Where the T1 was hardest the fatigue response has been unchanged from that of the hardened and tempered condition. The best response has occurred at a core hardness which is about the same as that in the hardened and tempered samples. This might imply an optimum core hardness, as suggested by Garwood et al[115].

More importantly, the best response on both steels has resulted from a treatment which did not give maximum surface hardening.

Therefore it is proposed that: (1) the surface hardness is of less importance to the fatigue response of the plasma nitrided steel than is the core hardness and, (2) the case depth is a dominant factor in the material response after plasma nitriding.

As with M2, it could be said that where case depth is small the hardness of the material becomes an important factor - particularly the core hardness. So, as long as the case gives a moderate strength improvement and is not softer than the core material (as might occur with an improperly carried out treatment), fatigue response should benefit from case hardening.

These steels have not really benefitted from the high residual stresses generated within the case. The best fatigue improvements have come from a plasma treatment which has produced a lower level of residual stress [Figure 4.7(a)]. The stresses present here are similar to those produced in M2 steel after 450°C to 500°C treatments.

The fracture surface of 450M16(25) is shown in Figure 4.5(c). A fairly tough fracture is apparent for the early stage of failure - the bottom right corner of photo-macrograph (b). Initiation of the fracture is shown to be from a surface 'thumbnail type' defect on the tension side of the fatigue specimen - (d) and has the characteristics of a cleavage type of fracture. The core of the specimen (c) shows primary carbide and an intergranular fracture structure with regions of cleavage failure. There is little, if any, evidence of secondary hardening carbide within this structure.

The end of failure - (a), shows a distinct difference between case and core fractures with a crack at the boundary between the two. The case has a cleavage appearance and the location of the crack approximates to the depth at which intergranular nitride/carbonitride, widely recognised as a detrimental feature of the nitriding process, was noted in the microstructure [Figure 4.3(i)]. It is evident that although surface compound layer formation has been effectively suppressed , intergranular nitride formation is a problem not as easily overcome.

Figure 4.5(d) shows the T1 fatigue fracture from 450T16(25). Again a tough fracture is apparent during the initial stages of failure - top left of macrograph (b). Initiation is seen to be from two adjacent sites on the surface of the sample, (a), and both have the appearance of cleavage failure which has propagated to the case/core interface and changed fracture mode. Close to the initiation sites and within the core material the fracture is seen to be intergranular in nature. Cleaved primary carbides and smaller secondary hardening carbides are also apparent.

The fracture surface of 450M16(15) is shown in Figure 4.5(e). The initial stage of fracture looks less tough than in the other fracture surfaces - (b). Adjacent to the fracture initiation the structure is intergranular. It is difficult to ascertain whether fracture has initiated at the surface or subcutaeneously. As in the other specimens, the end of failure is characterised by a dramatic change in fracture structure between case and core bounded by a crack - micrographs (a) and (c), and again the location of the crack is approximately the location of intergranular nitride/carbonitride.

450T16(15) is shown in Figure 4.5(f) and has similar characteristics to the other fracture surfaces. Surface initiation was not apparent on this specimen and the notch adjacent to the initiation site - micrograph (d), is thought to be damage incurred as the specimen impacted with the upper jig of the test rig. The difference in fracture structure between case and core at the end of failure is more apparent here - (c) and (a), and is again bounded by a crack at the interface.

It is thought that the samples treated in the higher N_2 potential plasma display a tendency towards surface initiation of the fatigue fracture and lower potential atmospheres cause a tendency towards subsurface failure. This might be supported by consideration of the residual stress levels and the hardnesses produced by each heat treatment.

The treatment providing the better fatigue response has the lower compressive residual stress, a deeper case and lower surface hardness. The case/core interface, where subsurface crack initiation might reasonably be expected to occur, would experience a lower degree of tensile stress due to the loading situation since it is effectively closer to the neutral axis of the test bar. Also the smaller residual stress inherent in the deeper cases would have a smaller resultant tensile stress acting in the core adjacent to the case/core interface. Thus subsurface yielding and microvoid formation would be less likely to occur at structural discontinuities such as the interface between carbide inclusion and matrix, or the interface between harder case and softer core.

Conversely the higher stresses associated with the smaller case depths produced by low potential atmospheres, would serve to exacerbate the problem at the case/core interface. The tensile stress felt at the interface of a small case would be higher due to its location relative to the neutral axis and the balancing tensile residual stress acting within the core would also be larger. Yielding within the core material in the vicinity of the case/core boundary might therefore be more likely and a tendency towards subsurface failure would prevail.

6. Conclusions

6.1. Plasma Nitriding Characteristic of M2

6.1.1. Pre-Treatment of The Steel

In general underhardening has resulted in substantial loss of core strength for all of the plasma nitriding conditions studied here. Undertempering has not resulted in material response radically different to that of the fully hardened and tempered condition. There is, therefore, no real advantage to altering the hardening and tempering conditions from those already in common use where a plasma nitriding treatment is under consideration. Underhardening does offer benefits if a softer core is necessary and plasma nitriding for 64 hours at 450°C gives both maximum surface hardening and a tough core.

6.1.2. The Effect of Treatment Temperature.

The undertempered and underhardened conditions both show core strengthening for increasing plasma nitriding temperatures up to 500°C whereas the fully hardened and tempered condition has unchanged core hardness up to 550°C. Surface hardening has been shown to reach a maximum at 450°C as reported by previous researchers studying other steel types[54,77,78], and does not depend upon either prior hardened and tempered condition or the steel type being treated.

Case development varies in a linear manner as a function of treatment temperature according to the relationship:

$$CD = a + b(T)$$

where a and b are constants and depend upon treatment time and steel type. T is in °C.

For 4hr and 16hr treatments, at least 313°C and 413°C respectively are necessary to initiate case development on M2.

Surface compound layer formation increases with increasing treatment temperature up to approximately 550°C. The degree of intergranular nitride penetration has not been radically affected by treatment temperature.

6.1.3. The Effect of Treatment Time

Core hardness of undertempered and underhardened steel both benefit by plasma nitriding for up to 64 hours at 450°C. A treatment time of 16 hours gives maximum core hardness at this temperature. The fully hardened and tempered core hardness is unaffected by treatment times up to 64 hours at 450°C. Undertempered and underhardened steels achieve maximum surface hardness after 64 hours at 450°C and fully hardened and tempered steel gains maximum hardness after 16 hours.

Maximum surface hardness at the higher temperature of 550°C is achieved after 4 hours but is not as high as that achieved by the 450°C treatment probably due to growth of the precipitates as suggested by Robino and Inal[78].

Case depth varies as a function of treatment time according to the equation:

$$CD = a + b\sqrt{t}$$

where a and b are constants dependent upon treatment temperature and steel type. t is measured in hours.
An incubation period is indicated (by equations 4.1 and 5.1) for case development and this is probably due to a gradual

build up of the nitrogen potential at the metal surface prior to case development - the mechanism reported by Rozendaal et al[76].

Surface compound layer increases with treatment time. A threshold thickness of about 11 μm on M2, beyond which surface layer has not grown, was achieved by a 16 hour treatment.

6.2. Plasma Nitriding Characteristic of M50 & T1

6.2.1. Effect of Treatment Atmosphere

Core hardness has been unaffected by changing the nitrogen content of the treatment atmosphere and M50 is softer than T1 for all treatment atmospheres examined. Surface hardness achieves a maximum in an atmosphere containing approximately 10-15% nitrogen for both steels. T1 develops a greater surface hardness than does M50 for all of the atmospheres examined.

Case development follows a logarithmic rule such that:

$$CD = a + b \ln(\%N_2)$$

where a and b are constants dependent upon the material.

Surface compound layer formation has been suppressed by all of the plasma atmospheres studied. This is not in agreement with the general findings of Staines and Bell[74] who suggest a threshold of about 10% nitrogen - giving suppression of white layer formation below 10% and probable layer formation above 10%. Use of a low power plasma for the nitriding of these steels has probably been instrumental in the inhibition of white layer formation on the metal surface. Intergranular penetration of nitride has not been eliminated and was observed in all of the samples microstructures. However the lower potential atmospheres did reduce the amount.

6.3. Contact Stress

Acoustic emission testing is an easily executed technique for surface crack detection, but careful analysis of the results obtained is necessary to detect the load at which cracking first occurs.

6.3.1. M2 - The Effect of Treatment Temperature

Low temperature plasma nitriding treatments give good case cracking resistance when applied to a fully hardened and tempered steel. Underhardened and tempered M2 benefits by higher treatment temperatures. A relationship is implied for Hertz stress as a function of treatment temperature so that:

$$\sigma_H = a - b(T)$$

where a and b are constants and depend upon prior heat treatment condition and plasma nitriding time. An optimum core hardness is indicated for best contact stress performance as reported previously[103,104].

6.3.2. M50 and T1 - The Effect of Plasma Nitrogen Content

Both M50 and T1 give superior contact stress performance when treated in lower nitrogen content atmosphere but this is at the expense of case depth. Surface hardness is maximum in the lower potential atmospheres, and so is surface residual stress.

6.3.3. The Loads Measured on all Three Steels.

The case cracking loads observed are all sufficient to cause plastic deformation of both test material and ball indentor. Predicted contact stresses are therefore higher than actually exist. Predicted stresses are nevertheless much higher than those operating in rolling bearings in service.

It is suggested that the current case depth criterion is overconservative for tool steels and should be reduced to 1.5 times the depth to maximum shear stress. Therefore, a plasma nitriding treatment of 16 hours at 450°C would be able to accommodate the case depth criterion on all of the steels tested.

6.4. Residual Stress

The largest residual stresses were measured in the M50 steel - the smallest in the M2 steel. The hardened and tempered condition in all of the steels have tensile stresses present.

6.4.1. M2

Maximum compressive residual stresses are produced in 450°C to 500°C treatments and shorter treatment times give larger stresses than longer times. Maximum residual stress corresponds to maximum surface hardening. Maximum stresses are produced in cases of approximately 140μm and decrease as case depth is increased.

6.4.2. M50 & T1

Maximum stress is produced in leaner plasma nitriding atmospheres and corresponds to smaller case depths and higher surface hardnesses. T1 shows an optimum case depth of 140μm to generate maximum surface compressive residual stress and this is similar to the optimum in M2. M50 steel has an optimum case depth of 260μm for the highest compressive residual stress.

6.4.3. The Effect Upon Contact Stress

Compressive surface residual stresses produced by case hardening treatments will be beneficial to contact stress in rolling contact fatigue. Maximum shear stress will be reduced by a surface compressive stress if it occurs within the case. Rolling contact will be adversely affected in heavier loading situations if the maximum shear stress occurs at a depth greater than the case depth where residual stresses may no longer be compressive.

6.5. Unidirectional Bending Fatigue Resistance

Mean fatigue strength is improved by plasma nitriding. Up to 300% improvement has been achieved on normal air melt M2. Only 20% to 30% improvement has been achieved for the EFR - T1 and VIM-VAR - M50 steels.

6.5.1. M2 - Temperature and Case Depth Effects

Lower temperature plasma nitriding treatments give better fatigue strength improvements on M2 where a compromise between case depth and case and core hardness has been achieved. Case depth is thought to be the dominant factor in fatigue strength improvement but for high-load high-cycle fatigue conditions core hardness gains in importance due to an increasing tendency towards subsurface initiation of the fatigue failure.

The failure in plasma nitrided M2 was brittle in nature and initiated where tensile external stresses prevailed. Thin cases are more likely to fail due to subsurface initiation of fatigue cracks whereas deeper cases would be likely to fail by surface initiation of the fatigue crack.

6.5.2. M50 & T1 - Plasma N_2 Content and Case Depth Effects

Best fatigue strength improvement has been achieved from samples treated in plasma nitriding atmospheres containing greater proportions of nitrogen. This corresponds to the occurrence of deeper case depths and confirms the suggestion that case depth is the dominant factor in controlling fatigue performance of case hardened steels.

As with M2, failure was by a brittle mechanism with the surface showing a cleavage type mechanism operating to the extent of the case. Failure of the samples with deeper cases has been from surface initiated fatigue cracks.

Best fatigue performance of these steels has not been from treatments giving the largest compressive residual stresses.

7. Recommendations

There is no hard and fast rule to determine the best treatment for these steels since the various properties studied are not optimised by one treatment or another.

A good compromise treatment for the M2 steel would be to treat for 16 to 20 hours at 450°C using a 75%hydrogen/25%nitrogen atmosphere controlled at 2 to 4 torr pressure.

The T1 and M50 steels should be treated for 16 to 20 hours at 450°C and pressure of 2 to 4 torr using an atmosphere of 85 to 90%hydrogen/10 to 15%nitrogen.

It is suggested that use of resistance heating is beneficial to plasma nitriding since the results obtained here imply an improved measure of control over the formation of surface intermetallic compound layer.

8. Future Work

It is apparent that case depth has a dominant effect on the fatigue properties of M2, and since this has not been studied effectively here, the effect of case depth for constant core hardness ought to be investigated ie. a series of case depths produced by treatment at different times for one temperature such as 450°C should be tested for fatigue performance. Additionally the benefit of a tough core should be examined by a similar set of tests on underhardened M2.

The contact stress experiments implied an optimum core hardness for best performance and this might be tested by treating the steel for constant case depth at different treatment temperatures. Since residual stress is of importance to both contact and bending fatigue, case depth effects for constant core hardness should be studied further with a closer look at the change in stress at different depths into the case.

The work on M50 and T1 was not very detailed due to both a lack of time and material to test. Therefore the work on the effect of nitrogen content of the treatment atmosphere should be consolidated to assess the reality of optimum nitrogen content to achieve maximum case hardness, residual stress and contact stress. Further the rolling contact fatigue tests intended for this work ought to be done using either the cone and ball test or the RC polymet fatigue tester. A reasonable starting point for these tests would be on materials plasma nitrided in approximately $12\%N_2/88\%H_2$ for 16 to 20 hours at 450°C.

An interesting possibility for control of layer formation on M50 and T1 has been the use of a lower power plasma due to an independent heat source. The effectiveness of this on layer formation could be examined by variation of power input to the resistance heating to obtain a fixed treatment temperature and for one or more treatment times under a constant treatment atmosphere of say 12% nitrogen/88% hydrogen.

9. Appendix 1

E	- Modulus of Elasticity
ν	- Poissons Ratio
a	- Semi-major Axis of a Contact Ellipse
b	- Semi-minor Axis of a Contact Ellipse
F_ρ	- Curvature Difference of Mating Surfaces of Revolution
Σ_ρ	- Curvature Sum of Mating Surfaces of Revolution
a^*	- Dimensionless Semi-major Axis
f	- Applied Force
σ_{max}	- Contact Stress (Hertzian Stress)
τ_0	- Orthogonal Subsurface Shear Stress
τ_1	- Subsurface Shear Stress
z_0	- Depth to Orthogonal Subsurface Shear Stress
z_1	- Depth to Subsurface Shear Stress

9.1. Calculation of Contact and Shear Stresses - and Depth of Shear Stress

As an example:-

Consider a steel ball, 12.5mm dia acting on a steel plate of semi-infinite thickness and with axially applied load of 120 kgf.

i. Surface Stress and Deformation Dimensions

a) to find semi-major and minor axes:

$$F_\rho = \underbrace{\left[\frac{1}{6.25} - \frac{1}{6.25}\right] + \left[\frac{1}{\infty} - \frac{1}{\infty}\right]}_{\Sigma_\rho} = 0$$

$$\Sigma_\rho = \frac{1}{6.25} + \frac{1}{6.25} + \frac{1}{\infty} + \frac{1}{\infty} = 0.32 mm^{-1}$$

From tables : using $F_\rho = 0$ then a^*, $b^* = 1$ (for circular contact) - from Tedric Harris : Rolling Bearing Analysis)

$$a = a^* \left[\frac{3f}{2\,\Sigma_\rho} \left(\frac{(1-\nu_1{}^2)}{E_1} + \frac{(1-\nu_2{}^2)}{E_2} \right) \right]^{1/3}$$

where $E_1 = E_2 = 2.1101 * 10^4$ kgf mm^{-2} (for steel)

$\nu_1 = \nu_2 = 0.29$ (for steel)

$\therefore$ $\underline{\underline{a = b = 0.366 \text{ mm}}}$

Assuming a flat contact : contact Area $= \pi r^2 = 0.42$ mm^2 (where $r = a$)

b) To find maximum contact stress

$$\sigma_{max} = \frac{3f}{2\pi ab} = \frac{3 * 120 \quad kgf}{2 * \pi * 0.366^2} = 427.72 \text{ kg mm}^{-2}$$

$$\underline{\sigma_{max} = 4.20 \text{ GPa}}$$

ii. Subsurface Stresses

a) To find maximum reversing shear stress and depth :

(from graphs in Tedric Harris : Rolling Bearing Analysis)

for b/a = 1 ; $^{2\tau_0}/_{\sigma_{max}} = 0.4282$

and $^{z_0}/_b = 0.3505$

since $\sigma_{max} = 4.20$ GPa

The Maximum Reversing Shear Stress, $\tau_{(0)max}$

$$\tau_{(0)max} = \frac{0.4282 * 4.20}{2} = \underline{0.90 \text{ GPa}}$$

and $z_0 = 0.3505 * 0.366 \text{ mm} = \underline{0.13 \text{ mm} = 0.005"}$

This is the depth to maximum reversing shear stress

b) To find maximum shear stress at centre of contact area

$a = b = 0.366$ mm and $\sigma_{max} = 4.20$ GPa

(from graphs in Tedric Harris : Rolling Bearing Analysis)

for b/a = 1 ; $^{2\tau_1}/_{\sigma_{max}} = 0.3235$

and $^{z_1}/_b = 0.4676$

$$\therefore \tau_{(1)max} = \frac{0.3235 * 4.20}{2} = \underline{0.68 \text{ GPa}}$$

and $z_1 = 0.4676 * 0.366 \text{ mm} = \underline{0.17 \text{ mm} = 0.007"}$

This is the depth to maximum shear stress

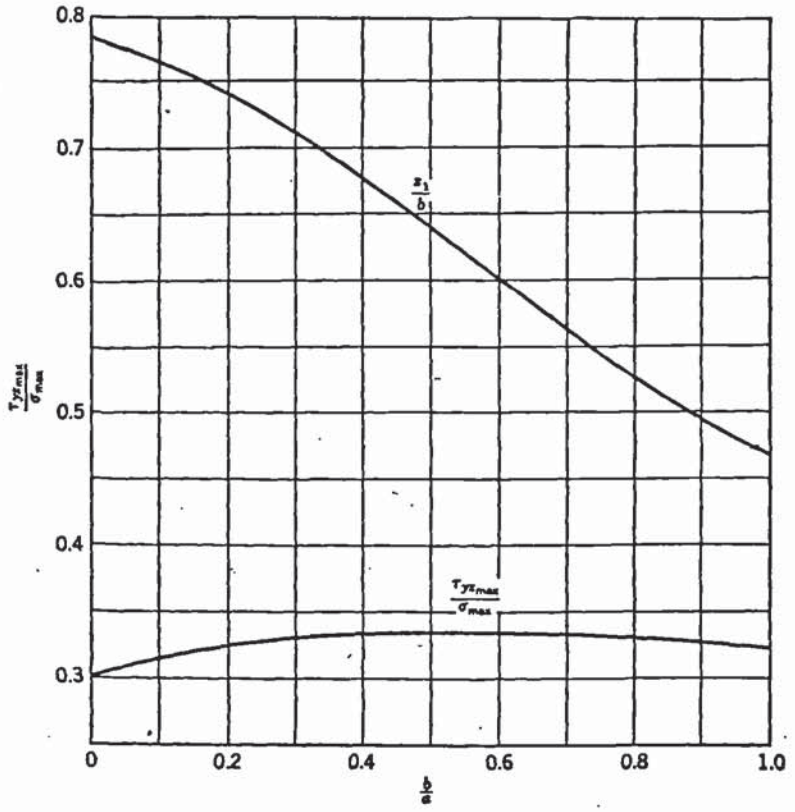

FIG. 5.12. $\tau_{yz\,max}/\sigma_{max}$ and z_1/b v b/a.

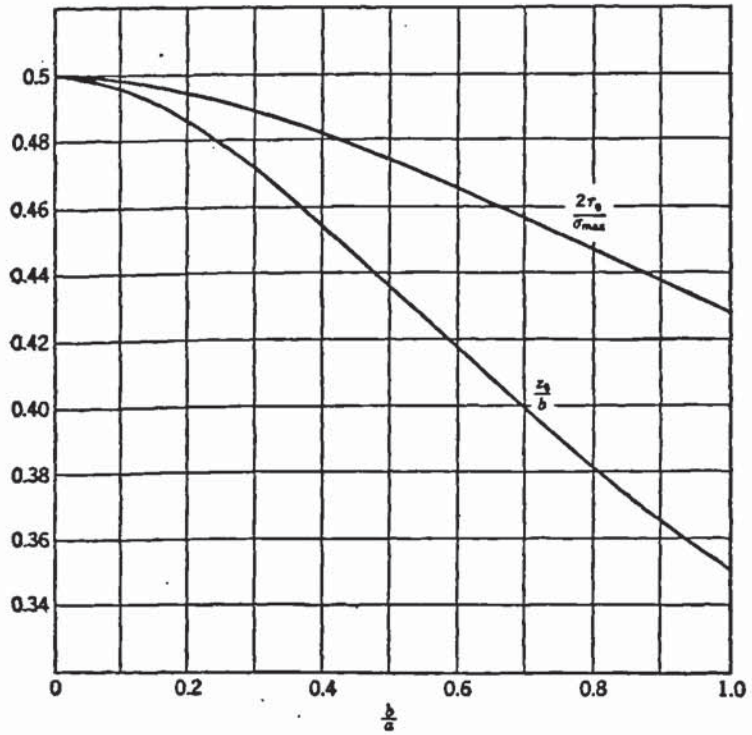

FIG. 5.14. $2\tau_0/\sigma_{max}$ and z_0/b versus b/a (concentrated normal load).

From Tedric Harris : Rolling Bearing Analysis

TABLE 5.1. Dimensionless Contact Parameters

$F(\rho)$	a^*	b^*	δ^*
0	1	1	1
0.1075	1.0760	0.9318	0.9974
0.3204	1.2623	0.8114	0.9761
0.4795	1.4556	0.7278	0.9429
0.5916	1.6440	0.6687	0.9077
0.6716	1.8258	0.6245	0.8733
0.7332	2.011	0.5881	0.8394
0.7948	2.265	0.5480	0.7961
0.83495	2.494	0.5186	0.7602
0.87366	2.800	0.4863	0.7169
0.90999	3.233	0.4499	0.6636
0.93657	3.738	0.4166	0.6112
0.95738	4.395	0.3830	0.5551
0.97290	5.267	0.3490	0.4960
0.983797	6.448	0.3150	0.4352
0.990902	8.062	0.2814	0.3745
0.995112	10.222	0.2497	0.3176
0.997300	12.789	0.2232	0.2705
0.9981847	14.839	0.2072	0.2427
0.9989156	17.974	0.18822	0.2106
0.9994785	23.55	0.16442	0.17167
0.9998527	37.38	0.13050	0.11995
1	∞	0	0

Hertz Stress Analysis -BBC Micro

```
100 DIM Y$(1),Z(3),T(3)
105 CLS
110 PRINT "HERTZ STRESS RESULTS"
120 REM R1 to 4 are the axes of the contacting bodies
130 R1=6.25:R2=6.25:R3=1E32:R4=1E32
140 PRINT:PRINT "ENTER LOAD"
150 INPUT L
160 REM P1 to 2 are the Poisson ratios for the two materials
170 P1=0.29:P2=0.29
180 PRINT:PRINT "ENTER YOUNGS MODULI IN MPa"
190 PRINT:PRINT "Enter the ball mat'l first"
200 INPUT E1,E2
205 E1=E1/9.806:E2=E2/9.806
210 C=(1/R1+1/R2+1/R3+1/R4)
220 D=((1/R1-1/R2)+(1/R3-1/R4))/C
230 CLS:PRINT "Curvature Difference 'D'= ";D
240 PRINT:PRINT "Consult Table 5.1(Harris) for a* and b*
    using D"
250 PRINT:PRINT "Note - For Circular Contact, D=0 and
    a*=b*=1"
260 PRINT:PRINT "ENTER a* AND b*"
270 INPUT ASTAR, BSTAR
275 PRINT ASTAR,C,L,P1,E1,P2,E2
280 A=ASTAR*(((3*L/(2*C))*(((1-P1^2)/E1)+
    ((1-P2^2)/E2)))^0.3333)
290 B=BSTAR*(((3*L/(2*C))*(((1-P1^2)/E1)+
    ((1-P2^2)/E2)))^0.3333)
300 Q=3*L/(2*PI*A*B)
310 CLS:VDU2
320 PRINT "Major Ellipse Axis 'a'= ";A," Minor Ellipse Axis
     'b'= ";B
330 PRINT "Curvature Sum 'C'= ";C," Curvature Difference
     'D'= ";D
340 PRINT "Load 'L'= ";L,"Contact Stress 'Q'= ";(Q*9.806)
350 VDU3
360 F=B/A
370 CLS:PRINT "B/A = ";F
380 PRINT:PRINT "Consult Fig.5.14(Harris) for 2T(0)/Max
    Stress(MPa) and Z(0)/B using F"
390 PRINT:PRINT "NOTE:For Circular Contact B/A=1 and these
    values are 0.4282 and 0.3505 respectively"
400 PRINT:PRINT "ENTER 2T(0)/Q AND Z(0)/B"
410 INPUT T,Z
420 T(0)=T*(Q*9.806)/2
430 Z(0)=Z*B
440 PRINT:PRINT "Consult Fig.5.12(Harris) for 2T(1)/Max
    Stress(MPa) and Z(1)/B using F"
450 PRINT:PRINT "NOTE:For Circular Contact B/A=1 and these
    values are 0.3235 and 0.4676 respectively"
460 PRINT:PRINT "ENTER 2T(1)/Q AND Z(1)/B"
470 INPUT T,Z
480 T(1)=T*(Q*9.806)/2
490 Z(1)=Z*B
500 CLS:VDU2
510 PRINT:PRINT "Orthogonal shear [Tau(0)max]= ";T(0)
520 PRINT:PRINT "Orthogonal depth [Z(0)]= ";Z(0);"mm"
530 PRINT:PRINT "Maximum shear [ Tau(1)max]= ";T(1)
540 PRINT:PRINT "Maximum depth [Z(1)]=   ";Z(1);"mm"A
```

```
550 VDU3
560 CLS
570 PRINT "Another Load ?"
580 INPUT Y$
590 IF Y$="N" THEN END ELSE IF Y$="Y" THEN 600 ELSE 570
600 PRINT "Same Moduli ?"
605 INPUT Y$
610 IF Y$="N" THEN 105 ELSE IF Y$="Y" THEN 620 ELSE 600
620 PRINT:PRINT "ENTER LOAD"
630 INPUT L
640 GOTO 210
650 END
```

10. Appendix 2

```
 49 REM **********************
 50 REM ** RESIDUAL STRESS **
 51 REM **********************
 80 DIM A(100):DIM PAR(5)
115 DEF PROCMENU
120 CLS:PRINTTAB(1,5);
130 PRINT "THE FOLLOWING OPTIONS ARE AVAILABLE:":PRINT
150 VDU31,8,9:PRINT"1.Enter Data."
160 VDU31,8,11:PRINT"2.Save Data."
170 VDU31,8,13:PRINT"3.Display and Modify Data."
180 VDU31,8,15:PRINT"4.Compute Results."
190 VDU31,8,17:PRINT"5.Plot Data Graphically."
195 VDU31,12,21:PRINT"WHICH?";:A$=GET$:PRINT A$
196  FOR WAIT=1 TO 1500:NEXT
200 FLAG=VAL(A$):IF FLAG>5 THEN 120
210 ON FLAG GOTO 400,550,700,840,7000
220 ENDPROC
400 CLS:REM ***DATA ENTRY***
405 VDU31,10,2:PRINT"**** DATA ENTRY ****"
410 PROCDATAIN
420 PROCMENU
550 REM
555 CLS:REM ***SAVE DATA***
557 VDU31,9,2:PRINT"**** DATA SAVING ****"
560 PROCCAUTION
570   VDU31,5,14:INPUT"DO   YOU   WISH   TO   GO   BACK   TO
THE MAIN MENU";Z3$
580 IF Z3$="Y" THEN 620
590 IF Z3$="N" THEN 600
595 GOTO 570
600 VDU31,5,17:INPUT"ENTER FILE NAME";F$
610 PROCWRITEFILE
620 PROCMENU
630 REM
700 REM
705 CLS:REM ***DISPLAY AND MODIFY***
707 VDU31,6,2:PRINT"**** DATA MODIFICATION ****"
710 VDU31,7,5:INPUT"IS THE DATA ON DISC";Z4$
720 IF Z4$="Y" THEN 740
730 IF Z4$="N" THEN 780
735 CLS:FOR WAIT=1 TO 1000:NEXT:GOTO710
740 VDU31,7,8:INPUT"ENTER FILE NAME";F$
750 PROCREADFILE
760 PROCDATAMOD
770 GOTO 830
780 PROCCAUTION
790 VDU31,5,14:INPUT"DO YOU WISH TO GO BACK TO THE MAIN
    MENU";Z5$
800 IF Z5$="N" THEN 820
810 IF Z5$="Y" THEN 830
815 GOTO 790
820 PROCDATAMOD
830 PROCMENU
840 CLS:REM ***COMPUTATION***
845 VDU31,10,2:PRINT"**** COMPUTATION ****"
850 VDU31,5,5:INPUT"ENTER SAMPLE NO.";C$
860 VDU2:PRINT"SAMPLE NO."; C$:VDU3
865 VDU31,5,8:INPUT"IS THE DATA ON DISC";Z6$
870 IF Z6$="N" THEN 890
```

```
 880 IF Z6$="Y" THEN 1030
 885 GOTO 865
 890 PROCDATAIN
 900 PROCCOMPUTE
 910 REM
 920 VDU2:PRINT "PEAK POSITION FOR PSI ";P;" IS ";PK
 930 PRINT "SQR(VK)= ";SQR (VK):VDU3
 940 IF P<>0 THEN 980
 950 T1=PK:V2=PK
 960 GOTO 890
 970 REM
 980 T2=PK:V2=VK
 990 VDU2:PRINT "DELTA 2 THETA= ";(T1-T2)
1000 PRINT "STD(2 THETA)= ";SQR (V1+V2):VDU3
1010 PROCRESCALC
1020 GOTO 1190
1030 VDU31,5,11:INPUT"ENTER FILE NAME FOR PSI=0";F$
1040 PROCREADFILE
1050 PROCCOMPUTE
1060 REM
1070 VDU2:PRINT "PEAK POSITION FOR PSI= ";P;" IS ";PK
1080 PRINT "SQR(VK)= ";SQR (VK):VDU3
1090 T1=PK:V1=VK:VDU3
1100 VDU31,5,14:INPUT"ENTER FILE NAME FOR PSI=45";F$
1110 PROCREADFILE
1120 PROCCOMPUTE
1130 REM
1140 VDU2:PRINT "PEAK POSITION FOR PSI= ";P;" IS ";PK
1150 PRINT "SQR(VK)= ";SQR (VK):VDU3
1160 T2=PK:V2=VK
1165 PRINTTAB(2,20);"PRESS A KEY TO CONTINUE":A$=GET$
1170 PROCRESCALC
1180 REM
1190 PROCMENU
1200 END
1500 DEF PROCDATAIN
1505 CLS:REM ***DATA INPUT SUBROUTINE***
1507 VDU31,10,2:PRINT"**** DATA INPUT ****"
1510 VDU31,5,6:INPUT "PAR1. STARTING ANGLE (201) ";PAR(1)
1520 VDU31,5,8:INPUT "PAR2. ANGLE PSI ";PAR(2)
1530 VDU31,5,10:INPUT "PAR3. NUMBER OF POINTS ";PAR(3)
1540 VDU31,5,12:INPUT "PAR4. STEP (2D0) ";PAR(4)
1550 VDU31,5,14:INPUT "PAR5. NUMBER OF COUNTS ";PAR(5)
1560 FOR I=1 TO 100
1562   TIME=0
1565   NEXT I
1570 DUMMY=PAR(1)-PAR(4)
1580 FOR J=1 TO PAR(3)
1590   DUMMY=DUMMY+PAR(4)
1600   PRINTTAB(5);J;TAB(17);DUMMY;TAB(29);
1610   INPUT A(J);
1620   NEXT J
1630 ENDPROC
2000 DEF PROCWRITEFILE
2005 REM ***WRITE TO FILE***
2010 X=OPENOUT F$
2015 PTR£X=6*100
2017 CLOSE£X
2018 X=OPENUP F$
2020 FOR I=1 TO 5
```

```
2030   PRINT£X,PAR(I)
2045   NEXT I
2050 FOR J=1 TO PAR(3)
2070   PRINT£X,A(J)
2100   NEXT J
2110 CLOSE£X
2120 ENDPROC
3000 DEF PROCREADFILE
3005 REM ***READ FROM FILE***
3010 X=OPENIN F$
3020 FOR I=1 TO 5
3030   INPUT£X,PAR(I)
3050   NEXT I
3060 FOR J=1 TO PAR(3)
3080   INPUT£X,A(J)
3107   NEXT J
3110 CLOSE£X
3120 ENDPROC
4000 DEF PROCDATAMOD
4005 CLS:VDU14
4010 REM ***DISPLAY AND MODIFY***
4020 VDU31,6,2:PRINT"**** DATA MODIFICATION ****"
4030 VDU31,5,6:PRINT"PAR1. STARTING ANGLE (201) ";PAR(1)
4040 VDU31,5,8:PRINT"PAR2. ANGLE PSI ";PAR(2)
4050 VDU31,5,10:PRINT"PAR3. NUMBER OF POINTS ";PAR(3)
4060 VDU31,5,12:PRINT"PAR4. STEP (2D0) ";PAR(4)
4070 VDU31,5,14:PRINT"PAR5. NUMBER OF COUNTS ";PAR(5)
4075 DUMMY=PAR(1)-PAR(4)
4080 FOR J=1 TO PAR(3)
4090   DUMMY=DUMMY+PAR(4)
4100   PRINT J;"      ";DUMMY;"      ";A(J)
4106   N=J
4110   NEXT J
4120 PRINT
4130 INPUT "ANY CORRECTIONS ";Z1$
4140 IF Z1$="Y" THEN 4160
4150 IF Z1$="N" THEN 4310
4155 GOTO 4130
4160 INPUT "WHICH ITEM DO YOU WISH TO CHANGE_(PARAMETER
     OR TIME) ";Z2$
4170 IF Z2$="PARAMETER" THEN 4190
4180 IF Z2$="TIME" THEN 4250
4185 GOTO 4160
4190 INPUT "WHICH PARAMETER ";I
4200 INPUT "ENTER NEW VALUE ";PAR(I)
4210 INPUT "ANY MORE ";Z3$
4220 IF Z3$="N" THEN 4120
4230 IF Z3$="Y" THEN 4190
4240 GOTO 4210
4250  INPUT "WHICH DATA ITEM ";J
4260 INPUT "ENTER NEW VALUE ";A(J)
4270 INPUT "ANY MORE ";Z4$
4280 IF Z4$="N" THEN 4120
4290 IF Z4$="Y" THEN 4250
4300 GOTO 4270
4310 VDU15:ENDPROC
5000 DEF PROCCOMPUTE
5005 REM ***MAIN PEAK COMPUTATION***
5010 CM=0:YB=0:S2=0:C=0
5020 N=(PAR(3)-1)/2
```

```
 5030 CM=(N*(N+1)*(2*N+1)*(2*N+3)*
      (2*N-1)*(2*N+3)*(2*N-1))/2700
 5040 P=PAR(2)*PI/180:D=PAR(4):CT=PAR(5)
 5050 S1=PAR(1)-PAR(4)
 5060 FX=-(2*N+3)*(2*N-1)/30
 5070 M=N*(N+1)/3
 5080 M1=0:M2=0
 5090 FOR X=-N TO N
 5100   S1=S1+PAR(4)
 5110   J=X+N+1
 5120   Y=A(J)
 5140   S=S1*PI/180
 5150   F=2*(SIN(S/2)^2)/((1+COS(S)^2)*(1-TAN(P)/TAN(S/2)))
 5160   Y=Y/F
 5170   C=C+Y
 5180   M1=M1+X*Y
 5190   M2=M2+(X^2-M)*Y
 5200   NEXT X
 5210 YB=C/(2*N+1):S2=(YB^2)/(CT)
 5220 K=FX*M1/M2
 5230 VK=((D^2*S2*CM)/(M2^2))*(1+60*K^2/((2*N+3)*(2*N-1)))
 5240 PK=(S1-N*D)+K*D
 5250 P=P*180/PI
 5260 ENDPROC
 6000 DEF PROCRESCALC
 6003 REM ***STRESS COMPUTATION***
 6005 CLS
 6007 VDU31,5,2:PRINT"**** STRESS CALCULATION *****"
 6010 VDU31,7,5:INPUT"WHAT YOUNG'S MOD. ";E
 6015 VDU31,7,7:INPUT"WHAT POISSON RATIO ";Q
 6020 T1=T1*PI/360
 6030 T2=T2*PI/360
 6040 P=P*PI/180
 6050 NUM=(SIN(T1)/SIN(T2)-1)
 6060 DEN=(1+Q)*(SIN(P)^2)
 6070 Z=E*NUM/DEN
 6080 VDU31,3,12:VDU2:PRINT "THE RESIDUAL STRESS IS ";Z ;
      "MPA":VDU3
 6085  PRINTTAB(2,20);"PRESS A KEY TO CONTINUE"
 6090 A$=GET$:PROCMENU:ENDPROC
25000 DEF PROCCAUTION
25050 PRINTTAB(15,7);"CAUTION":VDU10:PRINT"THIS ROUTINE WILL
      NOT WORK UNLESS DATA  HAS BEEN ENTERED."
25100 ENDPROC
```

Residual Stress - Sine Square Psi Program

```
  1 ON ERROR VDU3:REPORT:PRINT " AT ";ERL:END
  5 DIM P(5),T(5),D(5),DELTA(5),PSIS(5),A$(6),SAM$(2)
 10 REM *** Sine Squared Psi Program ***
 15 CLS:PRINTTAB(4)"*** SINE SQUARED PSI PROGRAM ***"
 20 PRINT:PRINT " Radiation Wavelength ";:INPUT TAB(25) A;
 25 N=0:I=0:X=0
 40 FOR N=1 TO 4
 50   PRINT " Psi Angle ";N;" ";:INPUT TAB(25) P(N);
 60   PRINT " Psi=";P(N);" Two-Theta Angle ";:INPUT
      TAB(25) T(N);
 70   REM * Calculation *
 80   D(N)=(A/(2*SIN(RAD(T(N)/2))))
 90   DELTA(N)=(D(N)-D(1))/D(1)
100   PSIS(N)=SIN(RAD(P(N)))^2
110   CLS
120   NEXT N
130 REM * Printout of Data *
140 X=1:Y=4:I=0
145 PRINT "SAMPLE IDENT ":INPUT SAM$;
148 MODE 3
150 *FX6,1
152 VDU2
155 PRINTTAB(X,Y-2)"SAMPLE :";SAM$
158 RESTORE
160 FOR I=1 TO 4
165   READ A$(I)
170   PRINTTAB(X) A$(I);
180   X=X+20
190   NEXT I
210 FOR N=1 TO 4 :Y=Y+2
220   PRINTTAB(2);P(N);TAB(20);PSIS(N);TAB(40);
      D(N);TAB(60);DELTA(N)
230   Y=Y+2
240   NEXT N
250 VDU3
260 Z=INKEY(500)
300 DATA Psi,Sin^2Psi,d,Dd/d0
390 MODE 7
400 REM * Regression Analysis *
410 X=0:Y=0:N=1
430 C=0:D=0:E=0:F=0:G=0:H=0:J=0
440 FOR N=1 TO 4
450   C=C+(PSIS(N)*DELTA(N)):D=D+PSIS(N)
460   E=E+DELTA(N):F=F+(PSIS(N)^2)
470   G=G+(DELTA(N)^2)
480   NEXT N
490 H=D^2:J=E^2:N=4
500 B=((N*C)-(D*E))/((N*F)-H)
510 AA=(E-(B*D))/N
515 R=((N*C)-(D*E))/SQR(((N*F)-H)*((N*G)-J))
520 PRINT "POISSONS RATIO FOR THE MATERIAL ":INPUT M;
530 PRINT "AND THE YOUNGS MODULUS (MPa) ":INPUT Z;
540 Q=(Z/(1+M))*B
545 VDU2
550 PRINT"THE EQUATION FORMAT IS:-"
560 PRINT:PRINTTAB(17)"y=A+Bx"
570 PRINT:PRINTTAB(2)"A= ";AA;TAB(2)"B= ";B
580 PRINT:PRINTTAB(2)"r= ";R
```

```
590 PRINT:PRINT"RESIDUAL STRESS = ";Q;"(MPa)"
600 VDU3
610 PRINT "ANOTHER SET OF DATA ":INPUT Y$;
615 IF Y$="N" THEN END ELSE 620
620 IF Y$="Y" THEN PRINT "SAME RADIATION ":INPUT Y$;
630 IF Y$="N" THEN GOTO 10 ELSE 640
640 IF Y$="Y" THEN CLS:GOTO 25
```

11. References.

1 P.S.Houghton;Ball & Roller Bearings;Applied Science Publishers Ltd. ;London; 1976

2 R.K.Allen;Rolling Bearings;Pitman & Sons Ltd.; London; 1960

3 D.Scott;Proceedings of a Symposium;"Fatigue Rolling Contact";Inst. Mech. Eng.; 1964;p103-105

4 J.M.Hampshire;J.V.Nash;G.E.Hollox;"Materials Evaluation by Flat Washer Testing";Rolling Contact Fatigue Testing of Bearing Steels;ASTM STP771;Ed.-J.J.C.Hoo;ASTM; 1982;p46-66

5 D.Scott;"Rolling Contact Fatigue";Treatise on Materials Science & Technology;vol13; 1979;p321-361

6 R.L.Johnson;E.E.Bisson;SAE Journal;63;6; 1955

7 Fred.T.Schuller;"Operating Characteristics of a Large Bore Rolling Bearing to Speeds of 3*10E6 DN";NASA Technical Paper 1413; 1979

8 J.R.Brown;P.F.Bogardus;R.D.Dayton;D.R.Schulze; "Evaluation of Powder Processed Metals for Turbine Engine Ball Bearings";Rolling Contact Fatigue Testing of Bearing Steels;ASTM STP771;Ed-J.J.C.Hoo;ASTM; 1982;p323-341

9 D.Scott;J.Blackwell;Proceedings of the Institution of Mechanical Engineers;London;180;3K; 1966;p32-37

10 E.N.Bamberger;E.V.Zaretsky;H.Signer;"Endurance and Failure Characteristic of Main-Shaft Jet Engine Bearing at $3*10^6$DN";Journal of Lubrication Technology;vol98; no4; Oct1976;p580-585

11 J.Boussinesq;Compte. Rend.;114;Paris; 1892;p1465

12 H.Hertz;"On the Contact of Rigid Elastic Solids and on Hardness";Miscellaneous Papers;Macmillan & Co.;London; 1896;p163-183

13 S.P.Timoshenko;J.N.Goodier;Theory of Elasticity; McGraw Hill;New York;3rd Edition; 1970

14 Tedric A.Harris;Rolling Bearing Analysis;John Wiley & Sons Inc.; 1966

15 W.J.Davies;K.L.Day;"Surface Fatigue in Ball Bearings, Roller Bearings and Gears in Aircraft Engines"; Proceedings of the Symposium on Fatigue in Rolling Contact;Inst. Mech. Eng.;London; March 28th 1963;p23-40

16 J.Halling;K.A.Nuri;"Contact of Surfaces";Principles of Tribology;J.Halling-Ed.; 1983

17 H.R.Thomas;V.A.Hoersch;"Stresses due to the Pressure of one Elastic Solid upon Another";University of Illinois Bulletin 212; 1930

18 A.B.Jones;"Analysis of Stresses and Deflections";New Departure Engineering Data; 1946;p12-22

19 G.A.Roberts;J.C.Hamaker;A.R.Johnson;Tool Steels;ASM Metals Park;Ohio; 1962

20 D.J.Blickwede;M.Cohen;G.A.Roberts;Trans ASM;42; 1950; p1161

21 T.Mukherjee;"Physical Metallurgy of High Speed Steels" ;ISI P126; 1970;p80-96

22 G.Steven;A.E.Nehrenberg;T.V.Phillips;Trans ASM;57; 1964;p925

23 F.Kayser;M.Cohen;Metals Progress;6; 1952;p79

24 M.Cohen;M.P.Gordon;Trans ASM;vol30; 1952;p569

25 W.W.Cias;Climax Molybdenum Co. Internal Report; RP-54-70-09; 1971

26 S.A.Horton;"The Relationship of Segregation Structure and Properties in High Speed Steel";PhD Thesis; University of Aston in Birmingham; Sept 1980

27 Sanderson Kayser Ltd.;Steel Data Sheet for Kelock A157 5-6-2 High Speed Steel

28 P.Payson; Trans ASM; 51; 1959; p60

29 R.W.K.Honeycombe;"Some Strengthening Mechanisms in Alloy Steels";ISI Special Report 86 - Metallurgical Developments in High Alloy Steels;Joint BISRA-ISI Conference held at Scarborough; 2-4June 1964

30 R.W.K.Honeycombe;"Structure and Strength of Alloy Steels";Reprint from the Climax Molybdenum Co. Ltd.; London

31 K.Kuo; JISI; vol174; 1953; p223

32 C.Dawes;D.F.Tranter;"Production Gas Carburising Control";Heat Treatment of Metals;4; 1974;p121-130

33 C.Dawes;R.J.Cooksey;"Surface Treatment of Engineering Components";Heat Treatment of Metals 1966;p77-92

34 R.Bennett;"Lean Endothermic Gas for Case Hardening"; Lucas Electrical Co. Internal Report;RB/BJ/10472; Oct 1980

35 H.C.Child;S.A.Plumb;"Optimisation of Tool and Die Heat Treatment";An Interim SERC Project Report;No GR/A/75729

36 A.J.F.Paterson;C.G.Smith;"An Appraisal of Gaseous Carriers for Carburising";Heat Treatment of Metals; 2; 1981;p27-32

37 H.C.Child;S.A.Plumb;G.Reeves;"The Effect of Thermochemical Treatments on the Mechanical Properties of Tool Steel"Part I & II;Materials and Design;vol4; Feb/March & April-May 1983;p681-686, 716-722

38 A.G.Duce;C.Dawes;"Effects of Sulfinuz Treatments and Activated Nitriding on the Fatigue Strength of Mild and Alloy Steels";Lucas Gas Turbine Research Laboratory Report; B.48,135; 1962

39 T.Bell;"Ferritic Nitrocarburising";Heat Treatment of Metals; 2; 1975;p39-49

40 R.H.Shoemaker;"Advances in Low Temperature Liquid Nitriding";SAE 750195; Feb 1975

41 C.Dawes;D.F.Tranter;C.G.Smith;"Reappraisal of Nitrocarburising and Nitriding when Applied to Design and Manufacture of Non-Alloy Steel Automobile Components";Heat Treatment '79;The Metals Society; May 1979;p60-68

42 R.Davies;C.G.Smith;"A Review of the Properties and Application of Low Temperature Nitrocarburising Treatments";Lucas Electrical Co. Internal Report;E & D 70248; April 1976

43 R.T.McKenzie;J.Stokes;"The Production of Wear Resistant Layers at Low Temperature";Lucas Electrical Co. Internal Report;E & D 70251; July 1976

44 W.Schroter;W.Graf;"Gas Mixtures and Process for Gas Nitriding";Patent No 1441092; June 1976

45 V.O.Homerberg;J.P.Walstead;Nitriding Symposium; Transactions of the American Society for Steel Treating; 16; Oct 1929;p67-110

46 N.L.Loh;"Plasma Nitriding and the Fatigue Properties of 722M27 Steel";PhD Thesis;Liverpool University; 1980

47 J.J.Egan; U.S. Patent No 1837256; 1931

48 Malcolm; U.S. Patent No 1929392; 1933

49 B.Edenhofer;"Physical and Metallurgical Aspects of Ionitriding" -Part 1;Heat Treatment of Metals;1; 1974;p59-67

50 A.M.Staines;T.Bell;"Plasma Nitriding of High Alloy Steels"; Proceedings of Conference on Heat Treatment Methods and Media;University of Aston in Birmingham; 1979;p58-69

51 C.K.Jones;S.W.Martin;D.J.Sturges;M.Hudis;"Ion Nitriding";Heat Treatment '73;The Metals Society; London; 1975;p71-77

52 G.J.Dixon;S.A.Plumb;H.C.Child;"Processing Aspects of Plasma Nitriding";Heat Treatment '81;The Metals Society; London; Sept 1981;p137-146

53 T.Bell;Z.L.Zhang;J.Lanagan;A.M.Staines; "Plasma Nitriding Treatments for Enhanced Wear and Corrosion"; Proceedings of Conference on Surface Treatment for Wear and Corrosion Resistance; Institution Corrosion Science and Technology; Newcastle; 1983;p164-177

54 A.M.Staines;"Thermochemical Treatments in a Glow Discharge Environment"; Metals and Materials;vol1;12; Dec 1985;p739-744

55 H.Michel;M.Gantois;Memoirs Scientifique de la Revue de Metalurgie;69;10; 1972; p739-749

56 B.Edenhofer;"The Ionitriding Process-Thermochemical Treatment of Steel and Cast Iron Materials";The Metallurgist and Materials Technologist; Aug 197;p421-426

57 S.C.Brown;Basic Data of Plasma Physics;John Wiley and Sons; 1959

58 F.W.Aston;Proceedings of the Royal Society (London);79(A); 1906; p80-95

59 M.Hudis;Journal of Applied Physics;44(4); April 1973; p1489-1496

60 P.Sigmund;Physical Review;184(2); Aug 1969; p383-416

61 F.H.Field;J.L.Franklin;Electron Impact Phenomena;Academic Press; 1957

62 K.H.Jack;"Nitriding";Heat Treatment '73;The Metals SocietyLondon; December 1973

63 H.C.F.Rozendaal;P.F.Colijn;E.J.Mittemeijer;"Morphology, Composition and Residual Stresses of Compound Layers of Nitrocarburised Iron and Steels";Heat Treatment '84;The Metals Society;London; May 1984

64 P.Astley;"Liquid Nitriding - Development and Present Applications";Heat Treatment '73;The Metals Society;London; December 1973

65 D.H.Jack;B.J.Lightfoot;"The Kinetics of Nitriding with and without Layer Formation";Heat Treatment '73;The Metals Society;London; December 1973

66 P.Ferguson;K.H.Jack;"The Quench-Ageing and Strain-Ageing of Nitrogen-Ferrite";Heat Treatment '81;The Metals Society;London; September 1981

67 B.Billon;A.Hendry;"White Layer Formation on Nitrided Stainless Steel";Heat Treatment '84;The Metals Society;London; May 1984

68 G.G.Tibbets;"Role of Nitrogen Atoms in Ion-Nitriding";Journal of Applied Physics;vol45;11; November 1974; p5072-5073

69 M.Hudis;Journal of Applied Physics;vol44;4; April 1973; p1489-1496

70 K.Keller;"Layer Structure of Iron Materials Nitrided in a Glow Dischatge";Harterei-Technische Mitteilungen;26; 1971; p120-130;[Translation INC 746-114]

71 E.Lehrer;Z. Electrochem;36; 1930; p383-392

72 B.Edenhofer;"Physical and Metallurgical Aspects of Ionitriding - Part2";Heat Treatment of Metals;2; 1974; p59-67

73 M.Zlatanivić;B.Tomčik;"Plasma Nitriding in a Low Power Discharge";Heat Treatment '84;The Metals Society;London; May 1984

74 A.M.Staines;T.Bell;"Technological Importance of Plasma Induced Nitrided and Carburised Layers on Steel";Thin Solid Films;86; 1981; p201-211

75 K-T.Rie;Th.Lampe;"Effect of Carbon on the Microstructure of Plasma Nitrocarburised Steels";Heat Treatment '84;The Metals Society;London; 1984

76 H.C.F.Rozendaal;E.J.Mittemeijer;P.F.Colijn;P.J.Van Der Schaaf;"The Development of Nitrogen Cocentration Profiles on Nitriding Iron";Metallurgical Transactions Abstracts;vol14(A); March 1983; p395-399

77 B.Edenhofer;T.J.Bewley;"Low Temperature Ion Nitriding: Nitriding at Temperatures Below 500°C for Tools and Precision Machine Parts";Heat Treatment '76;The Metals Society;London; May 1976

78 C.V.Robino;O.T.Inal;"Ion Nitriding Behaviour of Several Low Alloy Steels";Materials Science and Engineering;59; 1983; p79-90

79 O.T.Inal;C.V.Robino;"Structural Characterisation of some Ion-Nitrided Steels";Thin Solid Films;95; 1982; p195-207

80 Yu.M.Lakhtin;Ya.D.Kogan;G.A.Solodkin;"Strengthening Mechanism of Nitrided Layers of Alloy Steels"; Translated from Metallovedenie i Termichaskaya Obrabotka Metallov;no2; February 1983; p25-29

81 Residual Stress Measurement by X-Ray Diffraction;SAE Handbook J784a;SAE;Warrendale,USA; 1971

82 H.C.Child;"Residual Stress in Heat-Treated Components";Heat Treatment of Metals;4; 1981; p89-94

83 D.Kirk;"The Role of Residual Stress Measurement in Improving Heat Treatment";Heat Treatment of Metals;3; 1985; p77-80

84 E.J.Mittemeijer;H.C.F.Rozendaal;P.F.Colijn;P.J.van der Schaaf;R.Th.Furnee;"The Microstructure of Nitrocarburised Steels";Heat Treatment '81;The Metals Society;London; September 1981

85 D.R.Gabe;J.M.West;"The Measurement of Internal Stress in Electrodeposits";Transactions of the Institute of Metal Finishing;vol40; Spring 1963; p6-12

86 C.A.Stickels;A.M.Janotik;"Controlling Residual Stresses in 52100 Bearing Steel by Heat Treatment";Proceedings of Symposium of Case Hardened Steels: Microstructural and Residual Stress Effects;AIME;Atlanta,USA; March 1983; p21-40

87 B.D.Cullity;Elements of X-Ray Diffraction;Addison-Wesley Publishing Co Inc; 1978

88 R.E.Smallman;Modern Physical Metallurgy;Butterworths;London; 1976

89 L.H.Van Vlack;Materials Science for Engineers;Addison-Wesley Publishing Co Inc.; 1974

90 J.M.Cowling;J.W.Martin;"Fatigue of Nitrided EN41B Steel: Effect of Internal Stress Distribution;Metals Technology;8;8; August 1981; p289-296

91 A.H.Cottrell;D.Hull;Proceedings of the Royal Society;A242;London; 1957; p211

92 N.F.Mott;Acta Metallurgia;6; 1958; p195

93 J.M.Cowling;J.W.Martin;"Effect of Internal Residual Stresses on the Fatigue Behaviour of Nitrided EN41B Steel";Heat Treatment '79;The Metals Society;London; May 1979

94 Chongmin Kim;"Fracture of Case-Hardened Steels and Residual Stress Effects";Proceedings of Symposium of Case Hardened Steels: Microstructural and Residual Stress Effects;AIME;Atlanta,USA; March 1983; p59-87

95 D.E.Diesburg;C.Kim;W.Fairhurst;"Microstructural and Residual Stress Effects on the Fracture of Case Hardened Steels";Heat Treatment '81;The Metals Society;London; September 1981

96 B.K.Jones;J.W.Martin;Metals Technology;5;6; July 1978; p217-221

97 T.Bell;N.L.Loh;"The Fatigue Characteristics of Plasma Nitrided Three Percent Cr-Mo Steel";Journal of Heat Treating;vol2;no3; June 1982; p232-237

98 H.C.Child;S.A.Plumb;G.Reeves;"Optimisation of Tool and Die Heat Treatment";SERC Report No GR/A/75729; 1982

99 D.Kirk;Private Communication on Residual Stress Testing and Techniques; 1983

100 D.Kirk;"Experimental Features of Residual Stress Measurement by X-Ray Diffractometry";Strain;Vol7;no1; January 1971

101 D.L.Sikarskie;"On a Series Form of Correction to Stresses Measured Using X-Ray Diffraction";Transactions of the Metallurgical Society of AIME;vol239; April 1967; p577-579

102 M.G.Moore;W.P.Evans;"Mathematical Correction for Stress in Removed Layers in X-Ray Diffraction Residual Stress Analysis"; SAE Transactions;vol66; 1958; p340-345

103 D.Scott;"The Effect of Mathematical Properties, lubricant, and Enviroment on Rolling Contact Fatigue";Proceedings of Symposium on Fatigue in Rolling Contact; Institute of Mechanical Engineers, London; March 1963; p103-115

104 P.H.Frith;"Fatigue Tests on Rolled Alloy Steels Made in Electric and Open-Hearth Furnaces";Iron & Steel Institute;Special Report;no50; 1954

105 E.V.Zaretsky;W.J.Anderson;"Relation Between Rolling Contact Fatigue Life and Mechanical Properties for Several Aircraft Bearing Steels";Proceedings of the ASTM; June-July 1960;p627-649

106 E.V.Zaretsky;R.J.Parker;W.J.Anderson"NASA Five Ball Fatigue Tester-over 20 Years of Research";Rolling Contact Fatigue Testing of Bearing Steels;ASTM STP771;J.J.C.Hoo-Ed;ASTM; 1982; p5-46

107 K.L.Day;"Unisteel Testing of Aircraft Engine Bearing Steels";Rolling Contact Fatigue Testing of Bearing Steels;ASTM STP771;J.J.C.Hoo-Ed;ASTM; 1982;p67-85

108 E.N.Bamberger;J.C.Clark;"Development and Application of the RCF Test Rig";Rolling Contact Fatigue Testing of Bearing Steels;ASTM STP771;J.J.C.Hoo-Ed;ASTM; 1982;p85-106

109 S.Ito;N.Tsushima;H.Muro;"Accelerated RCF Test by a Cylinder to ball Rig;Rolling Contact Fatigue Testing of Bearing Steels;ASTM STP771;J.J.C.Hoo-Ed;ASTM; 1982;p125-136

110 N.J.T.Cotterill;"A Study of Vacuum Carburising and Ionitriding on the Surface Fatigue Properties of Two High Speed Bearing Steels";MSc Thesis;University of Aston in Birmingham; 1982

111 E.J.Mittemeijer;"The Relation Between Residual Macro-and Microstress and Mechanical Properties of Case-Hardened Steels";Proceedings of Conference on Case Hardened Steels: Microstructural and Residual Stress Effects;Metallurgical society of AIME;Atlanta,USA; March 1983; p161-187

112 T.Ericsson;S.Sjostrom;M.Knuutila;B.Hildenwall; "Predicting Residual Stresses in Cases";Proceedings of Conference on case Hardened Steels: Microstructural and Residual Stress Effects;Metallurgical Society of AIME;Atlanta,USA; March 1983; p113-139

113 W.J.Harris;Metallic Fatigue;Pergamon Press;London; 1961

114 P.H.Frith;"Fatigue Tests on Crankshaft Steels";Journal of the Iron and Steel Institute;vol159; 1948; p335

115 M.F.Garwood;H.H.Zurburg;M.A.Erickson;American Society for Metals;Ohio,USA; 1951; p1-77